Investigation and comparison of GaN nanowire nucleation and growth by the catalyst-assisted and self-induced approaches

DISSERTATION

zur Erlangung des akademischen Grades

doctor rerum naturalium
(Dr. rer. nat.)
im Fach Physik

eingereicht an der
Mathematisch-Naturwissenschaftlichen Fakultät I
Humboldt-Universität zu Berlin

von
Frau M.Sc. Caroline Chèze
geboren am 06.03.1977 in Chambéry, Frankreich

Präsident der Humboldt-Universität zu Berlin:
Prof. Dr. Dr. h.c. Christoph Markschies

Dekan der Mathematisch-Naturwissenschaftlichen Fakultät I:
Prof. Dr. Lutz-Helmut Schön

Gutachter:
1. Prof. Dr. H. Lüth
2. Prof. Dr. W. T. Masselink
3. Prof. Dr. H. Riechert

eingereicht am: 20.08.2009
Tag der mündlichen Prüfung: 04.03.2010

Abbreviations

AFM	atomic force microscopy
C-plane	GaN growth along [0001]
CBED	convergent beam electron diffraction
cw-PL	continuous wave photoluminescnece
(D^0,X_A)	neutral to donor related bound exciton
EDXS	energy dispersive x-ray spectroscopy
EELS	electron energy-loss spectroscopy
ES barrier	Ehrlich-Schwoebel barrier
FFT	fast Fourier transform
FWHM	full width at half maximum
Ga	Gallium
ML	monolayer
μ PL	micro-photoluminescence
MOVPE	metal-organic vapor-phase epitaxy
N	neutral atomic nitrogen
NW	nanowire
PAMBE	plasma-assisted molecular beam epitaxy
PL	photoluminescence
QMS	quadrupole mass spectrometry
RF	radio frequency
RBS	Rutherford back scattering
RHEED	reflection high-energy electron diffraction
RT	room temperature
SEM	scanning electron microscopy
SAED	selected-area electron diffraction
SF	stacking fault
SK	Stranski-Krastanov
STM	scanning tunneling microscopy
TEM	transmission electron microscopy
1D, 2D, 3D	one-, two-, three-dimensional
UV	ultra violet
VW	Volmer-Weber
WZ	wurtzite
XEDS	X-ray energy dispersive spectrometry
XRD	X-Ray diffraction
XTEM	cross-sectional transmission electron microscopy
ZB	zinc blende

Abstract

This work focuses on the nucleation and growth mechanisms of GaN nanowires (NWs) by molecular beam epitaxy (MBE). The two main novelties of this study are the intensive employment of in-situ techniques and the direct comparison of self-induced and catalyst-induced NWs. On silicon substrates, GaN NWs form in MBE without the use of any external catalyst seed. On sapphire, in contrast, NWs grow under identical conditions only in the presence of Ni seeds. NW nucleation was studied in situ by reflection high-energy electron diffraction (RHEED) in correlation with line-of-sight quadrupole mass spectrometry (QMS). The latter technique allows to monitor the incorporated amount of Ga.

For the catalyst-assisted approach, three nucleation stages were identified: first incorporation of Ga into the Ni seeds, second transformation of the seed crystal structure due to Ga accumulation, and last GaN growth under the seeds. The crystalline structure of the seeds during the first two stages is in accord with the Ni-Ga binary phase diagram and evidenced that only Ga incorporates into the Ni particles. GaN forms only after the Ga concentration is larger than the one of Ni, which is in agreement with the Ni-Ga-N ternary phase diagram. The observation of diffraction patterns generated by the Ni-Ga seed particles during the whole nucleation evidences the solid state of the seeds. Therefore nucleation is ruled by the vapor-solid-solid mechanism. Moreover, the QMS study showed that it is not Ga incorporation into Ni but GaN nucleation itself that limits the growth processes.

For the self-induced NWs, QMS and RHEED investigations indicate very similar nucleation processes on Si(001) and Si(111) and two nucleation stages were identified. Transmission electron microscopy on samples grown on Si(001) revealed that the first stage is characterized by the competition between the nucleation of crystalline Si_xN_y and GaN. During this stage, the Si surface strongly roughens by the formation of pits and Si mounds. At the same time, very few GaN islands nucleate. During the second stage, the amorphization of the Si_xN_y layer leads to the massive nucleation of GaN islands that are free of the substrate lattice constraint and therefore form in the wurtzite (WZ) structure.

The processes leading to NW nucleation are fundamentally different for both approaches. In the catalyst-assisted approach, Ga strongly reacts with the catalyst Ni particles whose crystal structure and phases are decisive for the NW growth. In the catalyst-free approach, N forms an interfacial layer with Si before the intense nucleation of GaN starts, and the lattice-mismatch to the substrate plays the most important role.

Both approaches are viable to produce NWs within the same range of substrate temperatures and *V/III* ratios, provided the latter is larger than one (N-excess). Both yield monocrystalline GaN NWs of WZ structure, which grow in the Ga-polar direction. However, strong differences are also observed. First, the catalyst-assisted NWs are longer than the catalyst-free ones after growth under identical conditions (duration, substrate temperature and *V/III* ratio), and the former grow at the rate of the supplied N. This observation can be explained by the local Ga-excess established at the Ni-particle position. Therefore, this result is in good agreement with the catalyst-assisted nucleation model described above. In contrast, the self-induced NWs grow with an intermediate rate between the supplied Ga- and N-rates. Second, the catalyst-assisted approach provides GaN NWs that contain many stacking faults, while the catalyst-free ones are largely free of defects. Third, the photoluminescence (PL) of the catalyst-free NWs is narrower and much more intense than the one of the catalyst-assisted NWs. All of these differences can be explained as effects of the catalyst. The seed captures Ga atoms arriving at the NW tip more efficiently than the bare top facet in the catalyst-free approach. In addition, stacking faults could result from both the presence of the additional solid phase constituted by the catalyst-particles and the contamination of the NWs by the catalyst material. Finally, such contamination would generate non-radiative recombination centers and in turn reduce the PL intensity. Thus, the use of catalyst seeds may offer an additional way to control the growth of NWs, but both the structural and the optical material quality of catalyst-free NWs are superior.

Zusammenfassung

Diese Arbeit befasst sich mit der Keimbildung und den Wachstumsmechanismen von GaN-Nanodrähten (NWs), die mittels Molekularstrahlepitaxie (MBE) hergestellt wurden. Die Hauptneuheiten dieser Studie sind der intensive Gebrauch von in-situ Messmethoden und der direkte Vergleich zwischen katalysatorfreien und katalysatorinduzierten NWs. In der MBE bilden sich GaN-NWs auf Silizium ohne Katalysator. Auf Saphir dagegen wachsen NWs unter den gleichen Bedingungen nur in der Anwesenheit von Ni-Partikeln. Die Nanodraht-Keimbildung wurde in situ mittels Beugung hochenergetischer Elektronen in Reflexion (RHEED) sowie Quadrupol-Massenspektrometrie in Sichtlinie (QMS) studiert. Die letztere Methode ermöglicht die Beobachtung der eingebauten Ga-Menge.

Für den katalysatorinduzierten Ansatz wurden drei Nukleationsstadien identifiziert: erstens der Einbau von Ga in die Ni-Partikel, zweitens die Umwandlung der Partikelkristallstruktur durch Ga-Anreicherung und drittens das GaN-Wachstum unterhalb der Ni-Partikel. Die Partikelkristallstrukturen während der zwei ersten Stadien stimmen mit dem binären Ni-Ga Phasendiagramm überein und bestätigen, dass nur Ga in die Ni-Keime eingebaut wird. GaN wächst erst wenn die Ga-Konzentration größer als jene von Ni wird, was mit dem ternären Ni-Ga-N Phasendiagramm übereinstimmt. Die Beobachtung von durch die Ni-Ga Partikel verursachten Beugungsbildern während der gesamten Nukleation beweist den festen Aggregatszustand der Partikel. Daher ist die Nukleation durch den Gas-Festkörper-Festkörper (VSS) Mechanismus bestimmt. Überdies zeigt die QMS Studie, dass das GaN Wachstum nicht durch den Einbau von Ga in Ni begrenzt ist, sondern durch die GaN-Keimbildung selbst.

Für die katalysatorfrei auf Si(001) und Si(111) gewachsenen NWs weisen QMS- und RHEED-Untersuchungen auf sehr ähnliche Nukleationsabläufe hin, und zwei Nukleationsstadien wurden identifiziert. Transmissionselektronenmikroskopie von auf Si(001) gewachsenen Proben zeigt, dass das erste Stadium durch die konkurrierende Bildung von kristallinem Si_xN_y und GaN charakterisiert ist. In diesem Stadium wird die Si-Oberfläche durch die Bildung von Gruben und Si-Hügeln immer rauer. Gleichzeitig nukleieren einige wenige GaN Inseln. Während des zweiten Stadiums führt die Amorphisierung der Si_xN_y-Schicht zur starken Nukleation von GaN-Inseln, die von der epitaktischen Beschränkung durch das Substrat frei sind und deswegen die Wurtzitstruktur (WZ) bilden.

Die Nukleationsprozesse sind für beide Ansätze fundamental verschieden. In dem katalysatorinduzierten Ansatz reagiert Ga stark mit den Ni-Keimen, deren Kristallstruktur für das Nanodraht-Wachstum entscheidend sind. In dem katalysatorfreien Ansatz bildet N eine Zwischenschicht mit Si vor der ausgeprägten GaN-Nukleation, und die Gitterfehlanpassung mit dem Substrat spielt die wichtigste Rolle.

Mittels beider Ansätze wachsen NWs in den gleichen Bereichen von Temperatur und *V/III*-Verhältnis. Beide liefern einkristalline GaN-NWs mit WZ-Struktur, die in Ga-polarer Richtung wachsen. Allerdings wurden auch starke Unterschiede beobachtet. Erstens sind unter denselben Wachstumsbedingungen (Dauer, Temperatur und *V/III*-Verhältnis) die katalysatorinduzierten NWs länger als die katalysatorfrei gewachsenen. Außerdem wachsen erstere schneller, nämlich mit der Rate des angebotenen N. Diese Beobachtung wurde auf den lokalen Ga-Überschuss im Ni-

Partikel zurückgeführt. Daher stimmt dieses Ergebnis mit dem obigen Nukleationsprozess überein. Im Gegensatz dazu liegt die axiale Wachstumsrate der katalysatorfreien NWs zwischen den angebotenen Ga- und N-Raten. Zweitens enthalten die mit Katalysatorhergestellten GaN NWs viele Stapelfehler, während die katalysatorfreien größtenteils defektfrei sind. Drittens ist die Photolumineszenz (PL) der katalysatorfreien NWs schärfer und viel intensiver als jene der katalysatorinduzierten NWs. Alle diese Unterschiede können auf den Katalysator zurückgefürt werden. Die Ni-Partikel sammeln die an den Nanodraht-Spitzen ankommenden Ga-Atome effizienter ein als die unbedeckte oberste Facette im katalysatorfreien Fall. Außerdem können Stapelfehler sowohl aus der zusätzlichen Festkörperphase des Ni-Katalysators als auch aus der Verunreinigung der NWs mit Katalysatormaterial resultieren. Solch eine Kontaminierung würde schließlich nicht-strahlende Rekombinationszentren verursachen und so die PL-Intensität verringern. Somit mag die Verwendung von Katalysatorkeimen zusätzliche Möglichkeiten bieten, das Wachstum von NWs zu kontrollieren. Jedoch sind sowohl die strukturellen als auch die optischen Materialeigenschaften der katalysatorfreien NWs überlegen.

Contents

1 Introduction and objectives

The ongoing miniaturization of semiconductor devices has been driven by the need for cost and energy consumption reduction along with the improvement of productivity and performance. Reaching the nanoscale is all the more interesting in that new phenomena, functionalities and technological concepts become possible. To synthesize such innovative devices, the conventionally employed top-down processes are getting cost-prohibitive. In contrast, bottom-up methods might emerge as an inexpensive future alternative. These latter methods are based on the natural organization of matter at various length scales, from atomic and molecular species to individual nanoscale building blocks, and further to higher-level functional assemblies [1, 2]. These fabrication processes offer the potential of low-cost high-volume production with a diverse range of materials associated to the advantage of new device designs [1, 3–5]. However, before development and commercialization, these building-blocks have first to be synthesized with predictable physical, electronic and optoelectronic properties for their integration in reliable devices. In addition, a hierarchical architecture has to be developed for their assembly into functional devices in a reproducible way [6].

Among such building-blocks, nanowires (NWs) are of both fundamental and technological interest. These nanostructures have a large surface-to-volume ratio and can also exhibit a reduced dimensionality [7]. This quasi one-dimension morphology offers the possibility to investigate surface-mediated phenomena, and dielectric and quantum confinement effects which strongly affect the NW physical properties. In addition, compared to quantum dots, NWs are easier to contact and to handle and they can be used as active devices, as well as as interconnects or waveguides [8, 9]. Furthermore, their small cross-sections can accommodate much larger lattice mismatch and thermal expansion difference compared to planar layers, because strain is released at the free NW sidewalls [10]. Hence, NWs offer a larger design freedom for the heteroepitaxy of highly lattice-mismatched materials, which is crucial for the monolithic integration of high performance III-V semiconductors with Si technology.

The design and fabrication of many different types of devices have already been demonstrated for applications in electronics, computing, photonics, sensing, and biology [1, 2, 6, 9]. In the context of the global need for renewable energy sources, this interest has been extended to photovoltaics. In this latter case, radial p-type/intrinsic/n-type junctions offer the additional advantage of decoupling light absorption and carrier collection into orthogonal directions, yielding shorter carrier collection lengths and in turn, a higher collection efficiency [11].

GaN and its related III-nitride compounds have received significant attention over the past 20 years since the first fabrication of blue light-emitting diodes (LED) [12]. These materials are of primary interest for solid-state lighting and photovoltaics because their direct bandgap covers the ultraviolet to the infrared region of the electromagnetic spectrum. For instance, the "multigap" of InGaN offers a great opportunity to create ultrahigh efficiency tandem solar cells sensitive to the full solar spectrum [13]. In addition, the potential of III-nitrides extends to many other fields from high-power and high-temperature electronics to medical and sensor applications. However, the lack of lattice-matched substrates is the main impediment for achieving high quality material and constant efforts have been employed in order to reduce the density of extended defects which degrade the efficiency and the lifetime of the devices. Hence, NWs appear as an ideal solution to this dilemma, and for GaN evidence of their almost perfect crystal quality has already been supplied, along with their strongly improved luminescence compared to the one of the best HVPE layers available [14, 15].

So far, many growth techniques have been employed for the synthesis of GaN NWs. Using molecular beam epitaxy (MBE), these NWs can grow catalyst-free [16, 17] or by a catalyst-assisted approach [18, 19] depending on the choice of the substrate, and the respective growth windows (V/III ratio and temperature) are similar. This observation constitutes a unique opportunity to directly compare the properties of NWs grown by both pathways under otherwise identical conditions. Indeed, typically the growth parameters are very different to form NWs by each approach and for many material systems only one of the two pathways is viable. The comparison of the catalyst-free and catalyst-assisted approaches is all the more pertinent since in the case of the catalyst-assisted approach, the use of a catalyst raises concerns over the contamination of the NWs by the seed material and the deterioration of their properties in comparison to the catalyst-free NWs. Thus, an assessment of the respective advantages and drawbacks of both approaches is crucial for further applications.

The precise control over the NW chemical composition, structure, size, morphology, position and growth direction is required for device integration, as these parameters dictate the physical properties of the NWs [20] and the feasibility and the final performance of the device. However, despite many studies [19, 21–28], the nucleation and growth mechanisms of GaN NWs have not been fully clarified yet. Therefore, a deeper understanding of the mechanisms and processes involved in NW growth is essential. To this aim, only in-situ monitoring techniques can provide information on the actual situation during nucleation and growth. Such studies have been rather scarce up to now, and the lack of real-time information is even more severe for *III-V*-related materials and catalyst-free methods than for Si-related materials and catalyst-assisted methods. Thus, the in-situ investigation of the nucleation of GaN NWs grown by both approaches would be very valuable.

The purpose of this work is to gain comprehension of the GaN NW nucleation and growth mechanisms by in-situ monitoring techniques. In addition, the interrelation between their structural and physical properties is investigated ex situ. For all of the above studies, emphasis is given to the comparison of the two approaches mentioned above, i.e. the catalyst-assisted and the catalyst-free growth of NWs.

Chapter 2 describes the fundamental concepts of molecular beam epitaxy (MBE) and the MBE equipment with the in-situ monitoring techniques which were employed for this thesis. These are reflection high-energy electron diffraction (RHEED) and quadrupole mass spectrometry (QMS), a recently developed technique which provides the growth rate versus time. This chapter also gives an introduction to NW growth approaches. Chapter 3 presents the experimental results on the real-time investigation of GaN NW nucleation by QMS and RHEED in the framework of both the catalyst-assisted and the self-induced approach. The different nucleation stages identified in situ are further investigated ex situ by atomic force microscopy (AFM), scanning electron microscopy (SEM) and transmission electron microscopy (TEM) on samples for which the growth was stopped at various instants of the nucleation. To extend these basic studies, the evolution of these stages in dependence on the growth temperature and the *V/III* ratio is studied by QMS. In addition, an overview of the current status of NW nucleation studies precedes these experimental results at the outset of this chapter. Chapter 4 deals with the material properties and the growth mechanisms of GaN NWs in the framework of the catalyst-assisted and catalyst-free approach. At first, a brief survey of the GaN NW growth studies by MBE is presented. The major part of this chapter is devoted to the analysis of the various characterization results (SEM, TEM and photoluminescence (PL)). At the end of this chapter three main aspects are discussed in which the two approaches significantly differ, i.e. the NW crystal quality, the growth mechanism, and the optical properties. Lastly, chapter 5 concludes on the important results of this work and gives an outlook on future interesting investigations.

2 Epitaxial growth of nanowires

This chapter entails a brief overview of the experimental techniques and methods employed along this thesis. First, a description of the fundamental concepts of MBE growth is proposed to the reader, which also entails experimental details on the MBE equipment and the in-situ monitoring techniques. These in-situ monitoring techniques, that are the reflection high-energy electron diffraction (RHEED) and the quadrupole mass spectrometry (QMS) have been largely employed to investigate the nucleation of GaN NWs that will be presented in chapter 3. It follows an overview on the NW growth approaches and at last, details on the experimental procedures. Table 1 in appendix 5.2 lists all the samples focused on in this work and their respective growth parameters.

2.1 Molecular beam epitaxy

"MBE deserves a place in the history books", so is entitled an article published in Nature Nanotechnology in 2007 giving an overlook on nanotechnology' s "hidden history" [29]. Developed at the end of the 1960's [30] in Bell Laboratories, MBE contributed largely to the nanoscience and nanotechnology development by enabling fabrication of tailored compound semiconductor structures with atomic layer precision.
The demonstration of a blue violet laser diode fabricated by MBE in Sharp Laboratories in 2004 [31] definitely showed the potential of MBE to rival MOVPE technique also for commercial applications. However, MOVPE stays the workhorse for industrial III-V epitaxy due to its versatility for the gas sources, its large range of controllable growth rates, and its high productivity with high uniformity achieved during deposition on large surface areas. In contrast, advantages of MBE over the other important growth techniques are the ultra-high vacuum (UHV) environment favorable to in-situ growth analytics, the reduced consumption of the source materials, and its ability for accurate control on deposition rate that makes it successful as a research tool.

2.1.1 Fundamental growth processes

The principle of MBE is the crystallization of thin films with a rate of typically 1 ML/s in UHV via reactions between thermal-energy beams of the constituent elements and a crystalline substrate surface maintained at an elevated temperature in order to enhance surface diffusion. An important aspect of this growth technique is that the atoms and / or the molecules in the beams do not interact with each other before they reach the substrate. Typically, MBE is used to grow epitaxial films i.e. the crystal structure and orientations of the films are determined by the crystalline substrate.

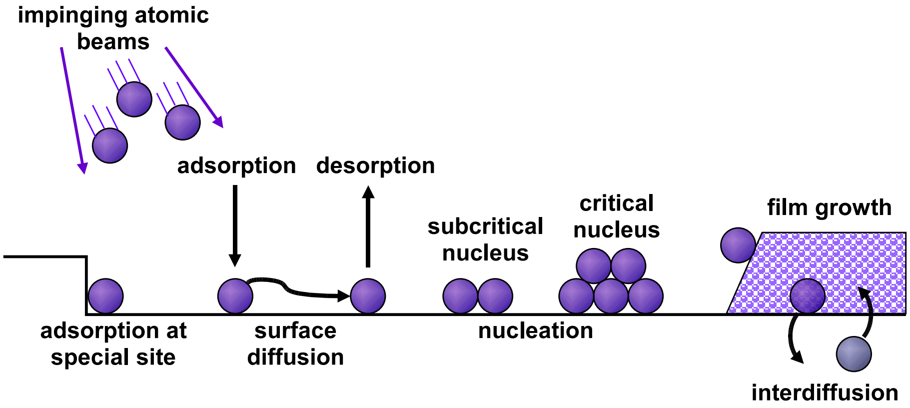

Figure 2.1: Schematics of the surface processes occurring during film growth by MBE.

Figure 2.1 illustrates the individual atomic processes which determine the film growth in its initial stages. The molecules or atoms impinging on the substrate are adsorbed through physisorption (Van der Waals forces type) or chemisorption (chemical reaction with electron transfer). The adsorbed atoms or molecules may then migrate on the substrate surface with a diffusivity determined by the substrate temperature and the surface conditions. When they find a lower-energy site at ledges, kinks or defects they may incorporate into the substrate lattice. Additionally, an adsorbed atom or molecule may interact with others and form a stable or critical nucleus that might evolve into a film for further incorporation. The not incorporated species re-evaporate due to thermal desorption. All these processes are related to activation energies to be overcome and their temperature-dependent rate constant k obeys an Arrhenius law [32]:

$$k \propto \exp(E_a/k_B T), \tag{2.1}$$

where E_a is the activation energy, k_B the Boltzmann constant and T the temperature. At the substrate surface, growth occurs far from thermodynamic equilibrium and is governed mainly by the kinetics of the reaction between the topmost layers and the impinging species.

On a mesoscopic scale, the film morphology develops according to one of the three possible growth modes sketched in figure 2.2. The growth modes depend on many factors like surface free energies, difference in lattice parameters and forces between atoms of the deposited material and temperature. In the Frank-van der Merwe or layer-by-layer growth mode, atoms in the film are more strongly bound to the substrate than to each other and the energy is minimized when the substrate is entirely covered by the planar (2D) film. In the Volmer-Weber (VW) mode, the substrate is not wetted by the film, and three-dimensional (3D) islands grow directly on the substrate surface. Atoms in the film are more strongly bound to each other than to the substrate. The Stranski-Krastanov (SK) mode often appears for heteroepitaxial growth due to a lattice mismatch between the substrate and the deposited layer inducing strain in the latter. In this case growth occurs first in a layer-by-layer way before strain is elastically relaxed

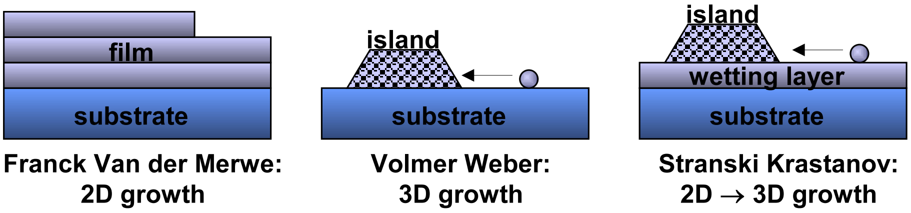

Figure 2.2: Schematics of the three crystal growth modes: layer by layer (Frank-van der Merwe), island (Volmer-Weber) and layer plus island (Stranski-Krastanov).

by the formation of 3D islands. The transition 2D - 3D occurs once the elastic energy counterbalances the surface energy required to form facets [33]. For further material deposition, depending on the lattice mismatch plastic relaxation can also occur leading to the formation of dislocations.

In the case of homoepitaxy, thermodynamics predicts a layer by layer growth mode. However, under conditions far from equilibrium, kinetic limitations associated with finite rates of mass transport processes can greatly affect the growth mode. For a vicinal surface consisting in terraces and atomic steps, adatom transport implies not only transport across terraces (intralayer) but also across steps (interlayer). Each transport is related to different activation barriers. Their difference constitutes the *Ehrlich-Schwoebel* barrier (*ES* barrier) and corresponds to the reduction of the coordination of an adatom while crossing the step-edge as illustrated in figure 2.3. Thus, the probability for an atom to diffuse onto the lower terrace depends on the *ES* barrier that can be negligible or insurmountable. Depending on this barrier, three possible growth modes are observed leading to different morphologies [34, 35]. The step-flow mode occurs when the adatom intralayer mobility is high so that all adatoms reach the step before nucleation sets in and the step advances. In the case where the adatom migration is shorter than the terrace width, layer-by-layer or multilayer growth takes place depending on the rate of the interlayer mass transport. In the extreme case where this transport is zero, the adatom cannot escape from the top of the island and 3D growth is promoted.

Because the adatom mobility depends greatly on the growth parameters, the growth mode can thus be altered by changing the deposition rate or / and the temperature. Last, surfactants also affect the growth mode by modifying the surface energies, the intralayer diffusion or / and the intralayer diffusion barriers.

2.1.2 MBE Equipment

During growth, the constituent elements to be deposited are evaporated from the aperture of effusion cells containing Knudsen-type crucibles. The maximum evaporation rate is given by the Knudsen effusion equation:

$$d\Gamma_e = \frac{dN_e}{A_e dt} = p_{eq}\sqrt{\frac{N_A}{2\pi M k_B T}}\ [m^{-2}s^{-1}], \tag{2.2}$$

with N_e the number of molecules evaporating from the surface A_e, N_A the Avogadro

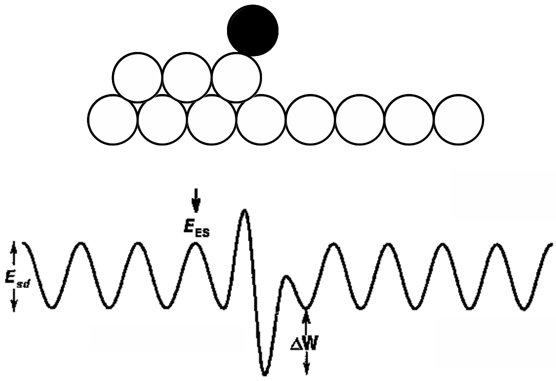

Figure 2.3: Schematic drawing of the potential for an atom moving toward a step edge with an ES-barrier E_{ES}. ΔW is the binding energy to a step site and E_{SD} the activation energy for the terrace diffusion.

constant, T the temperature, p_{eq} the equilibrium evaporant pressure, k_B the Boltzmann constant and M the molecular weight of the evaporated material. The conventional crucibles are of conical shape, made of pyrolytic boron nitride (PBN) and their aperture gives rise to a $\cos^2$ intensity distribution. The stability of the deposition rate is guaranteed by the accurate control of the cell temperature as seen in equation 2.2, achieved by proportional-integral-derivative (PID) controllers. This stability is indispensable for the precise control of layer thickness and composition. In addition, mechanical shutters in front of each cell allow the very rapid interruption of the molecular beams in order to switch from a component to another and get abrupt heterostructure interfaces.

The growth experiments presented in this work were carried out in a V80H type MBE system designed by VG Semicon equipped with two Ga, one Al, one In, one Si and one Ni cells. The beam sources (except for the Ni and Si cells) were standardly kept at temperatures higher than the melting point of the evaporant (29.8°C for Ga, 660.4°C for Al, 156.6°C for In) in order to prevent the possible cracking of the crucible during solidification. A radio-frequency (RF) plasma source (EPI Unibulb or Oxford *HD 25*) was mounted on a standard port for effusion cells to dissociate molecular nitrogen with purity 5N. Further information is given in reference [36]. The RF generator was operated at the frequency of 13.56 MHz and at an output power of 580 W in order to produce neutral atomic nitrogen (N). Indeed, a recent appearance mass spectrometry (AMS) study coupled to a separate reflection high-energy electron diffraction (RHEED) one [37] clarified that this nitrogen species mostly contributes to GaN growth in plasma-assisted molecular beam epitaxy (PAMBE).

A low background pressure (10^{11}-10^{-10}mbar) was maintained in our MBE system by the employment of an ion and a cryogenic pump, along with a liquid-nitrogen-filled cryoshroud used to trap impurities and condense unused beam flux. The preparation chamber and the load lock were equipped with another ion pump and a turbomolecular pump, respectively.

These UHV conditions (background pressure $< 10^{-9}$ Torr) are also indispensable to guarantee films of very high quality with infinitesimal impurity level. On the one hand, the UHV environment preserves the beam nature of the molecules toward the substrate by preventing the scattering of the latter with the eventual residual gas molecules. The maximum admissible value of the residual gas pressure was estimated to be $p_{max} = 8{\times}10^{-4}$ mbar in order to insure a mean free path of Ga atoms large enough (approximately 20 cm) to reach the substrate surface [38]. This condition is thus fulfilled in UHV.

On the other hand, the contamination concentration of the growing surface has to remain as low as possible, and therefore the limitation on the maximum admissible value of the residual gas pressure imposed by the very low growth rates is much more restrictive. Considering that for growing a sufficiently clean epilayer the deposition time t_v of a monolayer of the background vapor species must be at least 10^5 times longer than the deposition time t_b of a monolayer of the evaporant, then for a growth rate of 1 ML/s the admissible background pressure must not be higher than 10^{-11} mbar [38]. However, the concentration of each incorporated element depends also on its sticking coefficient, which is relevant to consider because the typical deposition rate used during the growth of GaN NWs is even lower than 1 ML/s (about 0.15 ML/s in this work) and so is the growth rate of GaN NWs (0.75 ML/s for the catalyst-assisted NWs and 0.34 ML/s for the self-induced NWs). For oxygen, a sticking coefficient of 0.12 ± 0.08 at 300 K on clean GaN(0001)$1{\times}1$ surfaces has been reported, and this coefficient could be reduced a hundred times in the presence of an additional monolayer of gallium [39]. In this case, a background pressure higher than 10^{-11} mbar would be acceptable, even considering the already low sticking efficiency of atomic N of 0.36 at 600°C [37] (the one of group III elements is assumed to be unity at moderate temperature).

Additionally, contamination might have a strong effect on the nucleation phenomena, especially under the unusual conditions for GaN NWs growth, i.e. N-rich and at a low growth Ga-rate. Hydrogen, for instance, is known to enhance the diffusion length of adatoms [40, 41]. Importantly, Northrup *et al.* calculated that the H-terminated GaN(000-1) surface is the most stable one under N-rich MBE growth condition (for residual hydrogen pressure of 10^{-9} mbar) [42]. H-covered surfaces are expected to be relatively inert toward N, which could account for the much reduced N sticking coefficient compared to Ga-covered surfaces. Therefore, Northrup et al. [42] suggested that this reduced sticking coefficient on the N-face surface as compared to the Ga-face one could lead to the generally observed lower growth rate of the GaN(000-1) surface. The residual partial pressure measured for hydrogen in our chamber was about $2{\times}10^{-10}$ mbar which corresponds to $2.4{\times}10^{15}$ atoms cm^{-2}s^{-1} of hydrogen impinging on the sample surface at 1000 K. Disregarding the sticking coefficient, this is one order of magnitude more than the incorporated flux of Ga atoms corresponding to about $1.8{\times}10^{14}$ atoms cm^{-2}s^{-1}, so that H-adsorption may not be negligible under standard NW growth conditions.

One more advantage that MBE offers is the in-situ control of growth, providing thus instantaneous feedback on the influence of growth conditions on the forming structure. Structural information is usually provided by reflection high-energy electron diffraction (RHEED), but kinetic and composition information is also gathered by quadrupole mass spectrometry (QMS) in light-of-sight operation [36] developed primarily in our laboratory as a novel in-situ method. These methods are briefly introduced in the following section.

2.2 In-situ monitoring techniques

2.2.1 Reflection High-Energy Electron Diffraction

RHEED offers the possibility to determine in situ the evolution of the morphology and the crystal structure of the growth front. The geometry of this technique is illustrated in figure 2.4. In our case, an electron gun from Staib RH 20S was employed to produce a 15 kV electron beam. This high-energy electron beam is directed in grazing incidence (1-3°) onto the sample surface in order to limit the penetration depth and to get a sensitivity only to the few outermost atomic layers. The diffracted beams are observed at similar angles on a phosphorous-coated screen that is mounted perpendicularly to the sample surface. The diffraction patterns observed on the screen correspond to the intersection of the reciprocal lattice of the sample with the Ewald sphere of radius $k_i = 2\pi/\lambda$ where k is the wave number and λ the wavelength.

In the case of an atomically smooth and single-crystalline sample surface, the reciprocal lattice corresponds to a lattice of rods perpendicular to the surface in real space. The Ewald sphere intersection with this lattice should ideally form spots as seen in figure 2.5(a), but due to instrumental divergence and crystal imperfections a streaky pattern is obtained [43]. If the surface is rough, the diffraction is obtained in transmission through the asperities and the diffraction pattern is spotty [Figure 2.5(d)]. From the RHEED pattern, it is also possible to gather information on the crystal lattice. Indeed, the distance d between the streaks provides the lattice parameter in the surface plane. For rough surfaces the distance between the planes perpendicular to the growth direction can also be measured. Amorphous layers correspond to a halo without any structure and polycrystalline layers display ring patterns [Figure 2.5(b)]. Layers with misoriented grains as can be formed during NW growth exhibit the superposition of the individual patterns.

In order to follow the evolution of RHEED patterns in real-time, a 10-bit digital high-sensitivity charge-coupled device (CCD) camera and a frame grabber with full software control from k-Space Associates Inc. were used. This way RHEED images could be recorded on the fluorescent screen with a time resolution of up to 30 frames/sec. Such real-time acquisition is very useful for the determination of the strain evolution and the surface reconstructions. In addition, growth rates can be extracted during growth by measuring the period of intensity oscillations that are observed in the layer-by-layer mode.

For this thesis, RHEED was extensively employed to identify the modes and stages of the NW nucleation.

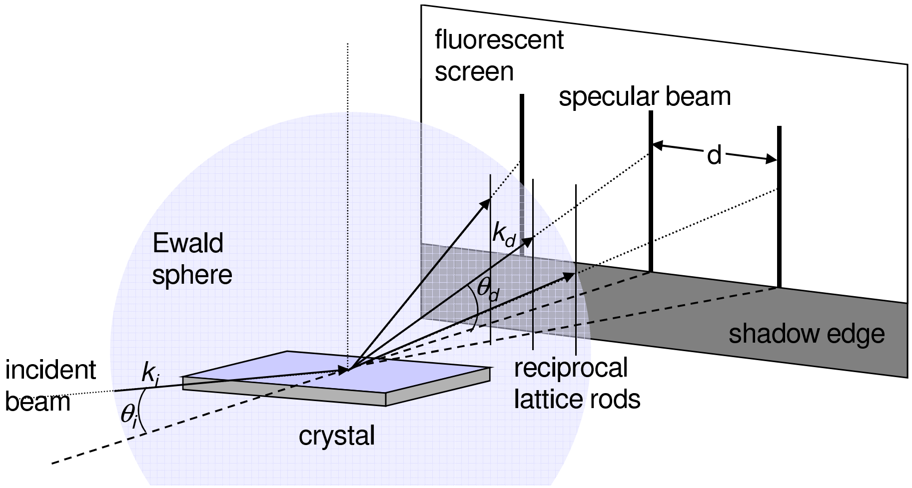

Figure 2.4: Geometry of RHEED set-up.

2.2.2 Quadrupole Mass Spectrometry

This technique was already applied at the end of the 1960's by Arthur Jr [44] to monitor the Ga evaporation on a clean GaAs surface in a modulated molecular beam epitaxy system. Later in 1996, Guha *et al.* [45] also used it to estimate the Ga surface lifetime on GaN in MBE. However, since 2002 Koblmüller *et al.* [36, 46] extended the method to the monitoring of the precise Ga adlayer coverage as well as of GaN nucleation on GaN, AlN, SiC, and sapphire. They definitely demonstrated the potential of this method to understand growth and surface kinetic processes. Since then, QMS in combination with RHEED monitoring has provided many remarkable results, for example a growth mode diagram for GaN [47] and a precise understanding of the GaN decomposition processes [48]. This technique is thus very promising for providing information concerning the NW nucleation phenomena but has not been applied to this field before.

As seen in subsection 2.1.1, the amount of atoms or molecules contributing to film growth corresponds to the net balance between impinging and desorbing flux. The line-of-sight QMS method relies on the quantitative measurement of the desorbing species during nucleation and growth. By a precise calibration during the full desorption of a known incident flux of the same species on a substrate brought to high temperature, the QMS signal of the impinging flux is obtained and converted into growth units. This way, by evaluating the difference between the known incident flux and the desorbing Ga flux (mass balancing), the growth rate also converted into growth unit can be determined at any stage during GaN growth as sketched in figure 2.6(a).

Figure 2.6(b) illustrates the configuration of the QMS device mounted in the line-of-sight to the wafer. By directing the ionizer of the mass spectrometer in direct line-of-sight to the sample and by restricting the acceptance angle by an aperture plate, local mass spectrometry of the atomic or molecular species desorbing from the substrate can be carried out. Under UHV conditions the mean free path of the desorbing species is

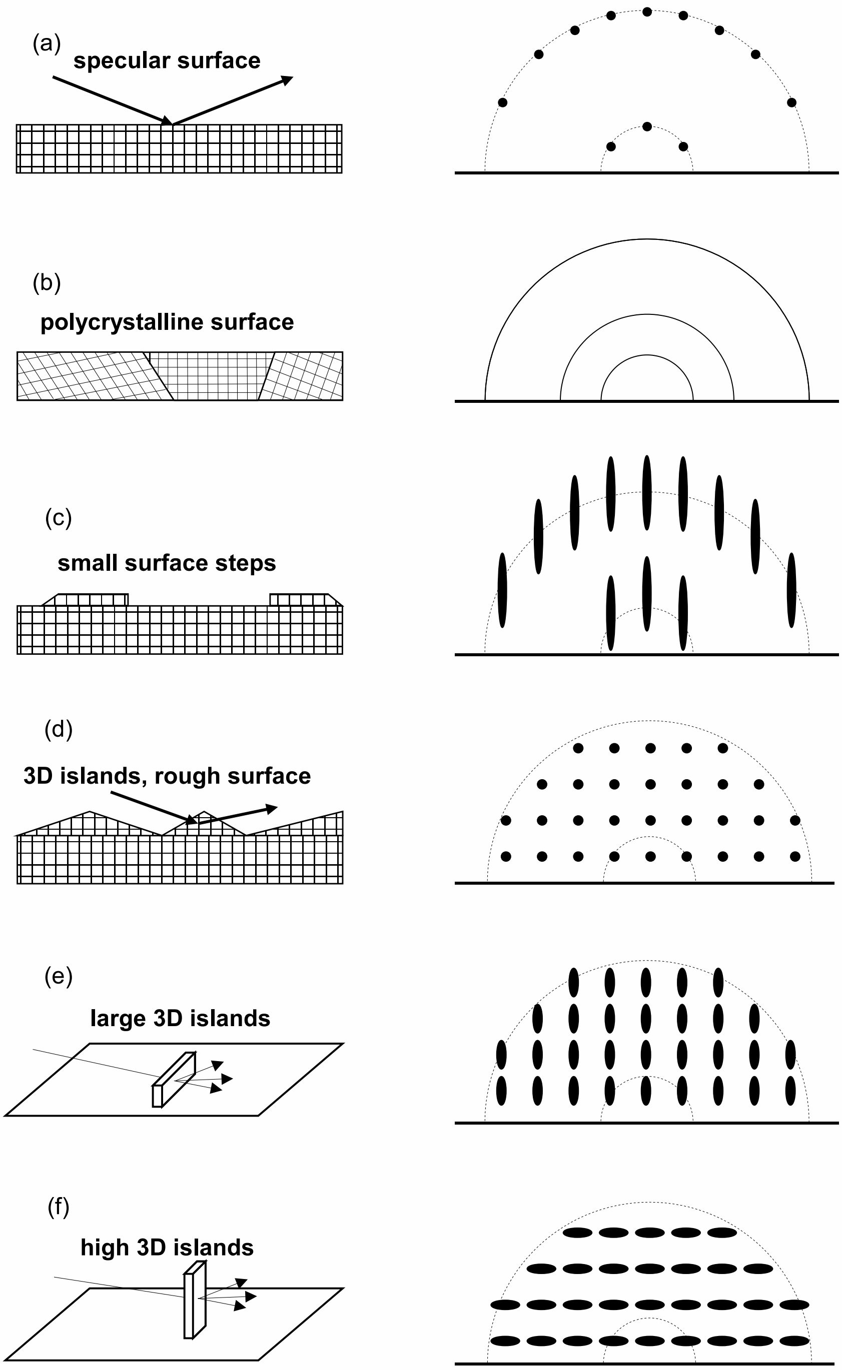

Figure 2.5: Surface morphologies deduced from corresponding RHEED patterns.

long enough to reach the ionizer. There, they are transformed into positive ions and separated according to their mass to charge ratio (m/Z) in the electric field of four electrode rods. At the exit of the quadrupole an ion detector measures either the ion current directly (Farraday Cup) or the electron current proportional to the ion current (Continuous Dynode Electron Multiplier, CDEM) and converts the measured current into an equivalent partial pressure. The aperture minimizes the background signal related to the desorption from the manipulator and the chamber walls while selecting the desorbing species originating merely from the center area of the sample [49].

A conventional state-of-the-art quadrupole mass spectrometer (Residual Gas Analyzer AccuQuad 300D from K. J. Lesker) was installed on a flange designed for beam sources. This QMS allows the detection of ions in a mass range of 1 to 300 atomic mass units (amus) with a resolution better than 0.5 amu at 10% peak height. The device was equipped with a CDEM in order to detect partial pressures not down to 5×10^{-14} mbar with a maximum time resolution of 2 sec. During the present studies, the considered desorbing species are the isotopes ^{69}Ga and ^{71}Ga with occurence 60.1% and 39.9%, respectively. The high nitrogen pressure required for the growth of GaN NWs lies at the limit of the recommended pressure for the CDEM operation. As a side effect, aging of the CDEM was accelerated. Indeed, the CDEM gain changes with time and the gain degradation is unavoidable particularly after exposure to such high quantities of reactive gas.

To correlate the Ga partial pressure with a desorbing flux in units of Å/s, a calibration can be done by measuring the partial pressure of Ga for a sequence of known incident Ga fluxes impinging on the substrate at a temperature high enough ($\geq$780°C) to ensure the full desorption. The measured partial pressure increases linearly as a function of the desorbing Ga flux [36]. However, due to the aging of the CDEM with operation time, the calibration routine has to be repeated frequently. Figure 2.7 illustrates the decrease of the QMS signal with operation time for calibrations of the same Ga flux done after the implementation of a new CDEM on the quadrupole.

2.2.3 Temperature calibration

Another advantage the QMS offers is the in-situ calibration of the substrate temperature by evaluating the Ga desorption characteristics along the GaN growth diagram illustrated in figure 2.8. This can be done for pulsed growth sequences during which either the substrate temperature is decreased for known impinging Ga and N fluxes, or the Ga flux for a given growth temperature and known N flux. In both cases, the range of variation must be selected in order to observe the difference in the Ga desorption behavior related to the formation of Ga droplets. At the borderline for Ga droplet formation, for a decrease of the temperature at constant Ga flux, the Ga desorption decreases due to the formation of Ga droplets, whereas for an increase of the Ga flux at constant temperature the Ga desorption increases more slowly. The crossover from the Ga-rich intermediate regime to the Ga-rich droplets regime obeys an Arrhenius dependence with temperature [50]:

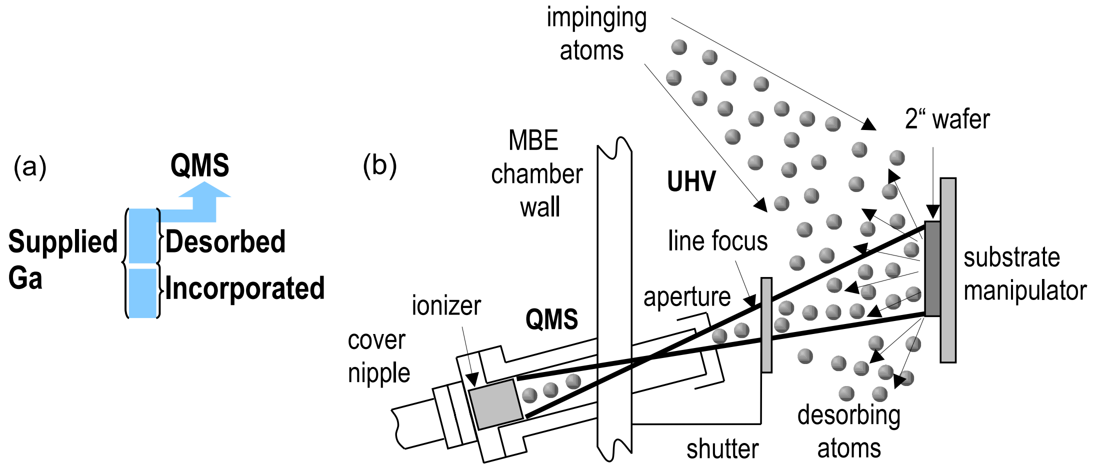

Figure 2.6: (a) Sketch of the mass balancing. (b) Schematic setup of a QMS in line-of-sight operation for monitoring the desorbing atoms [36]. An appropriate aperture plate limits the angle of acceptance to the size of the sample.

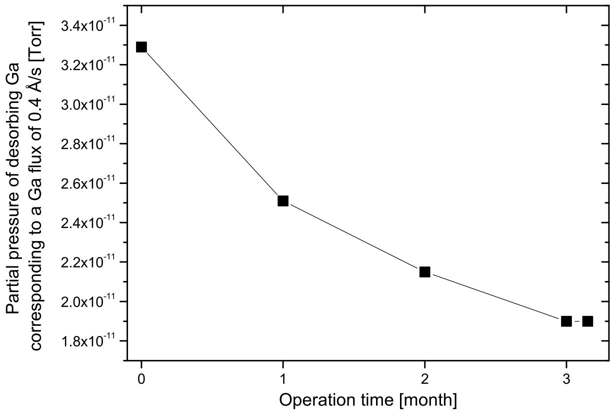

Figure 2.7: Calibration of the QMS signal for an impinging flux of 0.4 Å/s after various operation times.

$$\phi^{*}_{Ga} - \phi_{N} = (3.7 \times 10^{14}) \times \exp \frac{-2.83eV}{k_B T} [\AA/s], \tag{2.3}$$

Knowing the Ga and N fluxes at this crossover directly provides the absolute temperature of growth [36]. This method is thus particularly interesting for the determination of the absolute growth temperature of GaN independently of the substrate material used and the calibration of the pyrometer since it relies on the GaN growth phase diagram. For the study of the nucleation and growth of GaN NWs on sapphire and on silicon substrates, the control of the temperature displayed by the pyrometer calibrated by the previous method ensured identical growth conditions of GaN with the accuracy of ± 5°C.

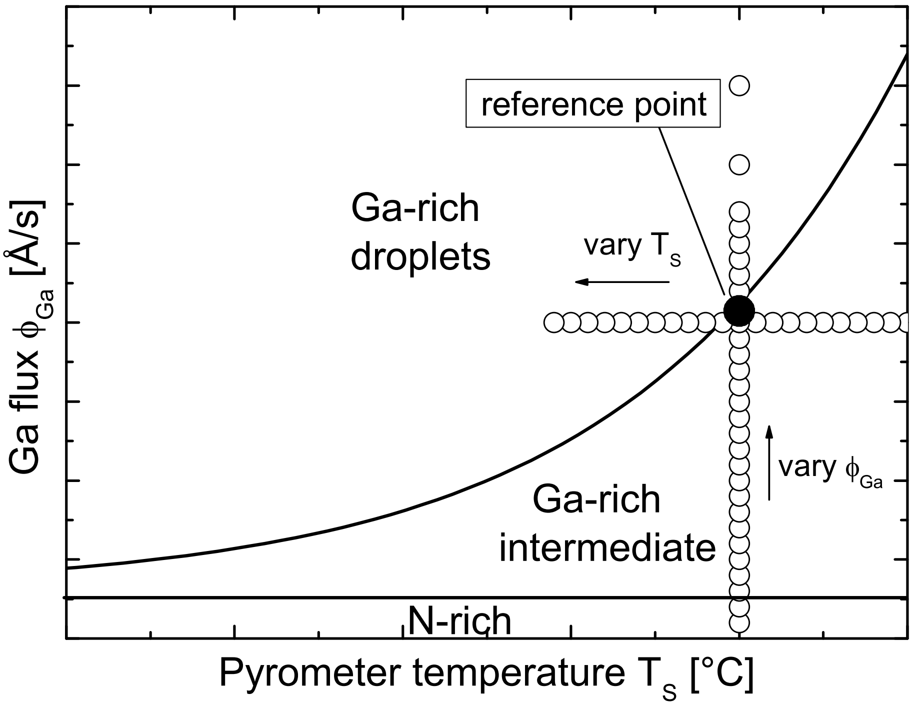

Figure 2.8: Schematic illustration of two GaN growth series along the GaN growth phase diagram for the calibration of the substrate temperature. The first series explores the Ga desorption characteristics for constant $T_{substrate}$ and N-flux, but variable Ga-flux, while the second series focuses on variable $T_{substrate}$, respectively. Extracted from [36]

2.3 Bottom-up approaches for NW growth

The preparation of NWs in a controllable way is a challenging task that can be achieved using a large range of approaches and fabrication techniques [51–54]. Two general approaches referred to as "bottom-up" and "top-down" are employed. In the former one, atoms are-self assembled to form increasing larger structures by control of the crystallization. In contrast, the top-down approach relies on the etching of narrow columns from planar structures by lithography [55].

These two approaches are combined with the conventional growth techniques. Besides MBE, the major fabrication technique in use is chemical vapor deposition (CVD) which is composed of several subclasses like the hydride vapor phase epitaxy (HVPE) and metal-organic CVD (MOCVD). In this case, instead of the physical deposition of elements, chemical precursors decompose and react at the substrate surface to produce the desired substance. The sticking coefficients are much lower than in the case of physical deposition unless enhanced by a catalyst. Metal-organic-MBE (MOMBE) or chemical beam epitaxy (CBE) is a hybrid technique which combines the advantages of UHV like MBE with the versatility of MOCVD.

Although largely employed in the past, the top-down approach is less attractive as the desired length scale of devices shrinks. The major concern stems from the limitation of the resolution achievable by lithographic and etching techniques. In addition, the necessary control over the lateral facets is difficult [56, 57] and process-induced damages are unavoidable [58, 59]. Last, this technique requires that the starting material is already of satisfactory quality in order to yield NWs of at least equivalent quality. For III-N material this is already particularly difficult since basically no lattice-matched substrate is available.

Therefore the bottom-up approach is advantageous to bypass those barriers. Many subtypes have been developed: the catalyst-assisted growth [60–62], the catalyst-free growth [17, 63–66], the self-catalysed growth [67], the oxide-assisted growth [68], the template-assisted growth [69, 70], and the selected area growth (SAG) [71, 72]. Next we will focus on two of these approaches: the catalyst-assisted and the catalyst-free ones.

2.3.1 Catalyst-assisted approach

The most common bottom-up method in the framework of the catalyst-assisted approach is the vapor-liquid-solid (VLS) technique whose model was proposed by Wagner and Ellis in 1964 [60]. In this technique nanometer-sized metallic particles form a low-temperature eutectic alloy with the NW material and act as a preferential sink for arriving atoms (physical catalyst) or in the case of precursor molecules as a catalyst for the necessary chemical process leading to the reactant incorporation [Figure 2.9(a)]. In any case these particles act as a collector for the deposited material [73] once the chemical potential of the surrounding vapor is higher than the one of the particle [74]. By further atom incorporation, the chemical potential of the particle increases until supersaturation is reached. At this point, the NW material precipitates under the particle at the liquid-solid interface. Crystal growth proceeds thus unidirectionally by lifting of the particle. More recently it was evidenced that these particles could also be solid [75–77], growth occurring then through the vapor-solid-solid (VSS) mechanism.

Several models were developed to account for the NW morphology in dependence on the different experimental growth parameters. Givargizov studied the growth rate of Si whiskers grown by CVD using Au as a catalyst in dependence of their diameters and showed that the growth was strongly affected by the Gibbs-Thomson effect causing faster growth of the wider whiskers and the cessation of growth for whiskers of diameter smaller than a critical value [78]. However, for growth by MBE, the opposite trend was ascertained by Schubert *et al.* [79], while Kodambaka *et al.* [80] observed no dependence. The apparent contradiction can be attributed to the very different growth conditions. As we will see next, the generally accepted growth mechanism implies the incorporation of atoms not only by direct impingement onto the NW tip but also by diffusion on the substrate and along the side-facets of the NW. In consequence, it is to expect that for growth techniques inducing different surface reaction and diffusivity, different dependences are obtained. From the observation of longer tilted thin whiskers nucleated at substrate steps, Givargizov concluded that the rate-limitation of whisker growth was the incorporation of the whisker material into the crystal lattice under the seed. Indeed, the nucleation barrier was expected to be strongly reduced at the step interface with the seed. In contrast, Bootsma and Gassen [62] earlier reported that the

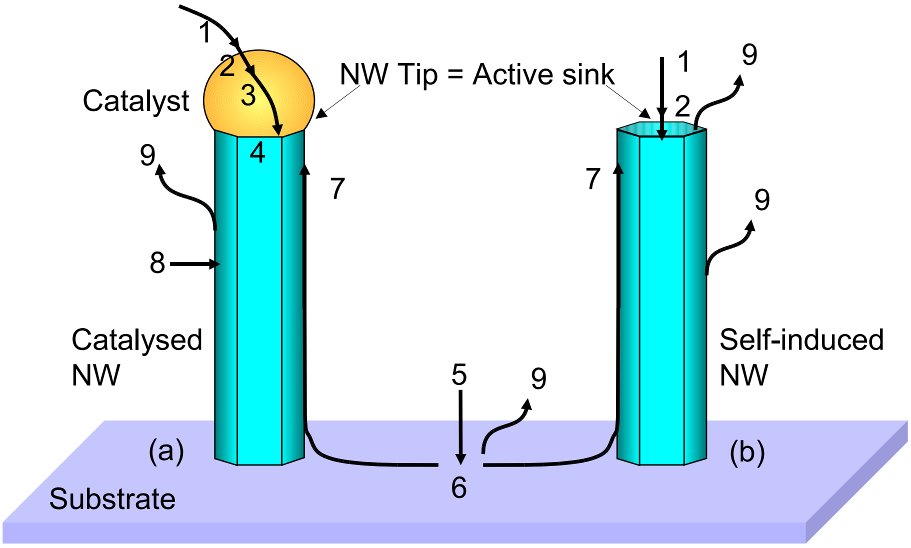

Figure 2.9: Schematic of the processes involved (a) in the catalyst-assisted and (b) in the catalyst-free growth. (1) Adsorption on the NW tip. (2) Incorporation. (3) Diffusion through the particle. (4) Precipitation. (5) Adsorption on the substrate. (6) Film growth. (7) Surface diffusion. (8) Adsorption on the NW side facets. (9) Desorption from the different surfaces.

chemical decomposition at the liquid-solid interface should be the rate-controlling process [Figure 2.9(a)]. The nature of this limiting step has been investigated not only for theoretical but also for economical interest and it is obviously dependent on the NW synthesis technique since different physical/chemical surface reactions occur.

The catalyst-assisted approach offers the immediate advantage that the NW location and size are defined by the particle ones. Thus, by combination with lithography, it is possible to precisely position NWs of desired dimension as long as tapering effects do not modify their shape [81–83]. However, in counterpart, it has been reported that the catalyst may also incorporate into the NW material, thus degrading its physical properties [84–87]. Hence there are constant efforts to develop other approaches not relying on any external catalyst.

2.3.2 Catalyst-free approach

This technique is usually preferred in order to grow NWs of high material purity, since no foreign catalyst material is required. However, it raises the question why matter prefers to grow unidirectionally. Already in 1921, Volmer and Estermann tried to explain the different growth rates on different crystal facets observed for the growth of Hg [88] and concluded that another mechanism than the simplest reflection or condensation must occur, suggesting that the molecules diffuse on the surface of adsorption. In the early 1950s Sears proposed a growth mechanism based on the presence of a built-in screw dislocation to account for the growth of Hg whiskers [89]. The screw dislocation introduces a regenerative step that would catalyse the formation of a new monolayer in agreement with the Frank model, by the incorporation of atoms impinging at the whisker tip and diffusing along the sidewall toward an active sink, as sketched in figure 2.9(b). More generally, Sears noted that uniform surface nucleation plays no role in the growth of whiskers and that the supersaturation required for whisker growth is much lower than the one to nucleate an atomic layer. Therefore, since this supersaturation is below the critical value for two dimensional nucleation, radial growth is hindered [90]. However, this diffusion-dislocation model has been contested by adepts of the catalyst-assisted approach [62, 78] first on the basis that only a few whiskers embody dislocations, and second because stepped whisker side facets still grow slower than the flat top one. The debate is still open after the recent observation of screw dislocations in PbS NWs [91] and in GaN NWs [92, 93].

The diffusion model postulated by Sears is very important for NW growth in general. It was further developed [94, 95] and also extended to the catalyst-assisted growth by Givargizov [78] who postulated that the active sink could also be a catalyst particle instead of a screw dislocation. According to this model the axial growth rate V is given by:

$$V = \frac{dl}{dt} = I + \frac{4I\lambda_s}{d} \tanh \frac{l}{\lambda_s}, \tag{2.4}$$

with l the whisker length, d the whisker diameter, t the time, I the impingement current at the whisker tip and λ_s the root mean square diffusion distance on the whisker surface.

The first term accounts for the growth by direct impingement of atoms at the tip while the second one is related to the surface diffusion on the surface of the substrate and on the side-facets of the NW. This model was experimentally verified for catalyst-free NW growth [25] as well as for the catalyst-assisted one [79, 96, 97] for different material systems and different growth techniques. Its sophistications take into account the adsorption - desorption processes on the NW tip surface, the effects of growth on the substrate surface and the growth parameters (supersaturation, temperature) [98] and explain the divergence observed for the NW length-diameter dependence [73, 78–80].

Last, an interesting simple model proposed in 1967 by Schwoebel [99] attracted much less attention although it is complementary. Starting from a surface covered by circular concentrary steps, this model assumes different adatom mobilities on top and side-facets and different capture rates at steps for atoms approaching either from the upper or the lower terrace of the step as a consequence of the ES barrier. This analysis predicted that for certain capture ratios a "filamentary crystal" with atomically flat sidewalls could be formed.

Importantly, all these models always consider the diffusion and impingement of only a single species, even in the case of compound materials. In particular, for the III-V semiconductors the group III atoms are considered as the surface-diffusing, rate-limiting species assuming that the group V atoms are always in excess [96]. But as reported by several experimental results on NW growth by MBE [19, 23, 100] and as we will see in chapter 4, the axial growth rate of the NWs was evidenced to be group

V limited. Also, it is clear that these different species exhibit different adsorption / desorption / diffusion behaviors that are dependent on their ratio [22, 45, 48, 101–103] (different sticking coefficient, different diffusion length, different residence time), so that the implementation of this consideration is still lacking in the present models.

2.4 Experimental procedures

All the samples used in this thesis are listed in Table 1 in appendix 5.2. These samples are labeled as follows: the substrate material is indicated by the first two characters A0 for *C*-plane sapphire, S0 for Si(001) and S1 for Si(111), while the last characters indicate the growth conditions.

2.4.1 Surface preparation

Catalyst-assisted GaN NWs on *C*-plane sapphire substrates: Catalyst Deposition

The catalyst-assisted method was employed for the growth of the GaN NWs on sapphire substrates <0001> oriented. In this case nickel (Ni) was chosen among other metals because it provided the most regular NW morphology, according to preliminary tests carried out in our research department. In order to form the Ni islands used as catalysts, a layer of Ni, typically 3-4 Å thin, was deposited on the sapphire surface ex-situ at room temperature in the chamber of an ion beam coater (Gatan 682 PECS, Ni purity 99.95% at.). These substrates were then transfered through air to the UHV environment of the MBE system where they were annealed in the MBE growth chamber for 15 min at a temperature in the range of 750°C to 780°C. The thickness of the Ni layer was controlled by a quartz microbalance calibrated by an alpha stepper. To obtain a higher precision, reference layers where measured by RBS, and the uncertainty of the Ni thickness was found to be ±1Å . Upon annealing a large amount of Ni islands formed as illustrated in figure 2.10. Their average diameter is 15 ± 8 nm and their height is about 5 nm. However, the Ni island shapes are not well defined as if the area surrounding the Ni islands were not fully depleted of Ni. The area covered by the islands averaged over several AFM images was estimated by the image processing and analysis software *ImageJ* [104] to be 30 % ± 10%, corresponding to 70 % ± 10% of sapphire surface potentially still free of Ni.

The annealing temperature of Ni was significantly lower than the melting temperature of bulk Ni (1453°C). However, a decrease in the melting temperature of nanometric-sized particles has been experimentally evidenced [105, 106] and extensively studied theoretically for Ni clusters [107, 108]. According to the results of Qi et al. [107], it is to expect that for a Ni cluster size N of 750 to 8007 atoms corresponding to the respective diameters of 2.7 to 5.7 nm, the melting temperature scales inversely with $N^{1/3}$. This yields a melting temperature as low as about 700°C for the smallest particles.

Another aspect to consider is the reaction of Ni with the sapphire substrate. Indeed, sapphire should be inert for the considered deposition temperature. However, during wetting experiments of Ni on sapphire at 1500°C [109] the segregation of oxygen and

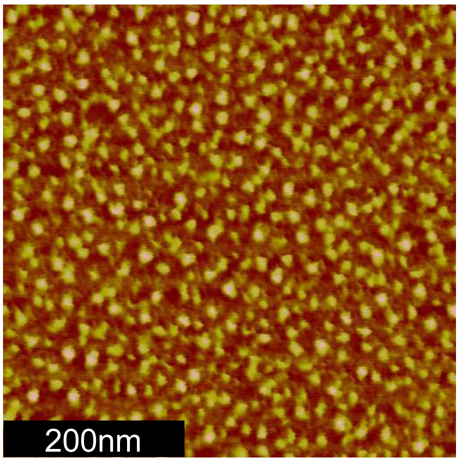

rms-roughness 0.65 nm
Height scale 5.5 nm

Figure 2.10: Ni islands formed from a 4 Å thin layer deposited ex situ on sapphire and annealed in UHV for 15 min at 780°C

aluminum resulting from the dissolution of sapphire into Ni was observed at the triple junction line between sapphire-liquid nickel-atmosphere. Additionally, depending on the quality of the Ni and the oxygen dissolved in it, the formation of $NiAl_2O_4$ spinel can occur at the interface sapphire-Ni [110]. According to thermodynamic calculations [110] at a temperature as low as 1000°C the threshold oxygen level necessary to stabilize the spinel is 0.006% or a minimum oxygen partial pressure of 8.5×10^{-10} mbar. The maximum thickness of the spinel layer was estimated from the solubility limit of oxygen into Ni to be 0.005 times the thickness of the Ni which would correspond to less than 0.02 Å of $NiAl_2O_4$ for the Ni thickness of 4 Å. Considering the poor purity of the Ni employed, which was exposed to the air before being loaded in UHV, it is possible that it contained enough oxygen to form an interfacial spinel layer. However it thickness would be so small that it would be undetectable. In agreement, the electron diffraction analysis presented in chapter 3 does not reveal the formation of the $NiAl_2O_4$ spinel.

Catalyst-free growth on Si(111) and Si(001) substrates: Cleaning procedure

For the catalyst-free pathway, samples were grown on silicon substrates <111> and <001> oriented that were cleaned by a two step wet chemical cleaning process: the standard RCA procedure [111]. Basically, it involves different cleaning steps, containing hydrogen peroxide as oxidizing agent and other chemicals to eliminate a selected contaminant. Details of the procedure are given in appendix 5.2. Immediately after the RCA etch leaving a thin native oxide layer, the wafers were transfered to the MBE chamber system and before growth oxide desorption was carried out for 15 min at a temperature of 950°C. The temperature was then lowered to the growth temperature.

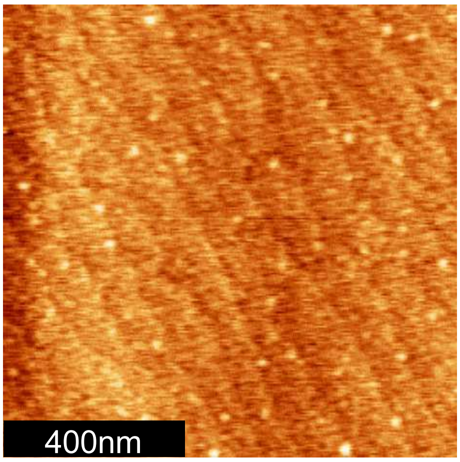

rms-roughness 0.14 nm
Height scale 1.3 nm

Figure 2.11: Si(001) surface cleaned by the RCA procedure.

Figure 2.11 illustrates the morphology of the Si(001) substrate obtained following this cleaning method. 80 nm wide terraces are obtained but residual particles are also observed. For this substrate the rms roughness measured from 1×1 μm^2 area amounts to 1.4 Å.

2.4.2 GaN growth

Following the preparation of the different substrates, NW samples were grown using two approaches: on the one hand in the catalyst-assisted framework on sapphire substrates covered by Ni particles, on the other hand in the catalyst-free framework on the cleaned surface of Si(111) and Si(001) substrates. In the latter case, particular care was taken in order to minimize the exposure of the Si substrate to nitrogen, and therefore the plasma cell was ignited only immediately before the subsequent growth of GaN.
Fluxes were calibrated by scanning electron microscopy (SEM) of the cross-sections of thick films grown at 700°C in both the N- and Ga- limited regimes and converted into effective growth rates. Indeed, GaN can be grown both under N-rich and Ga-rich conditions, and the growth rate is limited by the flux of the species in minority [112]. The quadrupole mass spectrometer signal was calibrated on a separate sapphire substrate at high temperature (780°C–800°C). This calibration consists in fully desorbing the impinging Ga atoms for previously evaluated effective Ga-rates used during the NW experiments as described in reference [47]. The separate calibration aimed to avoid any potential pre-incorporation of Ga during annealing in Ga atmosphere on surfaces different than bare sapphire. In addition, the transient in the Ga flux occurring during the first 10 minutes after opening of the cell shutter has also to be considered and its contribution in the amount of Ga desorption introduces an offset of at most 15% as estimated from the calibration profiles. Moreover, since the chamber pressure (2×10^{-5}mbar) im-

posed by the N-rich conditions necessary to grow the NWs (cf. chapter 4) was higher than the range for which the quadrupole mass spectrometer response is linear, this calibration has been done for several chamber pressures corresponding to the different N-rates investigated and updated along the experiments to adjust for the aging of the electron multiplier.

2.4.3 NW characterization methods

The morphology of the NWs has been at first investigated by SEM. The NW lengths were extracted from cross-sectional SEM images and converted into growth rates simply by division through the growth time. No systematic statistics has been carried out to account for the large variation in length. Instead an "averaged" growth rate was deduced from the NW lengths that were the most frequently observed, whereas error bars were provided by the NW length extrema. However, these extrema are not exception and were chosen in order to correspond to several NWs.

In order to assess the NW crystal structure, specimens were prepared either by NW harvesting from the substrate or by the standard mechanical thinning and ion milling processes for cross-sectional transmission electron microscopy (XTEM). Harvesting is easily carried out by sonication of a sample piece in isopropanol. In this case, evaporation of a droplet of the obtained solution dropped onto a TEM grid insures the transfer of many NWs.

Last, the optical properties of the as-grown NW samples were investigated with a photoluminescence (PL) set-up equipped with a Cryovac microscope cryostat. For excitation, the 325 nm line of a Kimmon He-Cd laser focused to a micrometer-sized spot by a 15× microscope objective has been used. The PL signal was collected by the same objective, and analyzed by a 0.8 m Jobin-Yvon monochromator equipped with a cooled Si charge-coupled-device (CCD) detector.

3 Nucleation of GaN nanowires in MBE

In order to synthesize NWs of arbitrary shape, position, and composition, a detailed understanding of the fundamental nucleation phenomena at the atomic scale is necessary. The cooling procedure following growth and the exposure to ambient atmosphere is known to alter the grown structures [113]. Thus, direct information about the exact processes governing NW nucleation can only be acquired by in-situ studies.

In this chapter, the nucleation of GaN NW ensembles grown by both the catalyst-assisted and the self-induced approach is investigated in real-time by two different techniques used in parallel to get complementary information. First, QMS monitored in situ the amount of Ga desorbing during NW nucleation and growth, yielding a time profile for the actual growth rate. Second, RHEED probed the crystal structure of the forming NWs during the very first steps of growth. This way, different nucleation stages could be identified and followed. The chapter is organized as follows. An overview of studies on NW nucleation is presented with an emphasis on results concerning the nucleation of GaN NWs. Then, for both the catalyst-assisted and the catalyst-free approach, the desorption of Ga atoms monitored by QMS is compared to the time evolution of the RHEED pattern. The different nucleation stages identified in this way are further studied by post-growth AFM and TEM characterizations carried out on additional samples for which growth was stopped accordingly. Last, the evolution of these stages in dependence of the growth temperature and the *V/III* ratio is further investigated by QMS. Finally, a comparison of the nucleation phenomena during both approaches is drawn.

3.1 NW nucleation studies

Several studies have been devoted to the nucleation of both catalyst-assisted and catalyst-free grown NWs. For the catalyst-assisted approach, principally three different nucleation stages have been identified: metal alloying, crystal nucleation and axial growth [60, 114–117]. The validity of this model has been demonstrated by in-situ TEM carried out during Ge NW nucleation from Au and Ge particles deposited on TEM grids [114]. In addition, by analysis of the catalyst volume change, the nucleation has been shown to occur from the supersaturated alloy. The VLS mechanism of Si NWs from Au seeds in CVD has been one of the most studied system: it has been modeled [115, 118] and investigated in-situ by TEM [80, 84, 117, 119] and optical reflectometry [116] as well as ex-situ by AFM, TEM, and SEM [115, 120]. For this material system, similar conclusion concerning the nucleation has been drawn. In agreement with the above-mentioned model, it was observed that the incubation time t_i for the onset of nanowire growth is the sum of two components. The first component corresponds to the eutectic time t_e for the solid Au to be converted into AuSi eutectic by propagation of AuSi through the Au seed. The second component t_n corresponds to the nucleation time during which sufficient supersaturation of Si in the eutectic must occur to initiate NW growth. t_e was observed to decrease when the precursor pressure was raised. In particular, t_n was found to vary inversely with the precursor pressure supporting the existence of a nucleation barrier [116]. In addition, the diffusion of the liquid AuSi front in solid Au has been modeled by applying the diffusion equation to a moving boundary corresponding to the liquid-solid interface through the catalyst [115]. A mathematic expression of the "incubation" time was derived from this model predicting a faster nucleation for higher growth temperatures. This result was also confirmed experimentally by SEM observation on samples grown for intermediate duration during the nucleation. Note however that the expression of the "incubation time" found in this reference corresponds more exactly to the above-defined eutectic time.

The limiting step in the growth processes has also been investigated by in-situ TEM on Si NWs grown from Au seeds [80]. In this particular system it was concluded that the adsorption of the Si-precursor is the rate-controlling step. In turn, this explained the growth rate dependence on the precursor pressure and the NW growth rate independence on the NW diameter.

Furthermore, the liquid or solid state of the catalyst during nucleation and growth has been the subject of intense debate. Importantly, for the Au-Ge system it was demonstrated that it strongly depends on the temperature history during the growth procedure [77]. A large undercooling relative to the bulk eutectic was evidenced and attributed to Ge supersaturation.

The composition of the catalyst has also been further investigated in order to collect more information on the catalyst state and the nucleation process. Results concerning the composition change at the solid-liquid interface during nucleation of Al-rich solid from Al-Si-Cu-Mg alloy have been obtained by in-situ TEM in combination with in-situ x-ray energy dispersive spectrometry (XEDS) [121]. This study also evidenced the presence of an undercooled metastable liquid phase preceding the nucleation of Al solid phase when the temperature was lowered during nucleation. In addition, the Si concentration in liquid Al was found to increase with temperature.

More specifically, the nucleation process and growth kinetics of solid Si from liquid AuSi catalyst particles has been studied in dependence of the Si supersaturation [117]. In this study, the increase of nuclei radius versus nucleation time could be fit by a simple kinetic model which allowed to deduce the supersaturation needed for nucleation. This model accounts for the rapid increase of the liquid supersaturation before nucleation, the capture of the excess Si in the liquid catalyst upon solid Si nucleation and the more slowly and linear growth continuation. The supersaturation was found independent of the droplet radius and the supplied disilane pressure but increases with temperature consistent with an Arrhenius behavior. The nucleation was observed to occur at the edge of the droplet. This location was suggested to be energetically more favorable to minimize the barrier present in heteroepitaxial nucleation and involves an important role of surface and interface in the nucleation.

Furthermore, the comparison of the VLS mechanism of Au-Si NWs with the VSS - growth of Si NWs assisted by Pd_2Si catalyst crystals has been drawn [122]. Particularly for the Pd-Si system, the interface catalyst/NW was observed to advance via a ledge flow propagating laterally, starting at the edge of the NWs. Apart from the above-mentioned precursor decomposition, a nucleation limited regime was concluded from the intermittent start of new steps and by the comparison of the Pd_2Si-mediated Si film crystallization rate with the Si NW growth rate that is ten times slower. Moreover, a mass transport model was proposed. According to this model, the catalyst material Pd was continuously expelled from the growing Si NWs by diffusion away from the Si NW-catalyst interface to the top surface of the catalyst, coupled to a flux of Si in the opposite direction to prevent the stress build-up at the interface.

For *III-V* material systems several studies point out the key influence of the interfacial energy minimization processes on the NW physical and crystalline properties [123, 124]. For InAs NWs grown on GaAs by MOCVD, the difference in interfacial energy between the catalyst and the substrate has been observed to lead to the formation of horizontal traces and moving catalyst before NWs start to nucleate [124].

Additionally, the state of the particle during nucleation and growth has also been investigated for the Au-GaAs system in MBE and CBE [75, 125]. Opposite conclusions were drawn for NW growth at comparable temperatures. However these results could be explained by different growth conditions (procedures and vapour/precursor pressures) employed in these two deposition techniques. To study this aspect, the catalyst composition was carefully investigated. For the growth of GaAs NWs by CBE, ex-situ selected-area electron diffraction (SAED) and energy dispersive x-ray spectroscopy (EDXS) after different growth termination and in-situ heating in TEM revealed a concentration in the Au-Ga seed particle that never reaches the level required for a eutectic melt. Thus, it was concluded that these NWs grew by a VSS mechanism. However, a similar analysis carried on GaAs NWs grown by MBE evidenced a higher Ga concentration of the Au-Ga catalyst particles pointing out the VLS mechanism [113]. Depending on the different growth terminations, different phases could be remarkably identified to well defined solid compounds of the Au-Ga phase diagram. This result suggested that the final composition of the metallic particle at room temperature depends on the growth history of the wire and may strongly deviate from the composition just after growth.

To further elucidate this question, in-situ RHEED monitoring of Au catalyst particles deposited by MBE on the GaAs substrate has been carried out upon temperature cycling before growth. This investigation revealed the appearance and disappearance of additional spots in the diffraction pattern of GaAs at different temperatures [125]. Importantly, these spots were generated by the solidification of the catalyst particles and the difference in temperature for their solidification and melting was attributed to the change in the composition of the particles that easily alloy with Ga coming from the GaAs surface. Also the liquid state of the particles during the growth was ascertained by the comparison of the particle solidification temperature prior to growth with the lowest temperature of the NW growth window.

Thus few studies on the VLS mechanism in the framework of the catalyst-assisted NW nucleation have already been carried out but they mainly concern the Si-material system. Even fewer studies were devoted to *III-V* semiconductors and they are not as detailed.

For the catalyst-free approach several studies were also carried out and many of them concern the III-V system but the elaboration of the growth mechanisms has been more challenging than for the catalyst-assisted growth. Park *et al.* [126] have studied the formation of InAs NWs on SiO_x in a quartz tube. They concluded that at high temperature the decomposition of SiO_x yield reactive nanometer-sized Si clusters that could enhance the In attachment rate (Si-assisted growth model). This group also compared the nucleation of catalyst-free Ge and InAs NWs and In nanoparticle-catalysed InAs NWs on porous Si [127]. They suggested that the NW growth starts from solid nuclei. They observed a correlation between the degree of porosity and the InAs NW formation, suggesting that the pits could act as energetically favorable nucleation sites.

More specifically concerning the *III*-nitride system and growth by MBE, nucleation studies have been intensively carried out but the proposed models did not get a general consensus. At first, the model based on the formation of GaN islands formed upon nitridation of Ga droplets ("Ga balling") on patterned Si/SiO_2 substrates has been proposed by Guha *et al.* [128] to explain the selective growth of GaN NWs by MOMBE. Similarly, Calleja *et al.* [129] proposed that a self-catalytic growth mechanism could originate the GaN NW formation on unpatterned Si substrates by solid-source RFMBE. In this model liquid Ga clusters formed by the restriction of the Ga surface mobility imposed by N-excess could act as a catalyst. In addition, a similar self-catalytic VLS process from Ga droplets was suggested for the nucleation of GaN NWs on top of a low temperature GaN buffer grown on Si(111) under N-excess [130, 131]. In this case NWs formed inside V-shaped craters connected to trenches which extended to the Si substrate. Therefore it was proposed that the concave geometry of the openings in the broken GaN buffer favors Ga nanocapillary condensation. In turn, NW crystal seeds would grow inside these openings. Upon variation of the *V/III* ratio, control on the NW density and diameter could be obtained. More specifically, Ga droplets formed from the thermal decomposition of HVPE GaN films heated in situ in TEM at 1050°C were observed to promote the growth of GaN NWs [132]. In this way, the VLS growth of GaN NWs was evidenced to occur by the redissolution of the decomposition products into the Ga droplets. Interestingly, ex-situ TEM investigation revealed that GaN NWs grown from a similar separate experiment grew along the $[0001]_{GaN}$ directly from GaN pellets and presented a smooth tip free of any Ga droplet [132]. Thus the absence of metal droplets at the tip of the NWs is not a sufficient argument to invalidate the Ga self-catalytic VLS model.

However, this model has been later largely refuted for RFMBE growth [22, 27, 133, 134]. To this aim, Calleja *et al* [134] investigated in detail the effect of Ga droplets predeposited on Si(111) substrates on the nucleation of GaN NWs. They observed that the NW size and density was independent of the Ga droplets' ones, and that large droplets even hinder NW growth. Instead of the Ga self-catalytic VLS mechanism, a model based on the formation of 3D islands acting as a seed for subsequent NW growth is now generally accepted [22, 23, 26], even though many aspects concerning the mode of formation of these islands are not elucidated.

Generally, NWs forms under N-excess and their density and size can be tuned by changing the V/III ratio and temperature [23, 134–137]. However, it has been observed in a few cases that Ga-excess could also lead to NW growth if the growth temperature is high enough to desorb the excess Ga atoms [66, 138].

For GaN NW growth on Si, Ristić *et al.* proposed that critical nuclei are formed by a VW mode driven by the important lattice mismatch with the substrate. They suggested that for further nucleation, island coalescence is blocked by the preferential incorporation of Ga on the island top side [22]. This idea was based on the experimental result that a wetting layer was not observed by HRTEM [22, 137]. However, the group of Calarco *et al.* reported the presence of a thin and rough wetting layer connecting GaN NWs and small GaN clusters. In this case, the critical diameter for nucleation was deduced from the smallest of those clusters and amounts to 7 nm. On Si(111), this GaN wetting layer forms on top of an interfacial silicon nitride one that is partly amorphous [26].

In contrast to the GaN wetting layer, the silicon nitride one has been invariably observed during GaN NW growth on Si [22, 23, 26, 134, 137]. It was suggested to form prior to GaN growth due to the strong affinity of N to bound to Si atoms [26, 134]. Its 2–3 nm thickness is usually not uniform. Therefore, locally tilted surface appears at Si_xN_y irregularity or at step bunches on the Si surface inducing in turn the tilting of the NWs [26, 134, 139]. However, almost epitaxial contact with the substrate could still remain for the NWs formed at the very early stage of the deposition [26]. Note that nitridation at 790°C of Si(111) substrates prior to GaN NW growth results in the attainment of a more homogeneous Si_3N_4 layer and in turn reduces the NW tilting angles. In this case, EELS measurement at the Si/GaN interface revealed that Si outdiffuses from the substrate within the NWs whereas no Ga was found within the intentionally formed SiN interfacial layer. Thus it was also concluded that the local accumulation of strain resulting from N penetration into Si or the local enrichment of Si could induce the nucleation of GaN NWs [137]. In any case, it is commonly observed that for thick Si_xN_y layer the NWs are growing with random orientation but along the *C*-direction [23, 26, 134, 137].

From post-growth SEM measurements of the NW density before and after the nucleation completion, Calarco *et al.* [24] evaluated the nucleation duration of GaN NWs grown directly on Si(111). The nucleation was observed to be completed when coalescence of the NWs started. Surprisingly the nucleation duration was very long (60 min at 785°C). No new NW nucleation was reported following the coalescence and the NW density decreased after a sudden increase at the early stage of the nucleation [24, 137]. A linear dependence of the mean values of the NW length and the NW diameter on time was found implying the lateral growth of the NWs [24, 137].

For GaN NW growth on AlN buffer, a SK or even a FM growth mode of the GaN islands was suggested to be promoted by the lattice mismatch reduction [22, 23]. It has been shown that the presence of this AlN buffer on top of Si(111) drastically improves the NW orientation in comparison to nucleation directly on top of the Si substrate [23, 134]. In addition, the thickness of such buffer has a strong influence on the NW diameter and density [15, 135, 140]. For AlN buffer layers thinner than 10 nm, this result was attributed to the growth of NWs at the edge of AlN grains [15]. In addition, by a post-growth SEM investigation similar to the one carried out by Calarco *et al.* [24], two nucleation regimes could be identified [23]. In the first one, the lateral and vertical growth rate of the islands, which are initially similar, rapidly drops and increases, respectively. This is accompanied by a rapid increase of the island density. In the second regime, the NW density and growth rates become constant. However, for AlN buffer thicker than 30 nm, a mixture of a faceted matrix and NWs is obtained due to the more favorable island coalescence [22]. In this case, it was observed that NWs nucleate in the center of hexagonal pits with $(\bar{1}102)$ facets and that atomic N has a stronger influence on the nucleation density than Ga [141]. Finally, it was concluded that NW nucleation and growth originate from the formation of specific planes that have different sticking coefficients for Ga, the one of the *C*-plane being the highest [141].

Lastly, the nucleation of InN NWs grown by RFMBE on MOVPE-GaN templates has been investigated by in-situ spectroscopic ellipsometry and RHEED [142] showing that the SK growth mode occurs after one ML deposition, yielding the formation of InN quantum dots. Another RHEED investigation on InN NWs grown on nitrided *C*-plane sapphire substrate [143] revealed the necessity of In droplet pre-deposition and nitridation to form InN NWs. Moreover the In droplet deposition was preceded by the sapphire nitridation in order to guarantee well oriented and thinner NWs. During nucleation a sudden coalescence of the NWs was observed to reduce the NW density. This coalescence was followed by the nucleation of new NWs while the first nucleated ones maintained their lateral dimension but grow vertically.

To conclude, only few studies have been devoted so far to the NW nucleation. The reason for this is the need for in-situ monitoring techniques in order to get information on the actual situation during nucleation and growth, and not after alteration by the cooling procedure. For the catalyst-assisted nucleation of NWs, these studies concern mostly the Si-related material system while for the *III-V*-related one no real-time information is available. For the catalyst-free NW nucleation, no in-situ investigation has been carried out so far and no detailed nucleation study is found either. Therefore, the investigation in real-time of the nucleation of GaN NW ensembles grown by both approaches by two different in-situ monitoring techniques presented in this chapter is particularly pioneering.

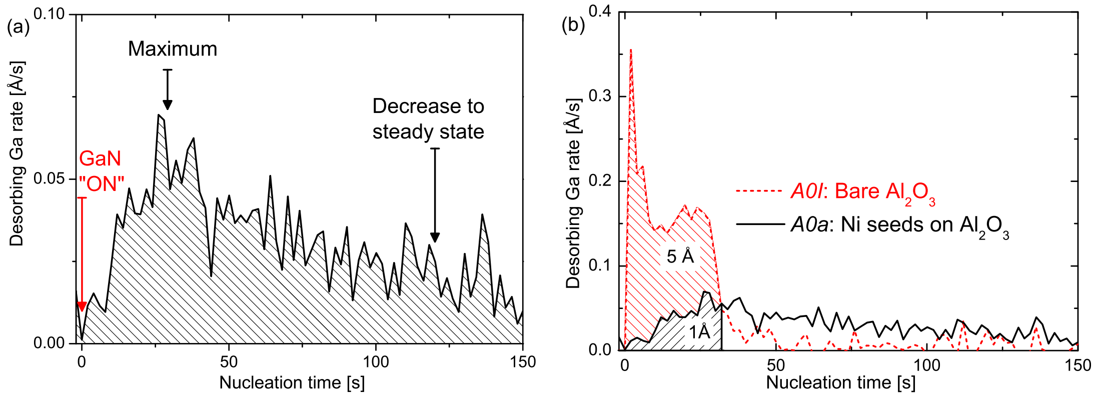

Figure 3.1: (a) Calibrated QMS profile of Ga desorption during nucleation on sapphire substrate covered by Ni islands (sample *A0a*). (b) Calibrated QMS profiles of Ga desorption during nucleation on bare sapphire substrate and on sapphire substrate covered by Ni islands (samples *A0I* and *A0a*, respectively). Note the different scale.

3.2 Catalyst-assisted GaN NWs on *C*-plane sapphire substrates

3.2.1 In-situ Quadrupole Mass Spectrometry Monitoring

Figure 3.1(a) presents the calibrated QMS profile of Ga desorption monitored during the nucleation of GaN on sapphire substrate covered by Ni particles (sample *A0a*) at a temperature of 730°C and for Ga- and N-rates of 0.4 Å/s and 2.0 Å/s, respectively. The growth of GaN is initiated by the opening of both Ga and N shutters simultaneously at t=0. Remarkably, the desorption signal increases only gradually from a value close to zero up to a maximum reached after about 30 s of nucleation. This indicates an initially negligible rate of desorbing Ga atoms, implying that at first almost all of the Ga arriving at the sample surface is incorporated. To assert if this effect could be related to the sapphire surface still exposed between the Ni islands, nucleation on bare sapphire under the same temperature and *V/III* ratio conditions has been investigated. Figure 3.1(b) compares the Ga desorption during nucleation on bare sapphire (sample *A0I*) and on sapphire covered by Ni particles (sample *A0a*). Clearly, in the case of nucleation on bare sapphire, the Ga desorption rate instantly increases to a value close to the supplied Ga-rate. Hence initially almost no Ga is incorporated, i.e. the nucleation is inhibited. Thus, in the case of nucleation on sapphire covered by Ni particles, the Ga incorporation observed during the first 30 s is directly related to the presence of the Ni particles. After this initial stage, the Ga desorption signal reaches a maximum, and after about 35 s the decrease in the Ga desorption sets in. For nucleation time longer than 380 s, steady state conditions are reached where again the full Ga flux from the effusion cell is incorporated.

Figure 3.2 presents the Ga desorption for similar experiments however with a lower N rate (N-rate = 1.1 Å/s). For those experiments, the Ga shutter was first opened while the N-shutter remained close before initiation of growth. At the opening of the Ga shutter, basically all the Ga desorbs from the surface of the bare sapphire substrate

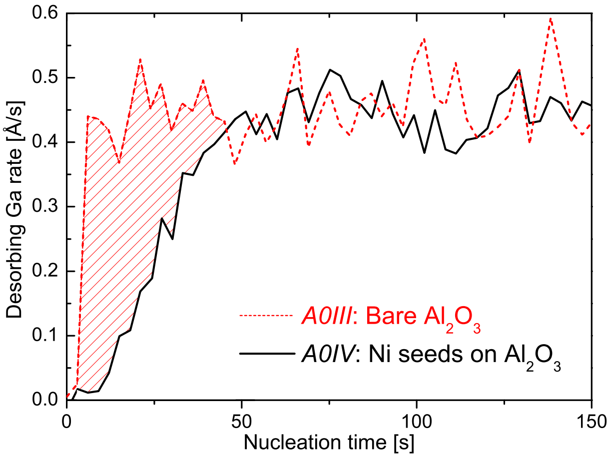

Figure 3.2: Calibrated QMS profile of Ga desorption during Ga exposure of a bare sapphire substrate and of a sapphire substrate covered by Ni islands (samples *A0III* and *A0IV*, respectively).

(sample *A0III*) while the Ga desorption is strongly delayed for the sapphire substrate covered by the Ni islands (sample *A0IV*), meaning that much more Ga is incorporated. Thus these experiments also ascertain the Ga incorporation into the Ni islands.

This initial incorporation of Ga into Ni is consistent with the model we proposed for the growth of these GaN NWs [19] (see chapter 4) and with the presence of Ga detected inside the Ni particles by post-growth electron energy-loss spectrometry [144]. These results for a similar NW sample are shown in Figure 3.3. In this study, it was found that the measured concentration of Ga within the Ni-seed is relatively uniform and amounts to 22 ± 3 at% in average while the concentration of N gets negligible about 2 nm from the seed-NW interface. The Ga to Ni concentration ratio found in this study agrees with the equilibrium phase Ni_3Ga or a Ni-Ga solid solution that is stable up to 1200°C at atmospheric pressure as indicated by the right-hand side shaded box in Figure 3.4 that presents the Ni-Ga binary phase diagram [145–147]. More recently the composition of Ni particles used to promote the growth of GaN NWs by MOCVD [148] was investigated by XEDS. Like in ref. [144], the Ni_3Ga phase was identified with a somewhat higher Ga percentage which ranged from 24.4 ± 3 at% to 26.8 ± 3 at%.

These results are also in agreement with previous studies on the reaction of GaN with Ni which is often used for device contacting. Ni indeed shows a high Ga solubility already at 600°C [149, 150] and annealing above 600°C of Ni deposited on top of GaN leads to the desorption of N and to the intermixing of Ni and Ga scaling with the annealing temperature [151]. Furthermore, as determined by thermodynamic modeling [149, 152, 153], no Ni-Ga-N ternary compounds are expected to form at temperatures higher than 500°C. Of course, those results correspond to equilibrium under much higher pressures. However, the poor solubility of N into Ni has been reported and the nickel nitrides Ni_4N and Ni_3N decompose at temperatures above 250°C and 600°C, respectively, unless the N_2 pressure is very high [154]. According to Gröebner *et al*, Ni_3N should start to form from the reaction $Ni + GaN$ only at N_2 pressure as high as 10^4 bar

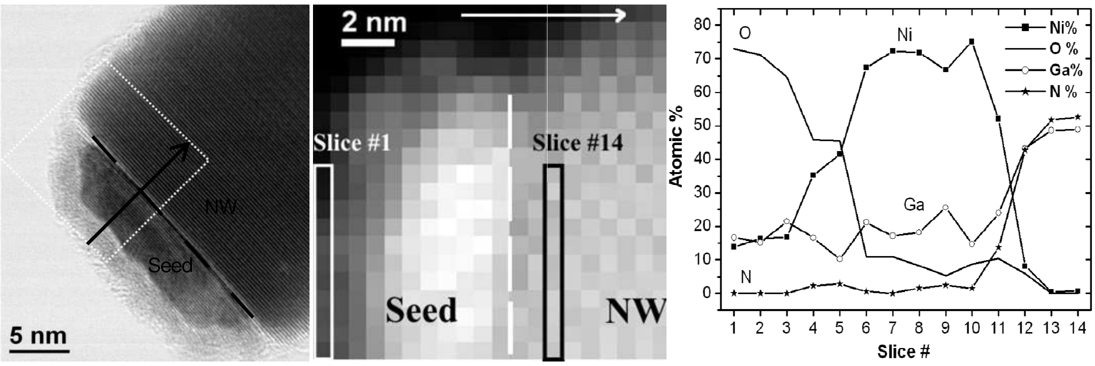

Figure 3.3: Left: High resolution XTEM (HRTEM) of the tip-end of a GaN NW. The dotted box shows the area of EELS mapping used in the middle figure. The arrow indicates the scan direction in the right figure. The interface between the GaN NW and the Ni-based seed is indicated by the white dashed line. Center: digital micrograph spectrum image with the intensity of each pixel corresponding to the maximum number of counts of the corresponding EELS spectrum. The boxes represent the first and the last summed areas used to provide the quantified composition line scans perpendicular to the NW-seed interface shown on the right hand side. The NW-seed interface is indicated by the white dashed line and the arrow indicates the scan direction. Right: Quantified compositional-EELS line scan across the Ni-based seed perpendicular to the NW-seed interface. Extracted from ref. [144].

at 500°C [149] and was not observed at experimental pressures of 100 bar, which is far from our experimental conditions. Thus, in the following only the chemical reaction of Ni with Ga will be considered.

The calibrated QMS profiles also provide information on the incorporated amount of Ga. In Figure 3.1(b), during the initial stage, the amount of Ga not incorporated can be estimated by integrating the area below the increasing curve (hatched areas). It corresponds to a planar layer of GaN with a thickness of 1 Å for sample *A0a* while it amounts to 5 Å for sample *A0I*. The supplied amount of Ga corresponds to an equivalent GaN thickness of $R_{Ga} \times t$, where R_{Ga} is the Ga-rate and t the elapsed time. This is 0.4 Å/s $\times$ 30 s $=$ 12 Å of supplied Ga in GaN equivalent thickness. Thus, the incorporated amount of Ga is $Ga_{A0a} = 12$ Å $- 1$ Å $= 11$ Å for sample *A0a* and $Ga_{A0I} = 12$ Å $- 5$ Å $=$ 7 Å for sample *A0I*. The fraction of the sapphire surface not covered by the Ni particles determined from AFM images at room temperature is $S = 70\% \pm 10\%$. Assuming that S is the same at 730°C during the growth of sample *A0a*, the amount of Ga incorporated into the Ni particles can be roughly estimated by $Ga_{A0a,Ni} = Ga_{A0a} - S \times Ga_{A0I} = 11$ Å $- 0.7 \times 7$ Å $= 6$ Å in GaN equivalent thickness. The equivalent Ga coverage is given by $C_{Ga} = Ga_{A0a,Ni} \times \rho_{GaN}/2$, where ρ_{GaN} is the number of atoms per volume unit and $\rho_{GaN}/2$ is taken as the amount of Ga atoms per volume unit for stoichoimetric GaN. This gives $C_{Ga} = 6 \times 10^{-8}$ cm $\times$ $8.79 \times 10^{22}/2$ at/cm^{-3} $= 2.7 \times 10^{15}$ at/cm^{-2}. However, the uncertainty of these very small values is relatively large: during the first 30 s the uncertainty of desorbing Ga is estimated to 2.3 Å related to the Ga flux transient at the opening of the Ga shutter (15% estimated from the calibration) and to the time resolution on the position of the maximum (estimated by integration over the range of

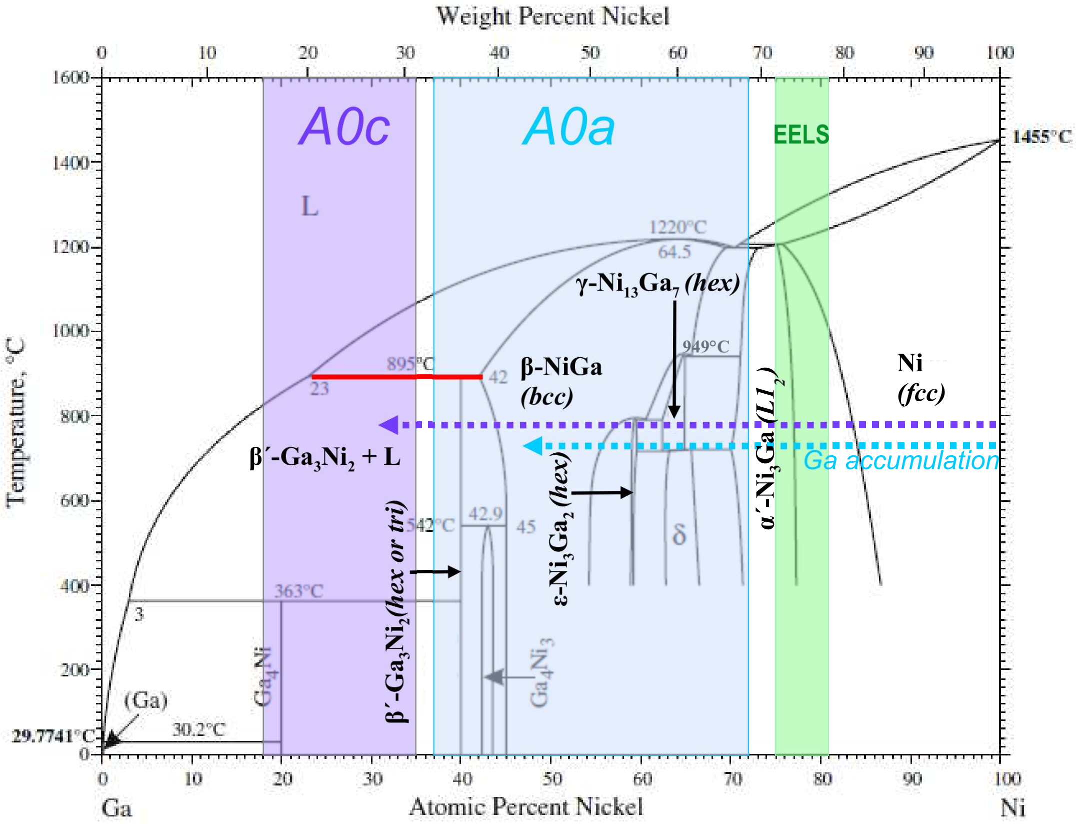

Figure 3.4: Ni-Ga phase diagram extracted from ref. [145]. The shaded area on the right-hand side corresponds to the composition range measured ex situ by EELS on a NW sample similar to sample *A0a*. The shaded areas in the center and on the left-hand side correspond to the composition range of sample *A0a* and *A0c*, respectively, deduced from the QMS experiments. The arrows indicate the reaction path for *A0a* and *A0c*. The invariant reaction at 895°C is indicated by the horizontal red line.

± 15 s around the maximum position), respectively. To this must be added the uncertainty for the sapphire surface left bare between the islands (0.7 Å). This corresponds to a total amount of 1.3×10^{15} at/cm^{-2}.

In Figure 3.2 a similar calculation can be carried out. During the first 52 s, the amount of Ga not incorporated corresponds to a GaN planar layer 20 Å thick for the bare sapphire substrate (sample *A0III*) while it amounts to 10 Å for sample *A0IV* for the sapphire substrate covered by Ni islands (sample *A0IV*). The supplied amount of Ga corresponds to an equivalent GaN thickness of 21 Å. The incorporated amount of Ga is then $Ga_{A0III} = 1$ Å for sample *A0III* and $Ga_{A0IV} = 11$ Å for sample *A0IV*. Assuming $S = 70\% \pm 10\%$, the amount of Ga incorporated into the Ni particles is estimated to $Ga_{A0IV,Ni} = 11$ Å $- 0.7 \times 1$ Å $= 10$ Å in GaN equivalent thickness, which leads to $C_{Ga} = 4.4 \times 10^{15} \pm 1.0 \times 10^{15}$ at/cm^{-2}. This result is thus in good agreement with the amount obtained from Figure 3.1 for sample *A0a*.

In comparison, a nominal Ni thickness of 4 Å corresponds to a coverage of $C_{Ni} = 3.65 \times 10^{15}$ at/cm^{-2} at 20°C. This amount is close to the Ni coverage which we have determined by Rutherford Back-Scattering (RBS) [155]. It ranges from 2.3×10^{15} at/cm^{-2} to 3.2×10^{15} at/cm^{-2} for different samples. Hence, the Ga concentration within the Ni-particles after 30 s of nucleation estimated from our QMS measurements lies in the range of 28 at% to 63 at% which correspond to the centered shaded area in the Ni-Ga phase diagram (Figure 3.4). This concentration is higher than the one deduced from EELS and for this Ga concentration range several other Ni-Ga phases might also have formed that are the γ-$Ni_{13}Ga_7$ phase, the ϵ-Ni_3Ga_2 phase, the β-NiGa phase or the β'-Ga_3Ni_2 phase. However, the α'-Ni_3Ga phase, whose existence domains is limited to 30 at% [145], is still to consider given the large uncertainty obtained by the present measurement.

The maximum in the Ga desorption of the QMS profile is intriguing and suggests the existence of a change in the system leading to a different incorporation behavior of the supplied Ga. For the range of growth temperatures employed, the Ni-particles might be, as discussed earlier, either solid or liquid. However, monitoring of the nucleation by RHEED should help to clarify this point, tell us when GaN is first synthesized and if this can in turn explain the drop in the Ga signal.

3.2.2 In-situ Reflection High-Energy Electron Diffraction Monitoring

For the monitoring of the nucleation by RHEED two different experiments were run for which the rotation of the manipulator was stopped during the growth in order to observe the development of the structure in both azimuths $[11\bar{2}0]_{GaN}$ (sample *A0m1*) and $[10\bar{1}0]_{GaN}$ (sample *A0m2*). During the first minute of these experiments, three different RHEED patterns appear subsequently, and consequently, nucleation can be divided into three stages. These stages are reported on the time profile of Ga desorption as seen in Figure 3.5 as well as the corresponding RHEED patterns seen along the $[11\bar{2}0]_{GaN}$ direction. It shows that a change in the diffraction pattern is accompanied by a change in the Ga incorporation behavior.

Figures 3.6 and 3.7 illustrate the evolution of the RHEED pattern during nucleation in both the $[11\bar{2}0]_{GaN}$ and $[10\bar{1}0]_{GaN}$ azimuths, respectively. The corresponding simulated pattern using the Electron Microscopy Image Simulation (EMS) software is presented under each RHEED pattern [156, 157].

As growth starts and throughout the first 25–30 seconds that delimit the first nucleation stage, the RHEED pattern does not change significantly [Figures 3.6(a) and 3.6(b) and Figures 3.7(a) and 3.7(b)] while the Ga desorption signal gradually increases (Figure 3.5). Following this initial stage, a different RHEED pattern briefly appears as seen in Figures 3.6(c) and 3.7(c) coinciding with the maximum in the Ga desorption signal in Figure 3.5. After about 35 s of nucleation the pattern characteristic for WZ GaN develops [Figures 3.6(d) and 3.7(d)] and remains for the rest of the growth. The appearance of this WZ GaN pattern corresponds to the decrease of the Ga desorption signal as indicated in Figure 3.5. It is remarkable that the succession of these three different stages is within 5 s the same in both azimuths $[10\bar{1}0]_{GaN}$ and $[11\bar{2}0]_{GaN}$ although these two

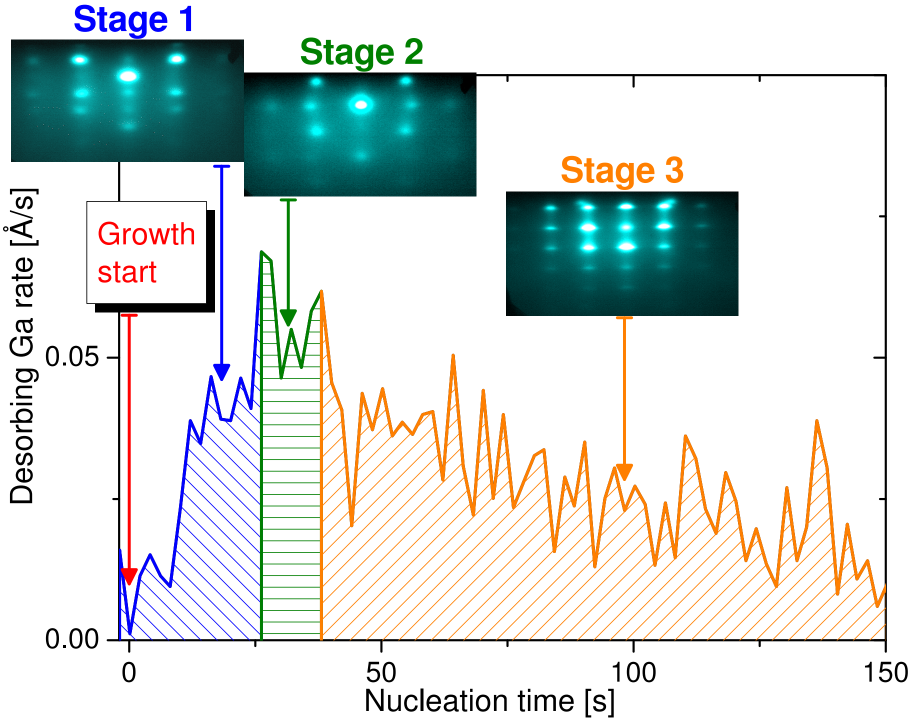

Figure 3.5: The 3 stages of the nucleation as identified by RHEED and correlated to the QMS profile of Ga desorption.

experiments were run separately.
Figures 3.6(a) and 3.7(a) illustrate the pattern obtained after annealing of the Ni particles at a temperature of 730°C, i.e. immediately before growth. Well-defined spots are superimposed onto faint streaks related to the *C*-plane sapphire, which vanish during subsequent growth. Spotty patterns are commonly seen for surfaces covered by 3D clusters. By a detailed analysis of this structure, two different twinned orientations of a face-centered cubic (*fcc*) crystal could be identified. The reciprocal lattice spacing was calibrated using the pattern of the sapphire substrate and the one of a rough layer of N-rich GaN. On this basis the lattice parameter of the *fcc* crystal was determined to 3.6 ± 0.1 Å , which is consistent with the lattice parameter of Ni. Indeed, the α-Ni phase has the *fcc* structure *A*1 and its lattice parameter at 730°C is 3.566 Å , as calculated using the thermal expansion coefficient of 18.534×10^{-6} at 730°C extrapolated from Ref [158]. Moreover NiO, which also has the *fcc* structure, was rejected as a potential origin of this pattern due to its much larger lattice constant of 4.217 Å at 730°C (extrapolated from Ref [159]). Lastly, a body-centered cubic (*bcc*) structure for Ni has also been reported to form from the *fcc* one to accommodate large plastic strain [160] but does not correspond to the observed pattern. Faint additional spots are also observable along the $[111]_{seed}$ direction [empty circles in Figure 3.6(a)] which either results from a double diffraction [161] or indicates the presence of another material with a larger lattice constant than Ni (from our measurement 6.4 Å) which is however too small to correspond to the

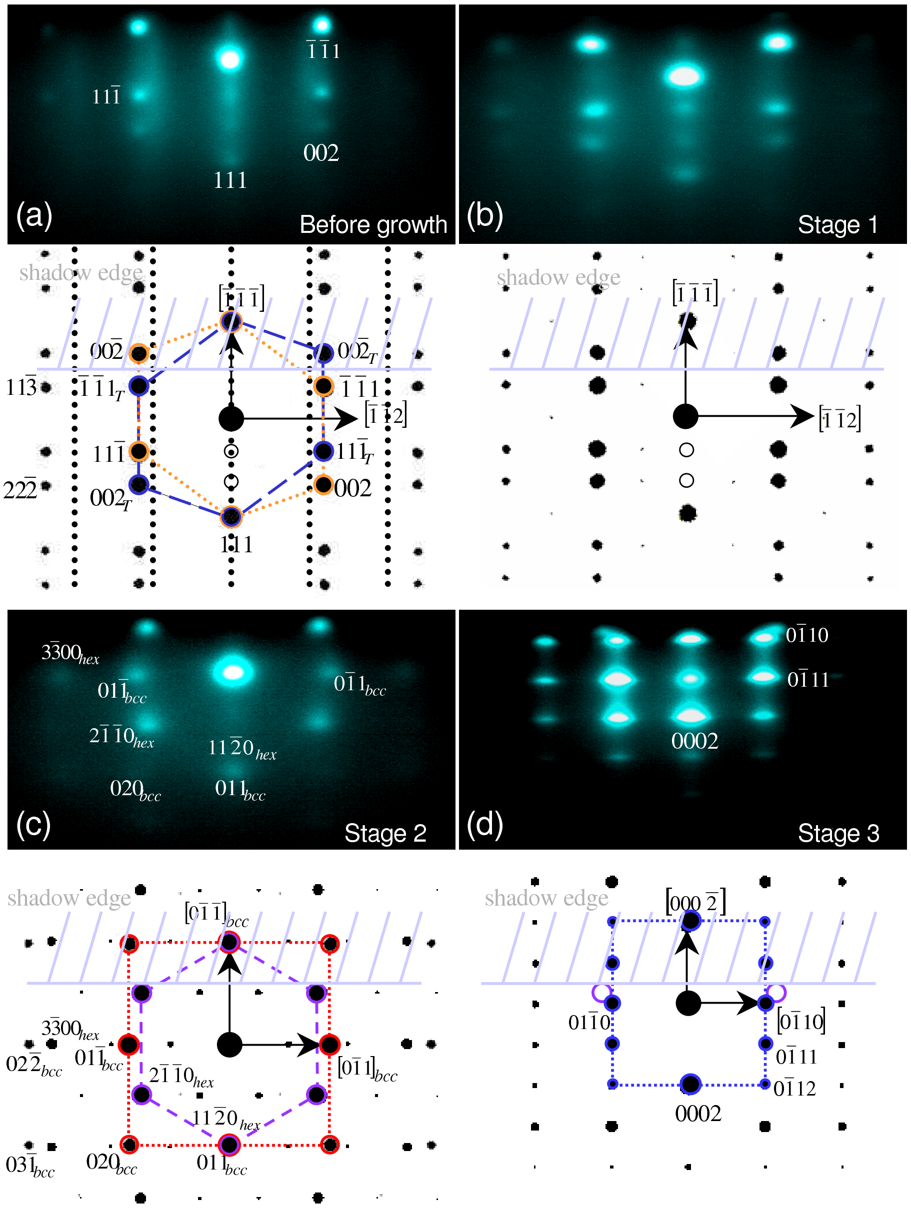

Figure 3.6: Evolution of the RHEED pattern in the $[11\bar{2}0]_{GaN}$ azimuth during the nucleation of GaN NWs. The corresponding kinematical diffraction pattern simulated with the EMS software for a camera length of 400 mm and an acceleration voltage of 15 kV is presented below each pattern. The patterns are presented chronologically (a) before growth, (b) after 5 s, (c) after 30 s, and (d) after 3 min 40 s of growth. The empty circles in the simulated pattern of (a) and (b) do not belong to the simulation. They could correspond to double diffraction. In (a) the vertical dotted lines stand for the sapphire substrate. The dotted and dashed hexagons stand for the twinned *fcc*-Ni structures. In (c), the dotted and the dashed lines stand for the *bcc*-NiGa structure and for another Ni-Ga compound of hexagonal structure (see text), respectively. In (d) the open circles stand for additional reflections generated by the additional Ni-Ga compound.

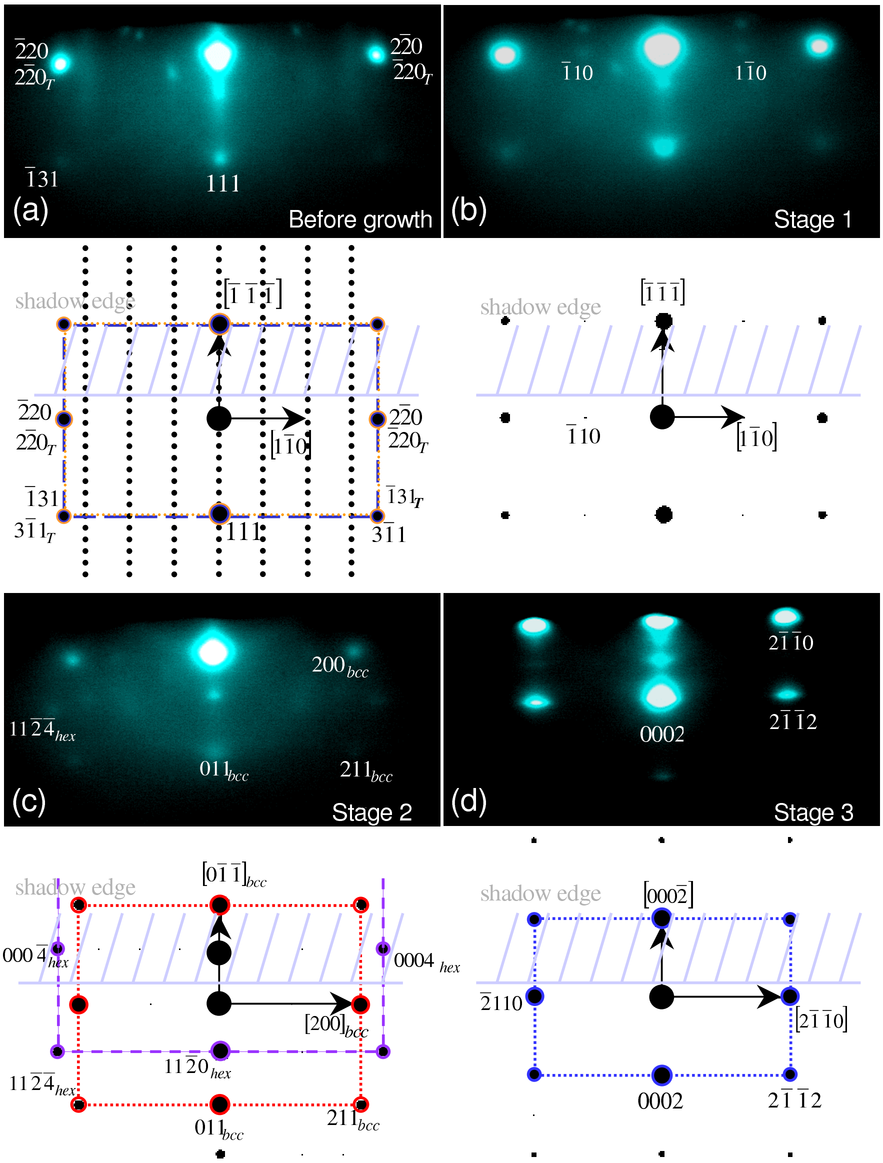

Figure 3.7: Evolution of the RHEED pattern in the $[10\bar{1}0]_{GaN}$ azimuth during the nucleation of GaN NWs. The corresponding kinematical diffraction pattern simulated with the EMS software is presented below each pattern. The patterns are presented chronologically (a) before growth, (b) after 5 s, (c) after 25 s, and (d) after 3 min 5 s of growth. In (a) the vertical dotted lines stand for the sapphire substrate. The reflections of the twinned structures are superimposed. In (b) additional $1\bar{1}0$ reflections appear. In (c), the dotted line and the dashed line stand for the *bcc*-NiGa structure and for another Ni-Ga compound of hexagonal structure (see text), respectively.

spinel $NiAl_2O_4$ (lattice parameter 8.05 Å at 780°C [162]). The twinning of the structure can only be resolved in the $[11\bar{2}0]_{GaN}$ azimuth while in the $[10\bar{1}0]_{GaN}$ azimuth all the reflections are superimposed and correspond to the pattern simulated with the EMS software. The twinning axis is $[111]_{seed}$ and the epitaxial relationship to the substrate is:
$[111]_{seed} \parallel [0001]_{Al_2O_3}$ and $[11\bar{2}]_{seed} \parallel [\bar{1}2\bar{1}0]_{Al_2O_3}$ (orientation 1)
and
$[111]_{seed} \parallel [0001]_{Al_2O_3}$ and $[\bar{1}\bar{1}2]_{seed} \parallel [\bar{1}2\bar{1}0]_{Al_2O_3}$ (orientation 2).
This first pattern evidences that the Ni particles are in the solid state before the initiation of growth at the temperature of 730°C.
Figures 3.6(b) and 3.7(b) illustrate the patterns obtained 5 s after the opening of Ga and N shutters. These patterns characteristic for the first stage of nucleation show that the crystal structure is unchanged in comparison to the one before growth. The twinning of the structure remains and the additional spots along the $[111]_{seed}$ direction are now clearly resolved. These spots do not correspond well to GaN since their corresponding lattice parameter is much larger. Also they were already detected before the GaN growth initiation. The epitaxial relationship to the substrate is the same as before growth and the estimation of the lattice parameter gives also a similar value within the range ± 0.1 Å. However, the spots are strongly stretched in reciprocal space in the in-plane direction which is typical for 3D islands with a high aspect ratio. This is an indication that the 3D Ni particles are elongated perpendicularly to the substrate surface. In addition, faint reflections are visible in the $[10\bar{1}0]_{GaN}$ azimuth. In order to identify them, the EMS pattern in this case was simulated using the $L1_2$ structure of α'-Ni_3Ga in agreement with the QMS results. Indeed by the same calculation as in the previous section, the Ga composition in the particle was determined to be 24 ± 16 at% corresponding to this structure although a Ni-Ga solid solution could still be involved. According to these EMS patterns, the ordered phase of Ni_3Ga would have a few extra diffraction reflections of weak intensity in comparison to the pattern of the α-Ni phase. These reflections could not all be detected in this study but the $(0,\bar{1},1)$ and $(0,1,\bar{1})$ ones were identified, confirming the presence of a Ni-Ga compound with low Ga content. Last, a small displacement of the $(\bar{1},1,1)$ spots during the first stage was detected, suggesting an increase in the lattice parameter as Ga is incorporated. According to Ref [163, 164] the lattice parameter of Ni_3Ga ranges from 3.575 Å to 3.691 Å and is expected to increase when the Ga content rises from 23.1 at% to 30 at%. Unfortunately, the variation in the lattice parameter with the dissolved amount of Ga cannot be resolved by our lattice constant estimation (± 0.1Å). Therefore, there is a strong presumption that the phase present during the first nucleation stage is Ni_3Ga or a disordered *fcc* solution of Ni and Ga in agreement with the QMS results which demonstrated the incorporation of Ga into the Ni particles.
Figures 3.6(c) and 3.7(c) illustrate the patterns obtained after 30 s and 25 s of growth, respectively. These patterns characteristic of the second stage are very different from the one observed during the first stage and indicate a sudden change of the seed structure. They are the result of at least two different superimposed structures. One of these structures has been identified to be a *bcc* crystal with the following orientation relative to the substrate normal:

$[011]_{seed} \| [0001]_{Al_2O_3}$ and $[01\bar{1}]_{seed} \| [\bar{1}2\bar{1}0]_{Al_2O_3}$.
The second structure corresponds to an hexagonal crystal aligned along the direction: $[11\bar{2}0]_{seed} \| [0001]_{Al_2O_3}$ and $[0001]_{seed} \| [10\bar{1}0]_{Al_2O_3}$.
Their lattice parameters estimated from these patterns are 2.9 Å for the *bcc* crystal, and a = 4.1 Å and c = 5.0 Å for the hexagonal crystal. In order to identify these structures, the range of 28 at% to 63 at% of incorporated Ga after 30 s of growth provided by the QMS monitoring was compared to the phase diagram of Ni and Ga compounds presented in Figure 3.4 [145]. This way the *bcc* β-NiGa phase (*B*2) could clearly be identified as the *bcc* phase observed by RHEED. Indeed, the existence domain of this phase ranges from 30 at% to 58 at% and its lattice parameter is 2.896 Å, which is in good agreement with the value measured by RHEED. Additionaly, the second structure superimposed corresponds to another hexagonal phase of Ni-Ga compound. This phase can not be undoubtedly identified. Indeed, according to ref. [145–147, 163] in this range of Ga composition and for the growth temperature of 730°C the hexagonal phase γ-$Ni_{13}Ga_7$ (a = 4.005 Å, c = 5.018 Å), the hexagonal phase ϵ-Ni_3Ga_2 (with a = 3.995 Å, c = 4.980 Å) and the trigonal or hexagonal one β'-Ga_3Ni_2 (a = 4.054 Å, c = 4.882 Å) might coexist with the $\beta - NiGa$ phase. Thus the second crystal structure observed by RHEED is most probably one of these three hexagonal phases.
Again the EMS software provided the simulated patterns presented in Figures 3.6(c) and 3.7(c). They result from the superposition of the β-NiGa phase with the γ-$Ni_{13}Ga_7$ one. In the experimental patterns, many faint additional reflections indicated by the simulation are not detected. However, note that the EMS patterns correspond to perfectly ordered phases which is most probably not the case here.
Figures 3.6(d) and 3.7(d) illustrate the patterns obtained in the last stage of the nucleation. In this stage, the spotty pattern characteristic for electron transmission through GaN develops and remains for the rest of the growth. At the same time, the Ga desorption decreases to the steady state conditions where again the full Ga flux from the effusion cell is incorporated. These data indicate that the formation of GaN NWs sets in about 35 s after growth was initiated by opening of the shutters. The epitaxial orientation of the GaN NWs is the same as the one for the planar layers:
$(0001)_{GaN} \| (0001)_{Al_2O_3}$ and $[11\bar{2}0]_{GaN} \| [10\bar{1}0]_{Al_2O_3}$.
Additional reflections characteristic for the NiGa phase of the second stage are still observable even after 3 min of growth. This strongly supports the conclusion that a substantial part of the seeds remains solid during growth.

3.2.3 Post-growth AFM and TEM investigations

In order to gather further information on the morphology and the crystal structure of the seeds and the developing NWs during nucleation, post-growth analysis was carried out by AFM and TEM on samples for which growth was stopped at the different stages of the nucleation. Figure 3.8 presents the surface of samples for which growth was stopped after 15 s (sample *A0p1*), 30 s (sample *A0p2*), 60 s (sample *A0p3*) and 120 s (sample *A0p4*). In all cases these samples exhibit a clear 3D morphology of particles whose diameter ranges from 10 to 30 nm. However, these dimensions are strongly de-

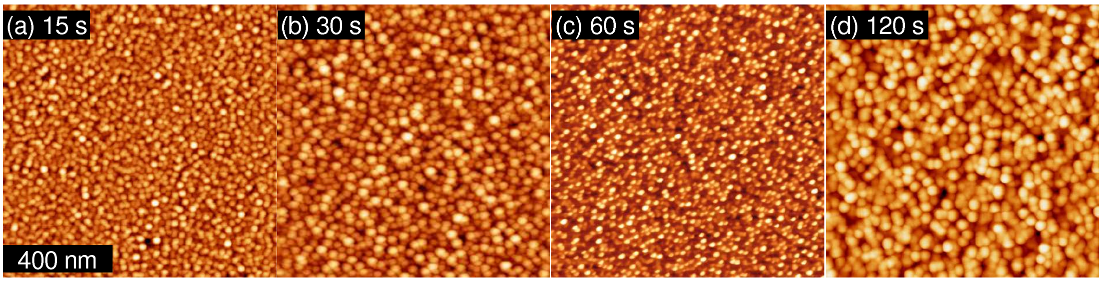

rms-roughness 0.5 nm
Height scale 4 nm

rms-roughness 1.5 nm
Height scale 12 nm

rms-roughness 3.6 nm
Height scale 23 nm

rms-roughness 4.7 nm
Height scale 31 nm

Figure 3.8: AFM images showing the evolution of the forming NWs in dependence of the nucleation time.

pendent on the size and shape of the probe tip so that no direct conclusion can be drawn on the diameter and density evolution. The rms-roughness and the average particle height are less affected by convolution with the probe tip, and these values are plotted in Figure (3.9) as a function of the growth time. During the first 15 s of growth they do not change significantly, suggesting that during the first stage of nucleation corresponding to the incorporation of Ga into the Ni particles no significant vertical growth occurs yet. Between 15 s and 30 s after opening of the shutters, both the rms-roughness and the average height strongly increase. The precise time cannot be deduced from Figure 3.9, but after about 30 s, vertical growth can be seen in the AFM images too. Figure (3.9) suggests that the growth rate slows down after about 120 s, but this may be an artifact caused by the probe tip not reaching the substrate surface anymore.

TEM analysis of the samples grown for 15 s and 30 s (*A0p1*, *A0p2*) provides more information concerning the morphology and structure during nucleation. Figure 3.10 presents TEM images of Ni particles seen along the $[10\bar{1}0]_{Al_2O_3}$ zone axis resulting from 15 s of growth (stage 1 in Figure 3.5, sample *A0p1*). Neither NWs nor GaN are detected on the TEM images, but a large number of particles of *fcc* structures. This confirms the earlier conclusion that in the first stage only Ga is incorporated into the Ni particles while GaN does not grow. These particles are mainly organized in populations of two different scales [Figure 3.10(a)]. The smaller particles are typically 5 nm wide and less than 2 nm high, and the values for the bigger particles are 7 nm and 5 nm. Independently of their dimensions, they are aligned along two different mirror orientations relative to the $[111]_{particle}$ axis [Figures 3.10(b) and 3.10(c)] that are identical to the ones found by RHEED:

$[111]_{seed} \parallel [0001]_{Al_2O_3}$ and $[11\bar{2}]_{seed} \parallel [\bar{1}2\bar{1}0]_{Al_2O_3}$ (orientation 1)

and

$[111]_{seed} \parallel [0001]_{Al_2O_3}$ and $[\bar{1}\bar{1}2]_{seed} \parallel [\bar{1}2\bar{1}0]_{Al_2O_3}$ (orientation 2).

The dark contrast located along the interface of the particles with the substrate is most probably the result of strain. Last, the lattice parameter of the particles was deduced from the Fourier transform of the HRTEM image. Using the lattice parameter of sapphire as a reference, the value of 3.61 ± 0.04 Å was obtained for the particle structure, which is consistent with the one deduced from RHEED during the first stage of nucle-

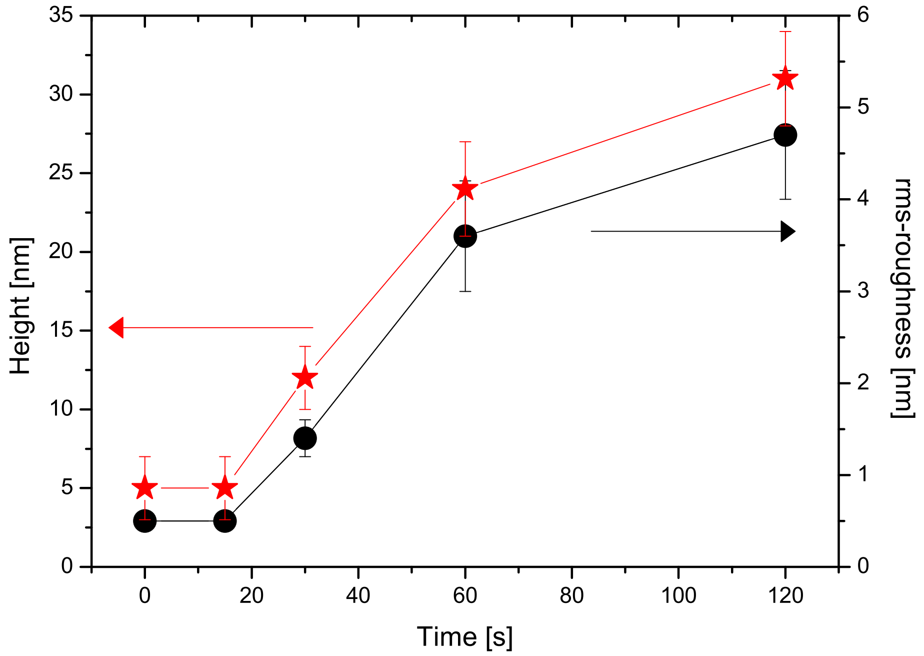

Figure 3.9: Time evolution of the height and rms-roughness during nucleation. Both values were measured on $1 \times 1\ \mu m^2$ images like the one shown in Figure 3.8.

ation.

Sample *A0p2* grown for 30 s was also investigated by TEM to assert the presence of particles with different structure or / and orientation than the one in the first stage. Cross-sectional TEM images [Figure 3.11(a)] reveal the presence of already formed GaN NWs whose length can reach up to 20 nm. Their epitaxial orientation relative to the sapphire substrate investigated by SAED confirms the one deduced by RHEED [Figure 3.11(b)]. Unfortunately, the small volume of the Ni particles does not generate any detectable spot in the pattern. However, all the particles on NW tips analyzed by HRTEM [Figure 3.11(c)] were found in the same state, phase and orientation as during the first stage of the nucleation. The lattice parameter of these particles deduced by comparison with the one of GaN is again 3.61 ± 0.04 Å in agreement with the one measured by RHEED and HRTEM during the first stage of nucleation. Thus no direct evidence of any *bcc* phase could be found. This apparent disagreement with the RHEED data for the second stage may be a result of a different time dependence when the rotation of the substrate is activated but also of the cooling procedure: Excess Ga present in the particles might have been consumed by reactive N still present in the chamber. Moreover, this is also suggested by the presence of a "hat" identified from its lattice parameter as GaN, found on the top facet of many particles observed by TEM and also seen in Figure 3.11(c). This hat might also have formed during cooling, because if it was present during the nucleation, the Ni particles would have been buried for longer growth duration. Also it is surprising that the particle does not cover the whole NW diameter. This could be explained by the phase transformation inducing a change of the lateral facet planes.

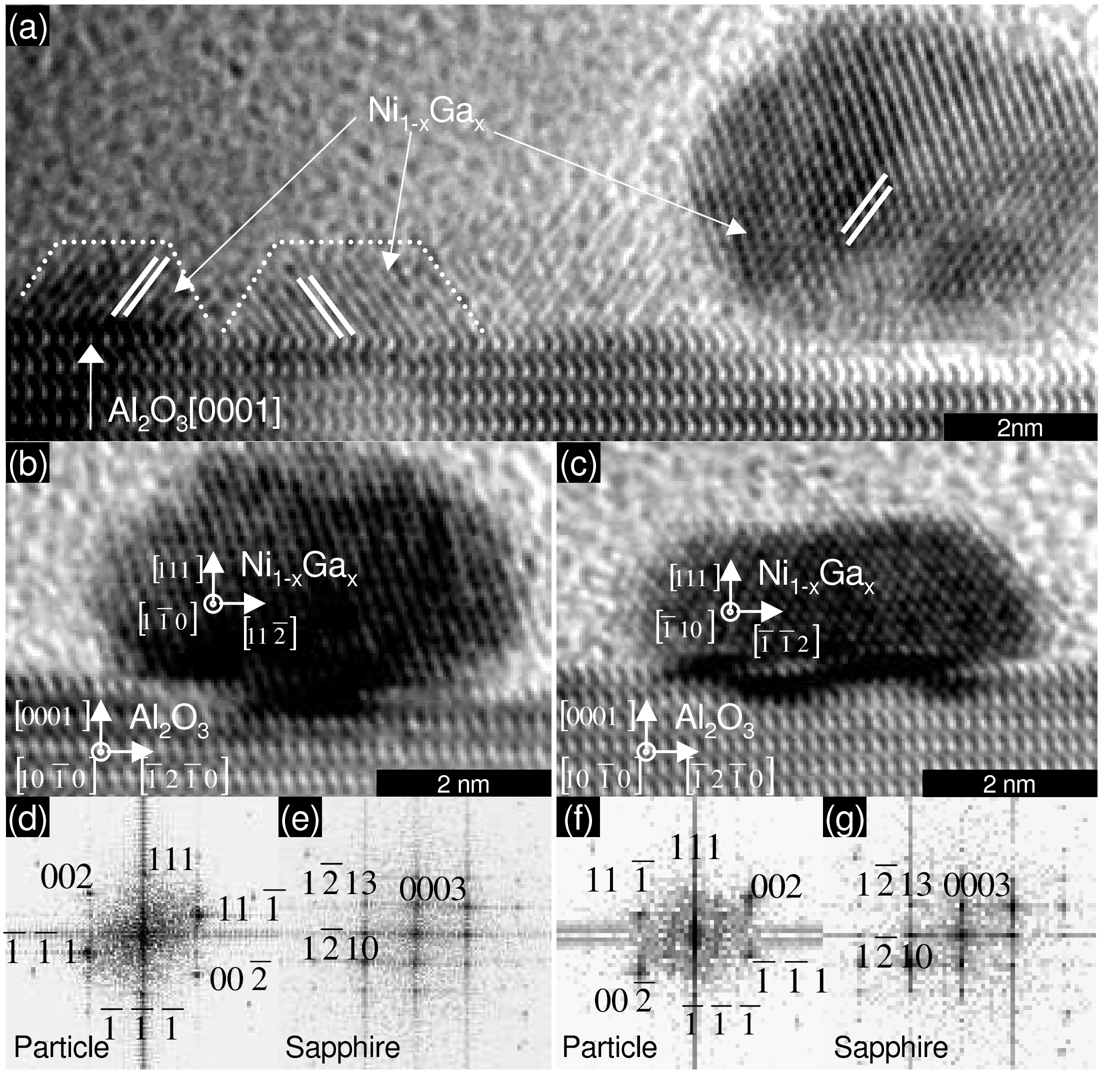

Figure 3.10: (a), (b) and (c) Cross sectional TEM images seen along $[10\bar{1}0]_{Al_2O_3}$ of $Ni_{1-x}Ga_x$ particles with mirror orientation. (b) and (c) illustrate two particles in the orientations 1 and 2, respectively.(d)–(g) are the calculated 2D Fourier transform of the particle and sapphire areas in (b) and (c).

Last, different orientations can coexist within a single catalyst particle as seen in Figure 3.11(d). This was also reported in ref [148]. Unfortunately, the size of the areas of different orientations is too small to assert if these are related to twins or different crystal structures.

The *bcc* β-NiGa phase was nevertheless found during a TEM investigation of two other samples (Figure 3.12). The particularity of these samples is that their growth procedure was carried out under Ga-excess. Sample *A0t1* results from 15 min exposure of the Ni particles to the same nominal Ga flux as for the previous experiments, but with the N-shutter remaining closed and at a substrate temperature of 780°C. This sample pre-

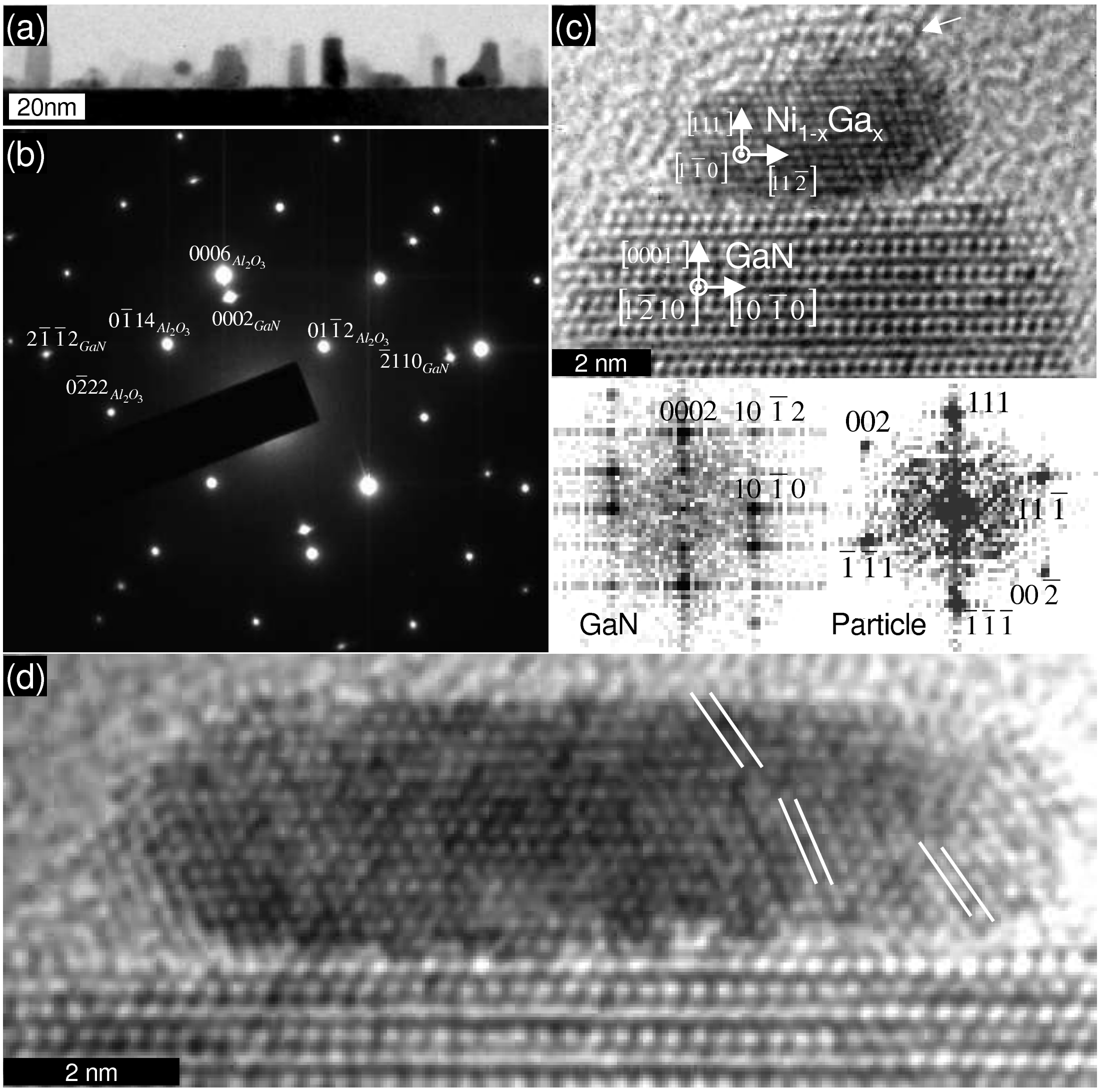

Figure 3.11: (a) Cross sectional TEM image and (b) SAED pattern along $[1\bar{2}10]_{Al_2O_3}$ of sample *A0p2* grown for 30 s. (c) HRTEM image illustrating a NW tip of the same sample. The arrow points to a "hat" of GaN. The bottom patterns are the corresponding 2D FFT calculated for the particle and GaN areas. (d) HRTEM image illustrating a catalyst particle with mixed orientations or structures.

sented in Figure 3.12(a) exhibits a mixture of both the β-NiGa and α'-Ni_3Ga phase and it is also seen that NWs are starting to form, possibly from the reaction with active N escaping from the source. For sample *A0t2* illustrated in Figure 3.12(b) extracted from ref. [165], growth was first conducted under N-excess and switched to Ga-excess at the end of the procedure as described in ref. [19]. Again, the β-NiGa phase is clearly observed and the measured lattice spacing of 2.08 Å is consistent with $d_{011} = 2.05$ Å for β-NiGa. Moreover, the presence of the 001 reflections indicates that this phase is ordered. Last, the epitaxial orientation of these seeds is the same as the one deduced by RHEED. Thus, the phase transformation observed in the second stage of the nucleation by RHEED is effectively observable by TEM, but only in the case where a large amount of Ga is supplied just before the end of the growth procedure in order to preserve enough Ga inside the Ni-Ga particles after the cooling.

3.2.4 Influence of the temperature and *V/III* ratio on the nucleation processes

In the previous study the succession of the nucleation stages could be identified by monitoring of the Ga desorption rate in real time. Similarly, the influence of the growth parameters on this Ga desorption is further investigated, and three different temperatures, Ga- and N-rates were explored separately. However, to make a detailed study as in section 3.2.1 one would need to compare each experiment with the reference one of growth on a bare sapphire substrate. This was not done for all of these samples, and RHEED monitoring was not carried out either. Thus, it is not possible to detect any change of the $\mathrm{Ni}_{1-x}Ga_x$ phases and determine the observation of stage 2. That is why this brief stage is ignored in the following and only stage 1 and 3 are considered. The identification of these stages is indicated on the QMS profile in Figure 3.13(a). As before, stage 1 corresponds to the increase in the desorption of Ga for the duration *t1* associated with the net amount of incorporated Ga *A1*, while stage 3 is the decrease in the Ga desorption to which the duration *t3* and the net amount *A3* are associated. The steady state is indicated as stage 4. At this point it is though necessary to point out that *A1* as well as *A3* correspond to Ga incorporated both into the Ni islands and on the bare sapphire left exposed between the Ni islands. Note that for both nucleation stages, if the Ga incorporation rate does not change with the modified growth parameter, an increase of the stage duration should produce an increase of the Ga amount incorporated. Last, to understand these results, it is necessary to recall the investigation of Koblmueller *et al* [46] on the nucleation of GaN on sapphire and SiC by QMS. They showed that the GaN nucleation under Ga-excess was extremely delayed and accompanied by a higher Ga reevaporation rate leading to an important GaN loss of thickness. This higher Ga reevaporation was related to the decomposition of unstable subcritical nuclei. Hence, similarly to these results *t3* can be associated to the nucleation delay for the growth of GaN.

Influence of the temperature on the nucleation processes

Figures 3.14(a) and 3.14(b) illustrate the evolution of *t1* and *t3* as well as *A1* and *A3* in dependence on the substrate temperature. To this aim samples *A0a*, *A0b* and *A0c* were grown at 730°C, 755°C, and 780°C, respectively, under the same nominal *V/III* ratio as previously. Their morphology is illustrated in Figure 4.16 in chapter 4 where it will also be commented. These graphs show that the durations *t1* of stage 1 and *t3* of stage 3, as well as the amount *A1* increase with the nucleation temperature only slightly between 730°C and 755°C but significantly between 755°C and 780°C, while the amount *A3* first increases between 730°C and 755°C and then drops at 780°C.

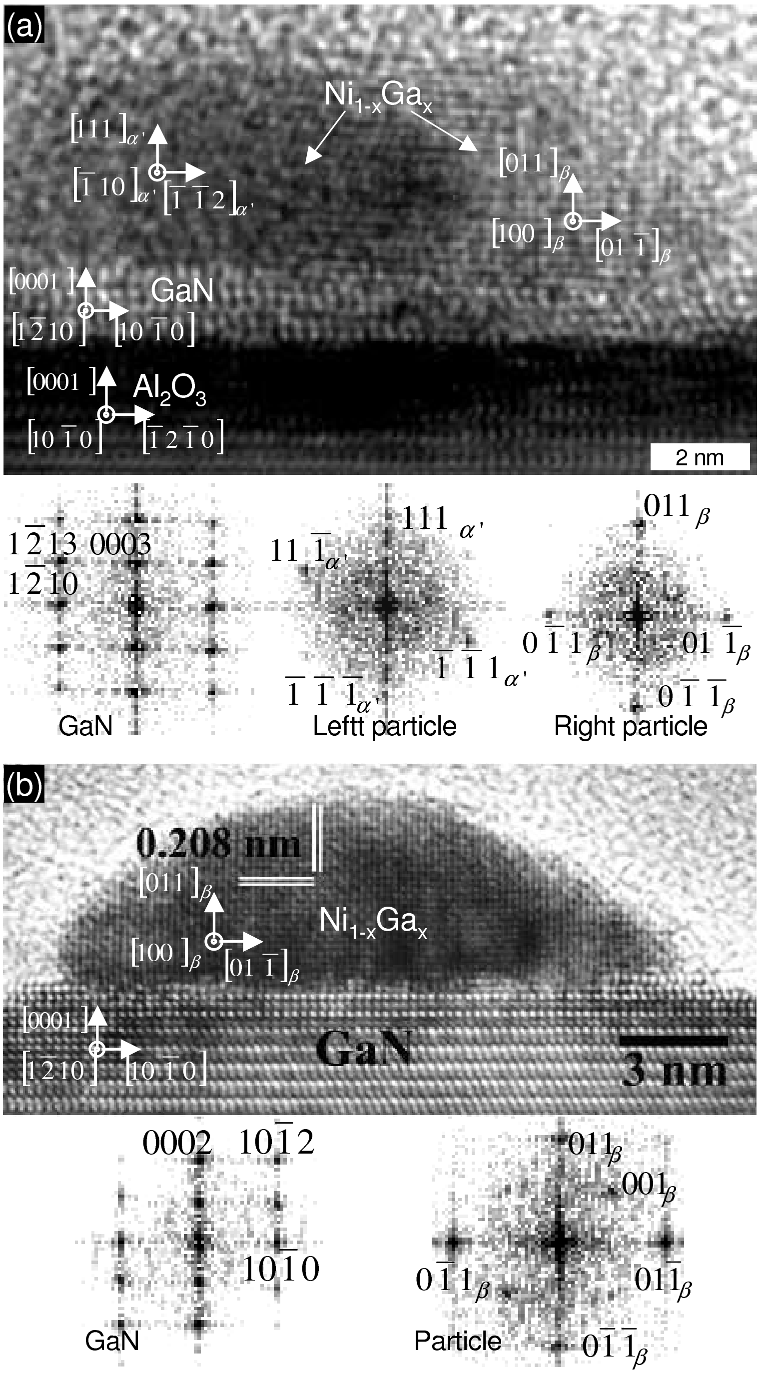

Figure 3.12: Cross sectional HRTEM images along $[1\bar{2}10]_{GaN}$ of (a) sample *A0t1* and (b) *A0t2*. In both cases, growth was terminated under Ga-rich conditions. Each image is followed by the calculated 2D Fourier transform of areas corresponding to (a) the sapphire, the left and the right particles, (b) GaN and the particle. The β-NiGa phase is unambiguously identified.

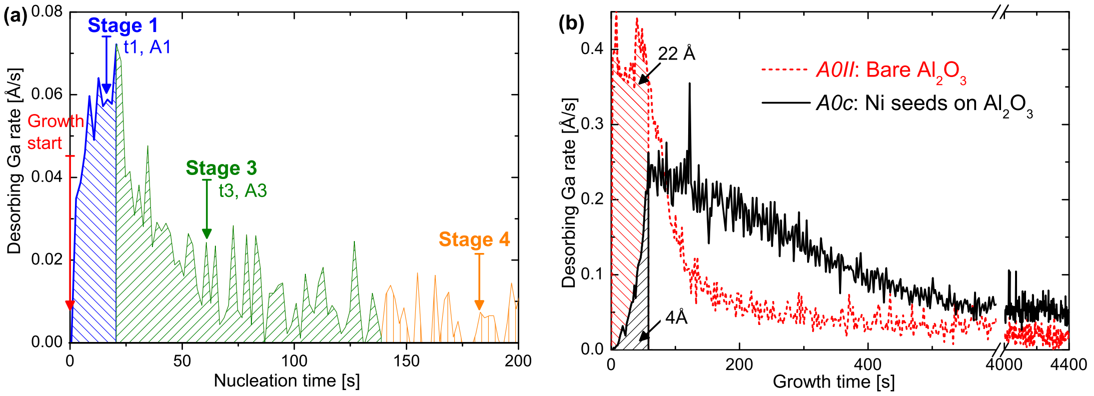

Figure 3.13: (a) The 3 stages of the nucleation as identified by QMS. Stage 1 corresponds to the incorporation of a Ga amount *A1* on the substrate surface (Ni particles and bare surface) during the duration *t1*. No GaN is formed yet. Stage 3 corresponds to the nucleation of GaN with the delay *t3* and the amount *A3* of GaN formed. Stage 4 corresponds to the growth of GaN in the steady state. The QMS profile corresponds to sample *A0g* grown at 730°C with a Ga-rate of 0.8 Å/s and a N-rate of 2.0 Å/s. (b) Calibrated QMS profiles of Ga desorption during nucleation at 780°C on bare and covered by Ni islands sapphire substrates (samples *A0II* and *A0c*, respectively).

The increase in nucleation time can be explained by a higher Ga-reevaporation during both stages. In addition, *A1* seems to vary linearly with *t1* although more statistic is required to evidence an exact dependence. In contrast, *A3* does not vary monotonously with *t3* indicating that the Ga incorporation rate changes with the temperature for stage 3. Thus the incorporation rate dependence on the growth temperature is different for each nucleation stage.

Assuming that during stage 1 no GaN has formed yet, for each stage different mechanisms would be in competition. During stage 1 only the mechanisms of Ga incorporation into the Ni seeds and Ga desorption would occur, while for stage 3 GaN nucleation and GaN decomposition would also to be considered. Thus the difference in Ga incorporation rate between both stages could be related to GaN growth and decomposition that would affect only stage 3. The assumption that no GaN forms during stage 1 is in agreement with the experiment done at 730°C. Moreover, for higher growth temperature, during stage 1 the Ga supplied is still fully incorporated into the Ni seeds in contrast to nucleation on bare sapphire where it almost fully desorbs as seen in Figure 3.13(b) presenting the QMS profiles of nucleation on bare sapphire and sapphire covered with Ni seeds at 780°C. In addition, the GaN nucleation time on bare sapphire also increases and less than 0.3 ML would have nucleated during stage 1 on the bare sapphire exposed between the Ni seeds. Last, the decrease in Ga incorporation *A3* related to GaN decomposition during stage 3 observed above 755°C would be consistent with experimental results on GaN decomposition [48]. These experiments showed that the rate of GaN decomposition exponentially increases above 750°C under active N-excess whereas under Ga-rich conditions or vacuum, decomposition sets in already for temperatures as low as 700°C [36].

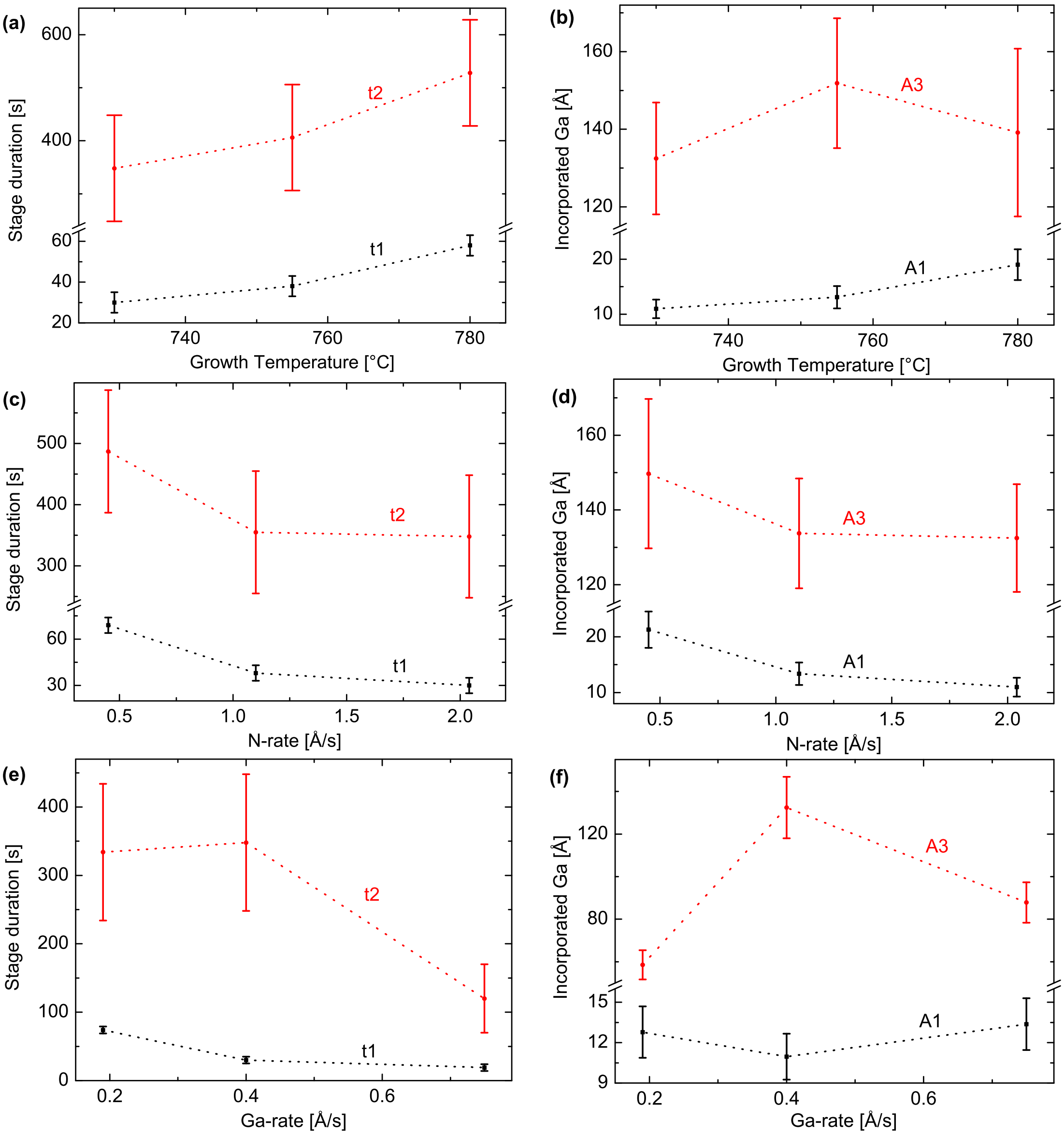

Figure 3.14: Duration of the nucleation stages and corresponding amount of incorporated Ga as a function of (a), (b) the growth temperature (Samples *A0a*, *A0b*, *A0c*), (c), (d) the N-rate (Samples *A0a*, *A0d*, *A0e*) and (e), (f) the Ga-rate (Samples *A0a*, *A0f*, *A0g*). The straight lines are guides to the eye.

The effect of the Ga desorption and thermal decomposition of GaN is directly observable in the QMS profile of sample *A0c* grown at 780°C for which the reference experiment of nucleation on bare sapphire (sample *A0II*) was also carried out. The corresponding Ga-desorption profiles are shown in Figure 3.13(b). In both cases, growth on bare sapphire and growth on sapphire covered by Ni islands, the duration of the whole nucleation process and the corresponding loss of thickness are significantly increased in comparison to the growth at 730°C (see Figure 3.1 for comparison). Moreover, in the steady state corresponding to stage 4, the Ga-desorption rate is different from zero. This means that the growth rate is effectively lower than the supplied Ga-rate and that Ga desorption and GaN decomposition are not negligible effects. Also, the decomposition rate might be slightly different between samples *A0c* and *A0II*. Possible reasons are that facets of different orientation are involved and that the effective surface of the NW sample *A0c* is larger.

Interesting enough is that during stage 1 the Ga desorption from the sample covered with the Ni islands (sample *A0c*) is still reduced in comparison to the one from bare sapphire (sample *A0II*). The duration of this stage lasts $t1 = 58$ s which is almost the double in comparison to one measured during nucleation at 730°C. The desorbed amount of Ga during the initial stage is in GaN equivalent thickness 4 Å for sample *A0c* and 22 Å for sample *A0II*. Still assuming a fraction $S = 70\%$ of the sapphire surface not covered by the Ni particles for sample *A0c*, by the same calculation as in section 3.2.1, a Ga concentration ranging from 65 % to 82 % is obtained. This range is higher than the one deduced at 730°C and would correspond in the binary NiGa phase diagram [145, 147] to the Ga-rich portion where for this temperature the β'-Ga_3Ni_2 phase is in equilibrium with the liquid one as illustrated in Figure 3.4 by the left-hand side shaded box. Hence in this case it is expected that the VLS mechanism probably sets in. However, it should be noted that the extraction of the composition from QMS profiles is not very exact and that the Ga concentration ranges for samples *A0a* and *A0c* almost overlap. Also it is questionable to what extent bulk phase diagrams can be applied to nanoscale particles [106]. In any case, the richer Ga composition of the Ni islands for higher temperature observed here is consistent with the results of Venugopalan *et al* [150] and Aurongzeb *et al* [166]. These groups reported an increasing dissolution of Ga into Ni with temperature in the range of 600°C to 900°C. A RHEED analysis as done in section 3.2.2 would be needed to assertain if effectively another phase than NiGa is observed before GaN growth sets in and whether it is solid or liquid.

Influence of the *V/III* ratio on the nucleation processes

Figures 3.14(c) and 3.14(d) illustrate the evolution of *t1* and *t3* as well as *A1* and *A3* in dependence on the N-rate. To this aim the samples *A0a*, *A0d* and *A0e* are now considered. These samples were grown at 730°C with a N-rate of 2.0 Å/s, 1.1 Å/s and 0.5 Å/s respectively, but with the same Ga-rate of 0.4 Å/s. Their morphology is illustrated in Figure 4.12 in chapter 4 where it will also be commented in detail.

For these samples, the durations *t1* and *t3* as well as the amounts of Ga incorporated *A1* and *A3* are very similar. When the N-rate is decreased from 2.0 Å/s to 1.1 Å/s, the durations and amounts of incorporated Ga barely change whereas when the N-rate is further reduced to 0.5 Å/s such that the stoichiometry is approached, these amounts all increase.

For the first stage, the increase of the Ga incorporation *A1* observed for the lower N-rate but its constant value for higher N-rate may indicate that the composition of the seed changes with the N-rate. Such dependence have already been observed by XEDS analysis ex situ on Au-Ga particles catalysing the growth of GaSb NWs by MOVPE [167]. In this case it was evidenced that the seeds exhibited only two different Ga compositions depending on the trimethylantimony flow (TMSb) whose reduction led to the larger Ga composition. This result was interpreted in term of ternary phase diagram for which two pseudobinary sections were evidenced between GaSb, Ga and Au so that it was concluded that growth occurs along both these sections. Note that the ternary phase diagram of the Ni-Ga-N system shown in appendix 5.2 also present similarly for the temperature range considered two pseudobinary sections with tie lines between GaN, NiGa and Ga_3Ni_2 and that for larger N-rate *t1* and *A1* are almost unchanged indicating a stable Ga incorporation *A1* into the Ni-seeds before GaN nucleation. However, a similar study by XEDS would be needed before such conclusion could be drawn.

The increase of Ga incorporation *A3* observed for a lower N-rate is apparently in contradiction with the lower decomposition rate of GaN occurring for higher active N-rich excess reported by Fernández *et al.*[48]. However, as the N-rate is decreased, *t3* increases faster than *A3*. Hence, the mean Ga-incorporation rate estimated form the ratio *A3*/*t3* during stage 3 effectively decreases when the N-rate is decreased in agreement with [48]. The rise of the Ga incorporation during stage 3 suggests an additional effect. The morphology of sample *A0e* reveals the presence of few short NWs embedded in a planar rough layer of GaN. This contrasts with the morphology of samples *A0a* and *A0c* that corresponds to thin NWs. For a small N-rate, i.e. smaller *V/III* ratio, this observation indicates that the Ni islands are competing with the sapphire surface exposed between the islands for the Ga-adatom incorporation and further GaN growth. In this case, it is highly likely that the NW nucleation is limited by the low N-rate, as will be discussed in more detail in section 4.4.1. Ga adatoms still incorporate preferentially into the Ni islands, which is indicated by negligible Ga desorption at the start of growth. However, if the Ga in the Ni islands is not consumed fast enough by the active N, the further arriving Ga atoms accumulate outside the particles, and planar growth also occurs leading to an increase of *A3*.

Last, the effect of the Ga-rate on the nucleation was also investigated. To this aim the Ga-desorption of samples *A0a*, *A0f* and *A0g* grown with a Ga-rate of 0.4 Å/s, 0.2 Å/s and 0.8 Å/s at a temperature of 730°C and with a N-rate of 2.0 Å/s was monitored. Their morphology is illustrated in Figure 4.14 in chapter 4.

In Figure 3.14(e), *t1* decreases when the amount of supplied Ga is increased. However, in Figure 3.14(f), the variation of *A1* is barely noticeable. This result indicates that at fixed temperature and N-rate, the supplied Ga-rate limits the Ga incorporation rate into the Ni seeds but has no influence on the amount of Ga incorporated into Ni before GaN nucleation.

For the second stage a different dependence is ascertained. *t3* is nearly the same for

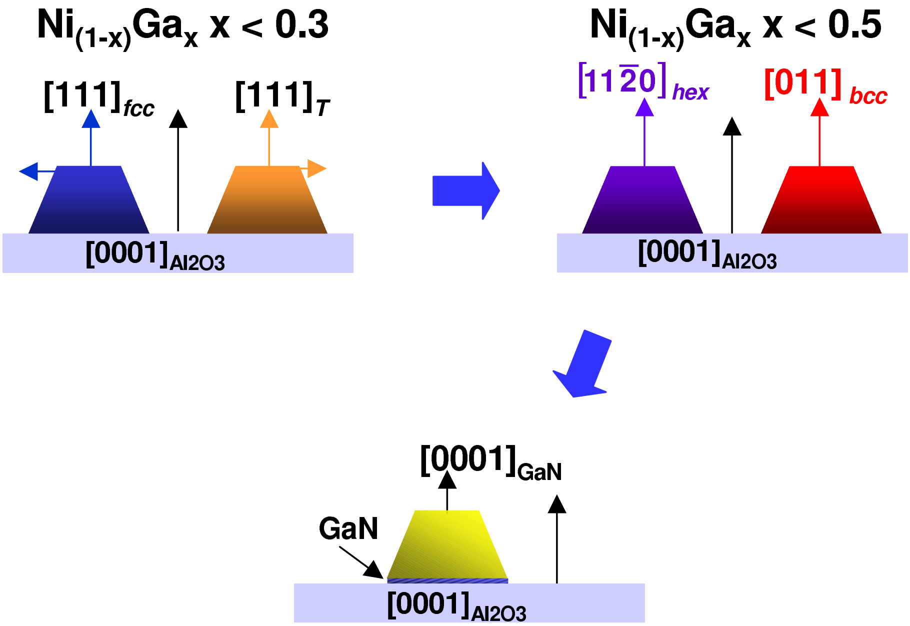

Figure 3.15: The 3 stages of the nucleation at 730°C of GaN NWs in the catalyst-assisted approach. In stage 1 (top-left), Ga is preferentially incorporated into the Ni seeds. At the beginning of the nucleation, the seeds have the *fcc* structure with orientations that are twinned. The Ni_3Ga $L1_2$ structure also most probably appears during this stage, due to Ga incorporation leading to a very similar diffraction pattern. In stage 2 (top-right), the transformation of the seed crystal structure induced by Ga accumulation occurs. Two different seed structures appear whereas the parent phase vanishes. The first one is the *bcc* NiGa structure and the second one corresponds to another Ni-Ga related compound of hexagonal structure. In stage 3 (bottom), GaN finally nucleates under the seeds. The compositions corresponding to the Ni-Ga and Ni-Ga-N phase diagrams are given here as an indication but may differ from the exact composition during the nucleation.

Ga-rates lower or equal to 0.4 Å/s while the Ga incorporation *A3* is much lower at the lowest Ga-rate corresponding to sample *A0f*. This indicates that the nucleation rate is largely reduced for the lowest Ga-rate. For the highest Ga-rate corresponding to sample *A0g*, the duration of the nucleation *t3* is three times faster than for the lower Ga rates whereas the incorporated amount of Ga *A3* decrease to one third in comparison to the amount obtained for the Ga-rate of 0.4 Å/s of sample *A0a*. This observation shows that the increase in Ga-rate also increases the incorporation rate as would be expected for the growth under N-rich conditions.

3.2.5 Discussion

The present study shows that the nucleation of GaN NWs grown by the catalyst assisted approach can be divided into three main stages. These stages are Ga incorporation into the Ni particles, transformation of the crystal structure of the Ni-Ga catalyst particles and finally GaN nucleation. The model of the resulting nucleation is sketched in Figure 3.15. In the following, this model is discussed by considering the binary Ni-Ga and

ternary Ni-Ga-N phase diagrams in order to get information on the different detected Ni-Ga structures. As discussed earlier, at nanoscale and far from equilibrium, phase diagrams might not apply. However they are useful in indicating reaction paths. Also, in order to understand how binary semiconductor material can be synthesized from a metal catalyst, it is necessary to understand the ternary phase diagram of the system. The ternary phase diagrams of Ni-Ga-N are presented for two different temperatures in appendix 5.2. As earlier exposed, no Ni-Ga-N ternary compounds are expected to form at temperatures higher than 500°C [149, 152, 153] and the nickel nitrides Ni_4N and Ni_3N are unstable at our growth temperature [154]. Thus, at the beginning of the nucleation, only the Ni-Ga system is considered. In Figure 3.4 the evolution of the composition of the Ni particles is indicated by arrows for two different temperatures in this system.
The starting point of the NW nucleation corresponds to the Ni particles in the solid state as indicated by RHEED. These particles have the *fcc* (A_1) crystal structure and their orientation relatively to the substrate normal is:
$[111]_{Ni} \parallel [0001]_{Al_2O_3}$.
In addition, their in-plane orientation is twinned around the $[111]_{Ni}$ direction as sketched in Figure 3.15. This point corresponds to the origin of the arrows in Figure 3.13. In the very early stage Ga diffuses into the Ni particles forming a Ni-Ga solid solution. This result is ascertained by the systematically reduced Ga desorption observed by QMS at the beginning of all the experiments where Ni particles were deposited onto the sapphire surface in comparison to nucleation on bare sapphire. However at this time RHEED evidences no nucleation of GaN. This was confirmed by TEM. When the solubility limit of Ga into Ni is reached (around 24.3 % at 1212 °C [147] for bulk) most probably the α'-Ni_3Ga phase with the $L1_2$ structure appears. Ideally, the $L1_2$ structure of Ni_3Ga can be obtained from the *fcc* one of Ni by the substitution of Ni atoms with Ga atoms at the corner sites of the *fcc* lattice so that no fundamental change in the lattice structure would occur and the epitaxial orientation of the seeds would remain unchanged. Therefore no obvious structural change at this stage could be evidenced but the Ga incorporation was confirmed by additional $1\bar{1}0$ reflections in the RHEED pattern in Figure 3.7. When Ga accumulates, the volume of the particles increases and strain most probably also appears at the interface with the sapphire substrate, as could indicate the contrast observed at the interface of some particles with the substrate in Figure 3.10(b) and (c). In addition, the gradual increase in the Ga desorption observed by QMS during this initial stage could also be the sign of strain accumulation within the particles constituting a barrier for adatom attachment as will be explained later in the second part of this chapter.
The second stage (called stage 2 in this work) that has been identified is still not the nucleation of GaN but an intermediate stage of the Ga incorporation corresponding to a marked change of the crystal structure of the particles. RHEED ascertains the appearance of two new structures induced by further Ga incorporation. The first one is undoubtedly the β-NiGa *bcc* structure. The second Ni-Ga related solid structure is hexagonal and could be Ni_3Ga_2, $Ni_{13}Ga_7$ or Ga_3Ni_2. Following the binary Ni-Ga phase diagram in Figure 3.4, at temperatures higher than 730 °C but lower than 895 °C, Ga enrichment of Ni should produce successively the phases α'-Ni_3Ga (*fcc*), γ-$Ni_{13}Ga_7$

(hexagonal), ϵ-Ni_3Ga_2 (hexagonal), β-NiGa (*bcc*), β'-Ga_3Ni_2 (trigonal or hexagonal) and finally a liquid Ga-Ni if Ga is not consumed faster by GaN nucleation. At this stage, the calculation of the amount of Ga incorporated into the Ni extracted from the QMS signal leads to the range of 28 up to 63 % at. This value is thus surprisingly comparable with the existence domain of Ni_3Ga whose upper limit amounts to 30 % at 720 °C [145]. In addition, the appearance of the two new structures coincides exactly with the disappearance of the parent Ni_3Ga one. These two new structures appears with the correspondence of crystal planes and directions:
$(111)_{\alpha'} \parallel (011)_{\beta}$ and $[11\bar{2}]_{\alpha'} \parallel [01\bar{1}]_{\beta}$
and
$(111)_{\alpha'} \parallel (11\bar{2}0)_{\gamma,\epsilon,\beta'}$ and $[11\bar{2}]_{\alpha'} \parallel [1\bar{1}00]_{\gamma,\epsilon,\beta'}$
Note that a decrease in the melting temperature could be expected for these particles of nanometric scale. However, the presence of the hexagonal additional phase superimposed to the NiGa one indicates that the eutectic reaction between Ni_3Ga, liquid, NiGa (1207°C) is not occurring. Nevertheless, the identification of this hexagonal Ni-Ga solid structure is of interest in order to determine whether the VLS mechanism could be coupled to the VSS one. The appearance of the Ga_3Ni_2 phase could enable an invariant equilibrium between the NiGa, the Ga_3Ni_2 and the liquid phase as underlined in Figure 3.4 by the horizontal red line at 895°C [147, 163]. In this case high Ga content liquid catalyst could also be present during the nucleation.

For the NiGa phase, the above-mentioned epitaxial correspondence with Ni_3Ga could be the signature for a Kurdjumov-Sachs martensitic phase transformation. Martensitic transformations have already been reported for pure Ni [160] and related compounds as well as for the Ni-Al system [168] subjected to external stress or alloying. Briefly, such a transformation is a diffusionless process which occurs very fast (it can reach the velocity of sound in steel) [169] and involves an anisotropic expansion of the crystal which is reversible. This observation could in turn explain the difficulty in observing Ni-Ga particles in the β phase after the cooling procedure, since the amount of Ga entailed by the Ni particles might be purged out inducing the reverse transformation. Last, the anisotropic expansion involves a further change of the particle dimensions which might present larger difficulties in controlling the NW diameter.

After this intermediate stage, finally GaN nucleation occurs as evidenced by the spotty RHEED pattern corresponding to WZ GaN. Additional reflections belonging to previous Ni-Ga phases which remain superimposed for over 3 min are a strong indication that a substantial part of the catalyst-particles are in the solid state also during growth. Therefore the mechanism accounting for these GaN NWs is rather the VSS than the VLS one. However, as proposed in ref. [170] and evidenced in ref. [121] a VLS mechanism could also still occur by an increase in the Ga concentration along the particle from the top surface to the interface such that the lowest part near the interface with the NW is liquid while the top surface of the particle remains solid.

Note that the phase sequence observed in this study at 730°C, corresponding successively to Ni, Ni-Ga solid-solution, probably Ni_3Ga and NiGa before the nucleation of GaN, is found in remarkable agreement with the Ni-Ga-N ternary phase diagrams [149, 152, 153] between 500°C and 850°C. Of course, at different temperatures different phase sequences are predicted. And most probably the larger amount of Ga incorporated into the particles before GaN nucleation detected by QMS for higher nucleation temperatures would correspond to another phase sequence, as sketched in Figure 3.4. Similarly, experimental observation by Venugopalan *et al* [150] showed that between 600 and 900°C annealing of GaN with Ni in N_2 atmosphere yields Ga-richer nickel gallide phases. However, for the considered temperature range, ternary diagrams all evidence that the equilibrium between $Ni_{1-x}Ga_x$ and GaN starts for $x \geq 50$ at%, as NiGa is the first Ni-Ga compound to present a tie-line with GaN as the Ga concentration is increased. In other words, between 500°C and 850°C, for $x \leq 50$ at% when N, Ga and Ni are present, only N gas and Ni-rich Ni-Ga compounds would be obtained at equilibrium. Thus this prediction is found comparable with the appearance of GaN from Ni-Ga particles in the NiGa phase or a Ga-richer phase.

By comparison with the existing literature, apparent divergences are observed. Apart from the axial growth (corresponding to stage 4 in Figure 3.13), usually two stages are reported in ref. [114–116, 122, 171] that are metal alloying and crystal nucleation. However, for the material systems considered in these references, the material phase sequence during nucleation is simple. For systems that have a more complicated phase sequence before the crystal nucleation it is most probable that the alloying stage could be divided in as many sub-stages as phases crossed following the phase diagram of the considered material system. Therefore, the additional intermediate stage evidenced in this study could be considered as a sub-stage of the Ga-incorporation into the Ni catalyst. Similarly, different phases of the catalyst particles have been observed in the Au-Ga system during the growth of GaAs NWs for different *V/III* ratio [113] as well as phase transformation of the catalyst induced by the switch of group V material during the formation of GaAs-GaSb NW axial heterostructure [167]. In both cases, an agreement with the corresponding phase diagram was reported. Such a change of the catalyst crystal phase could be a priori unwanted, since it might also induce a change in the particle diameter and contact angle, as also observed in Figures 3.11(c) and 3.12(b). Therefore such transformation of the catalyst's crystal structure may have important consequences on the crystal structure and shape of the NWs [123, 167].

In addition, the incorporation of Ga into the Ni seeds is not the limiting growth process since at first almost all the Ga supplied is incorporated. Also the abrupt change of the crystal structure during the second intermediate stage does not designate this stage either. Therefore, the most probable limiting growth process is the nucleation of GaN. This conclusion is confirmed by the observation (section 3.2.4) that the duration of stage 3 *t3* corresponding to GaN nucleation before steady state growth is always larger than the duration of stage 1 *t1* corresponding to the Ga incorporation into the Ni particles.

Last, at fixed temperature and N-rate, the Ga-rate was observed to limit the duration of both the first and third stages. However, for the first stage the amount of incorporated Ga was nearly constant independently of the Ga-rate and *t1* varied inversely with the Ga-rate whereas for the third stage the Ga-rate also enhanced the nucleation rate. The N-rate was shown to have little influence except when the *V/III* ratio was close to stoichiometry. Thus these results reveal that the nucleation rate is conditioned by the amount of Ga arriving at the growth front. In any case the NW growth is the result of a fragile equilibrium between temperature, N-rate and Ga-rate since these parameters strongly influence the composition, the crystal structure and the orientation of the catalyst. These results confirmed the catalyst particle is highly alterable [77, 84] and show that the alloying stage is decisive in determining the properties of NWs to grow.

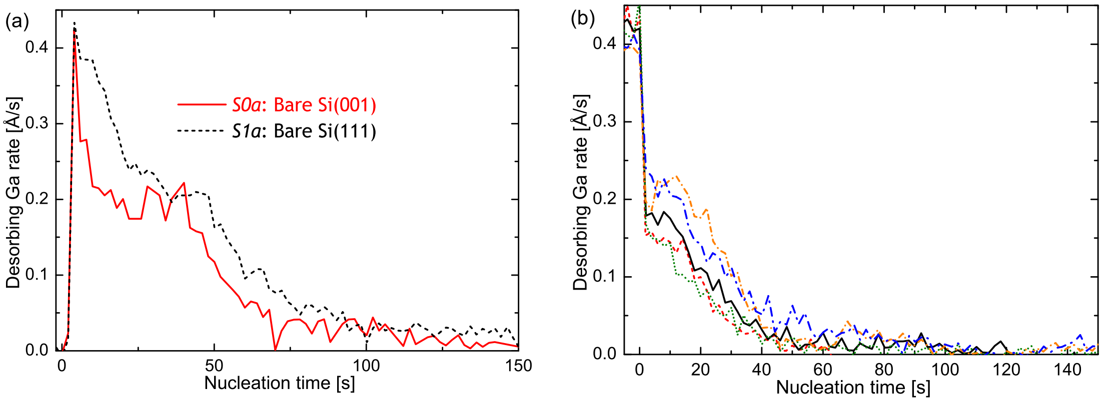

Figure 3.16: Calibrated QMS profile of Ga desorption during nucleation under the same conditions of fluxes and temperature (a) directly on silicon substrates (001) and (111) (sample *S0a* and *S1a*) with rotation of the substrate, (b) with 900 s Ga exposure before GaN growth on Si(001) (sample *S0r*) for samples reproduced with the same temperature and fluxes as for sample *S0r*.

3.3 Catalyst-free GaN NWs on Si(111) and Si(001) substrates

In the following, a similar study as in the case of the catalyst assisted approach was carried out for the catalyst-free approach. RHEED and QMS were employed to investigate the nucleation of GaN NWs grown on Si(001) and Si(111). As will be shown the results for the two surface orientations are quite similar. Si(001) is the standard substrate in the semiconductor industry. Thus, systematic AFM and TEM measurements on a series of samples with various short growth durations were carried out for this substrate orientation. The list of the samples reported here is given in appendix 5.2.

3.3.1 In-situ Quadrupole Mass Spectrometry Monitoring

Figure 3.16 presents the calibrated QMS profile of Ga desorption monitored during the nucleation of GaN on cleaned bare Si(001) and Si(111) substrates (samples *S0a* and *S1a*) at a temperature of 730°C and for Ga- and N-rates of 0.4 Å/s and 2.0 Å/s, respectively. The same procedure as for the growth on Ni covered sapphire was applied. When growth of GaN is initiated at t=0 s a different behavior is observed in this case. On both Si(001) and Si(111), the desorption signal immediately increases to about the level of the totally supplied rate of Ga similarly to the nucleation on bare sapphire substrate (see the profile of sample *A0I* profile in Figure 3.1). This indicates an initially negligible Ga incorporation, and thus a negligible growth of GaN for the very first seconds of nucleation. After about 3–4 sec, a decrease of the desorption signal occurs in two steps. The first decrease brings the desorption rate to about half the impinging rate. This decrease is in the case of Si(111) less abrupt than on Si(001). However on both substrate orientations, a second drop in the Ga desorption is observed after about 40 s for Si(001) and 48 s for Si(111) during which the Ga amount in GaN equivalent thickness of about 8 Å and 7 Å, respectively, is incorporated. The desorption signal then decreases to the steady state where all the supplied Ga is incorporated. The observed 2-step decay in the

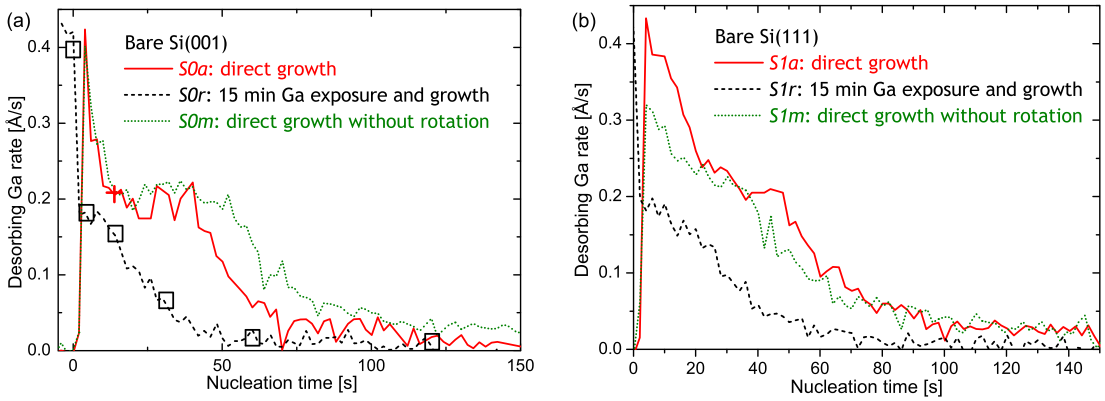

Figure 3.17: Calibrated QMS profile of Ga desorption during nucleation (a) on Si(001) and (b) on Si(111) substrates without rotation, with rotation and with Ga exposure before growth with rotation (samples *S0m*, *S0a*, *S0r* and samples *S1m*, *S1a*, and *S1r*, respectively). In (a), the squared and crossed symbols refer to the samples grown at intermediate time in the nucleation. The symbols refer to the samples grown with 900 s of Ga exposure prior to growth (squares, samples *S0p0*, *S0p1*, *S0p2*, *S0p3*, *S0p4*, *S0p5*) and grown without pre-exposure (cross, sample *S0p6*).

Ga desorption profile indicates an important impeded GaN incorporation and suggests that there is a structural change taking place during the nucleation.

The second decrease as well as the reaching of the steady state occur after a period of time which depends on the substrate surface conditioning and flux uniformity. Figure 3.17 presents three QMS profiles corresponding to three different growth procedures (a) on Si(001) and (b) on Si(111) substrates with the same growth parameters (sample cleaning procedure, fluxes and temperature). The dashed line (samples *S0r*, *S1r*) corresponds to the case where the wafer was first exposed to the flux of Ga for 900 s at 730°C while keeping the N-shutter closed. For both substrates, when the nucleation is initiated by opening the N shutter, it takes about 30 s less to observe the second decrease and to reach the steady state than when the nucleation is directly initiated (samples *S0a*, *S1a*). The dotted line corresponds to the same experiments as *S0a* and *S1a* but without rotation (samples *S0m*, *S1m*). A 15 s delay compared to the nucleation on Si(001) with rotation is observed. However, for the nucleation on Si(111) the opposite trend (in this case the nucleation with rotation lasts longer) is ascertained within the same delay. Particularly in the case of the experiment without any rotation, RHEED observations were carried out requiring focusing time before growth during which the substrates were facing the cells closed by the shutters. However, escaping atoms already reacting with the substrates might be the origin of the shift in the nucleation duration observed here. In particular, for sample *S1m* the focusing time was longer than for *S0m* and the maximum desorption at the beginning of the growth is lower than the totally supplied rate of Ga.

Reproducibility have been tested and Figure 3.1(b) presents the calibrated QMS profiles of experiments that have been done under the same flux and temperature conditions as for sample *S0r* with Ga pre-exposure. The two step decay is also observed although the first step is much more abrupt and a reproducibility with the uncertainty of 15 s is

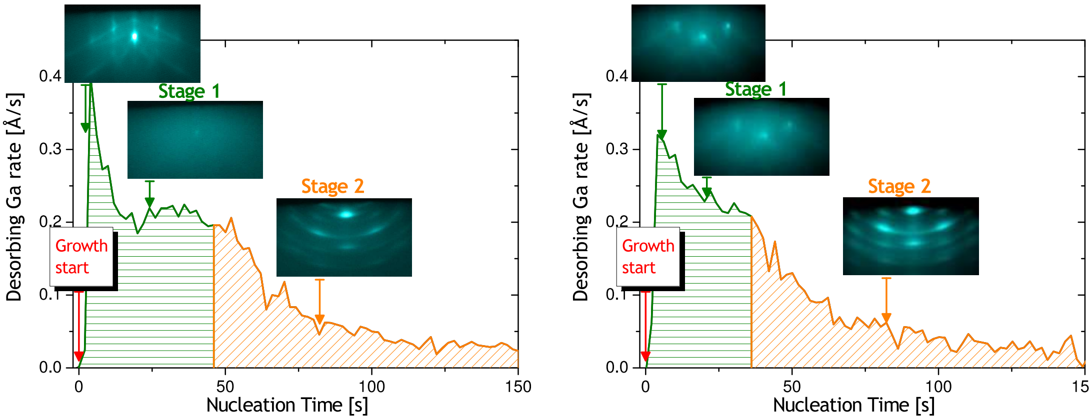

Figure 3.18: The 2 stages of the nucleation as identified by RHEED and correlated to the QMS profile of Ga desorption for (a) Si(001) and (b) Si(111) (samples *S0m* and *S1m*, respectively).

obtained. This could strongly be attributed to a small fluctuation in the supplied rate of Ga from one experiment to another. Indeed, a 0.01 Å/s difference in the supplied Ga-rate would lead to 9 Å more Ga supplied after 900 s Ga pre-exposure. This amount is three times larger than the difference in the amount of Ga incorporated between the traces corresponding to the shortest and longest nucleation durations in Figure 3.1(b). Thus, the difference of 15 s found for the time delay between the samples grown with and without rotation is not significant, while the difference of about 30 s obtained between the samples with and without Ga pre-exposure is significant and shows that Ga pre-exposure effectively shorten the nucleation.

In any case, there are at least two different stages in the nucleation on Si independently of the crystal orientation, and the time dependence is similar in both cases. Again, RHEED analysis could help to understand the complex Ga desorption behavior.

3.3.2 In-situ Reflection High-Energy Electron Diffraction Monitoring

As for the monitoring of the nucleation on sapphire, experiments were run for which the rotation of the manipulator was stopped during the growth, but in this case only one single azimuth was investigated since no pattern corresponding to an unidentified structure was detected. The experiment run on Si(001) was monitored in the azimuth $[110]_{Si}$ (sample *S0m*) while the one grown on Si(111) in the $[1\text{-}10]_{Si}$ (sample *S1m*) one. During the nucleation of GaN NWs on substrates of each orientation, two different RHEED patterns are observed. In consequence, two different nucleation stages are identified during the nucleation on both Si(001) and Si(111). These stages are correlated to the time dependence profile of the Ga desorption in Figure 3.18. In Figure 3.18(a) and (b), the corresponding RHEED patterns seen along the $[110]_{Si(001)}$ and $[1-10]_{Si(111)}$ are reported. The transition between the two stages was deduced from the profile of the RHEED spot intensity shown in Figure 3.19 that will be discussed below.

Figures 3.20 and 3.21 illustrate the detailed evolution of the RHEED pattern during nucleation on Si(001) and Si(111), respectively, showing that except for the initial surface,

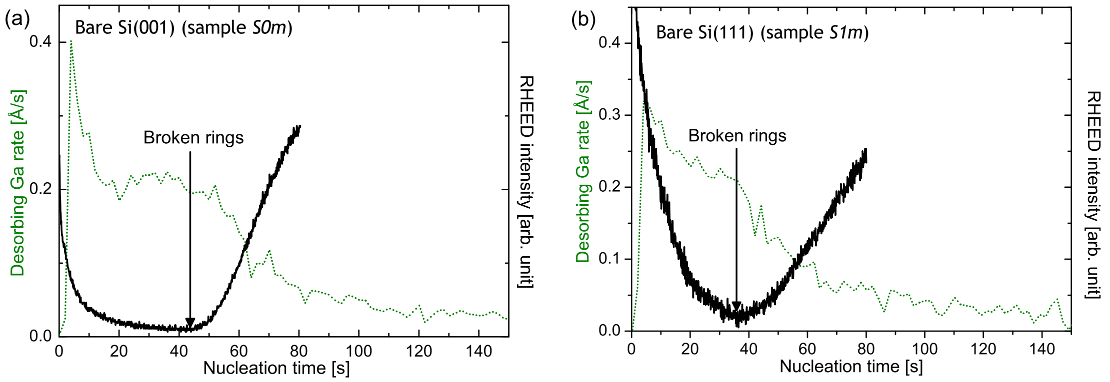

Figure 3.19: RHEED intensity and calibrated QMS profile of Ga desorption during nucleation (a) on Si(001) and (b) on Si(111) substrates without rotation (samples *S0m* and samples *S1m*, respectively).

nearly the same patterns and time dependence are obtained. After the oxide desorption and the growth temperature setting at 730°C, the (1×2) reconstruction appears for Si(001)[Figure 3.20(a)–(b)]. For Si(111) only a poor (7×7) reconstruction is obtained most likely due to an incomplete oxide desorption [Figure 3.21(a)–(b)]. Note that the initiation of GaN growth immediately induces the appearance of the (1×1) reconstruction on Si(001) and on Si(111). However, for the growth on Si(111) the obtained pattern is very diffuse and additional faint reflections were also observed. These reflections could result from experimental artifacts or from another reconstruction. (We note that for nitridation at 900°C an (8×8) surface reconstruction was attributed to Si_3N_4 [172]). As growth proceeds, these patterns become weaker and blurry. In the case of growth on Si(001) this pattern finally vanishes, while on Si(111) reflections are still very faintly distinguishable (Figures 3.20(c)–(d), 3.21(c)–(d), respectively). The appearance of the (1×1) reconstruction is accompanied by the abrupt and brief increase in the Ga desorption signal to nearly the full amount of supplied Ga at the very beginning of the nucleation and to the subsequent Ga desorption signal decrease to about half its value at slightly different times.

The second stage of the nucleation starts after about 43 sec for Si(001) and 35 sec for Si(111) (corresponding to 8 Å and 6 Å, respectively) when broken rings appear in RHEED and become more and more intense [Figures 3.20(e)–(f), 3.21(e)–(f)]. At the same time the second drop in Ga desorption takes place. The agreement in the evolution of the RHEED pattern and the QMS signal is clearly seen in Figure 3.19(a) and (b) where the RHEED spot intensity of the broken rings and the Ga desorption are plotted in the same diagram. These rings correspond to the pattern of GaN seen in transmission. The ring-like appearance of the reflections originates from the superposition of the patterns through the tilted GaN crystals growing with a misorientation relatively to the normal of the substrate. In addition, the superposition of reflections of both azimuths $[11\bar{2}0]_{GaN}$ and $[1\bar{1}00]_{GaN}$ indicates that the GaN crystals are also rotated around the *C*-axis.

The appearance of the rings corresponds to the second decrease of the Ga desorption signal reaching the steady state where all the arriving Ga is incorporated. Thus, this event points to the start of the massive growth of GaN 3D crystals. However, Ga incorporation prior to it is already detected during the first nucleation stage. Several hypotheses can be made. First, it can be assumed that Ga accumulates at the Si surface but does not form GaN yet whereas N preferentially bonds to Si and forms silicon nitride. Indeed, the Si-N bond energy (4.5 eV / bond) is much stronger than the one of GaN (2.17 eV / bond) [173], and this, in addition to the higher density of N and Si atoms favors silicon nitride formation rather than GaN [26]. This hypothesis would be consistent with the progressive blurring of the Si(1×1) reconstruction. However, the QMS profiles of experiments stopped during the first nucleation stage do not indicate immediate post-growth Ga desorption after the closing of the Ga and N shutters (data not shown), although this Ga desorption could be prevented by the excess N [36]. Therefore we also consider another hypothesis based on the formation of an intermixed layer of Si-N and Ga [26]. In order to elucidate this question, further investigations were carried out by AFM and TEM on samples for which growth was stopped at the different stages of the nucleation.

3.3.3 Post-growth AFM and TEM investigation

The QMS and RHEED results presented in the previous sections imply that the nucleation processes on the two Si orientations are fairly similar. Hence, only for one orientation post-growth analysis was carried out by AFM and TEM on samples for which the growth was stopped at various instants of the nucleation. As Si(001) is technologically much more relevant, this orientation was chosen. Indeed, the monolithic integration of V/III material on Si(001) is of larger interest but the attempts to grow planar GaN on Si(001) have so far resulted in the mix of wurtzite (WZ) and zinc-blend (ZB) phases [174, 175].

Note that for most of these samples the nucleation was initiated differently. GaN nucleation was preceded by the exposure of the clean Si surface to the Ga flux during 900 s at 730°C. During this time, the plasma cell was ignited but the N-shutter remained closed. This way, samples *S0p1*, *S0p2*, *S0p3*, *S0p4* and *S0p5* were further grown for 4 s, 15 s, 30 s, 60 s and 120 s, respectively. Sample *S0p0* received the same Ga exposure without any further growth. Another sample, *S0p6* was grown for 15 s without preceding Ga-exposure. Figure 3.22 presents the surfaces of these samples investigated by AFM. Their position in the evolution of the nucleation is reported in the corresponding QMS Ga desorption profile in Figure 3.17(a).

In Figure 3.22(a), the surface of sample *S0p0* resulting from only the exposure to Ga is very different from the one of clean Si(001) (chapter 2) although the height and the rms values of both samples are very similar. Here, the terraces of Si are not observable but instead a porous morphology is obtained. The diameter of these pores or pits can reach 20 nm. After 4 s of growth [sample *S0p1*, Figure 3.22(b)], a rougher surface is obtained with the formation of apparent mounds. Isolated islands up to 50 nm wide nucleate close to the edges of these mounds. The surface observed between the islands is similar to the one of sample *S0p0*. After 15 s of growth [sample *S0p2*, Figure 3.22(c)], smaller

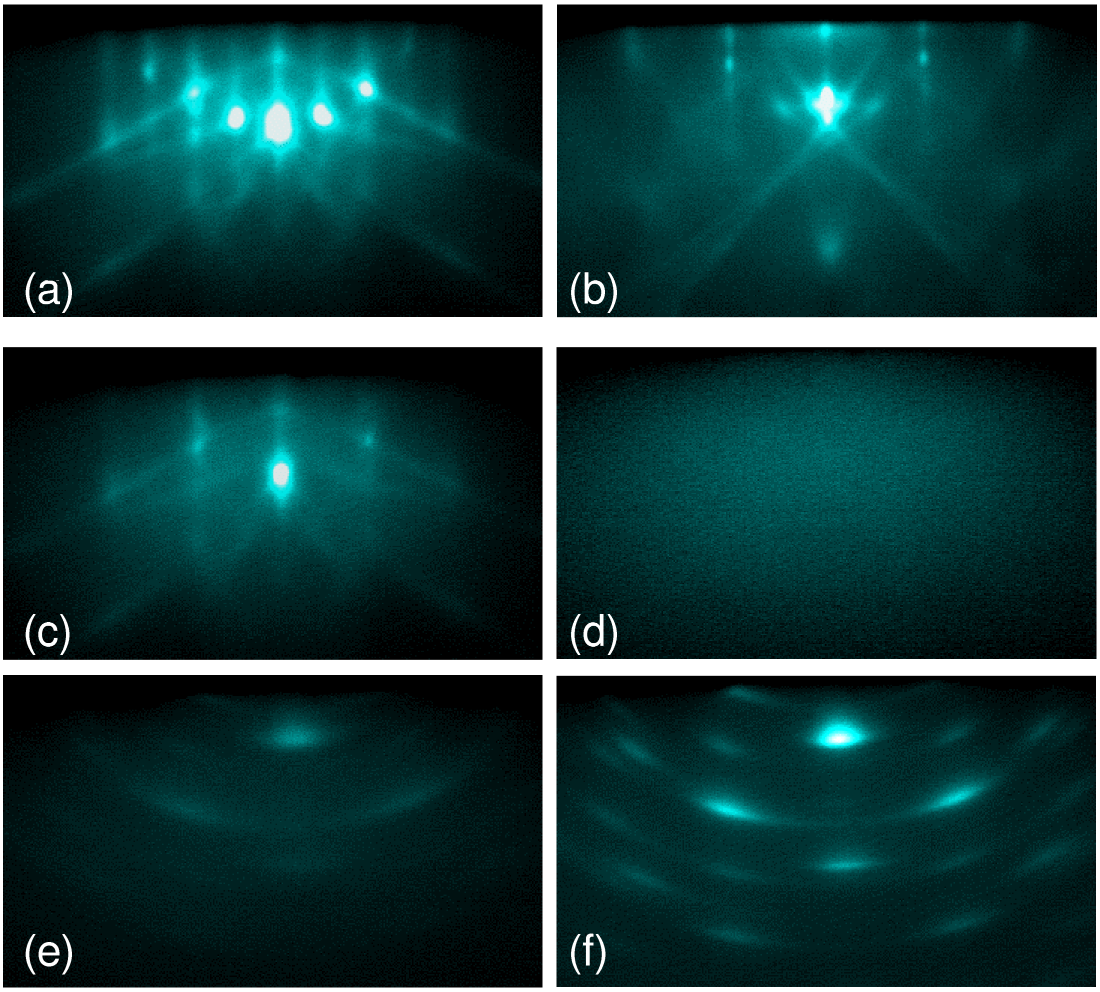

Figure 3.20: Evolution of the RHEED pattern during the nucleation of GaN NWs on Si(001) in the $[110]_{Si(001)}$ azimuth, apart from (b)in the $[311]_{Si(001)}$. The patterns are presented chronologically (a), (b) before growth, (c) after 1 s, (d) after 45 s, (e) after 60 s, (f) after 240 s of growth. (Sample *S0m*)

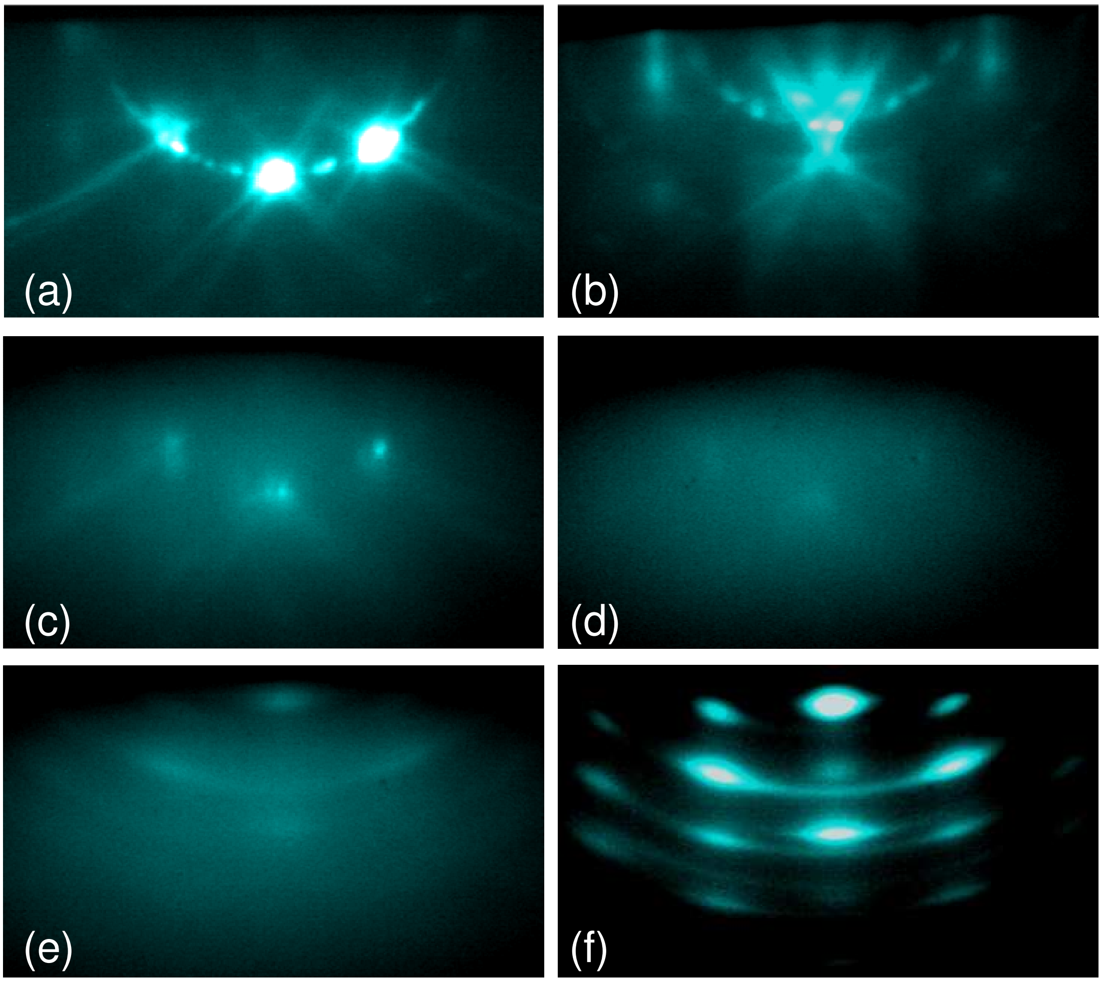

Figure 3.21: Evolution of the RHEED pattern during the nucleation of GaN NWs on Si(111) in the $[2\bar{1}\bar{1}]_{Si(111)}$ azimuth, apart from (b)in the $[1-10]_{Si(111)}$. The patterns are presented chronologically (a),(b) before growth, (c) after 15 s, (d) after 30 s, (e) after 60 s and (f) after 240 s of growth. (Sample *S1m*)

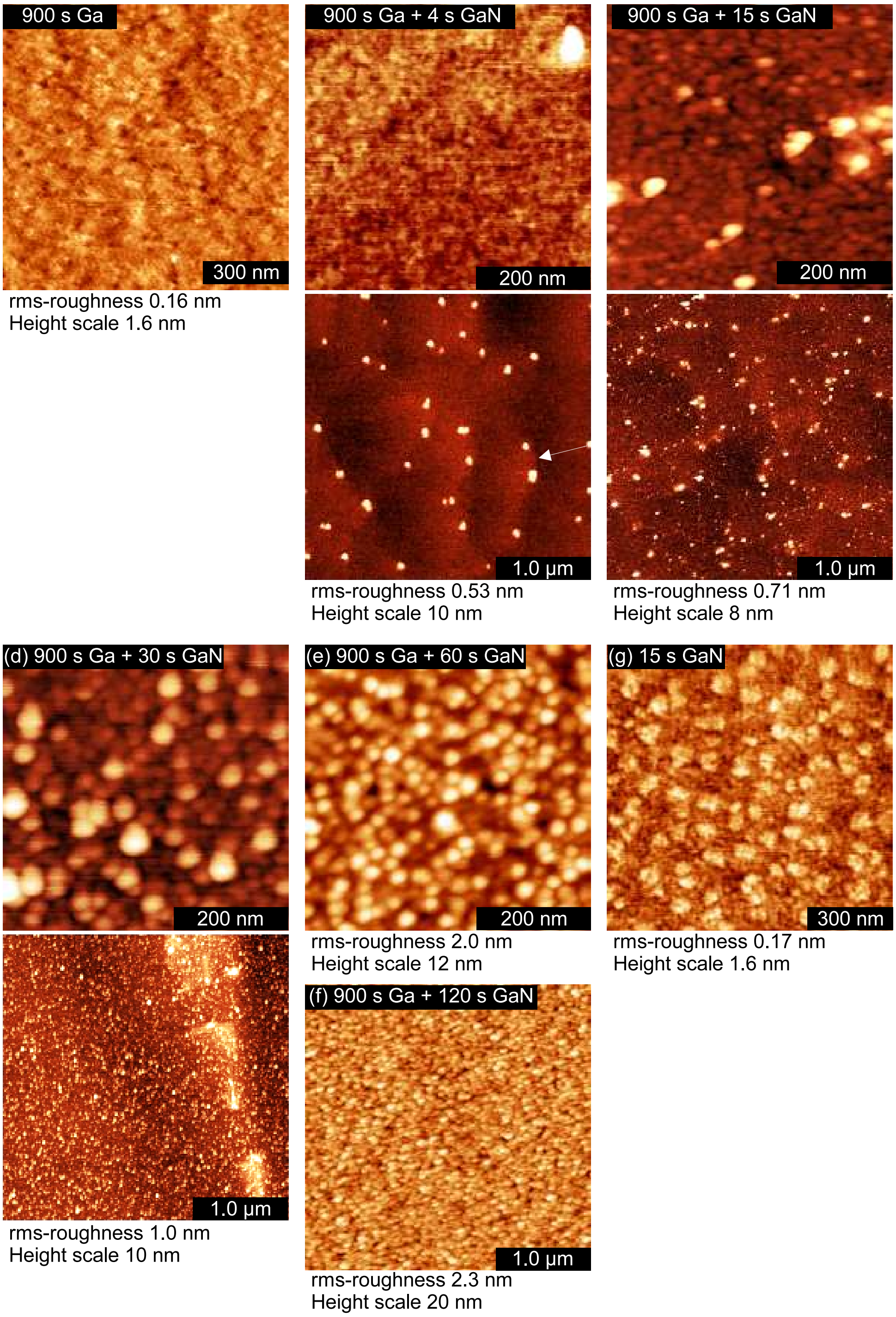

rms-roughness 0.16 nm
Height scale 1.6 nm

rms-roughness 0.53 nm
Height scale 10 nm

rms-roughness 0.71 nm
Height scale 8 nm

rms-roughness 2.0 nm
Height scale 12 nm

rms-roughness 0.17 nm
Height scale 1.6 nm

rms-roughness 1.0 nm
Height scale 10 nm

rms-roughness 2.3 nm
Height scale 20 nm

Figure 3.22: AFM images showing the evolution of the forming NWs in dependence of the nucleation time. For (a)–(f) the Si(001) surface was exposed to the Ga flux for 900 s before opening the N shutter for GaN growth (Samples *S0p0*–*S0p5*, respectively). For (g) GaN growth was directly initiated (Samples *S0p6*). In (b) the arrow point out a mound-like feature.

additional islands have nucleated between the formerly isolated ones and the surface is now completely covered by them. After 30 s of growth [sample *S0p3*, Figure 3.22(d)] the smaller islands' diameter increases, but their size is still inhomogeneous and the larger islands size is still about 50 nm. The mounds are not observable any more. After 60 s of growth [sample *S0p4*, Figure 3.22(e)] the rms-roughness has strongly increased and the surface is completely covered by islands of homogeneous diameter (50–60 nm). For further growth [sample *S0p5*, Figure 3.22(f)] the diameter size is similar but the height is strongly increased.

In comparison to these samples, the topography of sample *S0p6* grown without Ga pre-exposure seen in Figure 3.22(g) is different from the other samples since the surface is partially covered by large patches (about 50 nm wide). However, it presents some common features with sample *S0p0* since pits are also observed and the rms and the height scale are comparable. The morphology of sample *S0p2* grown for the same duration is very different from the one of *S0p6* and this can be explained by the QMS profiles in Figure 3.17(a). The desorption profile of samples with Ga pre-exposure was found to precede by 30 s the one of samples grown without Ga pre-exposure and this was observed for both substrate orientations Si(001) and Si(111). This suggests that sample *S0p6* grown for 15 s corresponds to an earlier stage in the nucleation than sample *S0p1* grown for 4 s with Ga pre-exposure. According to the QMS results, the Ga pre-exposure results in a nucleation 30 s shorter, thus the growth time of sample *S0p1* would be actually 4 s + 30 s long.

In brief, the AFM investigation shows that the nucleation begins with mound and isolated island formation and continues with the one of many new small islands between the previous ones. These new islands grow rapidly in size, faster than the ones that have nucleated first and at the end of the nucleation the surface is completely covered by islands of homogeneous size that grow vertically.

TEM investigation on samples *S0p1*, *S0p2*, and *S0p6* gives structural information on the features observed by AFM. The cross sections of samples *S0p1* and *S0p6* (Figure 3.24 and Figure 3.23, respectively) corresponding to stage 1 in Figure 3.17(a) are alike. First, several mounds with different facets than (001) cover the surface and their 2D Fourier transforms (2D FFT) [Figure 3.23(b),(c)] indicate that these mounds are made of Si. Second, numerous pores or pits observed by AFM were also detected by TEM as seen in Figure 3.24(c). Also, another interference pattern is detected inside these pits as pointed out by the arrow in Figure 3.24(d). This could be induced by a stronger contrast of the facet planes of the pits. However, in this case, a symmetrical effect on both side of the pit would be expected, which is not observed. This structure could also correspond to another material than Si forming inside the pits. Third, a crystalline but highly defective layer, about 2 ML thin, covers partially the surface between the mounds and pits [Figure 3.24(c), 3.23(g)–(i)].

This layer seems to be covered by an amorphous thin cap and has a different structure than Si. Its in-plane lattice distance calculated from the 2D FFT is 3.8 ± 0.3 Å. Assuming a hexagonal structure, the observed reflections could be generated by the $(\bar{2}110)$ lattice planes and in this case, a lattice parameter of a = 7.6 Å is deduced. This value matches quite well the lattice parameter of α-Si_3N_4 (a = 7.576 Å) or β-Si_3N_4 (a =

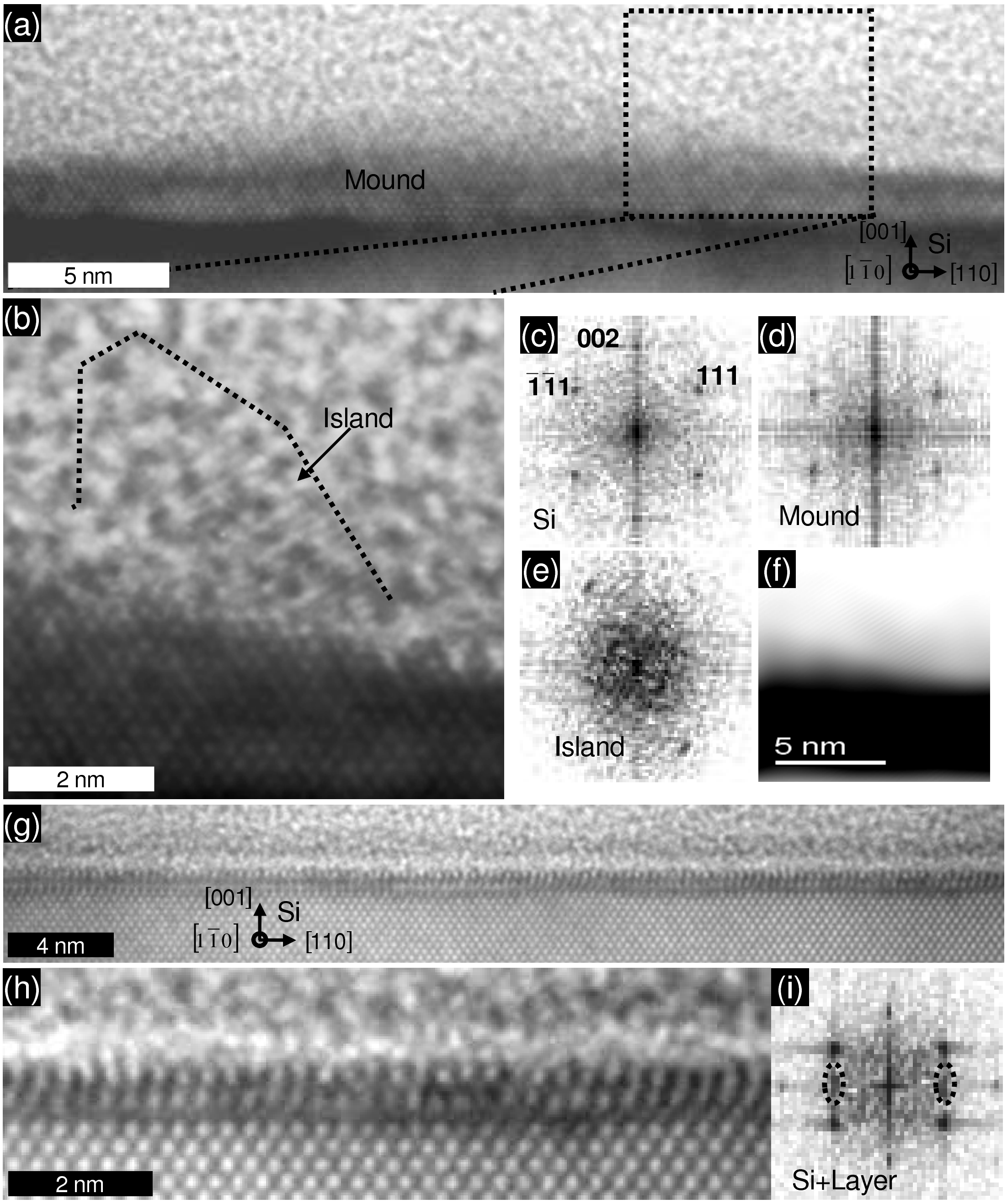

Figure 3.23: (a), (b), (g), and (h) Cross section TEM images along the $[1\bar{1}0]_{Si}$ zone axis of a sample grown on Si(001) for 15 s without Ga pre-exposure (sample *S0p6*). (a) illustrates a Si mound and (b) is an enlarged view where an island was detected. (c), (d), and (e) are the corresponding calculated 2D FFT. (f) is the inverse FFT of (b). (g) and (h) illustrate the crystalline layer formed and (i) is the 2D FFT of this area.

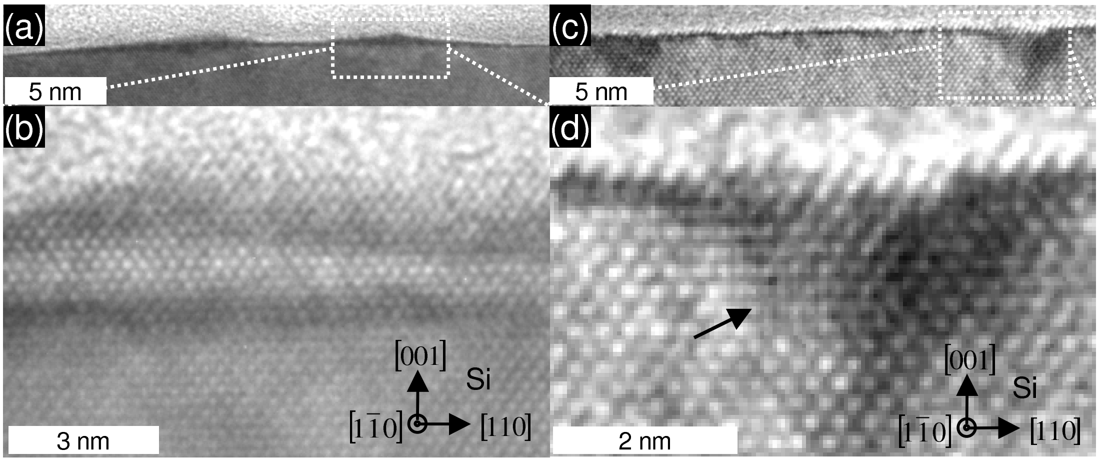

Figure 3.24: (a),(b),(c),(d) Cross section TEM images along the $[1\bar{1}0]_{Si}$ zone axis of a sample grown on Si(001) for 4 s after 900 s exposure to the Ga flux (*S0p1*). (a) illustrates a Si mound and (b) is a zoom of (a) showing that the mound have the same structure as the underlying Si(001). (c) evidences the presence of pits formed in the Si(001) substrate and (d) is an enlarged view of (c). The arrow points out the presence of another interference pattern detected in one of these pits.

7.722 Å), that both have the hexagonal crystal structure. The (200) lattice planes of cubic γ-Si_3N_4 (a = 7.695 Å) [176] could also be involved. However, our growth conditions differ fundamentally from the high pressure and temperature reported to be essential for the synthesis of the γ-Si_3N_4 phase [177]. The epitaxial relation of these silicon nitride partially ordered domains would be:
$[\bar{2}110]_{\alpha-,\beta-Si_3N_4} \parallel [110]_{Si}$
or
$[200]_{\gamma-Si_3N_4} \parallel [1\bar{1}0]_{Si}$
No interplanar distance of GaN, ZB or WZ was found to match the value of the in-plane lattice distance. In addition, this result would be in agreement with the formation of a Si_xN_y interfacial layer between GaN and Si. Several Auger electron spectroscopy (AES) studies performed on GaN samples grown on Si reported a stoichiometry similar to the one of Si_3N_4 at 700°C and of SiN at 950°C [178, 179]. Similarly, X-ray mapping and EELS analysis performed on one of our NW samples grown on Si(111) revealed the Si- and N-composition of the interfacial layer [180] in agreement with several studies on GaN NWs growth [26, 134, 137, 181]. However, a precise compositional analysis would be required to draw a definitive conclusion on this particular sample. Indeed, this Si_xN_y interfacial layer could also be sub-stoichiometric to Si_3N_4 as observed in reference [182] or intermixed with Ga as suggested in ref. [26]. This would contrast with the results of Furtmayr *et al* [137] who reported no traces of Ga in the Si_xN_y layer, but in this case the intentional nitridation process of the Si(111) substrate that they carried out before GaN growth could suppress the intermixing. For sample *S0p6* grown for 15 s the amount of incorporated Ga as determined by RBS was less than 1 ML (2.1 Å) and for sample *S0p1* it exceeds 2 ML (6.8 Å). Hence, it is intriguing not to observe any GaN wetting layer

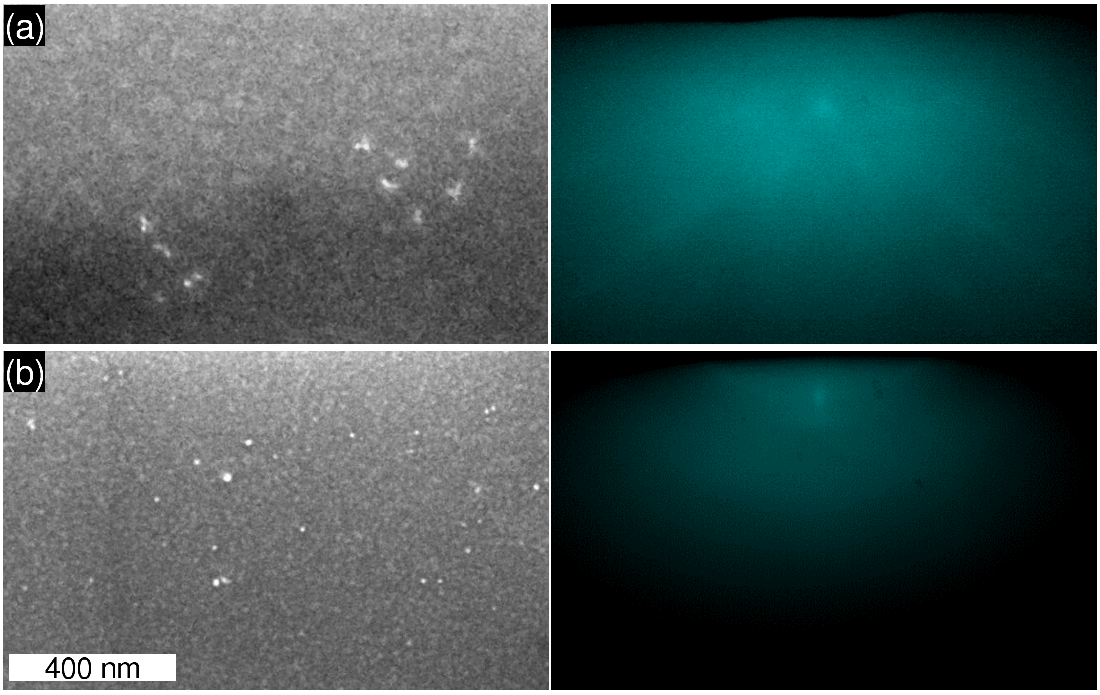

Figure 3.25: Left, plan view SEM image and right corresponding RHEED pattern of (a) sample *S0p6* grown for 15 s without Ga pre-exposure and (b) sample *S0p1* grown for 4 s with 900 s Ga pre-exposure. For sample *S0p1* the island density is larger although the growth duration is shorter while for sample *S0p1* very few islands are found. Note that the extended shape of the islands on sample *S0p1* could result from a bad focus of the SEM so that the islands' size of both samples are not directly comparable. In both cases the broken rings characteristics for GaN islands seen in transmission are not observed by RHEED carried out after growth.

for these samples. Note that the thin highly defective layer could still be composed of largely misoriented Si since the lattice distance of $(110)_{Si}$ is 3.84 Å, or also β-Ga_3O_2 whose interplanar distance of $(201)_{\beta-Ga_3O_2}$ amounts to 3.67 Å. Taking all of the above into account, most likely this layer consists of Si_xN_y.

Fourth, AFM evidenced a low density of isolated islands grown on the mounds for sample *S0p1* not observed by TEM for this sample, most probably because of the low density, but for sample *S0p6* [Figure 3.23(b)]. In addition, SEM images of this sample [Figure 3.25(a)] effectively revealed the presence of islands with an even much lower density than the one on sample *S0p1*[Figure 3.25(b)]. Note that the surface separating the islands is different in both cases. For sample *S0p6*, the surface seems also to be incompletely covered by patches, similarly to the corresponding AFM image in Figure 3.22(g), while for sample *S0p1* the surface looks very rough but more homogeneous. The RHEED pattern corresponding to sample *S0p6* does not indicates the presence of the islands, whereas for sample *S0p1* very faint reflections could correspond to rings superposed to a single spot. Figure 3.23(b) presents such an island 3–4 nm wide whose axis is tilted with respect to the Si mound. The lattice distance measured from the 2D FFT [Figure 3.23(e)] is 2.5 ± 0.3 Å which can correspond to the $(0002)_{GaN}$ (2.593

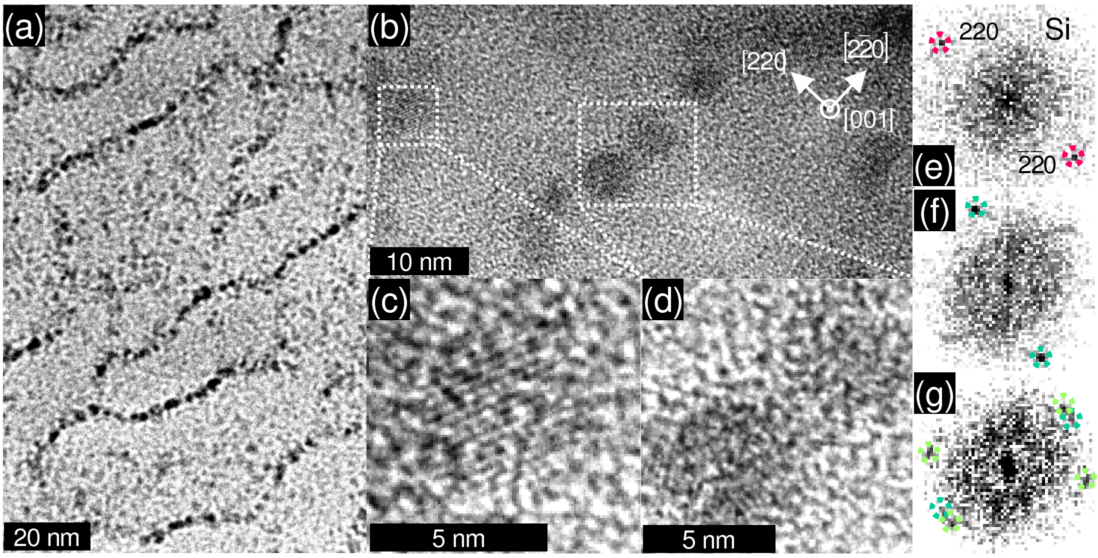

Figure 3.26: (a)–(d) Plan-view TEM images along the $[001]_{Si}$ zone axis of a sample grown on Si(001) for 4 s after 900 s exposure to the Ga flux (*S0p1*). (a) illustrates the preferential nucleation of islands along terraces with edges parallel to the $<110>_{Si}$ direction. (b)–(d) are enlarged views of (a) revealing the presence of individual islands. (e)–(g) are the corresponding calculated 2D FFT for Si, and islands (c) and (d), respectively.

Å), $(1\bar{1}01)_{GaN}$ (2.437 Å), $(111)_{GaN}$ (2.61 Å) or $(002)_{GaN}$ (2.26 Å) lattice distance. Unfortunately, no exact epitaxial relation or phase can be deduced since the in-plane information is missing. Note that the observation of the ZB phase would be consistent with earlier studies on GaN grown by MBE on Si(001) and Si(111) [174, 183, 184] and even on *C*-plane sapphire by HVPE [185] reporting polytypic phases of GaN. In addition, similarly to the pits observed in samples *S0p1* and *S0p6*, ref. [174] reported the presence of many crystallographic pits with (111) sidewall planes at the Si(001)/GaN interface and STEM analysis showed them to contain GaN. The facets of the pits we observed here are not well defined but could be of the same nature. Last, ref. [186] also reported the presence of these pits after nitridation of Si(001) substrate with the Si substrate exposed at the bottom. Their depth and diameter could reach up to 7.5 nm and 50 nm, respectively.

Since the island density was too low to be observed on cross-sectional samples by TEM, plan-view samples were also prepared. For both samples *S0p1* (Figure 3.26) and *S0p6* (Figure 3.27), incomplete coverage of the surface was revealed and numerous islands with a diameter of 3–5 nm were found. For sample *S0p1*, these islands preferentially nucleate at what is thought to be the edges of $[110]_{Si}$ oriented terraces 20–80 nm wide. Figure 3.27(a) recalls Figure 3.22 with the observation of island nucleation at the edges of mounds. However, here the terraces are narrower than the spaces between the first nucleated islands observed by AFM. For sample *S0p6* no such preferential nucleation site was observed. The islands have different epitaxial orientation relatively to the underlying Si(001) substrate that is still very faintly observable in Figure 3.27(a). There-

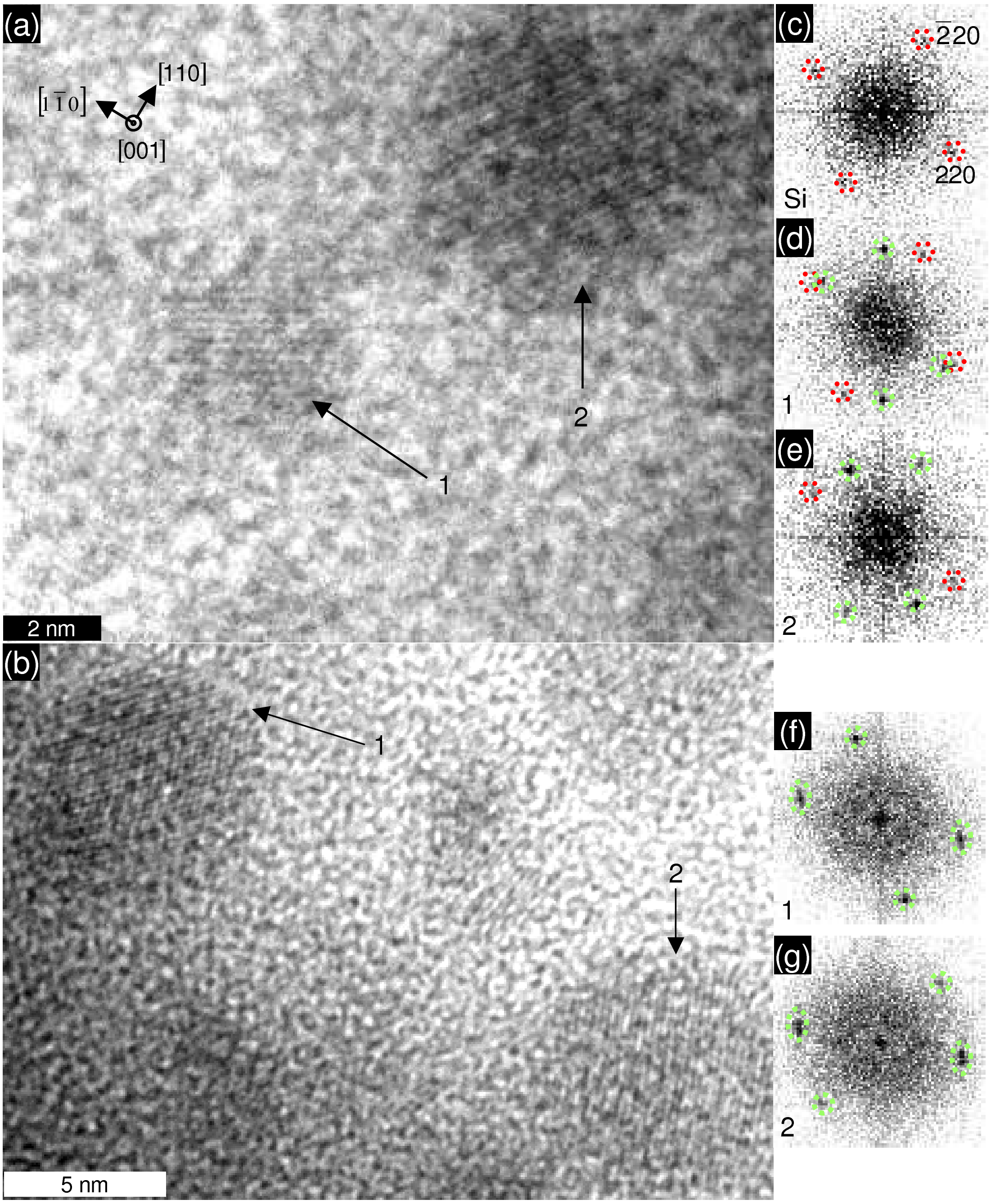

Figure 3.27: (a) and (b) Plan-view TEM images along the $[001]_{Si}$ zone axis of a sample grown on Si(001) for 15 s (sample *S0p6*). (c)–(e) and (f)–(g) are the corresponding calculated 2D FFT of Si and the islands area in (a) and (b), respectively.

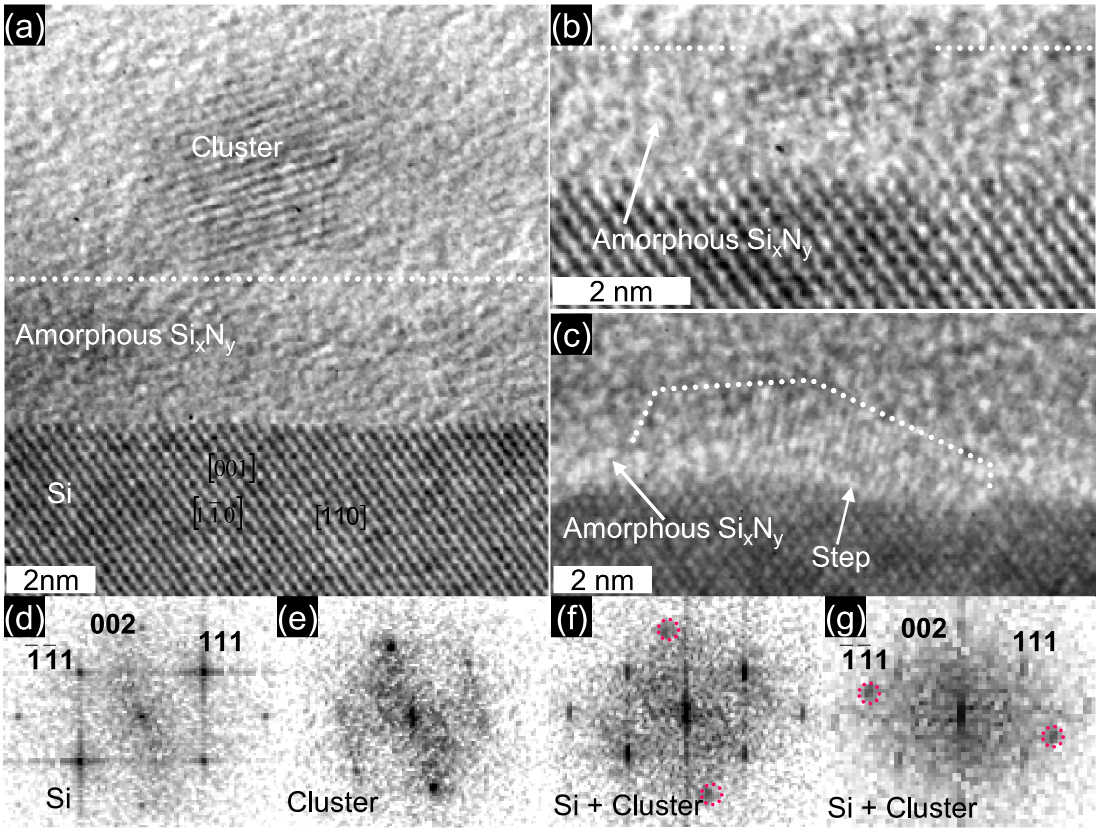

Figure 3.28: (a)–(c) Cross section TEM images along the $[1\bar{1}0]_{Si}$ zone axis of a sample grown on Si(001) for 15 s after 900 s exposure to the Ga flux (*S0p2*). (a) and (b) illustrate GaN clusters formed on top of the amorphous Si_3N_4 layer. (c) Island in contact to the underlying Si substrate at a step. (d)–(g) are the corresponding calculated 2D Fourier transforms of the clusters in (a), (b), and (c), respectively.

fore, $(022)_{Si}$ reflections are obtained in the 2D FFT [Figure 3.27(c)–(e)] and enabled to measure the interplanar lattice distance for the islands. It amounts to 2.0 ± 0.3 Å, which could correspond to the $(0\bar{1}12)_{GaN}$ (1.89 Å), or the $(002)_{GaN}$ (2.26 Å) lattice distance but also to the $(\bar{2}112)_{\beta-Si_3N_4}$ (2.27 Å). A closer look to the 2D FFT patterns indicates that some reflections generated by the islands are almost aligned with the $(022)_{Si}$ direction. Many of these islands are highly faulted and twinned polycrystals seem to form through coalescence [Figure 3.26(b)]. Considering that QMS and RBS measurements indicated the presence of Ga on these samples, it is most likely that these islands consist of WZ or ZB GaN. However, since ZB GaN has not been reported for GaN NWs grown by MBE, it is suggested that if this metastable phase forms, it dissolves away during further growth.

Sample *S0p2* corresponding to stage 2 in Figure 3.17(a) grown for 15 s with Ga pre-exposure was also investigated by TEM (Figure 3.28). The cross-section of this sample revealed a completely different structure than the one of samples *S0p1* and *S0p6*. No crystalline layer, nor mound are observed but a 3–4 nm thin amorphous layer covers the surface of the Si substrate with clusters either lying at its surface [Figures 3.28(a)–(b)] or encrusted into it [Figure 3.28(c)]. These clusters have different orientations relative to the Si substrate. Some of them are still in contact with the substrate like in Figure 3.28(c) which shows a cluster formed at a step of the Si. The interplanar distance measured from the 2D FFT in Figure 3.28(e) is 3.2 $\pm$ 0.3 Å which could correspond to $(011)_{GaN}$ (3.20 Å), $(111)_{Si}$ (3.14 Å), $(2\bar{1}\bar{1}0)_{\alpha-Si_3N_4}$ (3.37 Å), $(\bar{2}200)_{\alpha-Si_3N_4}$ (2.92 Å), $(\bar{2}020)_{\beta-Si_3N_4}$ (3.30 Å) or $(0001)_{\beta-Si_3N_4}$ (2.92 Å), but do not correspond to any WZ-GaN interplanar distance. The interplanar distance measured from the 2D FFT in Figures 3.28(f) and (g) is 2.7 $\pm$ 0.2 Å and 2.5 $\pm$ 0.2 Å, respectively, corresponding to several GaN interplanar lattice distances mentioned above. Hence, these clusters are most probably GaN and there are indications that ZB GaN also forms. Note however that the clusters observed here are about 5 nm wide, which is slightly smaller than the critical diameter for NW nucleation [26]. Therefore we suggest that clusters formed in the ZB structure may dissolve away during further growth. From these observations, we conclude that the beginning of the second stage of the nucleation corresponding to the second decrease of the Ga desorption is accompanied by the amorphization of the silicon nitride interfacial layer between the underlying Si(001) substrate and the formation of GaN islands.

Concerning the nitridation of Si(001), so far no crystalline $\alpha-$ or $\beta-Si_3N_4$ or other types of crystalline Si nitrides has been reported. This has been attributed to a lack of proper match in surface lattice constant and in symmetry [187]. However, first principles calculations predict the formation of uniform Si nitride structure on Si(001) up to a certain thickness (3–4 layers) limited by the increasing accumulation of local strain that prevents further nitridation [188]. Thus this result supports the instability of the crystalline Si_xN_y layer observed during the first stage. For multilayer deposition of TiN/Si_3N_4, the crystalline to amorphous transition has been experimentally observed when the thickness of Si_3N_4 increased above a critical value [189]. In addition, metastable phase diagram and thermodynamic calculations on solid solutions of metallic alloys or ternary nitrides such as TiSiN predicted that a change of the composition could result in the crystalline to amorphous transition [190, 191]. Lastly, for nano- and polycrystalline Si_3N_4 underlying anisotropic strength exceeding a critical value [192] amorphization was shown to be energetically favorable. Amorphization has also been predicted by molecular dynamics simulations for α-Si_3N_4 crystal underlying high local stress [193]. Several experiments showed that the nitridation processes are complex [194] and the resulting Si nitride depends on many parameters like the orientation of the Si substrate [194, 195], the nitridation rate and the temperature [188]. For nitridation by plasma source the processes seem to also strongly depend on temperature [179]. Scanning tunneling microscopy (STM) evidenced that radical nitridation occurs already at 350°C [196] and preferentially at the steps of Si(001) (2 × 1) surface and up to 600°C a layer-by-layer growth mode was evidenced [197]. At temperatures higher than 600°C, nitridation occurs by island growth mode preferentially along the [110] direction [198] and is suggested to be limited by the surface migration of Si adatoms independently of the type of reactive species [188]. Moreover, the island size increases with exposure time until a continuous and very flat film is formed [198]. Last, the nitridation processes are always accompanied by detachment and surface migration of Si atoms [197, 198] which is also thought to induce the pinholes [194].

These results can provide further understanding for our observations. They suggest that the patches observed by AFM for sample *S0p6* correspond to an incomplete nitridation while for sample *S0p0* nitridation probably already occurs at a different nitridation rate and is more regular. Indeed, whereas for sample *S0p0* the N shutter remained closed during the 900 s of Ga exposure, the Si step morphology was drastically changed and we have evidences from the catalyst-assisted experiment that active nitrogen can escape under such conditions and react with Si. In addition, the porous morphology observed by both TEM and AFM are explained by the Si detachment and migration out of the pores [194] which can lead to the formation of the mounds.

In conclusion of the TEM investigation, Si mounds and pits are detected during the first stage of the nucleation as well as islands that are most likely GaN. Most importantly, at this stage the surface is not amorphous and a layer that is attributed to Si_xN_y is detected between mounds and pits. For the second stage, TEM reveals the presence of an amorphous layer, also attributed to Si_xN_y, embedding numerous GaN islands. In addition, GaN islands nucleate on top of the amorphous Si_xN_y layer. The second stage establishes the final configuration for the NW growth that is always observed for longer growth duration.

3.3.4 Influence of the temperature and *V/III* ratio on the nucleation processes

In this section we investigate the influence of the temperature and the Ga- and N-rates on the nucleation stages indicated in the QMS profile in Figure 3.18. We associate to each nucleation stage a duration and a net amount of incorporated Ga (*t1*, *A1*, *t2*, *A2*, respectively), as previously done in section 3.2.4 for the nucleation of catalyst-assisted NWs. A detailed RHEED study for these samples was not done but could provide with more certainty the starting point of the GaN island nucleation during the second stage.

Influence of the temperature on the nucleation processes

Figures 3.29(a) and (b) show the evolution of *t1* and *t2* as well as *A1* and *A2* for NW samples grown on Si(001) and Si(111) at 730°C, 755°C, and 780°C with the nominal Ga-rate of 0.4 Å/s and N-rate of 2.0 Å/s (samples *S0a*, *S0b*, *S0c*, *S1a*, *S1b*, *S1c*). These graphs indicate again similar results for Si(001) and Si(111) substrates. The duration of both the first and the second stage increases with an increase of the growth temperature. The increase of *t2* is close to linear for the range of temperatures investigated in contrast to the increase of *t1* that is larger above 755°C. The comparison of the amount of Ga incorporated during the first stage *A1* and the second stage *A2* with their respective accumulation time indicates no obvious linear behavior. Surprisingly, *A1* is relatively stable. For the nucleation at 730°C, it amounts to about 8 ± 3 Å for Si(001) and 7 ± 3 Å for sample Si(111), which corresponds to 2.7 ML and 3 ML in GaN equivalent thickness, respectively and at 780°C the value of 7 Å is obtained for both substrates with a large uncertainty (up to 21 Å) due to the larger nucleation time. At 755°C a somehow reduced value is obtained but still within the measurement uncertainty. In this case *A1* amounts to 5 ± 3 Å and 2 ± 4 Å for nucleation on Si(001) and Si(111), respectively. In contrast, *A2* strongly increases with the temperature but not linearly as in the case of *t2*. Hence, there must be a difference in the Ga incorporation mechanism corresponding the each stage.

The increase in the time duration of both stages can be attributed to an effect of higher Ga and N desorption and decomposition rates for temperatures higher than 750°C as exposed in section 3.2.4. The increasing N desorption with the temperature has also been evidenced by a comparison of the composition of nitrided Si(111) surface at 700°C and 950°C determined by AES. This study revealed the poorer N-content of the highest temperature nucleated Si_xN_y polymorph [178]. Last, the total duration of the nucleation increases with the increase of the growth temperature in agreement with the results of Calarco *et al* [24] who reported a nucleation time as long as 60 min for NWs grown on Si(111) at 785°C. For sample *S1c* grown at 780°C the duration of the nucleation is about 3100 ± 250 s which is the same order of magnitude. The duration difference could stem from the temperature calibration but also from a different *V/III* ratio as discussed next.

Influence of the *V/III* ratio on the nucleation processes

Figures 3.29(c) and (d) illustrate the evolution of *t1* and *t2* as well as *A1* and *A2* in dependence on the N-rate. These data originate from the growth of samples *S0a*, *S0d* and *S0e* on Si(001) as well as *S1a*, *S1d* and *S1e* on Si(111) at 730°C with a N-rate of 2.0 Å/s, 1.1 Å/s and 0.5 Å/s, respectively and with a Ga-rate of 0.4 Å/s. Again similar Ga incorporation behavior on Si(001) and Si(111) substrates are observed. *t1* and *t2* decrease with the increase of the N-rate. This decrease is strong close to stoichiometry, but much less marked for higher N-rate. The amount of incorporated Ga during the first stage *A1* remains stable, around 7 Å except for the smallest N-rate where it amounts to up to 14 ± 10 Å which is however still of the same order of magnitude considering the uncertainty range. This time, the increase of *A2* follows closely the increase of *t2*. This indicates that the increase of N shortens the duration of the second nucleation stage without alteration of the Ga-incorporation rate. In other words, N has no influence on the Ga-incorporation rate during the second stage for the range of N rates investigated.

Last, the dependence on the Ga-rate of *t1* and *t2* as well as *A1* and *A2* was also investigated [Figures 3.29(e) and (f)]. To this end, samples *S0a*, *S0f* and *S0g* on Si(001) as well as *S1a*, *S1f* and *S1g* on Si(111) were grown at 730°C with a Ga-rate of 0.2 Å/s, 0.4 Å/s and 0.8 Å/s, respectively, and with a N-rate of 2.0 Å/s. Both substrate orientations provide comparable results. *t1* decreases linearly with the increase of the Ga-rate while *A1* remains unchanged (still about 7 Å). In contrast to what has been observed previously for the N-rate, here *t2* decreases while *A2* increases with the increase of the Ga-rate. This shows that the Ga-rate is the limiting factor during the second nucleation stage as expected under N-rich conditions. In this case, an increase of the Ga-rate not only shortens the nucleation processes of the second stage but also enhances them.

Interesting enough is that the amount of Ga accumulated during the first stage *A1* is nearly unchanged for the growth on both Si(001) and Si(111) whatever the temperature or *V/III* ratio. It seems that the only parameter that has at least some influence on the Ga amount accumulated during the first stage is the *N-rate* although the observed variation was still within the uncertainty. This could indicate that the first stage is rather limited by the *N-rate* than by the *Ga-rate* in contrast to the second stage where the *Ga-rate* is the most probable limiting factor.

3.3.5 Discussion

Figure 3.30 sketches the two nucleation stages we could identify. During the first nucleation stage, the QMS signal already indicates Ga incorporation whereas the RHEED pattern corresponding to the Si(1×1) reconstruction becomes more and more blurry. Hence, no evidence for any growing crystalline material is found. On Si(001), AFM indicates a severe roughening of the surface while TEM revealed the presence of a polycrystalline layer, most probably Si_xN_y or Si_xN_y intermixed with Ga, as well as the presence of Si mounds and clusters growing on them. These clusters are most likely GaN. The second stage starts with the appearance of a pattern of broken rings corresponding to the transmission through GaN crystals misoriented relatively to the normal of the surface. At this stage the QMS profile indicates a second decrease to the steady state of the Ga desorption in agreement with the formation of numerous additional clusters observed by AFM. TEM evidences the amorphization of the surface and also the appearance of the clusters. These clusters are of several types: some of them are still in contact with the Si substrate while others lie on the amorphous layer. The study of the influence of the temperature, N- and Ga-rate on the Ga desorption profile reveals that the amount of Ga incorporated during the first stage is relatively stable while during the second stage the Ga-rate seems to be the limiting factor as expected for N-rich conditions.

During the first nucleation stage, the QMS desorption profiles show that nearly the same amount of Ga adsorbs on Si(001) and Si(111) substrates. Thus, the question arises what happens to this Ga. AFM images clearly reveal the formation of islands on Si(001) along with the presence of many pinholes extending through the forming Si-nitride layer in the Si(001) substrate. These pinholes might act as a capillary tube for Ga atom condensation similarly to the model introduced by Seo *et al.* for the growth of GaN NWs in GaN V-pits on GaN buffer deposited on Si(111) [130, 131]. Such a pit morphology surrounding GaN NWs nucleating on AlN buffers was also reported [141] and for AlN nanotips embedded in pit-like AlN defective matrix [199]. Pits also formed during the epitaxial growth of self catalysed GaAs NWs on SiO_x layers [67] and in the latter case, Ga droplets present at the GaAs NW tips unambiguously attest that the VLS mechanism is ruling the growth.

However, as mentioned before the QMS experiments show no Ga desorption following the growth interruption during the first nucleation stage. At this point, note that the Si expelled form the pits might similarly to the Si-assisted growth model proposed by Park *et al* [126] constitute highly reactive nanometer sized clusters for Ga attachment. Also Si and Ga form a eutectic already at 29.77°C [200] but the atomic percentage of Ga

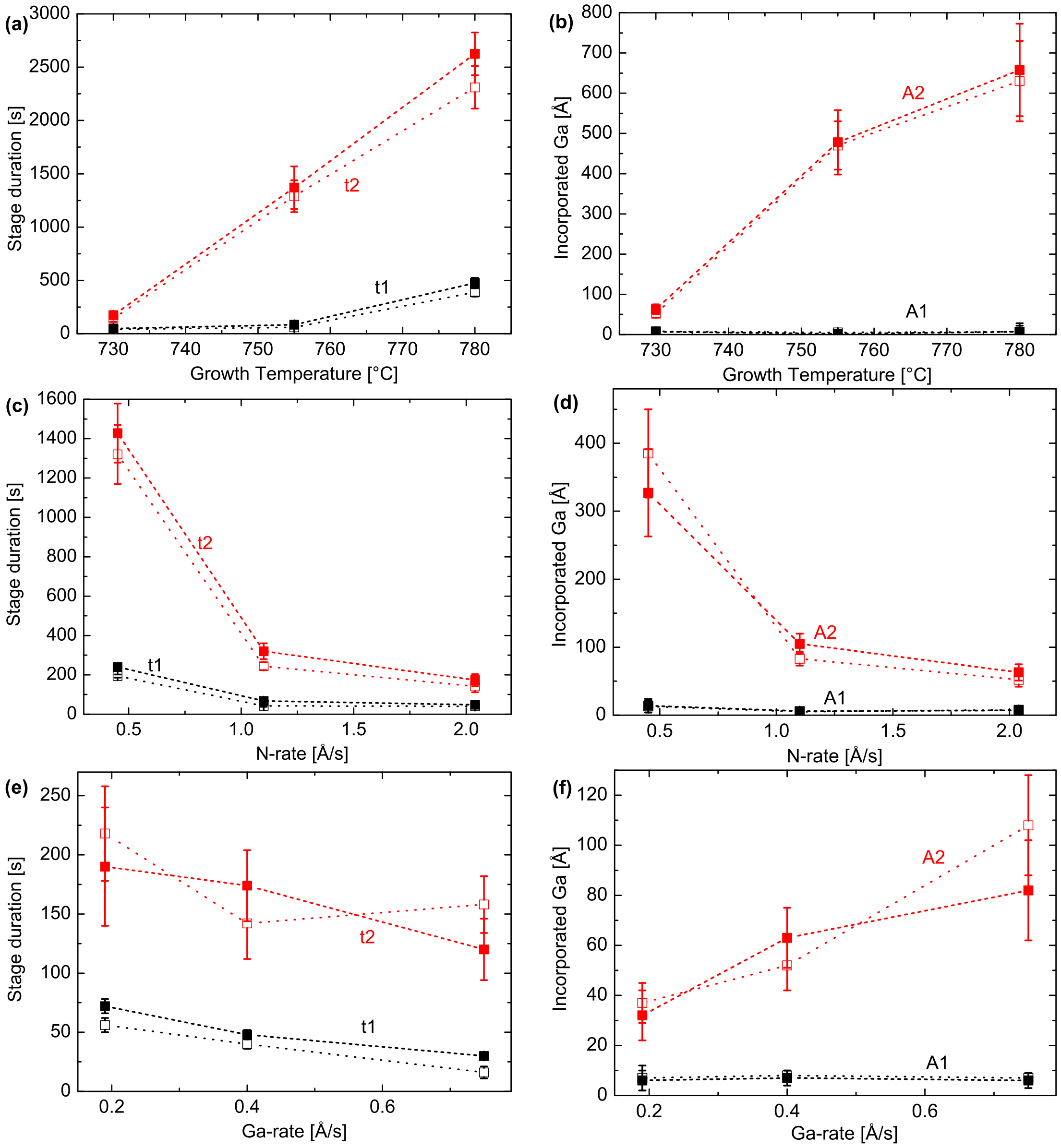

Figure 3.29: Duration of the nucleation stages and corresponding amount of incorporated Ga as a function of (a), (b) the growth temperature (Samples *S0a*, *S0b*, *S0c*, *S1a*, *S1b*, *S1c*), (c), (d) the N-rate (Samples *S0a*, *S0d*, *S0e*, *S1a*, *S1d*, *S1e*) and (e), (f) the Ga-rate (Samples *S0a*, *S0f*, *S0g*, *S1a*, *S1f*, *S1g*). The open squares correspond to Si(001), the solid ones to Si(111). The straight lines are guides to the eye.

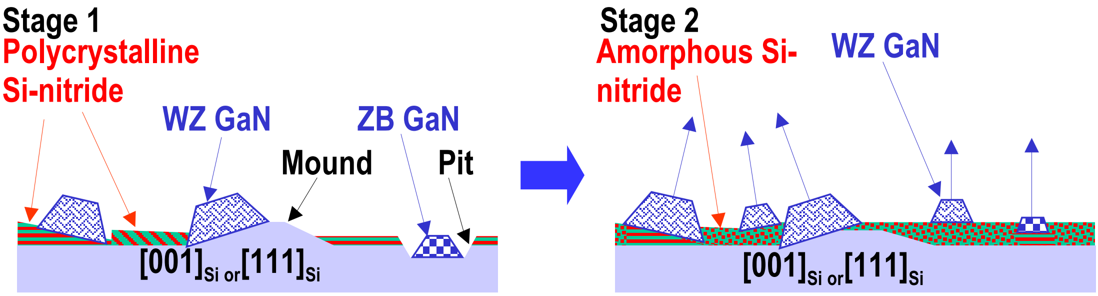

Figure 3.30: Model for the nucleation of GaN NWs on Si. During stage 1, Si-nitride is polycrystalline and GaN clusters nucleate epitaxially with the underlying material, Si or Si-nitride. Phase 2 starts with the amorphization of the Si-nitride and subsequent nucleation of new clusters free of the substrate epitaxial constraint on this different surface

at the eutectic temperature is larger than 99 % which is highly unprobable. In addition, Ga droplets were never observed at the tips of GaN NWs and VLS has been refuted. TEM observation reveals the presence of a different interference contrast within these pinholes. This most probably indicates the formation of another structure than Si which could also be GaN. There are two possible reasons for the preferential nucleation of GaN in the pits. First Ga condensates there as discussed above, and the excess of N leads to GaN formation. Thermodynamic calculations [201] have indeed shown that the nucleation of a critical nucleus in a such pit would occur faster than on the flat substrate and that the following growth would also be accelerated due to a more efficient capture of adatoms. Second, the pinhole side-facets might act as preferential site for GaN island nucleation related to a difference in surface energy of the Si facets. Selective nucleation of GaN deposited by MOVPE has already been evidenced on Si(111) facets fabricated on Si(001) [202].

The previous QMS and RHEED studies reveal very few differences during the nucleation either on Si(111) or on Si(001). This suggests that the nucleation mechanisms should not be fundamentally different. The formation of the pits observed on Si(001) during the first stage is indeed characteristic for the nitridation processes on both-Si(001) and Si(111) for the range of temperatures investigated. Several STM studies on the nitridation of Si(111) also revealed the presence of etch pits which can be as deep as 1.5 nm [187]. The position of these pits is either within the flat Si terraces or at the step edges and their size and shape are strongly dependent on the temperature [187, 203]. These pits are formed by surface etching related to N exposure and local removal of the top Si layer. Several suggestions have been made concerning the mechanism behind their formation, being either a channel for pumping bulk Si atoms from the substrate to the surface for outer formation of Si_xN_y [204] or a way to relieve strain [205]. Si_xN_y has been observed to nucleate at the vicinity of these pits leaving the Si(111) 7×7 reconstruction visible at their bottom [203]. The size of the pits increases with the nitridation temperature and partial nitridation of the pit bottom have also been observed at 800°C [203]. Therefore the material observed inside the pit revealed by TEM investigation could also be Si_xN_y. A deeper TEM investigation is required to confirm the nature of this material.

Concerning the structural properties of the Si_xN_y formed during the first stage, TEM observation reveals that the layer formed on the Si(001) surface is highly defective but crystalline. As explained earlier, this is surprising because the nitridation of Si(001) has been reported to gradually destroy the initial order leading to amorphous material [187] Si_xN_y. In contrast, the nitridation of Si(111) can lead to polycrystalline Si_3N_4 [172, 203] owing to a domain matching epitaxy of 1:2 for Si(111) (7×7) and Si_3N_4 evidenced by RHEED measurement [172]. The quality of the Si_3N_4 layer formed depends strongly on the nitridation temperature [178, 203]. Thus, the at-least polycrystallinity of the Si_xN_y on both Si(001) and Si(111) evidences that GaN formed during this stage must be epitaxial whatever the nucleation site, in the observed pinholes, on top of crystalline Si or on polycrystalline Si-nitride. Unfortunately, the TEM analysis does not allow to draw any clear conclusion, the only cluster observed by cross-sectional TEM was located on a Si mound but no GaN wetting layer was found. In any case, these observations account for the often reported preservation of the epitaxial relation of the NWs with the substrate [22, 181, 206]. Therefore, the clusters might be subjected to a strong strain due to the large lattice mismatch between Si, GaN and Si_xN_y. Thus, during the first stage, nitridation of Si occurs and leads to the formation of an unstable polycrystalline Si_xN_y surrounding Si mounds and pits which possibly constitute preferential nucleation site for GaN. Therefore GaN formed during in the first stage should grow epitaxially.

The second stage identified is the amorphization of the Si_xN_y layer on Si(001) accompanied by the subsequent increase of Ga incorporation to the steady state. This amorphization process occurs after GaN epitaxy has already set in as also suggested by Rawdanowicz *et al.* [182] during the growth of domain matching epitaxial GaN on Si(111) by laser-MBE. Amorphization of crystalline Si_xN_y on Si has not been experimentally observed to our knowledge, but simulations have been developed and showed that strain could induce such a transformation [192, 193]. The second increase of Ga incorporation is simultaneous to the nucleation of numerous new clusters revealed by AFM. This result is in agreement with the observation of Calarco *et al* [24] and Furtmayr *et al* [137] of a sudden increase in the NW density at the beginning of the nucleation. TEM shows at this stage different kinds of clusters. Some of them grow epitaxially on the underlying Si substrate or are embedded in the amorphous Si-nitride layer. Those have most probably nucleated during the first stage. Others lie on the top of the Si-nitride layer which could indicate that they have formed during the second nucleation stage. Similarly, Ploog *et al.* [175] concluded on two different parallel paths for GaN growth on Si(001). According to these authors, cubic GaN forms with an epitaxial relationship on the bare Si(001) surface, but complete coverage is inhibited by the simultaneous formation of amorphous Si-nitride. Thus, GaN condensing on top of it does not experience any epitaxial constraint from the substrate and adopts the hexagonal modification with random in-plane orientation. Both nucleation paths have also been confirmed by the compared growth of GaN nanorods on low-temperature GaN templates deposited on clean and on covered by native oxide Si(001) substrates [207]. Growth on both substrate types resulted in nanorods elongated along the [0001] direction without apparent in-plane orientation. However on the clean Si(001) the nanorods were observed inhomogeneously tilted and ZB GaN also formed at the interface GaN/Si$_x$N$_y$. Thus it was concluded that initially GaN growth on Si(001) proceeds under inhomogeneous conditions with N reacting not only with Ga but also with Si. This process lead to mixture regions of polycrystalline Si$_x$N$_y$ and GaN. In agreement with ref. [175, 207], our results also revealed those two nucleation paths, but the amorphization occurs after growth of GaN has started. The growth following the amorphization leads to the columnar structure of hexagonal GaN. Note that a few ZB GaN islands might also have nucleated during the first nucleation stage, but the ZB phase is metastable and so far, no ZB phase have been reported for GaN NWs grown by MBE. Therefore we suggest that those islands might dissolve away.

Few models [22–24, 26, 130, 137] have already been developed for the catalyst-free growth of GaN NWs by MBE as mentioned at the beginning of this chapter. However, none of them describes the formation or the amorphization process of the silicon nitride layer that is always found at the interface between the Si substrate and the NWs. In any case, the processes leading to the formation of these NWs are independent of the formation of this interfacial amorphous layer since other experiments performed on thick GaN or AlN buffer layers [66, 141, 208] produce as efficiently GaN NWs. However, during the nucleation on Si, the amorphization of the Si nitride interface probably strongly conditions the structural and physical characteristics of the NWs. This suggests that the nitridation is beneficial to the NW crystal quality and orientation when an homogeneous layer can be obtained since the clusters nucleating directly on the Si substrate are rather misoriented as observed in section 3.3.3 and are subject to high misfit strain [26, 137].

Finally, several open questions remain. For example, further studies are necessary to explain why nearly the same amount of Ga incorporated before amorphization has been evidenced under different growth conditions of substrate surface, temperature and N-rate, particularly if the topography of the Si-nitride changes with these parameters. The second concern lies in the origin of the transient of Ga-desorption occurring between the two decreases in the QMS profiles. A possible explanation stems from the already formed islands that are subjected to a large lattice mismatch. For strained islands it has been calculated that the strain energy distribution is concentrated at the island edges [209–211] and constitutes a barrier for adatoms attachment. Therefore, during growth the newly deposited atoms diffuse away from the larger islands and desorb or nucleate new islands which would then grow faster than the older ones. To this effect was also attributed an increased Ga desorption observed by Koblmüller *et al* [36] during the nucleation of GaN islands on top of AlN. However, keeping in mind that not only the islands are strained, the strain field below and surrounding these islands in the substrate and the polycrystalline Si-nitride interlayer may inhibit further islands to nucleate in the vicinity of the existing ones causing long range repulsive interaction [212, 213]. Therefore, once the Si$_x$N$_y$ amorphization sets in, the cause for the inhibition of new island growth is suppressed. Thus, it is not surprising to observe the nucleation of new islands at the beginning of the second nucleation stage marked by the second decrease of the Ga-desorption. At this stage these new islands nucleate under completely different epitaxial conditions: there is no epitaxial constraint of the substrate anymore.

In conclusion, the catalyst-free NW nucleation also occurs through several stages and we could identify two of them. During the first stage, competition for nucleation between polycrystalline Si_xN_y and GaN islands occurs. The GaN islands are in the WZ phase although the ZB phase may also appear. The second stage starts with the amorphization of the Si_xN_y and is immediately followed by an intensive nucleation of new GaN islands with the WZ structure which is attributed to the suppression of the epitaxial constraint of the substrate. This process yields two kinds of NWs. NWs that first nucleate grow epitaxially with the underlying substrate and may therefore have the WZ or the ZB structure which dissolves away. NW nucleation during the second stage occurs with a loss of proper epitaxy and the in-plane orientation may be suppressed while the perpendicular orientation to the substrate depends on the homogeneity of the underlying amorphous Si_xN_y layer [26, 137]. This result is also supported by the formation of vertically aligned NWs grown on amorphous SiO_x [26]. Since the nitridation processes strongly depend on temperature and substrate orientation, it is important to note that the model proposed here corresponds to nucleation at 730°C. Particularly on Si(111) substrates, an increase of nitridation temperature should lead to an improvement of the Si_xN_y quality [178, 203] and for instance at 900°C, epitaxial β-Si_3N_4 can be obtained [172] leading to epitaxial NW growth on such a layer [206].

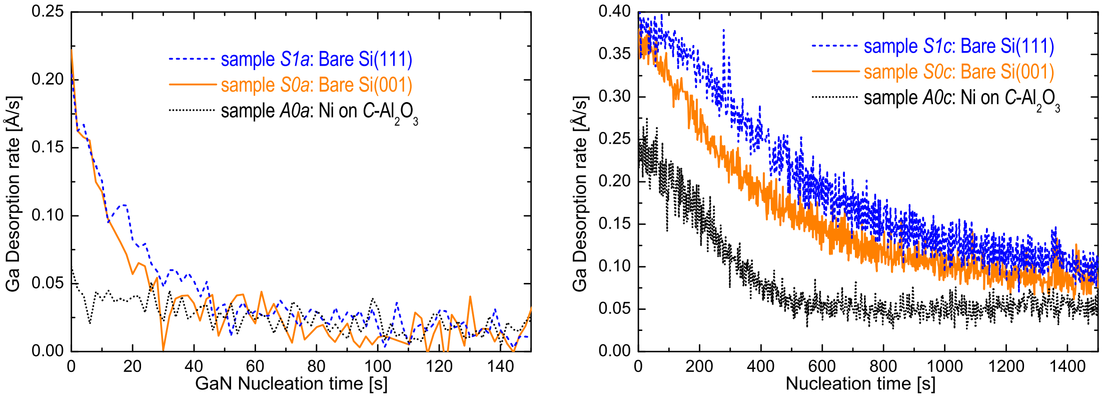

Figure 3.31: Ga desorption rate measured by QMS for the 3rd stage of the nucleation of catalyst-assisted GaN NWs on Al_2O_3 (dot) and the 2nd stage of the nucleation of catalyst-free GaN NWs on Si(001) (solid) and on Si(111) (dash) (a) at 730°C (samples *A0a*, *S0a*, *S1a*) and (b) at 780°C (samples *A0c*, *S0c*, *S1c*). The time scale has been shifted relatively to the opening of the Ga and N shutters in order to adjust to the beginning of the third stage for the catalyst-assisted growth and to the second stage for the catalyst-free growth.

3.4 Comparison of the approaches

As seen in the previous sections completely different mechanisms occur during the NW nucleation in the framework of both approaches. For the catalyst-assisted growth process, nucleation occurs preferentially at Ni islands deposited on sapphire substrates. For this method of growth, we were able to determine three different nucleation stages for the growth at 730°C. First the incorporation of Ga into the Ni occurs. A second stage observed for the growth at 730°C involves the transformation of the seed crystal structure that is directly related to Ga accumulation. Lastly, the third stage starts with the nucleation of GaN under the seed which causes the decrease of the Ga desorption signal to the steady state where all the Ga is incorporated. In this case, the whole NW nucleation process is based on the preferential incorporation of Ga but not N inside the catalyst as evidenced by this in-situ investigation. In comparison, for the catalyst-free approach nucleation is roughly divided in two main stages. In the first one, preferential reaction of N with the substrate occurs leading to roughening of the surface by formation of pits and Si mounds. At this stage a pre-incorporation of Ga occurs and few islands forms. During the second stage, the massive nucleation of WZ GaN islands acting as a sink for NW growth in the catalyst-free approach [26] results from the amorphization of the Si_xN_y layer.

Hence, in both cases an intense nucleation of GaN leading to the NW formation occurs during the last stage and we can compare the corresponding nucleation rates by comparing the QMS desorption profiles at the beginning of the 3rd stage for the catalyst-assisted growth and at the beginning of the 2nd stage for the catalyst-free growth. Figure 3.31(a) presents the Ga desorption profiles of samples *A0a*, *S0a* and *S1a* during the nucleation of GaN at 730°C. The nucleation duration of GaN is comparable for both approaches. However, the amount of Ga desorbed during GaN nucleation is strongly reduced for the catalyst-assisted approach in comparison to the catalyst-free approach leading to an incorporated amount of Ga two times larger.

In addition, for both approaches as seen in sections 3.2.4 and 3.3.4, the rise of the substrate temperature increases the nucleation duration of these stages. At 780°C [Figure 3.31(b)] again, much less Ga desorbs during the GaN nucleation stage of the catalyst-assisted approach than during the one of the catalyst-free approach and the GaN nucleation is completed more than 4 times earlier than for the catalyst-free growth. This result indicates that the Ga is still more efficiently captured by the Ni seeds than by the forming GaN clusters. Therefore this result suggests that the catalyst-assisted NWs grow faster than the catalyst-free ones, as will be further investigated in chapter 4.

3.5 Summary

In-situ monitoring by QMS and RHEED of the nucleation of GaN NWs in the framework of the catalyst-assisted and catalyst-free approach enabled the detection of different stages. For the catalyst-assisted approach, three stages were identified as follows. The first stage corresponds to Ga incorporation into the Ni seed. The second stage is the transformation of the crystal structure of the seed directly attributed to Ga incorporation. The third stage is the nucleation of WZ GaN under the Ni seeds. In this case the process limiting the growth is concluded to be GaN nucleation. The observation of a RHEED pattern generated by the Ni-Ga seeds during the whole nucleation strongly indicates that nucleation and further growth occurs by the VSS growth mechanism.

For the catalyst-free approach, two stages were revealed. The first one is the competition for nucleation between polycrystalline Si_xN_y and GaN islands, and in this case a strong reaction of N with the substrate occurs leading to appearance of pits and Si mounds. Few GaN islands that nucleate during this stage are in the WZ phase but unstable ZB islands might also have formed. The second stage starts with the amorphization of the Si_xN_y and is accompanied by an intensive nucleation of new GaN islands with the WZ structure which is attributed to the suppression of the substrate epitaxial constraint. Finally, an increase of the nucleation temperature raises the duration of these stages but for the catalyst-assisted approach GaN nucleation still occurs at least four times faster the for the catalyst-free approach.

4 Growth of GaN nanowires in MBE

In this chapter the focus is brought on the material properties and the growth mechanism of GaN NWs in the framework of the catalyst-assisted and catalyst-free approaches. After nucleation, the situation as GaN growth continues is very different for both these approaches. The different substrate surfaces surrounding the GaN nuclei most probably lead to different atom diffusivity. Also, in the catalyst assisted approach, the collection of solely Ga atoms by the catalyst implies local change in the *V/III* ratio that can further a induce significant change in the local diffusivity [101] and in the NW morphology [27], whereas the presence of the Ni-Ga catalyst particles at the growth front may induce a different GaN crystal phase to form [123]. Last, the use of a catalyst raises concerns over contamination of the NWs by the seed material and deterioration of their properties in comparison to the catalyst-free NWs. Thus, an assessment of the respective advantages and drawbacks of both approaches is crucial for further applications. The growth windows, temperature and *V/III* ratio, are very similar in both cases [17, 19, 21, 66], so that the direct comparison of the properties and growth mechanisms of the NWs grown through each pathway under otherwise identical conditions is enabled and presented in the following. At first, the different growth models concerning GaN NWs grown by MBE in the framework of both approaches are reviewed. Then, the respective morphology and the structural properties of both types of NWs are compared and the effect of the *V/III* ratio and temperature on the NW morphology is studied. Also, the luminescence properties of the NWs in dependence on the growth temperature are investigated. Finally, the discussion is focused on the main three divergent aspects of these approaches that are the crystal quality, the growth mechanism, and the optoelectronic properties. The growth parameters of the samples discussed in this chapter are indicated in Table 1 in appendix 5.2.

4.1 GaN NW growth studies in MBE

4.1.1 Catalyst-assisted GaN NW growth

The growth of catalyst-assisted GaN NWs by MBE has not been much investigated in comparison to the catalyst-free one. Mamutin *et al* [18] first reported VLS growth of GaN and InN whiskers on GaAs and Al_2O_3 substrates. In the case of GaN a low temperature GaN buffer was first deposited [214] and VLS growth was suggested to occur from Ga droplets. Droplets are also observable at the tip of the whiskers in ref. [18] but it is not mentioned how they formed. More recently, our group employed Ni as an external catalyst on *C*-plane sapphire substrate and found that the axial growth is governed by the preferential accumulation of Ga atoms in the seed particles over N leading to Ga-rich conditions inside the seed. In agreement with this model, we found that the NW growth rate was limited by the N-rate [19].

4.1.2 Catalyst-free GaN NW growth

At the end of the 1990's, the group of Kishino [16] reported the growth of GaN NWs on AlN buffer deposited on sapphire almost simultaneously to Grandjean *et al* [215] who observed the formation of catalyst-free GaN "crystallites" by gas-source MBE on nitrided sapphire substrate. These results were shortly followed by the synthesis of GaN NWs directly on Si(111) by the group of Calleja [17]. Since then, catalyst-free NW growth has been the subject of intense investigation, leading to the demonstration in 2004 of the first GaN-InGaN NW green-to-red LED [216] by MBE and in 2008 of the first GaN-AlGaN NW UV-LED [217].

Essentially, several equivalent explanations have been brought to justify the preferential growth in the Ga-polar direction generally observed [137, 218]. Their crucial point is that the atoms incorporated at the NW tip stem not only from direct impingement but also from sidewall diffusion, as in the VLS model. Bertness et al. [140] suggested that the contribution of atoms diffusing on the NW side-facets was the determining factor of the NW morphology. Debnath et al.[25] further showed that the NW length decreases inversely with their diameter due to strong adatom diffusion on the GaN NWs lateral surface toward the tip. This model led to an underestimated adatom diffusion length of 40 nm at 800°C while Ishizawa *et al.* [219] reported a diffusion length from patterned growth experiments over 300 nm on nitrided Si at 900°C. More specifically, Bertness et al.[27] proposed that the driving force for the self-induced growth of GaN NWs is a difference in the sticking coefficients of group III atoms on the NW tip and side-facets and the enhanced surface diffusion of group III atoms along the non-polar NW side-facets as compared to the polar one. A similar explanation based on different growth rates for the various facets was also suggested by Stoica et al.[26]. Ristic et al.[22] argued in addition that the number of dangling bonds and the surface energy are higher for *C*-plane facets than for *A*- and *M*-plane ones which leads to faster growth in the *C*-direction. These models are supported by recent first principles calculations of the surface thermodynamics and adatom kinetics [220] showing that there is a strong in-plane anisotropy of the diffusion barriers on nonpolar GaN surfaces for Ga adatoms and that these are intrinsically unstable against atomic N.

However, to fully complete the model, the comparison of growth rate and stability of the two polar facets must also be considered. For GaN NWs grown on sapphire, Araki et al. [41] assumed that the presence of inversion domains in the low temperature buffer layer would lead to the formation of Ga-polar NWs whose growth rate was thought to be enhanced compared to N-polar GaN. Indeed a faster growth rate of Ga-polar GaN had been reported earlier by Romano *et al.* [221] for the growth of planar layer under N-excess. Since then, this difference in growth rate between the two polar directions was also ascertained by Rouvière *et al.* who reported that GaN quantum dots formed on non-polar $[10\bar{1}0]$ AlN grow also faster in the Ga-polar direction [222]. Moreover, the diffusion barrier of Ga ad-atoms on Ga-polar plane has been calculated to be higher than on N-polar plane [101] under N-excess. Such a difference between the polarity of GaN NWs and the surrounding compact layer was also later confirmed [218, 223]. In addition, on the basis of first-principles calculations N-terminated Ga-polar GaN surfaces were found stable under N-excess but not the N-polar ones [224]. Last, experiments confirmed that the Ga-polar GaN surface is more stable against N-plasma exposure than the N-polar one [225] and this was suggested to be the cause of NW formation directly from the decomposition at 800°C of mixed polarity MBE grown GaN films placed in a tube furnace [226]. Finally, Foxon *et al.* [28] recently proposed a complementary model to consider the geometry of growing NWs exposed to tilted impinging atom fluxes. In this model, the lateral facets of the NWs exposed intermittently to the source fluxes grow by migration-enhanced epitaxy while growth on the top NW surface corresponds to the classical MBE process. This model was found to account for very flat lateral facets and an enhanced axial growth relative to the lateral one of a factor of 5–6 depending only on the tilt of the sources. However, this model is incomplete. It neglects the adatom diffusion and could not explain the bimodal morphology [218] in which Ga-polar NWs grow faster than N-polar ones and have a much larger axial to lateral growth rate ratio [24, 25]. Note that similarly, a more sophisticated model has been developed to explain not only the self-assembly but also the nucleation of 3D structures by shadowing effect [227] at oblique angle deposition for thin film formed by physical vapor deposition. This model showed that column width changed with column length according to a power law whose exponent depends on the surface diffusion and shadowing. In any case the obtained dependence would imply that thicker columns grow faster than thinner ones, in agreement with data extracted from TEM measurement on GaN NWs marked with AlN during the growth on AlN buffer [135]. This is however in contradiction with the result of Debnath et al.[25]. Interestingly, for the growth on AlN buffer a similar limitation by the supplied N-flux as the one found for the catalyst assisted approach has also been reported [23, 28]. Thus, several models account for the growth of catalyst-free GaN NWs in the Ga-polar direction but processes limiting the NW growth rate are still under debate. Apparently, for both approaches, the catalyst-assisted as well as the catalyst-free one, the N-rate could be the factor limiting the vertical growth kinetics as will be further investigated in this chapter.

4.2 Morphology

The morphology of catalyst-induced NWs grown on *C*-plane sapphire [sample A0a, Figure 4.1(a)], catalyst-free NWs grown on Si(111) and Si(001) (sample S1a and S0a, Figure 4.1(b) and 4.1(c), respectively) is presented in Figure 4.1.

For comparison, sample *A0I* has been grown on bare sapphire substrate, whereas samples *S0I* and *S1I* correspond to the growth on Si(001) and Si(111) covered by a 4Å thin Ni layer. In this case, the Ni layer was deposited in situ after the cleaning procedure consisting in a simple HF dip, subsequent loading into the chamber for MBE and oxide desorption step as describe in chapter 2. Those samples were all grown at 730°C with a N-, and Ga-rate of 2.0 and 0.4 Å/s, respectively. Moreover, the duration of GaN

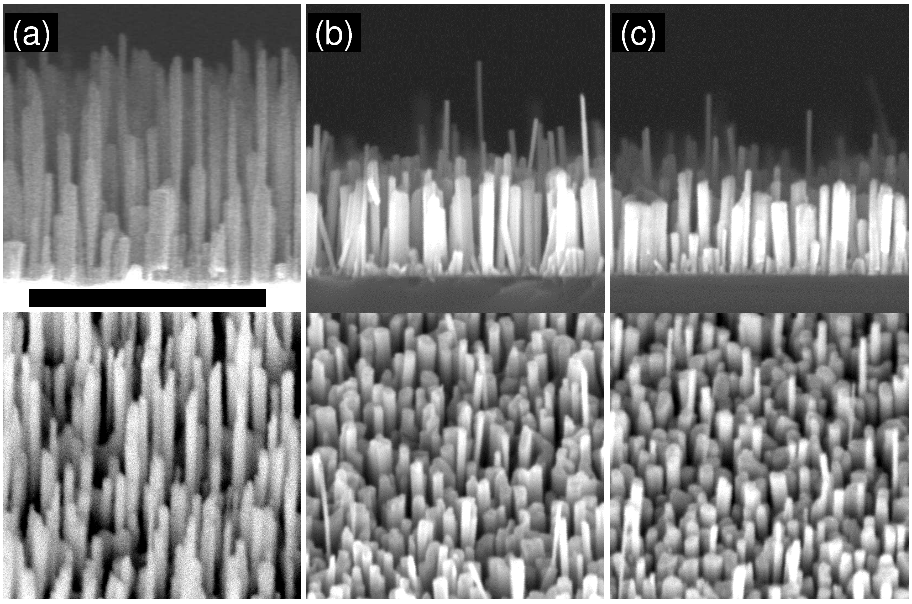

Figure 4.1: SEM images acquired at an angle of 90° (top) and 45° (bottom) to the surface normal of (a) Ni-induced GaN NWs on sapphire (Sample A0a) and (b) and (c) self-induced GaN NWs grown on Si(111) and on Si(001) (Sample S1a and S0a respectively). Scale bar corresponds to 1 μm.

deposition was the same (76 min) for each of these experiments, and corresponds to a compact layer with a nominal thickness of 180 nm if no NW growth had occurred. In addition, sample *A0V* has been grown under Ga-rich condition on a sapphire substrate covered by a 3 Å-thin layer of nickel annealed in-situ at 750°C for 15 minutes. The morphology of samples *A0I*, *A0V*, *S1I* and *S0I* is illustrated in Figures 4.2(a), 4.2(b), 4.2(c) and 4.2(d). Samples *A0a*, *S1a*, *S0a*, *S1I* and *S0I* were entirely covered by NWs oriented perpendicularly to the substrate and their morphology is further described in detail in the following subsections.

4.2.1 Catalyst-assisted growth

On sapphire substrates the NWs form only under N-rich conditions and only in the presence of Ni seeds. The diameter of these NWs grown in the presence of the Ni-particles under N-excess amounts to 35 ± 20 nm and their length to 880 ± 140 nm, which is almost 5 times larger than the nominal thickness. However, this length is not completely homogeneous since few shorter columns also grew between the long ones. The NW density measured from SEM images is 1.1×10^{10} NWs/cm^2. The NWs exhibit a hexagonal cross-section [Figure 4.3(a)]. However, changes in the NW shape and facets are observed for experiments identical to *A0a* but with longer duration as seen in Figure 4.3(b). This possibly indicates a rotation of the NW structure or a change of NW facet planes. Both growth under N-rich conditions directly on a bare sapphire substrate [Figure 4.2(a)] and growth under Ga-rich conditions in the presence of Ni-seed particles [Figure 4.2(b)] resulted in planar layers which underlines the crucial role

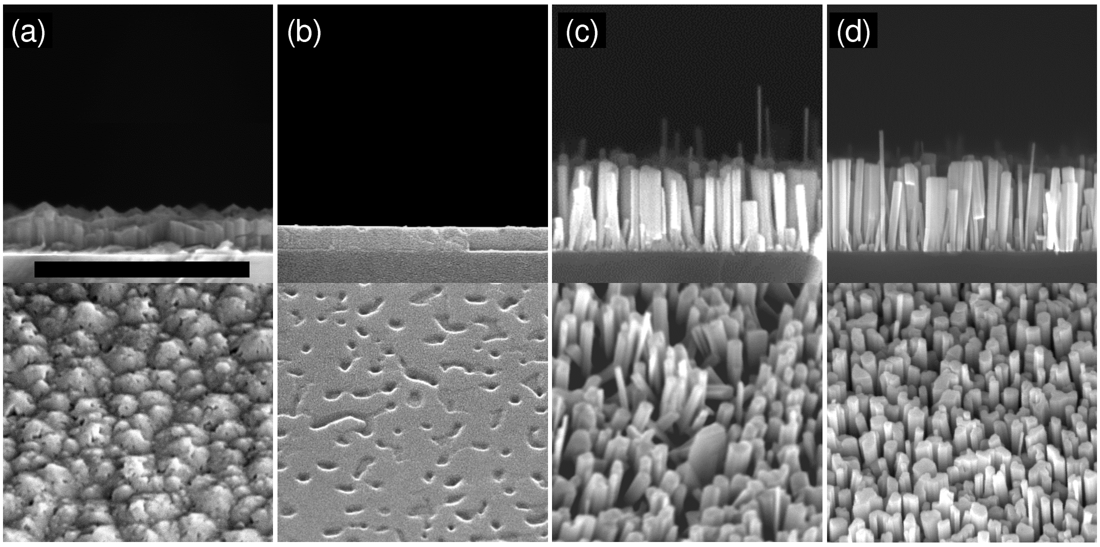

Figure 4.2: SEM images acquired at an angle of 90° (top) and 45° (bottom) to the surface normal of (a) GaN layer grown under N-excess on bare sapphire (sample *A0I*), (b) GaN layer grown under excess Ga on Ni-covered sapphire (sample *A0V*) and (c) and (d) Si(111) and Si(001) covered by Ni (samples *S1I* and *S0I* respectively). Scale bar corresponds to 1 μm.

of the Ni islands *V/III* ratio for the NW formation.

4.2.2 Catalyst-free growth

In contrast, on Si substrates of both orientations, the NWs grow without any catalyst, but also only under N-rich conditions [Figures 4.1(b) and 4.1(c)]. Neither the substrate orientation nor the presence of Ni particles [Figures 4.2(c) and 4.2(d)] influences the morphology of the catalyst-free NWs. On samples S1a and S0a, the diameters of the NWs are spread over the range of 50 ± 35 nm and their average length is shorter than the average length of the NWs induced by the Ni seeds on sapphire. The majority of the NWs are 380± 90 nm long, which is about twice the nominal thickness. The length of these NWs is comparable to the one of the shorter thick columns grown on sapphire.

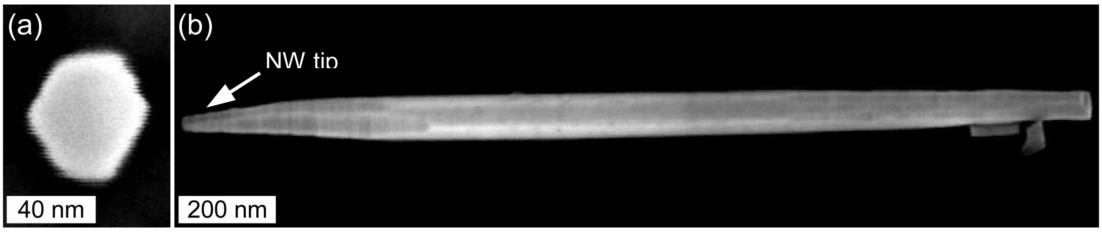

Figure 4.3: SEM images of a Ni-induced GaN NWs. (a) Top view showing the hexagonal cross-section of a NW grown for 76 min. (b) Harvested NW grown for 180 min showing twist of the facet orientation during growth.

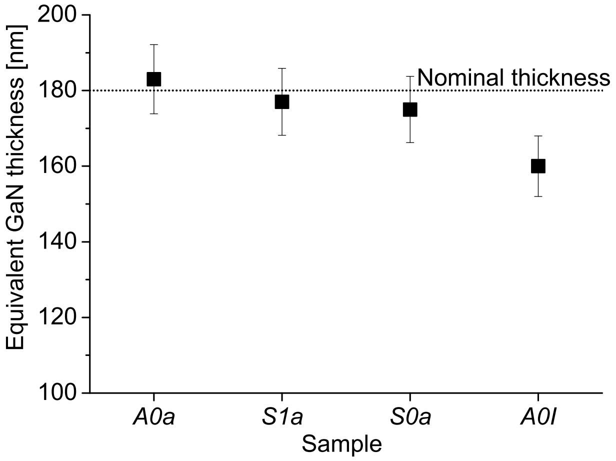

Figure 4.4: GaN coverage measured by RBS and converted into equivalent film thickness of samples *A0a* (Ni coated Al_2O_3 substrate), *S1a* (Si(111) substrate), *S0a* (Si(001) substrate) and *A0I* (bare Al_2O_3 substrate).

Very few longer NWs protrude from this shorter NW base and their length extends to 770 nm, which is more than four times the nominal thickness but still somewhat shorter than the length of GaN NWs grown through the catalyst approach. This dispersion in diameter and length has been attributed to the coalescence of short columns and enhanced growth of thinner ones through a diffusion induced growth mechanism [25, 136]. The catalyst-free NW density is 0.8 x 10^{10} NWs/cm2 and 0.9 x 10^{10} NWs/cm2 on Si(111) and on Si(001). These values are in agreement with reference [24] for growth time exceeding the nucleation time, when the occurring coalescence of short columns reduces the NW density.

4.2.3 Comparison of GaN thicknesses

The SEM images in Figure 4.1 show that under identical growth condition *a* very different morphologies and apparent growth rates can be obtained, depending on the substrate surface and on the presence/absence of a catalyst. This raises the question whether the total amount of GaN varies as well. Hence samples A0a, S1a, S0a and A0I (planar GaN on sapphire) were characterized by RBS to get a precise comparison of their GaN coverage. The results are presented in Figure 4.4 and show that the amount of GaN averaged over an area of 2 mm diameter is almost the same for all of these samples, although different morphologies were obtained. Also, the GaN coverage measured by RBS is in agreement with the nominal thickness. The GaN coverage of the NW-free sample *A0I* is slightly smaller than those of the other samples. However, the difference is within the experimental uncertainty, except for the comparison with A0a, and in any case much smaller than the absolute coverage. Thus, the amount of deposited GaN is independent of the morphology and the growth mode.

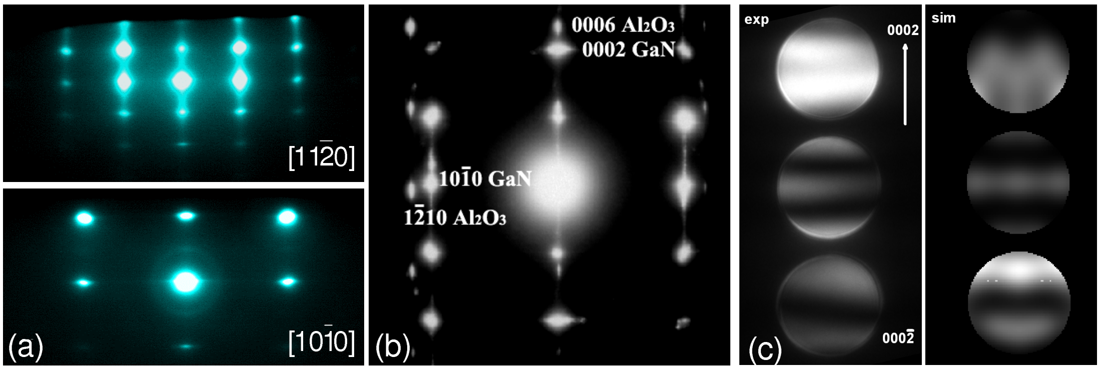

Figure 4.5: (a) RHEED patterns of Ni induced GaN NWs along the $[11\bar{2}0]_{GaN}$ (top) and $[10\bar{1}0]_{GaN}$ (bottom) azimuths.(b) SAED pattern along $[11\bar{2}0]_{GaN}$ and (c) CBED images of the corresponding sample. Left is the experimental image and right the corresponding simulation.

4.3 Structural properties

The vertical orientation of the NWs suggests epitaxial growth. Thus, in order to probe the epitaxy of the NWs following both pathways, we first gathered information on the crystal structure by RHEED images acquired at the end of each growth experiment. However, in order to get more specific information on the crystal quality of the NWs we complemented this study by conventional TEM analysis.

4.3.1 Catalyst-assisted growth

The RHEED images acquired at the end of the growth [Figure 4.5(a)] exhibit a spotty pattern as expected for surfaces covered by narrow 3D clusters, and the well defined spots correspond to the WZ GaN structure observed in transmission through the NW crystal [139]. The data confirm that the NWs grow along the *C*-axis and perpendicularly to the substrate. The patterns corresponding to the $[10\bar{1}0]_{GaN}$ and $[11\bar{2}0]_{GaN}$ azimuths clearly alternate every 30° when the sample is rotated around the [0001] direction, which is a sign for good in-plane orientation. This orientation is as for planar GaN growth on *C*-plane sapphire substrates:
$(0001)_{GaN} \parallel (0001)_{Al_2O_3}$ and $[11\bar{2}0]_{GaN} \parallel [10\bar{1}0]_{Al_2O_3}$.
The epitaxial orientation further investigated by SAED on a similar sample as *A0a* provides the pattern seen in Figure 4.5(b). The latter confirms the single crystalline nature and WZ structure of the GaN NWs, as well as the epitaxial relation determined by RHEED. The [0001] growth direction of the NWs is further specified by the CBED results depicted in [Figure 4.5(c)]. The comparison of experimental and simulated images indicates that the NWs yielded by this method are Ga-polar. This result is noticeable since it is usually reported that GaN layers exhibit N-polarity when grown by MBE on sapphire [224]. Actually, this aspect is more complex. Indeed Yoshikawa *et al.* showed that mixed Ga and N polarities can also appear on thermally cleaned sapphire substrates, and that the N polarity prevails by intensive nitridation of the substrate

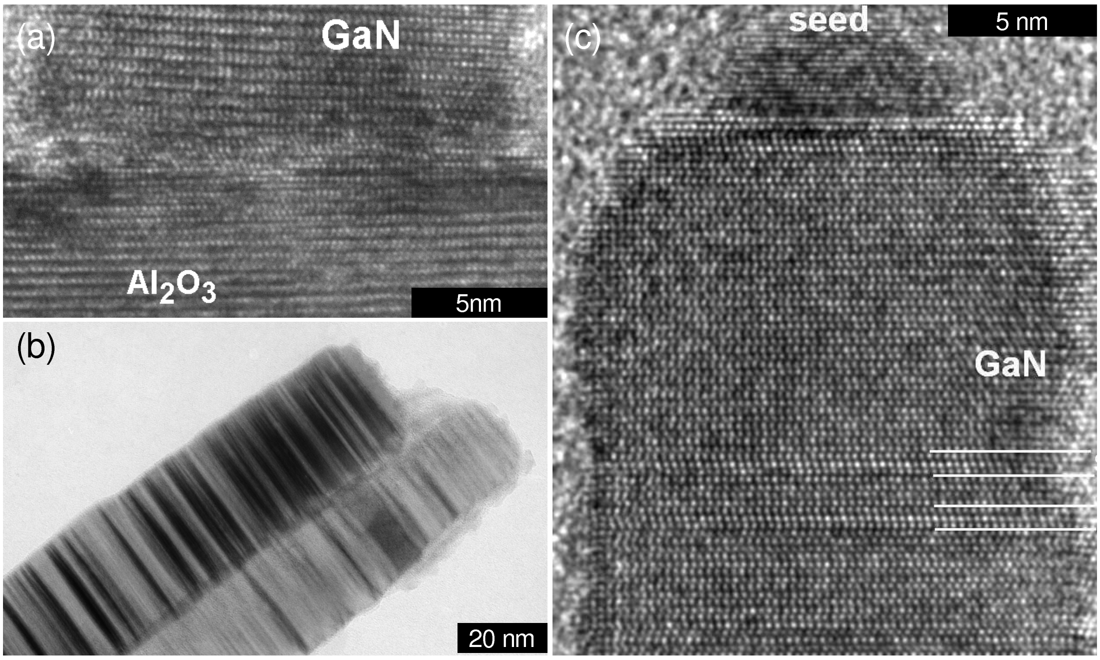

Figure 4.6: (a) HRTEM image of the interface between the GaN NWs and the sapphire seen along the $[10\bar{1}0]_{GaN}$ direction.(b) TEM image of NW tips. The SFs are identified by the black striation. (c) HRTEM image of a NW tip seen along the $[11\bar{2}0]_{GaN}$ direction. The white lines point to SFs.

before growth [228]. However, the opposite effect of the nitridation process was also observed [229]. Thus, the Ga polarity of these NWs cannot be directly related to the Ni seeds protecting the underneath sapphire surface from nitridation.

XTEM gives further information on the structural quality of the catalyst-induced NWs (Figure 4.6). The interface between GaN NW and sapphire substrate shown in Figure 4.6(a) is sharp, and there is no interfacial layer. However, the $(0001)_{GaN}$ planes are slightly tilted relative to the $(0001)_{Al_2O_3}$ planes, which is also supported by the slightly arc shaped reflections of GaN in the SAED pattern in Figure 4.5(b). Fairly many basal SFs are detected in most of these GaN NWs but no other extended defects. The SFs run parallel to the (0001) plane through the whole NW diameter and apparently form with a random distribution along the NW axis. A detailed investigation reveals their I_1 nature [230]. Their density was estimated to be 2×10^6/cm. Very importantly, observation of the Ni compound particles of 5-20 nm in diameter at the NW tips brings out the confirmation that the NWs grow on sapphire by a VLS or VSS mechanism. Similarly to the first nucleation stage (see section 3.2.3), the *fcc* or the *L1*$_2$ structure was revealed by post-growth HRTEM (Figure 4.7) corresponding either to Ni or to the phase α' Ni$_3$Ga, respectively. This result further supports the reversed phase transformation mechanism from the *bcc* NiGa phase to the *fcc*-like phase by Ga purge after growth completion.

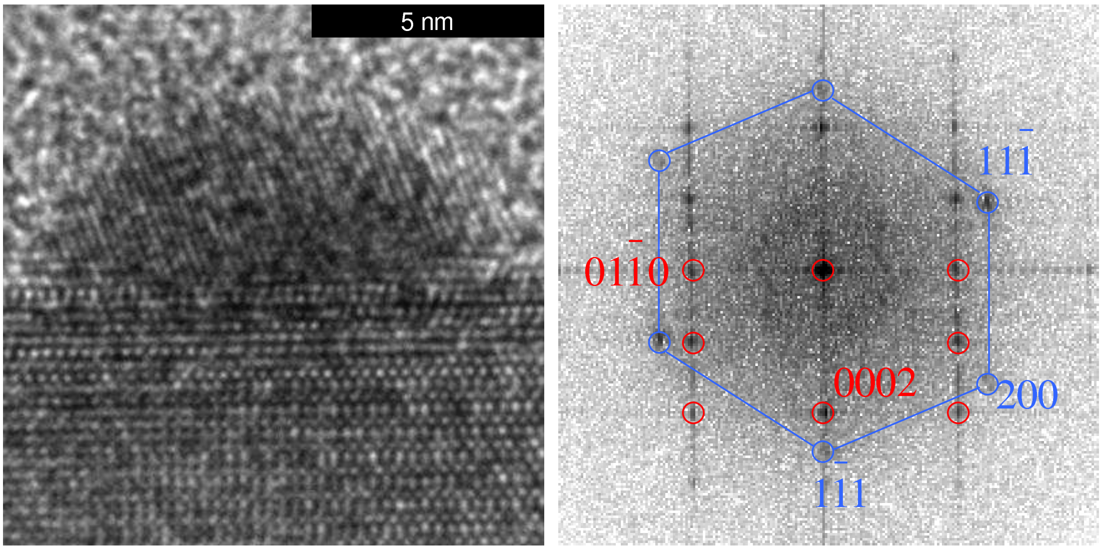

Figure 4.7: Zoom on the Ni-Ga particle area seen on the HRTEM image in Figure 4.6 and right the corresponding 2D-FFT revealing the *fcc*-like phase of the Ni-Ga particle.

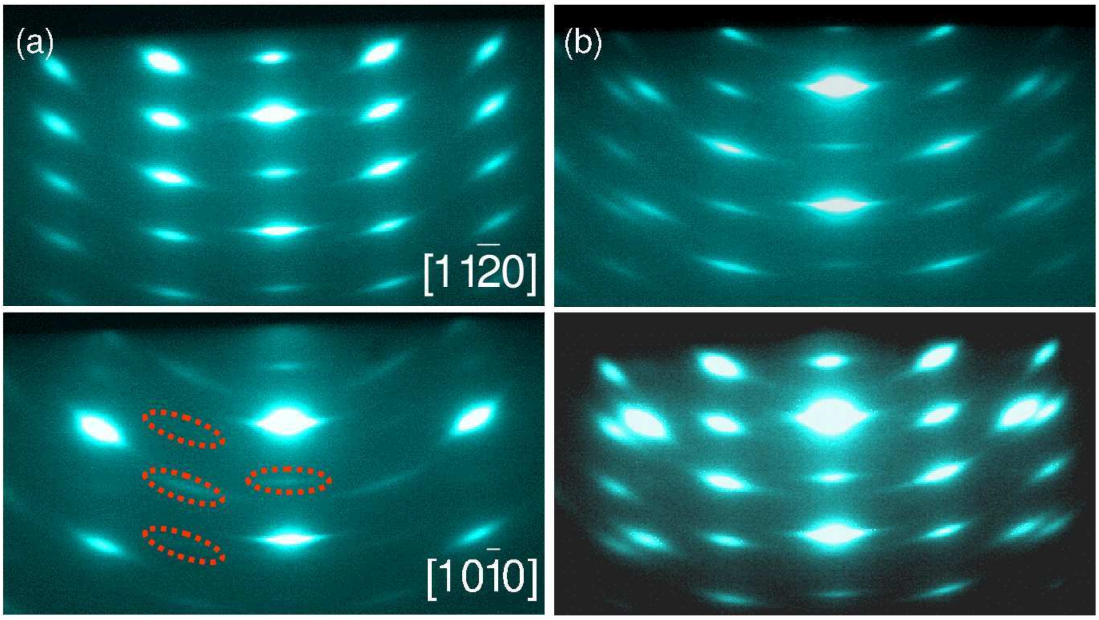

Figure 4.8: (a) RHEED patterns of self induced GaN NWs grown on Si(111) along the [11$\bar{2}$0] (top) and [10$\bar{1}$0] (bottom) azimuths. (b) Self induced GaN NWs grown on Si(001) produce the same patterns in both azimuths (top) which is comparable with the bottom pattern resulting from the sum of patterns seen in a.

4.3.2 Catalyst-free growth

Similarly to the catalyst-assisted growth, the RHEED patterns produced by the catalyst-free GaN NWs correspond to the hexagonal WZ structure of GaN. However, the spots appear as broken rings [Figures 4.8(a),(b)] as reported in [231] which indicates a slight misorientation of the NWs with respect to the Si substrate normal. For the growth on Si(111) the patterns in both azimuths [Figure 4.8(a)] are different but weak additional spots appear in the azimuth $[10\bar{1}0]$. In contrast, the pattern acquired on Si(001) [Figure 4.8(b)] was the same in both azimuths. This pattern contains additional spots compared to the $[11\bar{2}0]$ pattern obtained on Si(111). This is due to the superposition of the patterns of both azimuths $[11\bar{2}0]$ and $[10\bar{1}0]$ which indicates several in-plane orientations of the GaN-NWs relative to the Si(100) substrate. This feature is further illustrated by the bottom pattern in Figure 4.8(b) which was obtained by adding the top and bottom ones in [Figure 4.8(a)] with an image processing software. The reflexes of the yielded pattern are identifiable to the ones of the real pattern obtained for growth on Si(001) seen on top of Figure 4.8(b). Bertness *et al.* already observed two equivalent in-plane orientations of the GaN NWs grown on a 30 to 120 nm thick AlN buffer layer deposited on Si(001) by x-ray diffraction (XRD). This has been attributed to the two possible alignments of $< 10\bar{1}0 >_{GaN}$ along the $< 100 >_{Si}$ azimuthal directions [27]. For growth on Si(111), they also reported the same phenomenon but the in-plane orientation $< 11\bar{2}0 >_{GaN} \| < 1\bar{1}0 >_{Si}$ was significantly dominant. Largeau *et al.* also studied the in-plane orientation of GaN NWs grown on Si(111) with a nitrided Al intermediate layer equivalent to 8 MLs of AlN [232]. However, they found that the main orientation was $< 10\bar{1}0 >_{GaN} \| < 1\bar{1}0 >_{Si}$ and becomes prevalent with additional growth of 8 ML AlN on the intermediate layer. Last, Nakada *et al.* [178] studied the effect of Si(111) nitridation prior to the growth of GaN. They obtained the same dominant orientation as Bertness *et al* with or without nitridation, although an amorphous layer of silicon nitride formed between Si(111) and GaN. They suggested that GaN can grow by taking the epitaxial relationship of the Si(111) substrate if the orientation of the latter is transferred to the GaN layer by crystalline portions of silicon nitride, or if a short range order in the tetrahedral coordination of each atom is maintained. In our case, the RHEED patterns indicate the dominance of the $< 11\bar{2}0 >_{GaN} \| < 1\bar{1}0 >_{Si}$ in-plane orientation for growth on Si(111) without any AlN layer in agreement with the results of Bertness *et al.* and with Nakada *et al.*.

In comparison to the RHEED patterns, the ones obtained by SAED [Figure 4.9(a)] also confirm that the GaN NWs are single crystalline, have the WZ structure and grow in the [0001] direction. The CBED results in [Figure 4.9(b)] achieved on GaN NWs grown on Si(111) indicates that these NWs are also Ga-polar in agreement with previous reports [137, 218] pointing out the Ga polarity of long NWs embedded in an N-polar GaN matrix. However, on both types of Si substrates only one in-plane orientation was found, presumably due to the small area investigated with the beam. The in-plane orientation found on Si(111) is the same as the main one observed by RHEED.

In addition, the SAED patterns also show that the NWs grown on Si(111) and Si(001) substrates exhibit up to 10° misorientation relative to the (111) and (001) axis, respec-

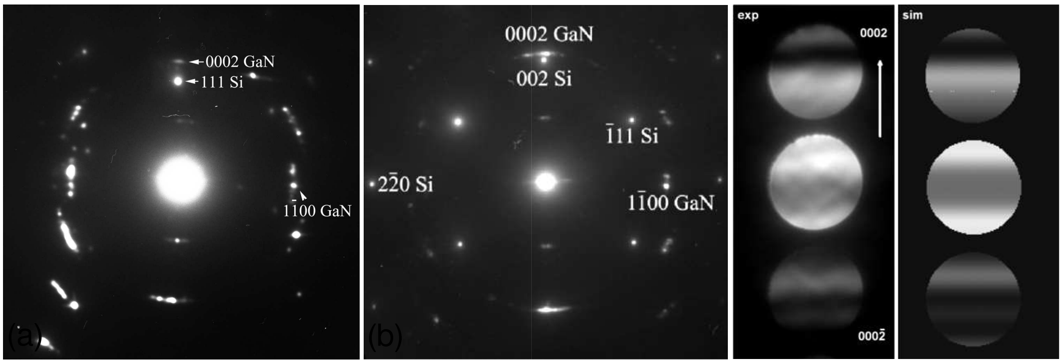

Figure 4.9: (a) and (b) SAED patterns of the GaN NWs grown on Si(111) and Si(001), respectively. (c) CBED images of GaN NW grown on Si(111). Left is the experimental image and right the corresponding simulation.

tively. This misorientation is attributed to the thin amorphous layer of $Si_{1x}N_y$ formed before or during the nucleation of the NWs 3, [134]. This interfacial Si_xN_y layer between NW and substrate of any orientation is also clearly seen in Figures 4.10(a) and 4.10(b). However, this layer is not always completely amorphous as can be seen in Figure 4.10(b) and (d). Ristić *et al.* conclude therefore that it rather forms after the nucleation [21]. The study in chapter 3 also reveals that some NWs nucleate before these interfacial layer becomes amorphous which can explain the strong tilt of the NWs observed in Figure 4.10(b). This can therefore also account for the observation of the peculiar in-plane orientation of the NWs.

Furthermore the good crystal quality of these NWs almost free of any stacking faults [Figures 4.10(e) and 4.10(f)] is confirmed by TEM. The tips of the NWs are flat and free of any particle [Figure 4.10(g)]. This result does not support the speculation that these NWs grow by a VLS-like mechanism induced by Ga-droplets, as also previously rejected [27, 133, 134].

In the particular experiments *S0I*, *S1I*, VLS-like NW growth could not be induced neither by the deposition of Ni on Si substrates before GaN growth. SEM investigation of sample *S1I* revealed elongated islands on the Si(111) surface that hinder the growth of NWs [Figures 4.11(a) and 4.11(b)]. These islands have also been observed on XTEM images [Figures 4.11(c), 4.11(d) and 4.11(e)] and their elemental distribution as investigated by x-ray mapping is a Ni-Si mixture. Indeed the formation of Ni_2Si starts already at around 200°C and the one of NiSi once that the Ni is fully consumed. Last for temperatures higher than 750°C the $NiSi_2$ phase forms [233]. Thus, the role of Ni is remarkably different on sapphire and on Si(111). While on sapphire Ni induces the growth of the NWs and is located at their tips, on Si(111) Ni locally reacts with the Si substrate and prevents NW growth. We note that this salicidation process is anisotropic [234], indeed these islands were observed only for the Ni deposited on Si(111) substrates only but not on Si(001)where the NWs grew everywhere. However, in both cases still no droplets were observed at the NW tip.

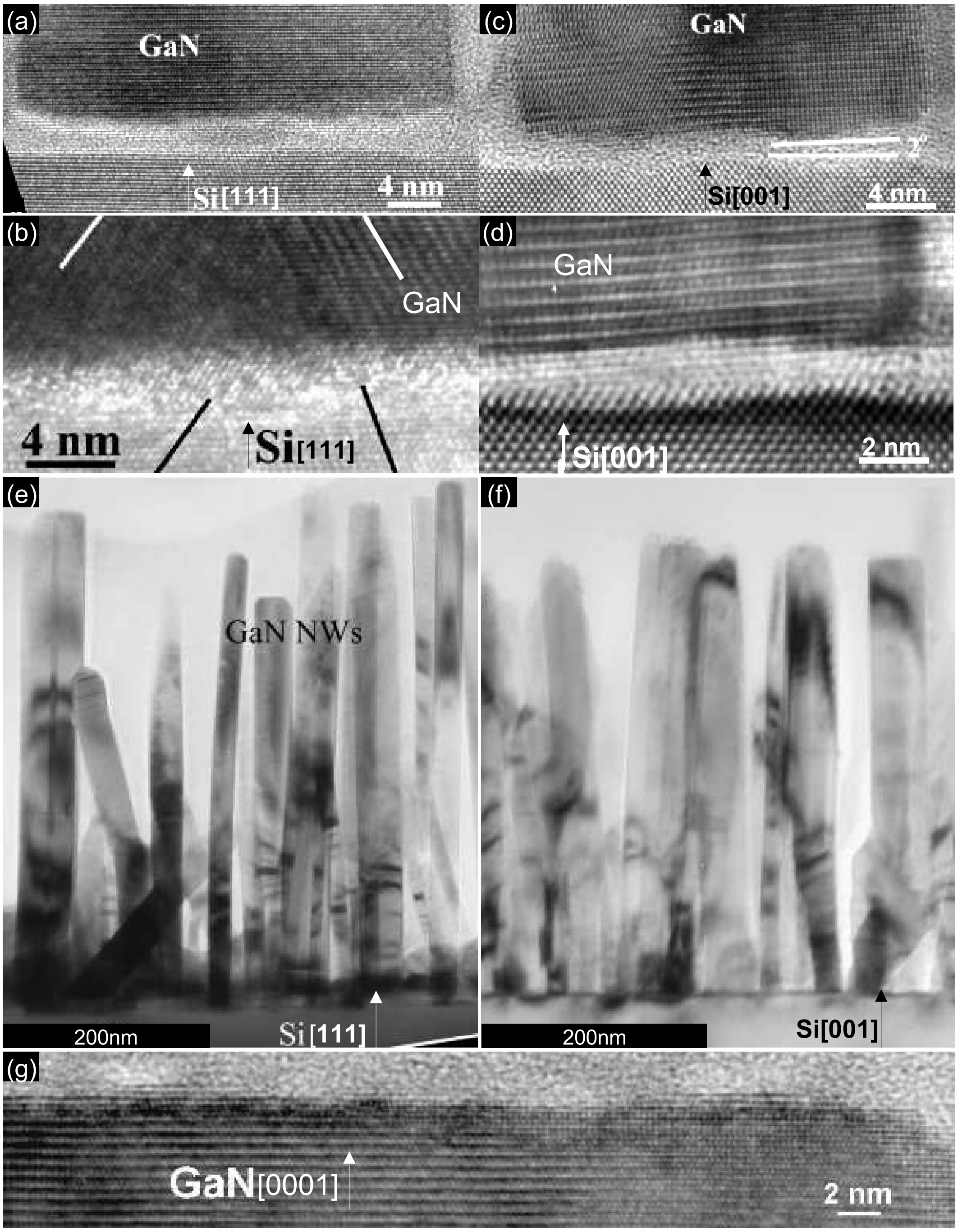

Figure 4.10: (a),(b) and (c), (d) HRTEM images of the interfaces between the GaN NWs and the Si(111) and Si(001) substrates, respectively. In (b) and (d) the interface is not amorphous so that in (b) NWs grow along two inclined direction relative to $[111]_{Si}$. (e) and (f) TEM images of GaN NWs grown on Si(111) and Si(001) substrates, respectively. (g) HRTEM image of a NW tip.

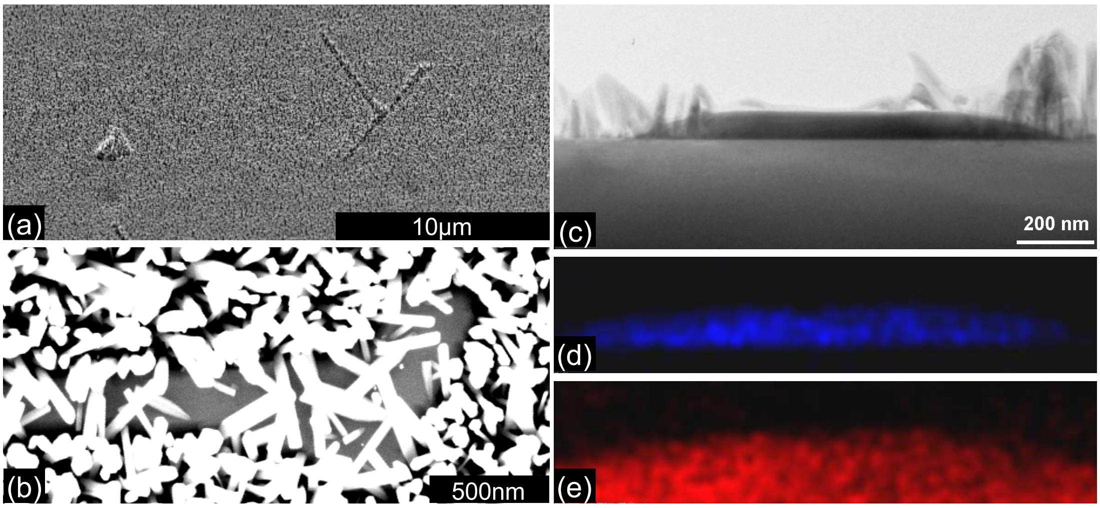

Figure 4.11: (a) and (b) plan view SEM and (c) XTEM images along $[1\bar{1}0]_{Si}$ of sample *S1I* revealing the formation of Ni-Si islands which hinder NW growth. (d) Ni (blue) and (e) Si (red) distribution in the island found by EDXS.

4.4 Influence of the *V/III* ratio and growth temperature

4.4.1 Influence of the *V/III* ratio

GaN and the other III-nitrides have the specialty to be grown either under Ga-excess or N-excess unlike other III-V semi-conductors. However, the N-rich growth conditions are required in both approaches for the NWs to develop [19, 134]. Thus, it seems that the *V/III* ratio is the most important growth parameter for the formation of GaN NWs by MBE. To study its influence on growth in more detail, both the Ga- and the N-rate were varied separately. NW growth rates were extracted from cross-sectional SEM images as described in chapter 2 and compared to the nominal growth rate corresponding to the rate of the species in minority. In principle, the NW growth rate determined this way could be wrong if the nucleation time is very long as seen in the previous chapter. However, at the growth temperature of 730°C the nucleation time is negligible in comparison to the growth time (see chapter 3) for all samples except for condition *e* (lowest N-rate) for which the nucleation time lasts up to 10 min for the catalyst-assisted growth (sample *A0e*) and already almost 30 min for the catalyst-free growth (Samples S1e and S0e). However, in these extreme cases, the loss of thickness was estimated from the QMS profiles to be on the one hand 6 nm (0.01 Å/s) and 40 nm (0.09 Å/s), and both values are within the range of uncertainty.

Influence of the N-rate

At first, the Ga-rate was kept constant while the N-rate was decreased down to a value close to but above stoichiometry (conditions *a*, *d*, and *e*). Figure 4.12 presents the morphology of the corresponding samples. Under these conditions, the NW length de-

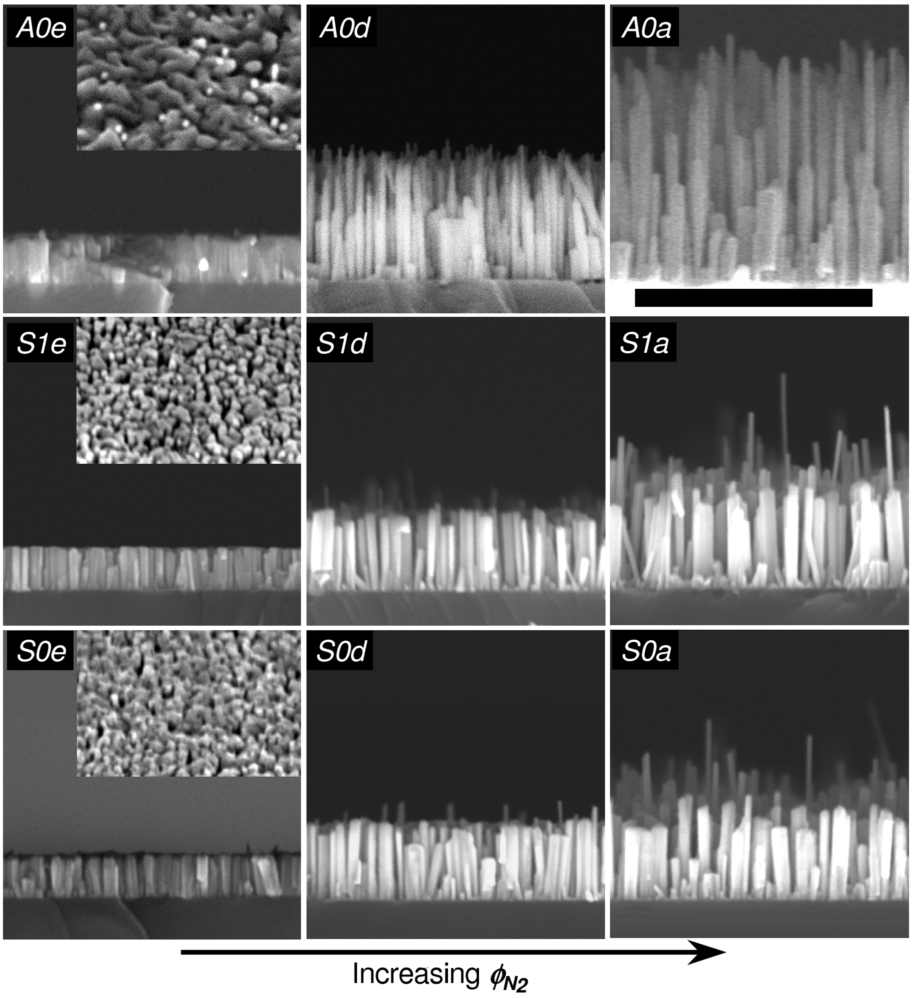

Figure 4.12: SEM images acquired at an angle of 90° and 45° (inset) to the surface normal of catalyst-assisted (first row) and catalyst-free GaN NWs on Si(111) and Si(001) (second and third rows, respectively) for various N-rates. Scale bar is 1 μm.

creases with the N-rate for the growth on sapphire with Ni-catalyst as well as for the growth on Si substrates without any catalyst. In the case of self-induced growth at a *V/III* ratio just above stoichiometry, Calleja et al.[129] already reported a low density of short nanocolumns emerging from a compact columnar layer. Similar results were observed for both approaches (see inset in Figure 4.12). The growth rate of this columnar layer, which is more compact for the growth on sapphire than on Si, matches the growth rate of sample *A0I* corresponding to the supplied Ga-rate. In general such a bimodal morphology is clearly obtained for moderate *V/III* ratio but when the excess of N is increased the NW growth rate is enhanced for both approaches and the columnar layer is not noticeable anymore, but instead there are thicker and shorter columns between the NWs.

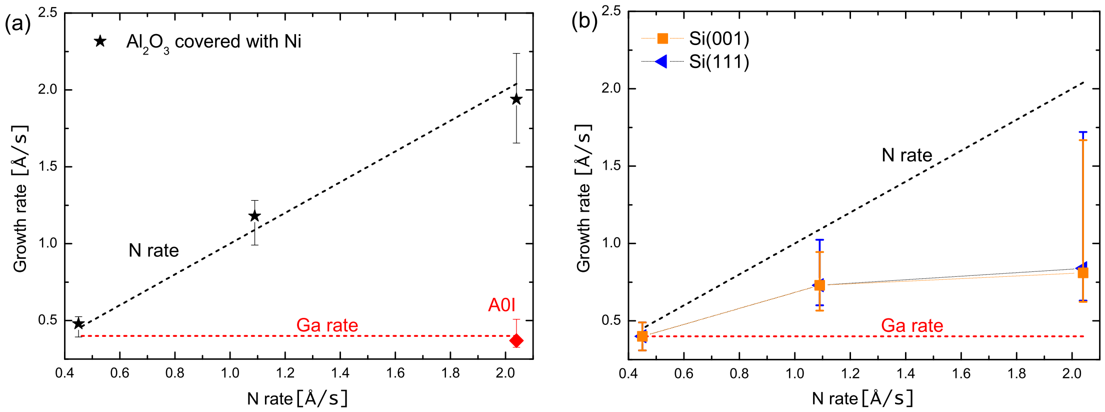

Figure 4.13: Growth rate of (a) catalyst-assisted (samples *A0a*, *A0d*, *A0e*) and (b) catalyst-free GaN NWs (samples *S0a*, *S0d*, *S0e*, *S1a*, *S1d*, *S1e*) as a function of the N-rate.

The growth rate of the NWs as a function of the N-rate is plotted for these experiments in Figure 4.13. For comparison, the N-rate and the Ga-rate are also reported in the graphs. In the case of growth on sapphire with Ni catalyst [Figure 4.13(a)], the NW growth rate matches closely the N-rate, similar to planar growth under Ga-rich conditions, instead of the present N-rich ones. This result can be fully explained by the growth model proposed in reference [19] that is described in detail in section 4.6.2. However, on bare Si substrates 4.13(b) a different situation is observed and the results are very similar for both orientations of the Si substrates. For *V/III* ratios higher than one, the average growth rate of the NWs is significantly lower than the N-rate but higher than the Ga-rate and only the few longest NWs grow at a rate approaching the N-rate. An interpretation of these observations is given in section 4.6.2 on the basis of the existing growth models [22, 23, 26, 27].

Influence of the Ga-rate

Next, the N-rate was kept constant and the Ga-rate was halved and doubled, respectively (conditions *a*, *f* and *g*). SEM images of the corresponding samples are presented in Figure 4.14. In the case of growth on sapphire with Ni catalyst, for the lowest Ga-rate (sample *A0f*) the NW length is strongly reduced while for the higher Ga-rate (sample *A0g*) the NW length is almost unchanged in comparison to the medium Ga-rate (sample *A0e*). In addition, for the lowest Ga-rate planar growth is observed between the very short NWs (see inset) whereas for the highest growth rate coalescence-like feature typical for low *V/III* ratio is forming a discontinuous base between the NWs. The growth rate of this base (0.9 Å.s) slightly exceeds the Ga-rate (0.8 Å.s). Note also that this base let the NWs root uncovered as if it will have formed after the NW nucleation. For the catalyst-free approach, no obvious difference is observed for the two different substrate, Si(001) and Si(111). The NW length increases with the Ga-rate and for condition *g*, the longest NWs are as long as the catalyst-induced NWs.
The growth rate extracted from Figure 4.14 as a function of the Ga-rate is plotted in Fig-

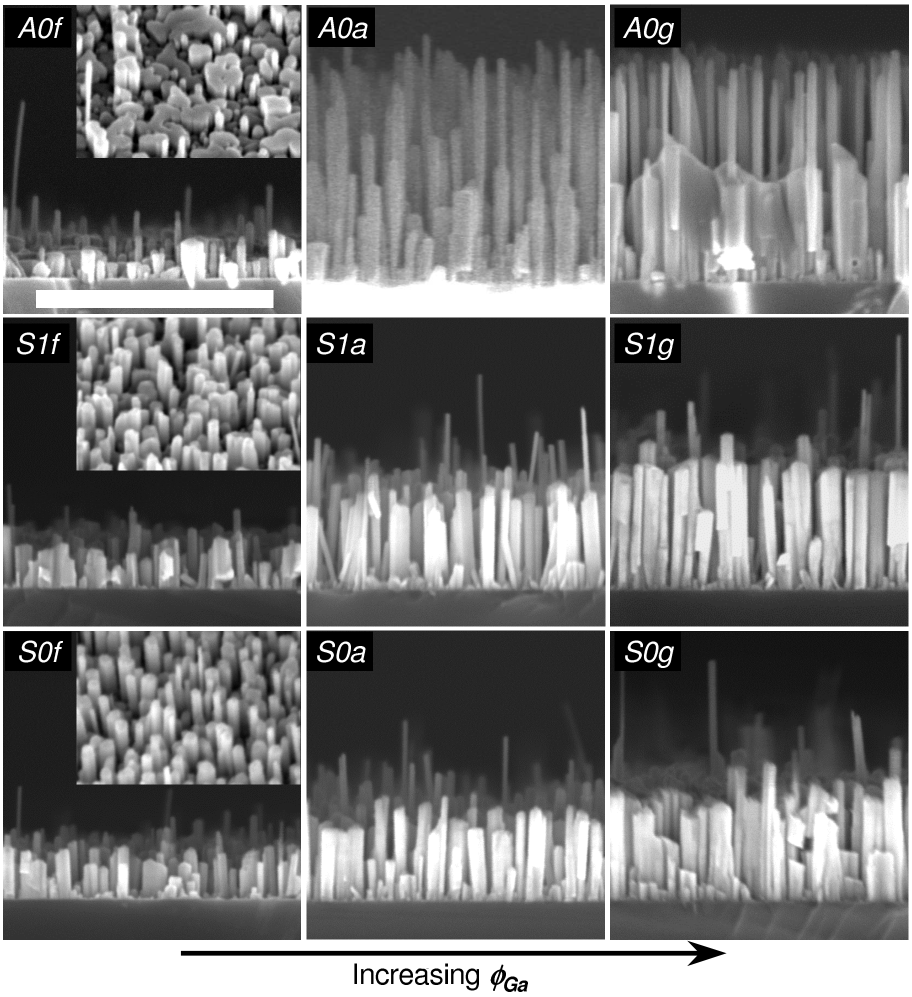

Figure 4.14: SEM images acquired at an angle of 90° and 45° (inset) to the surface normal of catalyst-assisted (first row) and catalyst-free GaN NWs on Si(111) and Si(001) (second and third rows, respectively) for various Ga-rates. Scale bar is 1 μm

ure 4.15. The N-rate and the Ga-rate are also reported on the graphs. For the catalyst-assisted NWs, the growth rate matches again closely the N-rate except for the lowest Ga-rate of condition *f*. Once the Ga-rate is set over a critical value, NW growth occurs and saturates at the N-rate, even for the higher Ga-rate. This further confirms that the supplied N-rate imposes the NW growth rate. In the case of growth on bare Si substrates, the average growth rate is still significantly lower than the N-rate but increases with the Ga-rate for the investigated range. For growth under condition *g*, the growth rate of the few longest NW reaches the N-rate. Therefore, we conclude that for the catalyst-free approach, the N-rate is the upper limit of the NW growth rate in agreement with the previous results of Songmuang et al. [23]. A possible explanation for this result is presented in section 4.6.2.

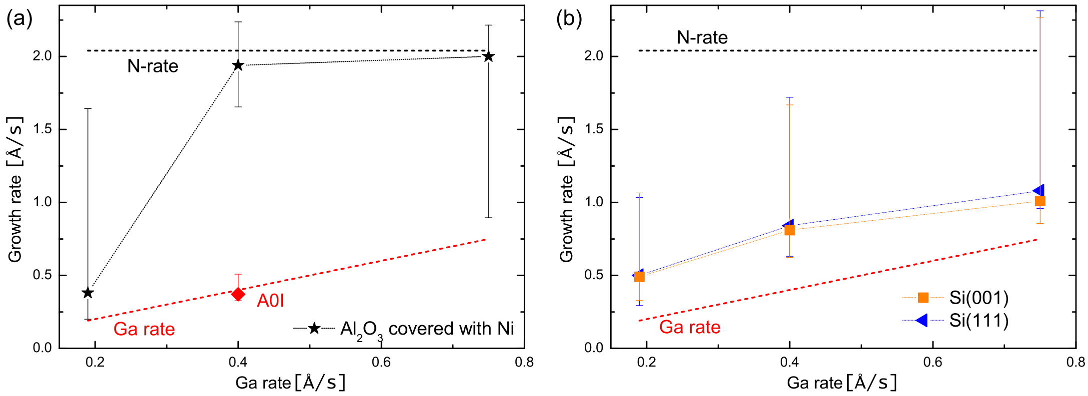

Figure 4.15: Growth rate of (a) catalyst-assisted (samples *A0a*, *A0f*, *A0g*) and (b) catalyst-free GaN NWs (samples *S0a*, *S0f*, *S0g*, *S1a*, *S1f*, *S1g*) as a function of the Ga-rate

4.4.2 Influence of the temperature

The growth temperature has already been reported to enhance the NW tapering morphology [136] grown in the catalyst-free approach and the NW growth rate [23]. In order to study its effect on both the catalyst-assisted and the catalyst-free NWs, samples were grown keeping the same nominal *V/III* ratio as condition *a* at 730, 750, and 780°C.

Figure 4.16 presents the morphology of the catalyst-assisted NWs grown under these conditions (samples *A0a*, *A0b*, *A0c*). When increasing the substrate temperature from

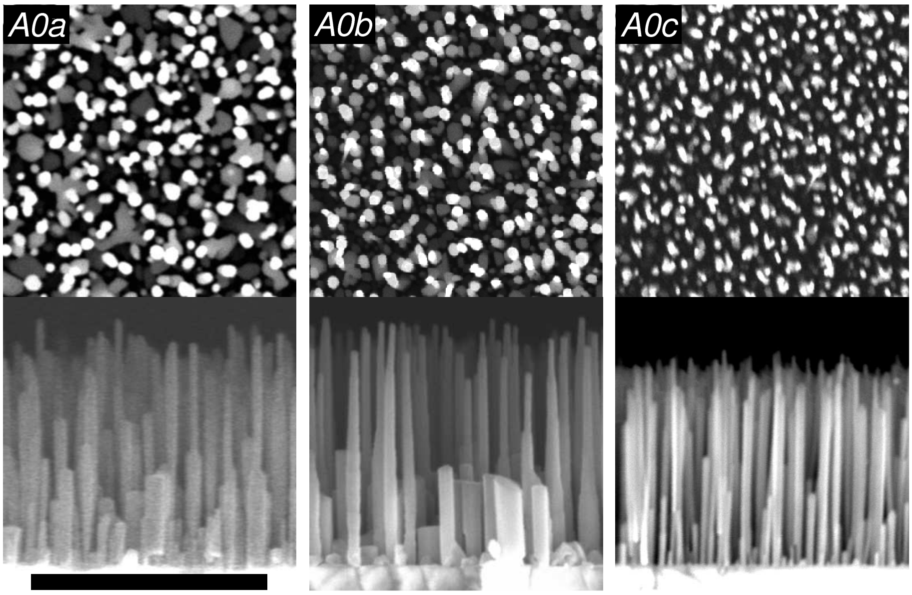

Figure 4.16: SEM images of samples *A0a*, *A0b* and *A0c* grown at 730, 755, and 780°C. Top and bottom rows correspond to plan and cross section views, respectively. Scale bar is 1μm.

Figure 4.17: TEM image of NW tips of sample *A0c*. The density of the SFs identified by the horizontal black striation is largely reduced compared to sample *A0a* in Figure 4.6.

730 to 755°C, the NW length remains almost constant [Figure 4.16(a) and (b)]. At 755°C, the NWs have a tapered shape with a tip thinner than their base. The diameter of the NW decreases along the length from 45 ± 10 nm at the NW base to 25 ± 10 nm at the tip. The shorter and thick columns observed for sample *A0a* at 730°C are for sample *A0b* grown at 755°C much thicker whereas for sample *A0c* grown at 780°C their growth is almost suppressed. Also, the NWs grown at 780°C have a more homogeneous length and are getting thinner with more uniform diameters of about 27 ± 10 nm, which is a strong indication for an increased diffusion length. However, at such high temperature, the NW length drops markedly by about 70 nm [Figure 4.16(c)] which is an effect of the enhanced Ga desorption. At 780°C the NWs density (2.5×10^{10} NWs/cm^2) is slightly increased compared to growth at 730°C. In addition, XTEM analysis on sample *A0c* still revealed the growth of WZ monocrystalline GaN NWs but with a crystal quality far superior since many fewer SFs were found along the NWs (compare Figure 4.17 with Figure 4.6).

Figure 4.18 presents the morphology of the catalyst-free NWs grown under the same

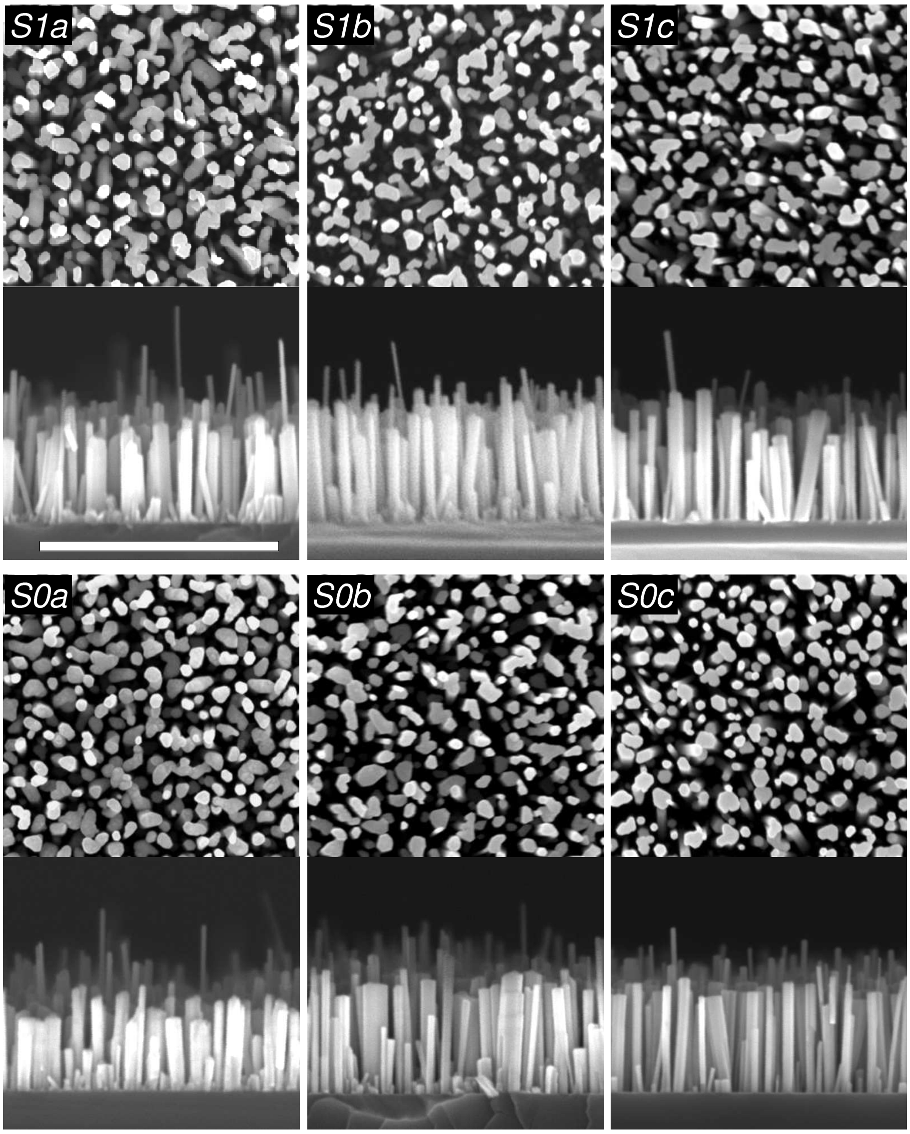

Figure 4.18: SEM images of the temperature set of samples grown catalyst-free on Si(111) and Si(001) at 730, 755, and 780°C (samples *S1a*, *S0a*, *S1b*, *S0b*, *S1c*, *S0c*, respectively). Top and bottom rows correspond to plan and cross section views, respectively. Scale bar is 1μm.

conditions on Si(001) and Si(111) (samples *S0a*, *S0b*, *S0c*, *S1a*, *S1b*, and *S1c*). The length of the NWs slightly increases with the growth temperature up to 755°C (samples *S0b* and *S1b*). Upon further temperature increase, the NWs grow in a more isolated way, the coalescence of the columnar base is strongly reduced and the NW density therefore increases to 1.8×10^{10} NWs/cm^2. A slight decrease of about 20 nm in NW length is also ascertained due to Ga desorption and GaN decomposition but also most probably to the much longer nucleation duration observed at 780°C (see 3.3.4. In this case the nucleation duration (3100 s $\approx$ 52 min) is not negligible anymore compared to the growth

duration (76 min). Thus at the highest temperature the effective growth duration following nucleation is reduced and the almost equivalent length obtained at different temperatures means that the NW growth proceeds actually faster.
Thus, higher temperature certainly also influences the NW growth, since it favors the adatoms diffusion, desorption and increases the GaN decomposition [134]. Moreover, it may improve the crystal quality of the catalyst-assisted NWs. However, in the framework of both approaches, no effect on the NW formation is observed for the range of temperatures investigated and the effects observed on the NW morphology, that are coalescence and tapering, are not as drastic as the changes observed upon the variation of the *V/III* ratio. Therefore the *V/III* ratio is considered the most important parameter for the growth of the NWs.

4.5 Optical properties

The direct and wide bandgap of GaN and its tunability by alloying with other III-metal nitrides are particularly attractive for optoelectronic applications. Associated with the NW one-dimensional geometry, material of improved crystal quality is expected and entails the opportunity of enhanced radiative efficiency and the potential for novel devices [9, 235]. However, the large NW aspect ratio might also be detrimental to the NW luminescence by an enhancement of the manifestation of surface defects [236, 237]. In addition, the observed strong difference in the nano-structural quality of the NWs supplied by the two approaches might affect their optical characteristics.
Therefore, characterization of the NW luminescence is of crucial interest to know how the material quality affects the optical characteristics of the NWs and whether there is any difference in this respect between the two pathways. In addition, earlier work showed that the luminescence collected from NWs grown on Si(111) in the catalyst-free approach [133, 136] was noticeably improved when the temperature of growth was raised. Thus, to verify if this result also holds for the NWs grown with the catalyst-assisted approach or with the catalyst-free approach on Si(001), LT-PL measurements (10 K) were performed (Figure 4.19) on the set of the as-grown NW samples under fixed Ga- and N-rates but different growth temperatures (conditions *a*, *b*, and *c* in Table 1).
In the following, the spectra of these NW samples are compared to transitions that have already been observed in GaN NWs [129, 133, 238–242], but also in compact layers [237, 243–245].
Three main near-gap transitions are characteristic for GaN NWs. The first one is the donor-bound-exciton (D^0,X_A) observed for strain-free GaN at 3.472 eV [239]. The second and third ones centered at about 3.42 eV and 3.45 eV are not usual for layers grown in the same MBE, suggesting that they are most likely not caused by impurities [246]. Therefore these transitions are most probably related to NW surface effect or to structural defects whose density in NWs would be higher than in planar layers, such as SF.
However, for the following reasons it is not possible to unambiguously identify the origin of the two low-energy transitions observed in those NWs. First, the transitions occurring in NWs at similar energy position than in GaN compact layers are difficult

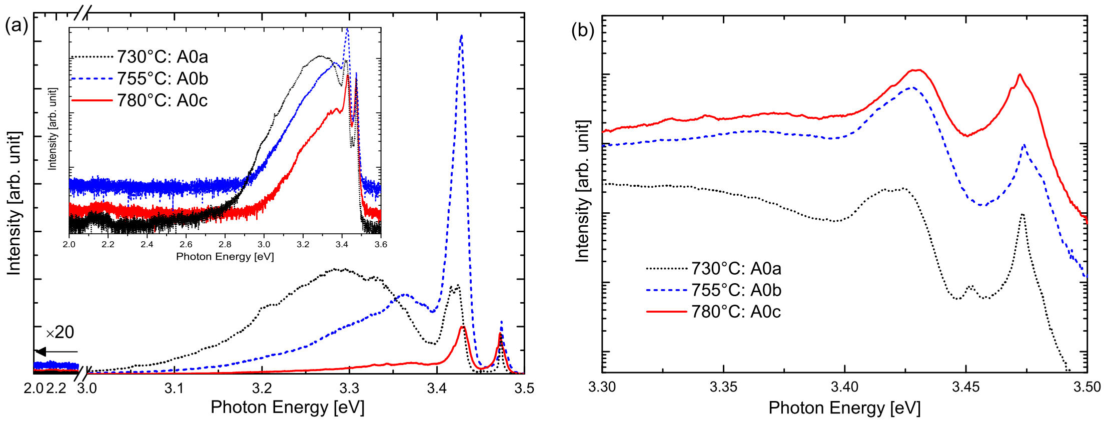

Figure 4.19: (a) Low temperature PL spectra of samples *A0a* (dots), *A0b* (dash) and *A0c* (solid) grown at 730, 755 and 780°C respectively. The inset is displayed in a semi-log scale in order to detect the presence of the yellow luminescence. (b) Detail for the near band edge of spectra (a) normalized to (D^0,X_A) (semi-log scale). Spectra are vertically shifted for clarity.

to identify due to broadening resulting from the sum of each NW contribution [246]. Second, the position and broadening of the transitions occurring at lower energy than the donor-bound-exciton (D^0,X_A) are not homogeneous through the samples. Third, the transitions in compact layers that have a common energy position with GaN NWs are unusual and their exact origin is also often questionable [237]. Nevertheless, in the following we will discuss the PL spectra of our NWs in conjunction with proposals from the literature.

4.5.1 Catalyst-assisted growth

The luminescence collected from samples *A0a*, *A0b*, and *A0c* grown at 730, 755 and 780°C, respectively, is presented in Figure 4.19. The first most striking feature is that none of these spectra is dominated by the (D^0,X_A) emission line, as it should be for good quality layers grown on sapphire [Figure 4.19(a)]. However, the (D^0,X_A) transition is clearly resolved at 3.473 ± 0.001 eV that corresponds to relaxed GaN [238, 239]. A blue-shift of this peak caused by the biaxial compressive strain resulting from the differences in thermal expansion coefficient and lattice mismatch between GaN and *C*-plane sapphire (13.8%) [247] could be expected. However, almost no effect of the growth temperature on the position of this transition is observed, which is attributed to an efficient stress accomodation enabled by the NW geometry [58, 238]. On the one hand, elastic strain can be relieved laterally at the free surface of the NW sidewalls [10]. On the other hand, dislocations may also form at the interface between the substrate and the NW or bend to the sidewalls at the bottom of the NWs [248]. In addition, it is surprising that very little change is observed for the intensity of the peak. Indeed, the NWs exhibit different morphologies as observed in section 4.4.2 and the change in dimension and density of the NWs suggests a different volume contribution. Moreover, the higher surface-to-volume ratio obtained for growth at higher temperatures should favor the manifestation of surface effects. However, several effects might compensate. For instance, at higher temperature, the volume contribution of the NWs is smaller but as ascertained by TEM, it is also of better quality than the more abundant one at lower temperature. Moreover, for samples *A0b* and *A0c* weak shoulders appear on the higher energy side of the (D^0,X_A) peak at about 3.481 eV and 3.485 eV that could be associated to free excitons and the smallest full width at half maximum of (D^0,X_A) (FWHM) is 3.4 meV obtained for sample *A0a* which does not present these shoulders.

Considering the lower energy side of (D^0,X_A) [Figure 4.19(b)], two groups composed of many lines are detected. The first group appears as a small peak for sample *A0a* between 3.451–3.453 eV. For the other samples this emission is not clearly resolved but a small bump around 3.458 eV is detected. In bulk material, lines at the same position (Y_1 lines) were attributed to excitons bound to inversion domain interfaces [237, 249] due to the inclusion of narrow Ga-polar domains in N-polar films. This interpretation could apply for instance for the bimodal morphology of GaN NWs grown on an AlN buffer layer on sapphire substrates that was observed by Cherns *et al.* [218]. They indeed reported that Ga-polar defect-free NWs were embedded in a N-polar lower highly defective layer. However, for the NWs samples considered here only one polarity was found and such a layer was not observed. Thus, the origin of this peak is still unclear.

The second group is detected between 3.41–3.43 eV. This emission dominates the spectra of samples *A0b*, *A0c*, and is very strong in sample *A0a*. On the one hand, for thin films, the Y_2 lines at similar position have been tentatively correlated to excitons bound to structural defects at the surface [237]. In addition, by cathodoluminescence (CL) measurement on *A*-plane GaN, Liu *et al.* [244] could relate peaks at 3.41, 3.33, and 3.29 eV to I_1 SFs, prismatic SFs, and partial dislocations, respectively. Interestingly, for our NW samples, the intensity of the emission entailed in the range of 3.41–3.43 eV compared to the one of the (D^0,X_A) first strongly increases when the growth temperature is raised from 730 to 755°C before decreasing for the highest growth temperature where it is the lowest. In agreement with this finding, TEM showed that the SF density is reduced in NWs grown at 780°C in comparison the ones grown at 730°C. Also, this emission is slightly shifted toward higher energy with the growth temperature.

On the other hand, CL measurement on catalyst-free NWs have correlated emission lines at 3.41–3.42 eV with structural defects at the NWs / substrate interface with a sample-dependent energy dispersion from 3.405 eV to 3.421 eV by PL and from 3.413 to 3.430 eV [129]. In addition, this emission was reported for catalyst-free NWs by other groups at 3.43 eV and is blue-shifted for increasing impurity concentration (Mg or Si) [241]. Hence, there appears to be a multitude of transition lines in the range 3.41–3.43 eV, and the pronounced broad peak at 3.43 eV for samples *A0b*, *A0c* may a priori have the same origin as the band at 3.41–3.42 eV for NWs grown on Si. Here the intensity of these lines is strongest for sample *A0b* which presents long NWs but also shorter and wider ones. For this sample, the density of defects formed at the interface to the substrate might thus be higher which could also account for an increased intensity of these lines. Therefore, the lines at 3.41–3.43 eV could be assigned to structural defects but their exact nature is at this point still unclear. At the same time, for sample *A0b* this broad peak extends to the energy of 3.437 eV for which a dominant emission was found in Ni-induced NWs grown by MOVPE [242]. The emission at 3.437 eV was tentatively attributed to neutral acceptor-bound excitons related to Ni contamination in those NWs that were free of SFs. Thus, the shift from 3.41–3.42 eV to 3.43 eV might be the result of structural defects and / or Ni contamination. However, it should be noted that we are not aware of any unambiguous identification of emission lines due to Ni in GaN and that SFs are known to be radiative defects. Therefore, it seems more reasonable to attribute the broad peak at 3.43 eV to structural defects.

The spectrum of sample *A0a* is very different from the ones of the two other samples grown at higher temperature in that it is dominated by a broad peak at 3.28–3.29 eV with a long tail toward lower energies and many shoulders. This broad peak is most probably assigned to the donor-acceptor-pair transition in WZ GaN (DAP) and to its replica. A broad shoulder at about 3.32–3.33 eV is found in the spectrum of all these samples. This defect transition could be an equivalent in planar films of the Y_6 lines. These lines have never been observed for films with flat surfaces and were attributed to a shallow DAP-type transition located on the GaN surface [237]. Sample *A0c* presents an additional line at 3.344 eV corresponding to the unusual Y_5 line in GaN films whose origin is unknown. For both samples *A0b* and *A0c* the intensity of this broad emission decreases relatively to the one of (D^0,X_A) and its position is shifted toward higher energy at 3.362 and 3.370 eV, respectively. These lines could be correlated to the Y_3 and Y_4 transition in GaN films, that have been tentatively attributed to excitons bound to structural defects [237].

The yellow luminescence (YL) band, located in GaN films at 2.2–2.3 eV, has been attributed to a transition from a shallow donor, O or Si, to a deep acceptor, presumably the Ga vacancies (V_{Ga}) [237]. For the samples grown at 755 and 780°C, this band is absent, while for the sample grown at 730°C a faint and 100 meV wide bump at 2.17 eV is found with an intensity more than two orders of magnitude smaller than the one of the (D^0,X_A) transition as seen in the inset of Figure 4.19(a). This is an indication for a very low density of the related point defects, for instance V_{Ga} [237, 243]. A similar result was already ascertained from PL on GaN needles in the early 1980's [243]. Recently Brandt *et al* suggested that these point defects may diffuse or segregate to the NW surface and annihilate during growth yielding an inherently superior optoelectronic quality compared to GaN films [246]. The absence of the YL in samples *A0b* and *A0c* attests to the improvement of the material quality when the growth temperature is raised. This result was already obtained for catalyst-free grown NWs [133]. Thus, for the catalyst-assisted grown NWs, the same conclusion can be drawn.

Note that for sample *A0a*, the position of the bump is slightly shifted toward lower energies and thinner than what has been observed for YL in bulk GaN. This might also be an effect of Ni incorporation into GaN. Pankove et Hutchby [245] have reported that GaN implanted with Ni exhibited at 78 K a band located at 2.05 eV but with an intensity 3 times larger than the YL of undoped GaN.

Thus the spectra of the catalyst-assisted NWs indicate numerous defect peaks that could be correlated with defect luminescence lines of GaN films. The increase of the growth temperature leads to the decrease of the intensity of these emissions, indicating an improvement in the quality of the NWs grown at higher temperature, similarly to

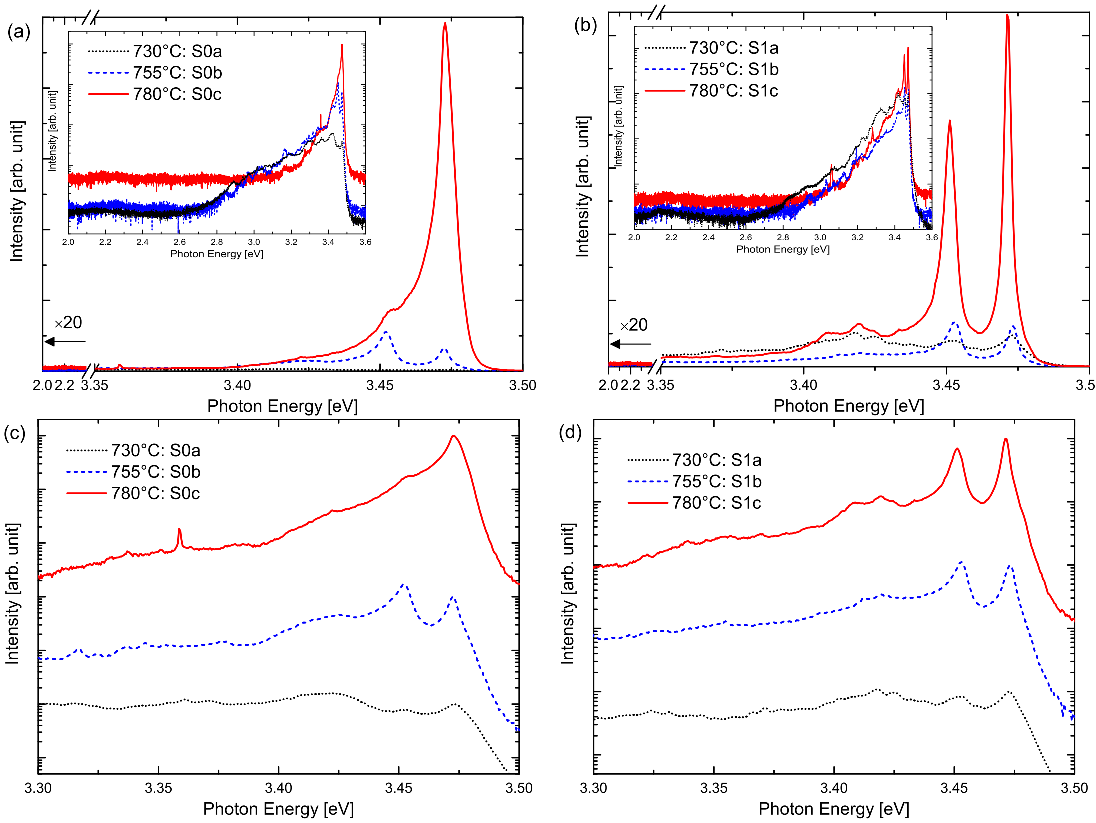

Figure 4.20: (a) and (b) LT-PL spectra of GaN NWs grown on Si(001)(samples *S0a*, *S0b*, *S0c*) and Si(111) (samples *S1a*, *S1b*, *S1c*) respectively. The same spectra in semi-log scale are presented in the insets in order to detect the presence of the yellow luminescence. (c) and (d) Detail of the near band edge of the spectra normalized to (D^0,X_A) (a) and (b) respectively (semi log scale), spectra are vertically shifted for clarity.

the result observed for the catalyst-free growth on Si(111).

4.5.2 Catalyst-free growth

Figure 4.20 presents the low temperature (10 K) PL spectra collected from samples *S0a*, *S0b*, *S0c* and *S1a*, *S1b* and *S1c*. Again, the spectra of all these samples reveal a clear emission line at 3.472 eV related to the donor bound exciton transition (D^0,X_A), characteristic for strain-free GaN despite the large lattice mismatch with the Si substrate (-17 %). With increasing growth temperature, the intensity of this peak increases while its FWHM decreases. For samples *S0c* and *S1c* this peak even dominates the spectra and the narrowest FWHM is obtained for sample *S1c* and amounts to 3.1 meV.

The emission at 3.45 eV is also detected for all of these samples. Its intensity relative to the (D^0,X_A) first increases when the temperature is raised to 755°C (samples *S0b* and *S1b*) whereas at 780°C it decreases (sample *S0c* and *S1c*). However in the case of growth on Si(111) the intensity of this peak remains very strong compared to the

(D^0,X_A) one even for sample *S1c*. This emission was studied in detail by Calleja *et al.* [129] who found it to be dependent on the NW surface to volume ratio whatever substrate used, *C*-plane Sapphire or Si(111). They assigned it to the doublet emission related to Ga_I point defects but under the assumption of a Ga-balling growth model which was later withdrawn. Recently, Furtmayr *et al.* [241] suggested that V_{Ga} at the NW sidewalls caused by the N-rich growth conditions could induce this emission, the intensity of which is quenched with the NWs coalescence. However, in the case of growth on Si(001), under the same *V/III* ratio and with nearly the same density of the NWs and degree of coalescence as on Si(111) (see Figure 4.18), the intensity of this line is significantly reduced. Therefore, its origin remains unclear.

The emission lines centered in the range of 3.41–3.425 eV are weaker in comparison to the (D^0,X_A) line for the samples grown above 755°C (*S0b*, *S0c*, *S1b*, and *S1c*) but not for the ones grown at 730°C (*S0a*, *S0a*) for which they dominate the spectrum. Hence, this evidences a decrease of the density of the structural defects associated to this line with an increase of the temperature for both types of substrates Si(001) and Si(111).

In addition, for all of these samples the DAP is not clearly resolved and many transitions are possible in the range of 3.26–3.29 eV. However, the luminescence intensity within this range is very low compared to the (D^0,X_A) transition [see Figure 4.20(a)]. Note that lines at 3.27 eV and at 3.16 eV have been assigned to an exciton bound to a shallow donor in ZB GaN and to the shallow DAP in ZB GaN, respectively. The presence of these lines could indicate the formation of ZB GaN but it is difficult to resolve them from the DAP in WZ GaN and its wide tail toward lower energies. At 730°C a wide shoulder appears at 3.30–3.32 eV for NWs grown on substrates of both orientation, which could be correspond to the Y_6 lines in GaN films. When the growth temperature is increased this shoulder is not detected anymore. Instead, a shoulder at 3.34–3.37 eV already present for the lower temperature samples is detected. This shoulder could be an equivalent to the Y_3, Y_4, Y_5 lines in GaN films.

Again, none of the samples exhibits yellow band lines for growth above 755°C, while for the sample grown at 730°C a faint and 230 meV wide bump at 2.19 eV is found with an intensity also more than two orders of magnitude smaller than the one of the (D^0,X_A) transition as seen in the inset of Figure 4.20(b).

Thus slight differences are observed in the spectra of the catalyst-free NWs grown on Si substrate of both orientations, but the main result is that in both cases, an improvement of the luminescence is also ascertained when the growth temperature is raised.

4.6 Discussion: Comparison of both approaches

The properties of the NWs obtained either by the catalyst-assisted or by the catalyst-free approach are in many respects very similar. The three aspects that are markedly different and that require an extensive discussion are the occurrence of SFs, the underlying growth mechanism, and the optical properties.

4.6.1 Crystal Quality

Like the bulk material, the NW material has a WZ structure and the growth axis coincides with the [0001] direction whatever the chosen growth approach. However, the crystal quality depends on the growth approach. The catalyst-assisted NWs contain a large number of SFs formed randomly along the NW axis. In contrast, the GaN NWs grown by the catalyst-free approach on Si are almost defect-free as previously reported by other groups [134, 181].

The SF density in the catalyst-assisted NWs is anomalously high even compared to planar films, where the SFs only occur close to the substrate-GaN interface [250, 251]. Thus, the SF formation in the NWs seems to have a different origin. A basal plane SF is a ZB inclusion of minimal size in a WZ host crystal, so it is important to consider under what conditions cubic GaN forms. GaN usually adopts the stable WZ phase but the rather low difference [252] in formation energy of the WZ and ZB phases is believed to ease polytypic growth. The preferential nucleation of the metastable ZB (111) phase on the WZ (0001) one usually occurs for growth conditions of excess Ga and low temperature [253, 254]. Also, the ZB phase can be obtained by epitaxial growth on cubic substrates [183]. Last, impurities or dopants are another factor that affects the formation of planar defects such as stacking faults and can induce a transition to ZB [255–258]. For instance, a HRTEM study showed that increasing Si doping of GaN generates a higher density of basal plane stacking faults in wurtzite GaN [258]. Moreover, if the impurity behaves as a surfactant and tends to diffuse away from the doped layer into the growth front, the crystal structure can changed to ZB for a continuous impurity supply exceeding a critical concentration [255, 256, 259, 260].

The presence of SFs in GaN NWs has been mainly reported for catalyst-induced growth by MOCVD, chemical vapor transport (CVT) and hydride vapor phase epitaxy (HVPE) [261–264]. Nevertheless mixed ZB and WZ phases also appear in NWs grown without any catalyst in a tube furnace [265]. For the catalyst-free growth of GaN NWs by MBE SFs are usually observed in the shorter columnar base between the NWs [138, 141, 218], and as for bulk material, SFs can be induced by Mg-doping [137]. SFs randomly distributed along the NWs have also been reported by Araki *et al.* for NWs grown by hydrogen-assisted electron-cyclotron resonance MBE [266]. Last, the appearance of the ZB phase in WZ GaN NWs obtained by cooling below 260 K was related to short range ordering and shown to be reversible [267].

As explained above, the occurrence of SFs is typical for catalyst-induced GaN NWs and not limited to our choice of growth technique and growth parameters. Also, it is clear that the presence of a catalyst can completely reverse the NW crystal structure from ZB to WZ, so an increased tendency for SF formation in WZ material is not surprising. Taking all of the above studies into consideration, the following factors are most relevant for our case. First, the catalyst material may affect the crystal structure of the NW material. The study of the nucleation by RHEED in chapter 3 and the characterization of the NW tip by element-resolved TEM [144] show that the catalyst is actually solid and a cubic Ni-Ga alloy. Thus, the binding configuration of the GaN nucleus at the NW-catalyst interface might adopt the ZB configuration because it enables a more favorable bond

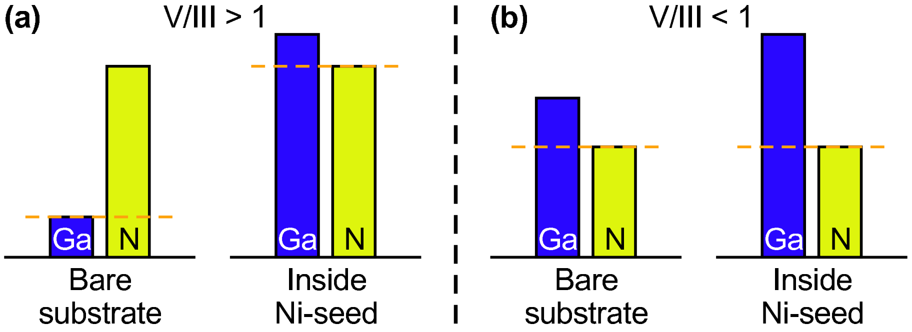

Figure 4.21: Growth model for (a) greater N-rate than Ga-rate and (b) greater Ga-rate [19]. The lengths of the bars correspond to the locally available amounts of Ga and N. Ga accumulates inside the Ni-seeds. The horizontal dashed lines indicate the local growth rates of GaN. The higher growth rate inside the Ni-seeds that is necessary for NW-formation and preferential axial growth occurs only for *V/III*>1.

orientation between the Ga-top layer and the cubic GaNi. This would be similar to the use of P as a surfactant that mediates cubic nucleation of GaN films [255]. As suggested by the PL analysis, Ni may also be incorporated to some extent, reduce the SF energy and stabilize the ZB phase as it has been concluded for Si or Mg doping [257]. Second, the catalyst introduces a triple phase line GaN-GaNi-vapor, and this may play a similar role as described by Glas et al. [123], leading to the opposite result of ZB nucleation for a WZ material. Third, the catalyst is known to drastically change the local *V/III* ratio to Ga-rich conditions [19], and this is one of the prerequisites for growth of cubic GaN. However, it should be noted that our growth temperature is significantly higher than what is the other prerequisite for growth of cubic GaN.

4.6.2 Growth mechanism

Since the VLS mechanism was proposed in 1964 by Wagner and Ellis [60] to account for the formation of Si whiskers with gold particles, the growth of NWs promoted by metal particles has been extensively investigated and similar mechanisms, like the VSS one [75, 76], have been evidenced. In any case, the influence of such mechanisms on the NW characteristics, if not always straightforward, is fairly well understood. In contrast, the mechanisms causing the catalyst-free growth of NWs are still under intensive discussion. A complete model should explain where NWs nucleate, what determines their diameter, and why axial growth is much faster than radial growth. The first two questions relate to nucleation which we already studied in chapter 3, so in the following we will focus on the third one.

Catalyst-assisted NW growth

As mentioned in chapter 3, it has been concluded from ex-situ studies that in case of *V/III* NW growth almost solely group III-species incorporate into the catalyst particles [19, 76, 113]. In addition, it has also been shown that the growth rate of the NWs in this case corresponds to the supplied rate of group V [19, 100, 167]. Last, several results have established that growth occurs at the triple phase line [74, 123, 268].

In the case of our GaN NWs, the NW growth rate dependence on the Ga and N rates can thus entirely be explained in the framework of the VLS or VSS mechanism, as a direct consequence of the nucleation processes. In chapter 3 the accumulation of Ga into the Ni seeds has been ascertained by in-situ monitoring that has evidenced the Ni-Ga composition of the catalyst-particles during the nucleation. Hence, this result strongly suggests that along further growth, the Ni particles still act as an efficient collector for Ga atoms impinging on their surface or diffusing on the substrate and along the forming NW side-facets. On the contrary they filter as efficiently the N atoms that do not accumulate into it as confirmed by ex-situ EELS investigation [144]. In turn local excess of Ga forms under the seed and as expected for such conditions, the growth rate of GaN is imposed by the N-rate as proposed in ref. [19] and sketched in Figure 4.21(a). Hence, the higher the N-excess, the larger is the difference between the enhanced growth rate at the NW tip and the Ga-limited growth rate between the NWs. Therefore, below the Ni seeds GaN grows faster than between the NWs.

However, if the supplied amount of Ga is too low to assure the locally Ga-rich conditions inside the seed, the NW growth is strongly impeded. In this case, the Ga incorporation into Ni is limited by the low Ga-rate supplied. In turn, the amount required to nucleate the NiGa phase which precedes GaN nucleation under the catalyst could not be collected before the nucleation starts outside the particles as observed on the SEM images in Figure 4.14(f). On the other hand, when the supplied amount of Ga is increased such that the global *V/III* ratio is decreased but still higher than unity, the NW growth rate remains unchanged because still imposed by N, but the growth rate of the surface between the NWs is enhanced. In the extreme case where the global *V/III* ratio is lower than unity [Figure 4.21(b)] no NW forms although Ga still accumulates inside the Ni seeds, because the Ga-rich conditions are now established inside and between the seeds, and the growth rate is then limited by the N-rate over the whole substrate surface. Thus the role of the Ni seeds is to maintain the inhomogeneity in the Ga distribution in order to locally reverse the *V/III* ratio in favor of group III during both nucleation and further growth of the NWs.

Catalyst-free NW growth

As seen at the beginning of this chapter, several arguments could explain the growth rate differences observed for each type of facet, polar and non-polar, and this would explain why all the NWs have the Ga polarity. The diagram in Figure 4.22(a) recalls the different occurring mechanisms. Different facets, polar and non polar, present different diffusivity (J_d), impinging (J_i), incorporation (J_I) and desorption rates (J_D) and this for each growth species Ga or N, leading to different growth rate and stability for each facet type.

The growth model proposed by Bertness *et al.*, Ristić *et al.*, and Stoica *et al.* [22, 26, 27] is at some point very similar to the one developed much earlier by Schwoebel [99] to account for locally enhanced growth perpendicular to the substrate surface. As already mentioned in chapter 2 this model predicts the growth of a "filamentary crystal" with atomically flat side walls assuming different adatom mobilities on top and side-facets and different capture rates at steps. Recently, an experimental study of GaN island nucleation on GaN(0001) in MBE [102] yielded indeed that for N-rich conditions adatoms incorporate mostly at the step edges from the upper terrace while hopping to the lower one is hindered by the ES barrier. Additionally this study showed that the ES barrier could be inverted for an excess of Ga that passivates steps of one or two monolayers, depending on the supplied excess of Ga. This result is in agreement with the observation that the *V/III* ratio is the most important parameter for the successful growth of GaN NWs.

Moreover, the recent first principles calculations of the surface thermodynamics and adatom kinetics further support this model [220]. On the one hand, it underlines that stoichiometric non-polar GaN surfaces are unstable against atomic N, while N-rich surface configurations are thermodynamically highly unfavorable. On the other hand, it points out the strong contrast with *C*-plane surfaces on which N adatoms can be thermodynamically or kinetically stabilized under extreme N-excess [101]. Therefore, a higher Ga adatom incorporation is expected to occur on the NW *C*-plane top surface than on the *M*-plane sidefacets under N-excess.

Lastly, Wacaser et al [74] suggested equivalently that the difference in edge and surface free energies of different planes induces a difference in Gibbs free energies and nucleation probabilities. Therefore they suggested a unidirectional growth mechanism based on preferential interface nucleation.

The experimental data presented in section 4.4.1 provide supportive information on the existing growth models [22, 23, 26, 27, 220]. First, the NW growth rate is higher than the Ga-rate impinging at the NW tip. This confirms that the diffusion of Ga atoms along the NW sidewalls is an important contribution to the amount of Ga that is available for incorporation at the NW tip. Second, there is a quantitative agreement between the data for growth on Si(001) and Si(111). This suggests that the phenomena causing preferential growth along the *C*-axis are related to GaN itself [220] and to the growth geometry [28]. However, these phenomena are independent of the substrate and nucleation processes, as it is the case for different diffusion and incorporation rates on polar and non-polar GaN facets, respectively. These effects responsible for the catalyst-free growth of NWs must hold for the catalyst-induced approach as well, since in both cases all structural properties relevant for diffusion and incorporation (i.e. crystal orientation and polarity) are identical. Hence, a simplified way to compare the two approaches of NW fabrication is to consider the catalyst-assisted growth as an extreme case where all the Ga arriving at the NW tip accumulates there inside the seed particle while for the catalyst-free approach some of the arriving Ga may also diffuse away. Therefore, the growth rate of the catalyst-induced NWs is given by the amount of impinging N while the growth rate of catalyst-free NWs is essentially determined by the ratio between the incorporation rates on the two types of facets. In other words, for the catalyst-induced case, N is the species in minority at the NW tip while it is Ga for the catalyst-free case as sketched in Figure 4.22(b). This figure compares the Ga and N rates that are supplied by the source (dark bars) and locally available (lighter bars) on the NW tip. For the

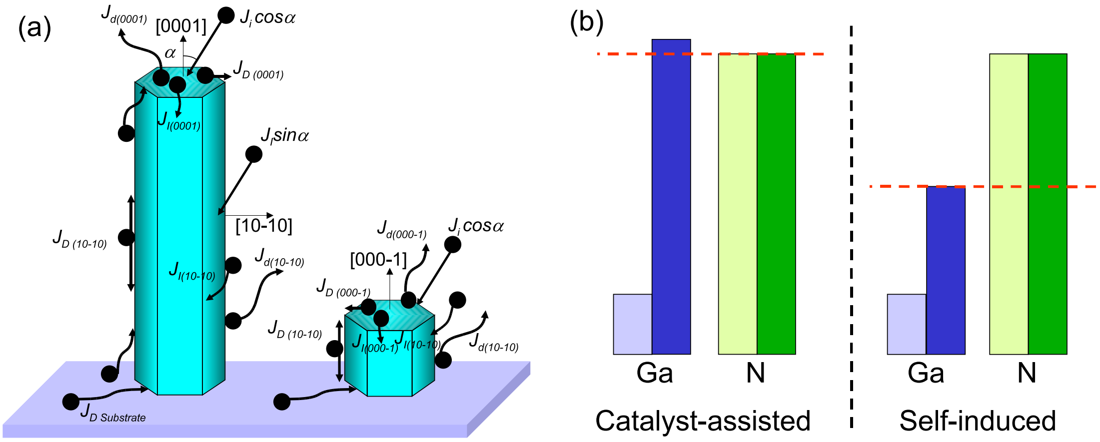

Figure 4.22: (a) Schematic of the different mechanisms occurring on the different facet planes. Different facet planes, polar and non polar, present different diffusivity (J_D), impinging (J_i), incorporation (J_I) and desorption rates (J_d) and this for each growth species Ga or N, leading to different growth rate and stability for each facet type. The incorporation rates for each facet depend on the sticking coefficient of each species on the different facet planes, but also on their arriving rates that are not equivalent for top or lateral exposition [28]. (b) Schematic comparison of the incorporation rate on the top *C*-plane facet in both approaches. The heights of the dark bars correspond to locally available amounts of Ga and N while the height of the lighter bars corresponds to the amounts of Ga and N supplied by the sources for a *V/III* ratio of 5. The horizontal dashed lines indicate the local growth rate of GaN. See text for explanation.

self-induced approach the incorporated amount of Ga on the (0001) planes is smaller than for the catalyst-assisted approach due to possible diffusion away or desorption. However, Ga incorporation is still higher than the supplied Ga rate due to the adatom diffusion along the NW side-facets. In contrast, $(10\bar{1}0)$ facet growth is strongly inhibited in both approaches. This is a consequence of the much lower Ga and N adatom amount arriving from the sources [28] and also of the smaller Ga adatom incorporation rate [220] on these facets. Indeed, considering only the lower adatom impinging rate from sources oriented at an angle of 30° to the substrate normal, it has been calculated that the axial growth should occur 5.4 time faster than the radial one [28]. However, for both the catalyst-assisted and the catalyst-free approach the radial growth rate amounts to 1 % and 3%, respectively, of the axial one [19, 23, 24]. Also, the side facets of the catalyst-free NWs are atomically flat supporting the results of Lymperakis *et al.* which indicate the suppression of the lateral growth of the NWs [220]. Therefore, the adatom incorporation rates on the different facet planes play probably the most important role in NW growth.

4.6.3 Optical properties

As concluded in section 4.5 the luminescence collected from NWs grown in the catalyst-assisted and catalyst-free approaches is noticeably improved when the growth temperature is raised. Thus, the samples grown at 780°C under the same *V/III* ratio that pre-

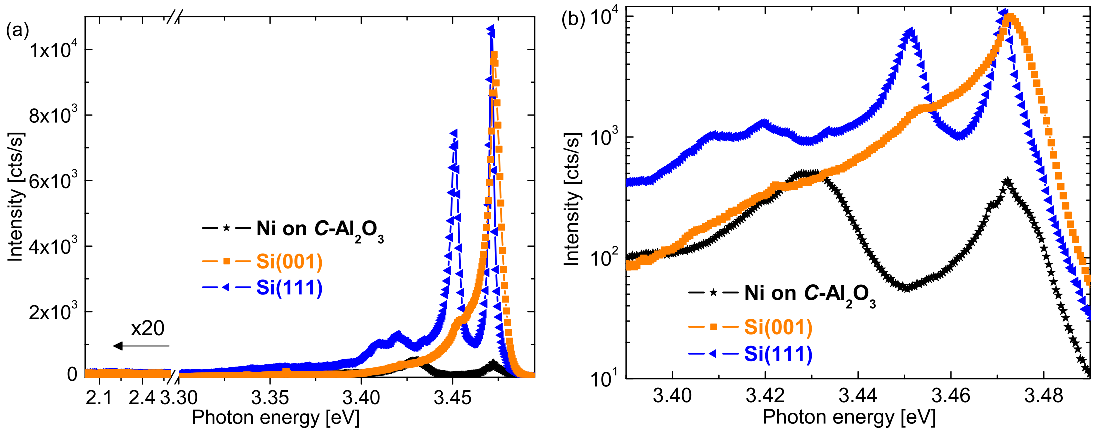

Figure 4.23: (a) LT-PL spectra of GaN NWs grown at 780°C on sapphire, Si(001), and Si(111) (samples *A0c*, *S0c*, *S1c*, respectively). (b) Detail for the near band edge of spectra (semi-log scale).

sented the best PL were compared. Figure 4.23 presents the low temperature (10K) PL spectra collected from these samples (samples *A0c*, *S0c*, and *S1c*). Essentially, there is a strong difference in the luminescence intensity of the NWs. The catalyst-free approach yields NWs with a strong (D^0,X_A) luminescence that is about 25 times more intense than the one of the catalyst-induced NWs and the sharpest peak is obtained for the NWs grown on Si(111) [Figure 4.23(a)].

The emission at around 3.45 eV appears with different intensities relative to the (D^0,X_A) in all of the samples. This line has been tentatively attributed to various structural features [129, 241] but none of the assignments reported in the literature explains our results and we cannot conclude further on the origin of this line. However, it should be noted that point defects related to Ga$_I$ as proposed by Calleja *et al* [129] appear unlikely as an origin of this line. Indeed, for the catalyst-assisted NWs, growth has been shown to actually occur under locally Ga-rich conditions. However, for the corresponding sample *A0a* this line is unresolved from the (D^0,X_A) transition and much weaker than in the case of growth on Si(001) and on Si(111) where such a defect might be less probable to appear.

In addition, the emission lines corresponding to the Y_2 defect-luminescence in GaN films are detected at 3.43 eV for the catalyst-induced NWs (sample *A0c*), while the catalyst-free NWs exhibit emission features centered at 3.41–3.42 eV [Figure 4.23(b)]. However, there appears to be a multitude of transition lines in the range 3.41–3.43 eV, and the pronounced broad peak at 3.43 eV for NWs grown on sapphire (sample *A0c*) may a priori as seen in section 4.5 have the same origin as the band at 3.41–3.42 eV for NWs grown on Si. The main difference in the crystal quality between the two approaches is the occurrence of SFs. Additionally, the emission of this peak is much stronger compared to the (D^0,X_A) transition for the catalyst-induced than for the catalyst-free NWs. Therefore, the peak at 3.43 eV for the catalyst-induced NWs could still be attributed to these SFs that are basically absent in the case of catalyst-free growth.

As already observed in section 4.5, none of the samples exhibits the yellow band which is an indication for a very low density of the related point defects for both the catalyst-assisted and catalyst-free pathways.
A quantitative comparison of PL intensities is difficult, but the difference between the catalyst-free and catalyst-induced NWs is so large that it must be a real effect. The morphologies of the samples are similar, so differences in light extraction efficiencies do not suffice as an explanation. As discussed above, the structural difference, i.e. the occurrence of SFs in catalyst-induced NWs, may explain additional emission lines but not the reduced PL intensity. Thus, there must be a non-radiative recombination center that is present only in the catalyst-induced NWs, and the most plausible explanation is Ni contamination from the catalyst-seeds. Indeed, in ref. [245] it was also noted that the intensity of the (D^0,X_A) transition of a Ni implanted GaN layer was only 15 % of the one of the undoped reference sample. However, no TEM investigation of these samples were carried out and structural defects induced by ion implantation might also have resulted. It should be noted here that the direct identification of contamination in nanostructures is a tremendous experimental challenge [85, 87, 269]. EDX of $Al_{0.2}Ga_{0.8}N$ catalyst-induced NWs grown through the same mechanism and under the same conditions as for GaN NWs in this work, showed Ni K-alpha line intensities at background level in the NW body [270]. However, the sensitivity of PL experiments is much higher. Therefore, although no direct evidence for contamination due to the catalyst seeds can be made, this optical investigation strongly suggests it.

4.7 Summary

GaN NWs were grown by the catalyst-induced and by the catalyst-free approaches under identical conditions except for the choice of substrate. Many properties of the resulting NWs are very similar. In both approaches the GaN NWs have the WZ structure and grow along the Ga-polar (0001) direction. The three major differences are that first, the catalyst-induced NWs contain a high density of basal-plane SFs. Second, vertical growth by the catalyst-induced approach proceeds faster. Third, the self-induced approach yields GaN NWs with stronger and sharper photoluminescence. All of these observations can be explained as effect of the catalyst Ni seeds. Several mechanisms are proposed by which the Ni seeds may induce the high density of SFs in the catalyst-assisted NWs. The difference in length between the catalyst-assisted and catalyst-free NWs is closely related to different dependencies of the NW growth rate on the supplied amounts of Ga and N. Thus, there must be differences in the processes underlying NW growth. The catalyst-assisted NWs grow at a rate that equals the amount of nitrogen impinging at the tip, because in the framework of the VLS mechanism Ga atoms diffuse on the NW sidewalls and are preferentially incorporated into the Ni seeds. In turn, this gives rise to locally Ga-rich condition at the NW tip. For the catalyst-free NWs, the growth rate is, independently of the substrate orientation Si(111) or Si(001), higher than the Ga-rate, but only the very longest NWs reach the limit imposed by the amount of impinging nitrogen. The former observation implies that the preferential growth along the *C*-direction must be inherent to GaN itself and can be explained by differences in diffusion and incorporation rates on the different types of facets. The growth experiments suggest that the Ni seeds capture essentially all of the Ga atoms diffusing to the NW tips while the axial growth rate of the catalyst-free NWs is determined by the ratio of the incorporation rates on the top and sidewall GaN facets. Lastly, the direct comparison of growth routines in the same MBE chamber under identical conditions strongly suggests that Ni contamination is the cause for the significantly reduced PL intensity of the catalyst-induced NWs. The use of catalyst seeds may offer an additional way to control the growth of NWs, but both the structural and the optical material quality of catalyst-free NWs is superior.

5 Conclusion and Outlook

5.1 Conclusion

The purpose of this work was to provide deeper comprehension of the growth mechanisms of GaN NWs, as well as of the interrelation between their structural and physical properties. GaN NWs are generally grown by MBE without the use of any external catalyst seed. However, the approach most frequently used to fabricate NWs is the VLS mechanism. This approach can also be applied in MBE since GaN NWs do not form on bare sapphire, but are promoted by Ni islands deposited on sapphire. Thus, the catalyst-induced and the catalyst-free NWs can be grown under identical conditions just by choosing either sapphire or silicon as the substrate. Both approaches have been investigated and compared in this thesis.

To gain understanding on the NW nucleation in the framework of both approaches, in-situ studies by RHEED in correlation with QMS have been carried out. For the catalyst-assisted approach, three nucleation stages could be identified: first, the incorporation of Ga into the Ni seeds, second, a transformation of the seed crystal structure, and lastly GaN growth. Thus, the main understanding is that only Ga incorporates into the Ni particles, which is ascertained by the identification of Ni-Ga structures formed during the nucleation upon Ga accumulation but before GaN starts to grow. This result is in agreement with the Ni-Ga-N ternary phase diagram and it is also consistent with observations for other materials systems, for instance Au-Ga-As [113] or Au-Ga-Sb [167]. RHEED monitoring of the nucleation ascertained that the seed particles are in the solid state, therefore the mechanism ruling the nucleation of these NWs at 730°C is most probably the VSS one. The QMS study showed that GaN nucleation is the rate limiting process. Last, the incorporated amount of Ga is nearly independent of the Ga-rate at constant substrate temperature and N-rate, whereas it is enhanced by the substrate temperature at constant nominal Ga- and N-rates.

For the self-induced NWs, a strong similarity in the nucleation processes on Si(001) and Si(111) was ascertained by QMS and RHEED. Two nucleation stages could be identified. During the first stage, there is a competition between the nucleation of crystalline Si_yN_y and GaN. The Si surface strongly roughens by the formation of pits and Si mounds. At the same time, very few GaN islands nucleate either on the Si mounds or possibly also inside the pits. There are indications that some of the GaN islands may nucleate in the ZB structure. During the second stage, the amorphization of the Si_xN_y layer leads to the massive nucleation of GaN islands that are free of the substrate epitaxial constraint and therefore form in the WZ structure. Since no ZB NWs are observed for longer growth duration, it is suggested that most probably the few metastable ZB nuclei that could have formed during the first nucleation stage dissolve away.

In any case, the processes leading to the NW nucleation are fundamentally different for both approaches. In the catalyst-assisted approach, Ga strongly reacts with the catalyst particles, whereas in the catalyst-free approach, N forms an interfacial layer with Si before the intense nucleation of GaN starts. In the former approach, the crystal structure and phases of the seed particles are decisive, while in the latter the lattice-mismatch to the substrate plays the most important role. QMS monitoring enables the comparison of the GaN nucleation rates for both approaches. At high growth temperature, it reveals the faster and larger Ga incorporation in the framework of the catalyst-assisted approach.

Both approaches are viable to produce NWs within the same range of substrate temperatures and *V/III* ratios, and the latter must be larger than one (N-excess). Both yield monocrystalline GaN NWs of WZ structure, which grow in the Ga-polar direction. However, strong differences are observed. First, the catalyst-assisted NWs are longer than the catalyst-free ones after growth under identical conditions of duration, substrate temperature and *V/III* ratio. The catalyst-assisted NWs grow at the rate of the supplied N. This result is in perfect agreement with the nucleation described above and attributed to the Ga-excess established at the Ni-particle location. In contrast, the self-induced NWs grow with an intermediate rate between the supplied Ga and N-rates. Second, the catalyst-assisted approach provides GaN NWs that contain many stacking faults, while the catalyst-free ones are largely free of defects. Third, the PL of the catalyst-free NWs is narrower and much more intense than the one of the catalyst-assisted NWs. All of these differences are explained as effects of the catalyst. The seed captures Ga atoms arriving at the NW tip more efficiently than the bare top facet in the catalyst-free case. In addition, both the presence of the additional solid phase constituted by the catalyst-particles and contamination of the NWs by the catalyst material may induce stacking faults. Finally, contamination by the catalyst material is the most likely cause for the reduced PL intensity, suggesting non-radiative recombination centers due to Ni contamination. Thus, the most suitable approach for promising novel III-N devices is the catalyst-free one.

5.2 Outlook

As explained in chapter 3, in-situ studies are essential to develop an elaborate understanding of NW nucleation and growth, and the present work shows that QMS in combination with RHEED can provide valuable information in order to elucidate the NW nucleation mechanisms. Distinct nucleation stages were identified both for the catalyst-induced and catalyst-free approach, thus enabling a new level of comprehension. In order to deepen this understanding, the investigation of the nucleation in dependence of the growth parameters is the next step. Indeed, GaN NWs in the self-induced approach are usually grown at high temperature in the range of 780–800°C because of the improvement of their crystal structure and optical properties. However, in this case the nucleation duration is much longer and not so many experiments could have been carried out in the framework of this thesis. Thus, for both the catalyst-assisted and catalyst-free approaches, the study of the influence of the Ga- and N-rate and temperature on the nucleation should be investigated by RHEED, QMS, AFM and TEM as comprehensively as done for the set of samples grown at 730°C.

In addition, HRTEM and EELS investigation on samples grown for short duration at higher temperature should also be performed. For the catalyst-assisted approach such measurement could further confirm the different Ni-Ga phase sequence appearance proposed in section 3.2. For the self-induced approach on both Si(001) and Si(111), they could help to identify the exact nature of the Si_xN_y layer formed before GaN nucleation. Moreover, the morphology of this layer should be compared to the diameter, orientation and location of the NWs forming on it.

In the present work, the optical properties of the NWs have been investigated on ensembles. The broadening of the different transitions related to the contribution of each NW prevents the unambiguous identification of the origin of the transitions at 3.42 and 3.45 eV characteristic to GaN NWs. This impediment could be overcome by the direct comparison of the crystal defects with the optical properties by PL and TEM characterization on the same single NW. Such studies have already been conducted on InP NWs and brought deep understanding on the radiative recombinations related to structural defects [271].

Finally, the investigations that have been carried out in this work provide only a modest part of the knowledge necessary to integrate NWs in functional devices. Therefore, the extension of the above studies to the whole III-N system as well as to doping processes is required to move toward photovoltaic and lighting applications covering the whole UV–IR range.

Appendix A

Radio Corporation of America (RCA) cleaning procedure

These cleaning solutions are based on Hydrogen Peroxide and were developed in 1970 for Silicon Semiconductor Technology [111].

1. Cleaning of the tools (quartz vessel, wafer holder, tweezers...)
   $NH_4OH/H_2O_2/H_2O$ 1:1:5 (solution RCA1) at 70–80°C for 10 min
2. Cleaning of the wafers with the RCA1 solution with agitation
   $NH_4OH/H_2O_2/H_2O$ 1:1:5 at 70–80°C for 10 min
3. Cleaning with overflowing high purity water for 10 min
4. Etching of the wafers by a few second dip in hydrofluoric acid (50% VLSI standard) in a Teflon bowl HF/H_2O 1:9
5. Overflow rinsing with high purity water
6. Cleaning of the wafers with the RCA2 solution with agitation
   $HCl/H_2O_2/H_2O$ 1:1:8 at 70–80°C for 10 min
7. Cleaning with overflowing high purity water for 10 min
8. Drying of the hydrophilic surface by nitrogen blowing and loading in MBE
9. Oxide desorption at 950°C for 15 min

The NW samples were grown on Si(001) and Si(111) substrates cleaned following this procedure. The RCA1 solution is aimed to remove organic contaminations while the RCA2 removes residual heavy metal contamination. Care has to be taken not to exceed 80°C since higher temperatures lead to a degradation of the solution and a concomitant reduction of the cleaning efficiency. Therefore, the temperature was controlled using a thermometer during the cleaning with RCA1 and RCA2 solutions.

Appendix B
Description of the samples and corresponding growth parameters

All the samples used in this thesis are listed in Table 1. These samples are labeled as follows: The substrate material is indicated by the first two characters A0 for *C*-plane sapphire, S0 for Si(001) and S1 for Si(111), while the last characters indicate the growth conditions.

Control samples *A0I*, *A0II* and *A0III* have been grown on bare sapphire substrate, -whereas samples *S0I* and *S1I* correspond to the growth on Si(001) and Si(111) covered by a 4 Å thin Ni layer. In this case, the Ni layer was deposited in situ on the Si substrates after the cleaning procedure consisting in a simple HF dip, subsequent loading into the chamber for MBE and oxide desorption step. Apart from these samples, the NW experiments were always carried out on sapphire substrates covered by a 3–4 Å thin layer of Ni or on the bare surface of the Si substrates.

The growth parameters of the NW samples that were fabricated for the investigation of the effects of the temperature and the Ga- and the N-rate are indicated in the first seven lines of Table 1 and are labeled *a*–*g*. For samples *A0III*, *A0IV*, *A0t1* and *S0p0-S0p5*, a particular growth procedure was employed. In this case, the growth was preceded by Ga exposure during 900 s while the keeping the N shutter closed. For sample *A0t2*, the growth was first initiated on a Ni-covered sapphire substrate under N-excess to form the NWs. The V/III ratio was later changed to Ga-excess and growth was continued. For sample *A0V*, growth was carried on a Ni-covered sapphire substrate under Ga-excess. Other samples were grown exclusively for the simultaneous investigation by QMS and RHEED. In this case the manipulator was not rotated during growth. These experiments correspond to samples *A0m1* and *A0m2* for growth on Ni-covered sapphire substrates seen along the two different sapphire azimuths, and to samples *S0m* and *S1m* for growth on Si(001) and Si(111) under the same temperature and *V/III* ratio as condition *a*. Last, NW samples were obtained from growth experiment with duration shorter than the one of the nucleation for AFM and TEM investigation. These samples are *A0p1*–*A0p4* for the nucleation on Ni-covered sapphire substrates and *S0p0-S0p6* for the one on Si(001) substrates.

Table 1: Parameters of Ni-catalysed GaN NW and catalyst-free GaN NW growth experiments. The label *A0* stands for the use of *C*-plane sapphire substrate, while the labels *S0* and *S1* indicate Si(001) and Si(111) substrates, respectively.

Sample	Growth temperature [°C]	N-rate [Å/s]	Ga-rate [Å/s]	*V/III* ratio	Growth duration [s]	Comment
A0a/S0a/S1a	730	2.0	0.4	5.0	4545	Temperature, N-, Ga-rate series
A0b/S0b/S1b	755	2.0	0.4	5.0	4545	Temperature series
A0c/S0c/S1c	780	2.0	0.4	5.0	4545	Temperature series
A0d/S0d/S1d	730	1.1	0.4	2.8	4545	N-rate series
A0e/S0e/S1e	730	0.5	0.4	1.2	4545	N-rate series
A0f/S0f/S1f	730	2.0	0.2	9.7	4545	Ga-rate series
A0g/S0g/S1g	730	2.0	0.8	2.5	4545	Ga-rate series
A0I	730	2.0	0.4	5.0	4545	Planar growth
A0II	780	2.0	0.4	5.0	4545	Planar growth
A0III	730	1.0	0.4	2.5	4545	900 s Ga pre-exposure
A0IV	730	1.0	0.4	2.5	4545	900 s Ga pre-exposure
A0V	730	1.1	1.6	0.7	5263	Ga-rich conditions
S0I	730	2.0	0.4	5.0	4545	Ni-deposition
S1I	730	2.0	0.4	5.0	4545	Ni-deposition
A0m1	730	2.0	0.4	5.0	4545	No rotation for RHEED experiment
A0m2	730	2.0	0.4	5.0	4545	No rotation for RHEED experiment
S0m	730	2.0	0.4	5.0	4545	No rotation for RHEED experiment
S1m	730	2.0	0.4	5.0	4545	No rotation for RHEED experiment
S0r	730	2.0	0.4	5.0	4545	900 s Ga pre-exposure
S1r	730	2.0	0.4	5.0	4545	900 s Ga pre-exposure
A0p1	730	2.0	0.4	5.0	15	Nucleation-time series
A0p2	730	2.0	0.4	5.0	30	Nucleation-time series
A0p3	730	2.0	0.4	5.0	60	Nucleation-time series
A0p4	730	2.0	0.4	5.0	120	Nucleation-time series
A0t1	730	2.0	0.4	5.0	0	900 s Ga pre-exposure: β-NiGa
A0t2	730	1.1	0.2/1.6	4.8/0.7	4167+877	N-rich→Ga-rich: β-NiGa
S0p0	730	2.0	0.4	5.0	0	900 s Ga pre-exposure: Nucleation-time series
S0p1	730	2.0	0.4	5.0	4	900 s Ga pre-exposure: Nucleation-time series
S0p2	730	2.0	0.4	5.0	15	900 s Ga pre-exposure: Nucleation-time series
S0p3	730	2.0	0.4	5.0	30	900 s Ga pre-exposure: Nucleation-time series
S0p4	730	2.0	0.4	5.0	60	900 s Ga pre-exposure: Nucleation-time series
S0p5	730	2.0	0.4	5.0	120	900 s Ga pre-exposure: Nucleation-time series
S0p6	730	2.0	0.4	5.0	15	Direct growth: Nucleation-time series

Appendix C
Ternary Phase Diagrams of the Ni-Ga-N system at 627°C and 850°C

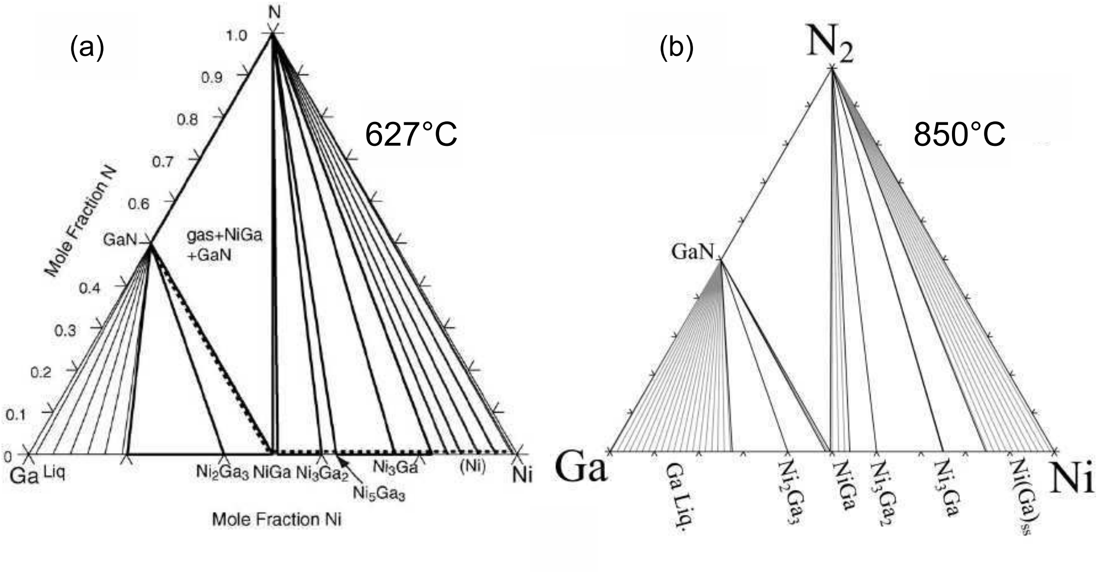

Figure 1: Isothermal section of the Ni-Ga-N system (a) at 627°C [153] and (b) at 850°C [152].

Bibliography

[1] Lieber Research Group. URL `http://cmliris.harvard.edu/index.php`.

[2] Yang Research Group. URL `http://www.cchem.berkeley.edu/pdygrp/main.html`.

[3] K. Dick. *Epitaxial Growth and Design of Nanowires and Complex Nanostrutures*. PhD thesis, Solid State Physics Lund University, 2007.

[4] M. S. Islam, S. Sharma, T. I. Kamins, and R. S. Williams. Ultrahigh-density silicon nanobridges formed between two vertical silicon surfaces. *Nanotechnology*, 15:L5, 2004.

[5] A. DeHon, C. M. Lieber, P. Lincoln, and J. Savage. Sub-lithographic Semiconductor Computing Systems. *HotChips*, 15:1, 2003.

[6] C. M. Lieber and Z. L. Wang. Functional Nanowires. *MRS Bulletin*, 32:99, 2007.

[7] L. Cademartiri and G. A. Ozin. Ultrathin Nanowires - A Materials Chemistry Perspective. *Adv. Mater.*, 21:1013, 2008.

[8] C. M. Lieber. Nanoscale science and technology: Building a big future from small things. *MRS Bulletin*, 28:486, 2003.

[9] P. J. Pauzauskie and P. Yang. Nanowire photonics. *Materials Today*, 9:36, 2006.

[10] F. Glas. Critical dimensions for the plastic relaxation of strained axial heterostructures in free-standing nanowires. *Phys. Rev. B*, 74:121302, 2006.

[11] B. M. Kayes, H. A. Atwater, and N. S. Lewis. Comparison of the device physics principles of planar and radial p-n junction nanorod solar cells. *J. Appl. Phys.*, 97: 114302, 2005.

[12] S Nakamura, T Mukai, and M Senoh. High-Power GaN p-n-Junction Blue-Light-Emitting Diodes. *Jpn. J. Appl. Phys.*, 30:L1998, 1991.

[13] P. Preuss. An unexpected discovery could yield a full spectrum solar cell, 2002. URL `http://www.lbl.gov/Science-Articles/Archive/MSD-full-spectrum-solar-cell.html`.

[14] K. A. Bertness, N. A. Sanford, J. M. Barker, J. B. Schlager, A. Roshko, A. V. Davydov, and I. Levin. Catalyst-Free Growth of GaN Nanowires. *J. Elec. Mater.*, 35:576, 2006.

[15] H. Sekiguchi, T. Nakazatoa, A. Kikuchi, and K. Kishino. Structural and optical properties of GaN nanocolumns grown on (0 0 0 1) sapphire substrates by rf-plasma-assisted molecular-beam epitaxy. *J. Cryst. Growth*, 300:259, 2007.

[16] M. Yoshizawa, A. Kikuchi, M. Mori, N. Fujita, and K. Kishino. Self-Organization of GaN Nano-structures on c-Al_2O_3 by RF-Radical Gas Source Molecular Beam Epitaxy. In *Summaries, 23rd Int. Symp. Compound Semicond. St. Petersburg, Russia*, volume 3, page 187. Inst. Phys. Conf. Ser., 1996.

[17] M. A. Sanchez-Garcia, E. Calleja, E. Monroy, F. J. Sanchez, F. Calle, E. Mu noz, and R. Beresford. Effect of the V/III ratio and substrate temperature on the morphology and properties of GaN- and AlN-layers grown by molecular beam epitaxy on Si(111). *J. Cryst. Growth*, 183:23, 1998.

[18] V. V. Mamutin. Growth of A(3)N whiskers and plate-shaped crystals by molecular-beam epitaxy with the participation of the liquid phase. *Tech. Phys. Lett.*, 25:741, 1999.

[19] L. Geelhaar, C. Chèze, W. M. Weber, R. Averbeck, H. Riechert, Th. Kehagias, Ph. Komninou, G. P. Dimitrakopulos, and Th. Karakostas. Axial and radial growth of Ni-induced GaN nanowires. *Appl. Phys. Lett.*, 91:093113, 2007.

[20] R. Calarco, M. Marso, T. Richter, A. I. Aykanat, R. Meijers, A. v.d. Hart, T. Stoica, and H. Lüth. Size-dependent Photoconductivity in MBE-Grown GaN Nanowires. *Nano Lett*, 5:981, 2005.

[21] J. Ristić. *Growth and Characterization of Group-III Nitride Nanonacolumnar Structures*. PhD thesis, Universidad Politécnica de Madrid Escuela Técnica Superior De Ingenieros De Telecomunicación, 2006.

[22] J. Ristić, E. Calleja, S. Fernández-Garrido, L. Cerutti, A. Trampert, U. Jahn, and K. H. Ploog. On the mechanisms of spontaneous growth of III-nitride nanocolumns by plasma-assisted molecular beam epitaxy. *J. Cryst. Growth*, 310: 4035, 2008.

[23] R. Songmuang, O. Landré, and B. Daudin. From nucleation to growth of catalyst-free GaN nanowires on thin AlN buffer layer. *Appl. Phys. Lett.*, 91:251902, 2007.

[24] R. Calarco, R. J. Meijers, R. K. Debnath, T. Stoica, E. Sutter, and H. Lüth. Nucleation and Growth of GaN Nanowires on Si(111) Performed by Molecular Beam Epitaxy. *Nano Lett.*, 7:2248, 2007.

[25] R. K. Debnath, R. Meijers, T. Richter, T. Stoica, R. Calarco, and H. Lüth. Mechanism of molecular beam epitaxy growth of GaN nanowires on Si(111). *Appl. Phys. Lett.*, 90:123117, 2007.

[26] T. Stoica, E. Sutter, R. J. Meijers, R. K. Debnath, R. Calarco, H. Lüth, and D. Grützmacher. Interface and Wetting Layer Effect on the Catalyst-Free Nucleation and Growth of GaN Nanowires. *Small*, 4:751, 2008.

[27] K. A. Bertness, A. Roshko, L. M. Mansfield, T. E. Harvey, and N. A. Sanford. Mechanism for spontaneous growth of GaN nanowires with molecular beam epitaxy. *J. Cryst. Growth*, 310:3154, 2008.

[28] C.T. Foxon, S.V. Novikov, J.L. Hall, R.P. Campion, D. Cherns, I. Griffiths, and S. Khongphetsak. A complementary geometric model for the growth of GaN nanocolumns prepared by plasma-assisted molecular beam epitaxy. *J. Cryst. Growth*, 311:3423, 2009.

[29] W P McCray. MBE deserves a place in the history books. *Nat. Nano.*, 2:259, 2007.

[30] J. R. Arthur. Molecular beam epitaxy. *Surf. Sci.*, 500:189, 2002.

[31] A J Heffernan, M Kauer, S E Hooper, V Bousquet, and K Johnson. InGaN violet laser diodes grown by Molecular Beam Epitaxy. *Phys. Stat. Sol. (a)*, 201:2668, 2004.

[32] H Lüth. *Solid Surfaces, Interfaces and Thin Films*. Advanced Texts in Physics. Springer Verlag, 2001.

[33] J. Tersoff and F. K. LeGoues. Competing relaxation mechanisms in strained layers. *Phys. Rev. Lett.*, 72:3570, 1994.

[34] K. Oura, V.G. Lifshits, A.V. Saranin, A.A.and Zotov, and M. Katayama. *Surface Science An Introduction*. Advanced Texts in Physics. Springer-Verlag, 2003.

[35] J Villain. Continuum models of crystal-growth from atomic-beams with and without desorption. *J. Phys. I*, 1:19, 1991.

[36] G. Koblmüller. *Studies of Nucleation and Surfaces Kinetics in Molecular Beam Epitaxy of GaN*. PhD thesis, T. U. Wien, 2005.

[37] J Osaka, M Senthil Kumar, H Toyoda, T Ishijima, H Sugai, and T Mizutani. Role of atomic nitrogen during GaN growth by plasma-assisted molecular beam epitaxy revealed by appearance mass spectrometry. *Appl. Phys. Lett.*, 90:172114, 2007.

[38] M A Herman and H Sitter. *Molecular beam epitaxy - Fundamentals and current status*, volume 24 of *Crystal Research and Technology*. Springer-Verlag Berlin-Heidelberg, 1989.

[39] O Janzen, C Hahn, and W Mönch. Oxidation of GaN(0001) surfaces at room temperature. *EJPB*, 9:315, 1999.

[40] Y. Okamoto, S. Hashiguchi, Y. Okada, and M. Kawabe. Effects of Atomic Hydrogen on the Growth of GaN by RF-Molecular Beam Epitaxy. *Jpn. J. Appl. Phys.*, 38: L230, 1999.

[41] T. Araki, Y. Chiba, M. Nobata, Y. Nishioka, and Y. Nanishi. Structural characterization of GaN grown by hydrogen-assisted ECR-MBE using electron microscopy. *J. Cryst. Growth*, 209:368, 2000.

[42] J. E. Northrup and J. Neugebauer. Strong affinity of hydrogen for the GaN(000-1) surface: Implications for molecular beam epitaxy and metalorganic chemical vapor deposition. *Appl. Phys. Lett.*, 85:3429, 2004.

[43] A Y Cho. GaAs Epitaxy by a Molecular Beam Method: Observations of Surface Structure on the (001) Face. *J. Appl. Phys.*, 42:2074, 1971.

[44] J R Arthur Jr. Interaction of Ga and As[sub 2] Molecular Beams with GaAs Surfaces. *J. Appl. Phys.*, 39:4032, 1968.

[45] S Guha, NA Bojarczuk, and DW Kisker. Surface lifetimes of Ga and growth behavior on GaN(0001) surfaces during molecular beam epitaxy. *Appl. Phys. Lett.*, 69:2879, 1996.

[46] G. Koblmüller, P. Pongratz, R. Averbeck, and H. Riechert. Delayed nucleation during molecular-beam epitaxial growth of GaN observed by line-of-sight quadrupole mass spectrometry. *Appl. Phys. Lett.*, 80:2281, 2002.

[47] G. Koblmüller, S. Fernández-Garrido, E. Calleja, and J. S. Speck. In situ investigation of growth modes during plasma-assisted molecular beam epitaxy of (0001) GaN. *Appl. Phys. Lett.*, 91:161904, 2007.

[48] S Fernández-Garrido, G Koblmüller, E Calleja, and J S Speck. In situ GaN decomposition analysis by quadrupole mass spectrometry and reflection high-energy electron diffraction. *J. Appl. Phys.*, 104:033541, 2008.

[49] S Schöffberger. Diplomarbeit. Master's thesis, FH Munich, 2001.

[50] B Heying, R Averbeck, LF Chen, E Haus, H Riechert, and JS Speck. Control of GaN surface morphologies using plasma-assisted molecular beam epitaxy. *J. Appl. Phys.*, 88:1855, 2000.

[51] Y. Xia, P. Yang, Y. Sun, Y. Wu, B. Mayers, B. Gates, Y. Yin, F. Kim, and H. Yan. One-Dimensional Nanostructures: Synthesis, Characterization, and Applications. *Adv. Mater.*, 15:353, 2003.

[52] K. A. Dick. A review of nanowire growth promoted by alloys and non-alloying elements with emphasis on Au-assisted III-V nanowires. *Progress in Crystal Growth and Characterization of Materials*, 54:138, 2008.

[53] Z L Wang. *Nanowires and Nanobelts*. Kluwer Academic Publishers, 2003.

[54] S. Noor Mohammad. Self-catalysis: A contamination-free, substrate-free growth mechanism for single-crystal nanowire and nanotube growth by chemical vapor deposition. *J. Chem. Phys.*, 125:094705, 2006.

[55] M. A. Reed, J. N. Randall, R. J. Aggarwal, R. J. Matyi, T. M. Moore, and A. E. Wetsel. Observation of discrete electronic states in a zero-dimensional semiconductor nanostructure. *Phys. Rev. Lett.*, 60:535, 1988.

[56] L. Samuelson. Self-forming nanoscale devices. *Materials Today*, 6:22, 2003.

[57] M Kuball, F H Morrissey, M Benyoucef, I Harrison, D Korakakis, and Foxon C T. Nano-Fabrication of GaN Pillars Using Focused Ion Beam Etching. *Phys. Stat. Sol. (a)*, 176:355, 1999.

[58] F. Demangeot, J. Gleize, J. Frandon, M. A. Renucci, M. Kuball, D. Peyrade, L. Manin-Ferlazzo, Y. Chen, and N. Grandjean. Optical investigation of micrometer and nanometer-size individual GaN pillars fabricated by reactive ion etching. *J. Appl. Phys.*, 91:6520, 2002.

[59] Q. Fan, S. Chevtchenko, X. Ni, S.-J. Cho, F. Yun, and H. Morkoç. Reactive ion etch damage on GaN and its recovery. *J. Vac. Sci. Technol. B*, 24:1197, 2006.

[60] R.S. Wagner and W.C. Ellis. Vapor-Liquid-Solid mechanism of single crystal growth. *Appl. Phys. Lett.*, 4:89, 1964.

[61] A. M. Morales and C. M. Lieber. A Laser Ablation Method for the Synthesis of Crystalline Semiconductor Nanowires. *Science*, 279:208, 1998.

[62] G. A. Bootsma and H. J. Gassen. A quantitative study on the growth of silicon whiskers from silane and germanium whiskers from germane. *J. Cryst. Growth*, 10:223, 1971.

[63] S. E. Hooper, C. T. Foxon, T. S. Cheng, L. C. Jenkins, D. E. Lacklison, J. W. Orton, T. Bestwick, A. Kean, M. Dawson, and G. Duggan. Some aspects of GaN growth on GaAs(100) substrates using molecular beam epitaxy with an RF activated nitrogen-plasma source. *J. Cryst. Growth*, 155:157, 1995.

[64] I. Akasaki, H. Amano, H. Murakami, M. Sassa, H. Kato, and K. Manabe. Growth of GaN and AlGaN for UV/blue p-n junction diodes. *J. Cryst. Growth*, 128:379, 1993.

[65] M. He, I. Minus, P. Zhou, S. N. Mohammed, J. B. Halpern, R. Jacobs, W. L. Sarney, L. Salamanca-Riba, and R. D. Vispute. Growth of large-scale GaN nanowires and tubes by direct reaction of Ga with NH_3. *Appl. Phys. Lett.*, 77:3731, 2000.

[66] M. Yoshizawa, A. Kikuchi, M. Mori, N. Fujita, and K. Kishino. Growth of Self-Organized GaN Nanostructures on Al2O3(0001) by RF-Radical Source Molecular Beam Epitaxy. *Jpn. J. Appl. Phys.*, 36:L459, 1997.

[67] A. Fontcuberta i Morral, C. Colombo, G. Abstreiter, J. Arbiol, and J. R. Morante. Nucleation mechanism of gallium-assisted molecular beam epitaxy growth of GaAs nanowires. *Appl. Phys. Lett.*, 92:063112, 2008.

[68] N Wang, YH Tang, YF Zhang, CS Lee, and ST Lee. Nucleation and growth of Si nanowires from silicon oxide. *Phys. Rev. B*, 58:16024, 1998.

[69] W. Han, S. Fan, Q. Li, and Y. Hu. Synthesis of Gallium Nitride Nanorods Through a Carbon Nanotube-Confined Reaction. *Science*, 277:1287, 1997.

[70] D. Al-Mawlawi, C. Z. Liu, and M. Moskovits. Nanowires formed in anodic oxide nanotemplates. *J. Mater. Res.*, 9:1014, 1994.

[71] S. D. Hersee, X. Sun, and X. Wang. The controlled growth of GaN nanowires. *Nano Lett*, 6:1808, 2006.

[72] K Kishino, T Hoshino, S. Ishizawa, and A. Kikuchi. Selective-area growth of GaN nanocolumns on titanium-mask-patterned silicon (111) substrates by RF-plasma-assisted molecular-beam epitaxy. *Electronics Lett.*, 44:819, 2008.

[73] J. Johansson, B. A. Wacaser, K. A Dick, and Werner S. Growth related aspects of epitaxial nanowires. *Nanotechnology*, 17:355, 2006.

[74] B. A. Wacaser, K. A. Dick, J. Johansson, M. T. Borgström, K. Deppert, and L. Samuelson. Preferential interface nucleation: An expansion of the vls growth mechanism for nanowires. *Adv. Mater.*, 20:1, 2008.

[75] A. I. Persson, M. W. Larsson, S. Stenström, B. J. Ohlsson, L. Samuelson, and L. R. Wallenberg. Solid-phase diffusion mechanism for GaAs nanowire growth. *Nat. Mater.*, 3:677, 2004.

[76] K. A. Dick, K. Deppert, T. Martensson, B. Mandl, L. Samuelson, and W. Seifert. Failure of the Vapor-Liquid-Solid Mechanism in Au-Assisted MOVPE Growth of InAs Nanowires. *Nano Lett.*, 5:761, 2005.

[77] S Kodambaka, J Tersoff, M C Reuter, and F M Ross. Germanium Nanowire Growth Below the Eutectic Temperature. *Science*, 316:729, 2007.

[78] E.I. Givargizov. Fundamental aspects of VLS growth. *J. Cryst. Growth*, 31:20, 1975.

[79] L. Schubert, P. Werner, N. D. Zakharov, G. Gerth, F. M. Kolb, L. Long, U. Gösele, and T. Y. Tan. Silicon nanowhiskers grown on <111>Si substrates by molecular-beam epitaxy. *Appl. Phys. Lett.*, 84:4968, 2004.

[80] S. Kodambaka, J. Tersoff, M. C. Reuter, and F. M. Ross. Diameter-Independent Kinetics in the Vapor-Liquid-Solid Growth of Si Nanowires. *Phys. Rev. Lett.*, 96: 096105, 2006.

[81] T Mårtensson, M Borgström, W Seifert, B J Ohlsson, and L Samuelson. Fabrication of individually seeded nanowire arrays by vapour-liquid-solid growth. *Nanotechnology*, 14:1255, 2003.

[82] T Mårtensson, P Carlberg, M Borgström, L Montelius, W Seifert, and L Samuelson. Nanowire Arrays Defined by Nanoimprint Lithography. *Nano Lett.*, 4:699, 2004.

[83] L. E. Jensen, Mikael T. Bjork, S. Jeppesen, A. I. Persson, B. J. Ohlsson, and L. Samuelson. Role of Surface Diffusion in Chemical Beam Epitaxy of InAs Nanowires. *Nano Lett.*, 4:1961, 2004.

[84] J B Hannon, S Kodambaka, F M Ross, and R M Tromp. The influence of the surface migration of gold on the growth of silicon nanowires. *Nature*, 440:69, 2006.

[85] J. E. Allen, E. R. Hemesath, D. E. Perea, J. L. Lensch-Falk, Z.Y. Li, F. Yin, M. H. Gass, P. Wang, A. L. Bleloch, R. E. Palmer, and L. J. Lauhon. High-resolution detection of Au catalyst atoms in Si nanowires. *Nat. Nano.*, 3:168, 2008.

[86] S. H. Oh, K. van Benthem, S. I. Molina, A. Y. Borisevich, W. Luo, P. Werner, N. D. Zakharov, D. Kumar, S. T. Pantelides, and S. J. Pennycook. Point Defect Configurations of Supersaturated Au Atoms Inside Si Nanowires. *Nano Lett.*, 8:1016, 2008.

[87] M. C. Putnam, M. A. Filler, B. M. Kayes, M. D. Kelzenberg, Y. Guan, N. S. Lewis, J. M. Eiler, and H. A. Atwater. Secondary Ion Mass Spectrometry of Vapor-Liquid-Solid Grown, Au-Catalyzed, Si Wires. *Nano Lett.*, 8:3109, 2008.

[88] M. Volmer and L. Estermann. Über den Mechanismus der Molekülabscheidung an Kristallen. *Z. Phys.*, 7:13, 1921.

[89] G.W. Sears. Mercury Whiskers. *Acta Metallurgica*, 1:457, 1953.

[90] G.W Sears. A mechanism of whisker growth. *Acta Metallurgica*, 3:367, 1955.

[91] M. J. Bierman, Y. K. A. Lau, A. V. Kvit, A. L. Schmitt, and S. Jin. Dislocation-Driven Nanowire Growth and Eshelby Twist. *Science*, 320:1060, 2008.

[92] D. Cherns, L. Meshi, I. Griffiths, S. Khongphetsak, S. V. Novikov, N. R. S. Farley, R. P. Campion, and C. T. Foxon. Defect-controlled growth of GaN nanorods on (0001) sapphire by molecular beam epitaxy. *Appl. Phys. Lett.*, 93:111911, 2008.

[93] B. W. Jacobs, M. A. Crimp, K. M. McElroy, and V. M. Ayres. Nanopipes in Gallium Nitride Nanowires and Rods. *Nano Lett*, 8:4353, 2008.

[94] J. M. Blakely and K. A. Jackson. Growth of Crystal Whiskers. *J. Chem. Phys.*, 37: 428, 1962.

[95] V. Ruth and J. P. Hirth. Kinetics of Diffusion-Controlled Whisker Growth. *J. Chem. Phys.*, 41:3139, 1964.

[96] J. Johansson, C. P. T. Svensson, T. Mårtensson, L. Samuelson, and W. Seifert. Mass Transport Model for Semiconductor Nanowire Growth. *J. Phys. Chem. B*, 109: 13567, 2005.

[97] V. G. Dubrovskii, G. E. Cirlin, I. P. Soshnikov, A. A. Tonkikh, N. V. Sibirev, Yu. B. Samsonenko, and V. M. Ustinov. Diffusion-induced growth of GaAs nanowhiskers during molecular beam epitaxy: Theory and experiment. *Phys. Rev. B*, 71:205325, 2005.

[98] V. G. Dubrovskii, N. V. Sibirev, G. E. Cirlin, J. C. Harmand, and V. M. Ustinov. Theoretical analysis of the vapor-liquid-solid mechanism of nanowire growth during molecular beam epitaxy. *Phys. Rev. E*, 73:021603, 2006.

[99] R. L. Schwoebel. A Diffusion Model for Filamentary Crystal Growth. *J. Appl. Phys.*, 38:1759, 1967.

[100] C. Colombo, D. Spirkoska, M. Frimmer, G. Abstreiter, and A. Fontcuberta i Morral. Ga-assisted catalyst-free growth mechanism of GaAs nanowires by molecular beam epitaxy. *Phys. Rev. B*, 77:155326, 2008.

[101] T. Zywietz, J. Neugebauer, and M. Scheffler. Adatom diffusion at GaN (0001) and (000(1)over-bar) surfaces. *Appl. Phys. Lett.*, 73:487, 1998.

[102] H. Zheng, M. H. Xie, H. S. Wu, and Q. K. Xue. Kinetic energy barriers on the GaN(0001) surface: A nucleation study by scanning tunneling microscopy. *Phys. Rev. B*, 77:045303, 2008.

[103] M. Borgström, K. Deppert, L. Samuelson, and W. Seifert. Size- and shape-controlled gaas nano-whiskers grown by movpe: a growth study. *J. Cryst. Growth*, 260:18, 2004.

[104] W. Rasband. Image J - Image Processing and Analysis in Java. URL `http://rsb.info.nih.gov/ij/`.

[105] Ph. Buffat and J-P. Borel. Size effect on the melting temperature of gold particles. *Phys. Rev. A*, 13:2287, 1976.

[106] E. Sutter and P. Sutter. Phase Diagram of Nanoscale Alloy Particles Used for Vapor-Liquid-Solid Growth of Semiconductor Nanowires. *Nano Lett.*, 8:411, 2008.

[107] Y. Qi, T. Çagin, W. L. Johnson, and W. A. Goddard III. Melting and crystallization in Ni nanoclusters: The mesoscale regime. *J. Chem. Phys.*, 115:385, 2001.

[108] A. N. Andriotis, Z. G. Fthenakis, and M. Menon. Correlated variation of melting and Curie temperatures of nickel clusters. *Phys. Rev. B*, 75:073413, 2007.

[109] G. Levi, C. Scheu, and W. D. Kaplan. Segregation of Aluminium at Nickel-Sapphire Interfaces. *Interface Science*, 9:213, 2001.

[110] K. P. Trumble and Rühle M. The thermodynamics of spinel interphase formation at diffusion-bonded Ni/Al2O3 interfaces. *Acta metallurgica et materialia*, 39:1915, 1991.

[111] W. Kern and D. A. Puotinen. Cleaning Solutions Based on Hydrogen Peroxide for Use in Silicon Semiconductor Technology. *RCA Rev.*, 31:187, 1970.

[112] H. Riechert, R. Averbeck, A. Graber, M. Schienle, U. Strauß, and H. Tews. MBE growth of (In)GaN for led applications. *Mater. Res. Soc. Symp. Proc.*, 449:149, 1997.

[113] J. C. Harmand, G. Patriarche, N. Péré-Laperne, M-N. Mérat-Combes, L. Travers, and F. Glas. Analysis of vapor-liquid-solid mechanism in Au-assisted GaAs nanowire growth. *Appl. Phys. Lett.*, 87:203101, 2005.

[114] Y. Wu and P. Yang. Direct Observation of Vapor-Liquid-Solid Nanowire Growth. *J. Am. Chem. Soc.*, 123:3165, 2001.

[115] B Kalache, P Roca i Cabarrocas, and A Fontcuberta i Morral. Observation of Incubation Times in the Nucleation of Silicon Nanowires Obtained by the Vapor–Liquid–Solid Method. *Jpn. J. Appl. Phys.*, 45:L190, 2006.

[116] T Clement, S Ingole, S Ketharanathan, J Drucker, and S T Picraux. In situ studies of semiconductor nanowire growth using optical reflectometry. *Appl. Phys. Lett.*, 89:163125, 2006.

[117] B J Kim, J Tersoff, S Kodambaka, M C Reuter, E A Stach, and F M Ross. Kinetics of Individual Nucleation Events Observed in Nanoscale Vapor-Liquid-Solid Growth. *Science*, 322:1070, 2008.

[118] Q. X. Liu, C. X. Wang, N. S. Xu, and G. W. Yang. Nanowire formation during catalyst assisted chemical vapor deposition. *Phys. Rev. B*, 72:085417, 2005.

[119] FM Ross, J Tersoff, and MC Reuter. Sawtooth faceting in silicon nanowires. *Phys. Rev. Lett.*, 95:146104, 2005.

[120] T. Kawashima, T. Mizutani, H. Masuda, T. Saitoh, and M. Fujii. Initial Stage of Vapor-Liquid-Solid Growth of Si Nanowires. *J. Phys. Chem. C*, 112:17121, 2008.

[121] S K Eswaramoorthy, J M Howe, and G Muralidharan. In Situ Determination of the Nanoscale Chemistry and Behavior of Solid-Liquid Systems. *Science*, 318: 1437, 2007.

[122] S Hofmann, R Sharma, C T Wirth, F Cervantes-Sodi, C Ducati, T Kasama, R E Dunin-Borkowski, J Drucker, P Bennett, and J Robertson. Ledge-flow-controlled catalyst interface dynamics during Si nanowire growth. *Nat. Mater.*, 7:372, 2008.

[123] F. Glas, J. C. Harmand, and G. Patriarche. Why does Wurtzite form in nanowires of III-V Zinc-Blende semiconductors? *Phys. Rev. Lett.*, 99:146101, 2007.

[124] X. Zhang, J. Zou, M. Paladugu, Y. Guo, Y. Wang, Y. Kim, H. J. Joyce, Q. Gao, H. H. Tan, and C. Jagadish. Evolution of Epitaxial InAs Nanowires on GaAs (111)B. *Small*, 5:366, 2009.

[125] M. Tchernycheva, J. C. Harmand, G. Patriarche, L. Travers, and G. E. Cirlin. Temperature conditions for GaAs nanowire formation by Au-assisted molecular beam epitaxy. *Nanotechnology*, 17:4025, 2006.

[126] H. D. Park, S. M. Prokes, M. E. Twigg, R. C. Cammarata, and A.-C. Gaillot. Si-assisted growth of InAs nanowires. *Appl. Phys. Lett.*, 89:223125, 2006.

[127] H. D. Park and S. M. Prokes. Study of the initial nucleation and growth of catalyst-free InAs and Ge nanowires. *Appl. Phys. Lett.*, 90:203104, 2007.

[128] S. Guha, N. A. Bojarczuk, M. A. L. Johnson, and J. F. Schetzina. Selective area metalorganic molecular-beam epitaxy of GaN and the growth of luminescent microcolumns on Si/SiO2. *Appl. Phys. Lett.*, 75:463, 1999.

[129] E. Calleja, M.A. Sánchez-García, F.J. Sánchez, F. Calle, F.B. Naranjo, E. Muñoz, U. Jahn, and K. Ploog. Luminescence properties and defects in GaN nanocolumns grown by molecular beam epitaxy. *Phys. Rev. B*, 62:16826, 2000.

[130] H. W. Seo, Q. Y. Chen, L. W. Tu, C. L. Hsiao, M. N. Iliev, and W. K. Chu. Catalytic nanocapillary condensation and epitaxial GaN nanorod growth. *Phys. Rev. B*, 71: 235314, 2005.

[131] C. L. Hsiao, L. W. Tu, T. W. Chi, H. W. Seo, Q. Y. Chen, and W. K. Chu. Buffer controlled GaN nanorods growth on Si(111) substrates by plasma-assisted molecular beam epitaxy. *J. Vac. Sci. Technol. B*, 24:845, 2006.

[132] E A Stach, P J. Pauzauskie, T Kuykendall, J Goldberger, R He, and P Yang. Watching GaN Nanowires Grow. *Nano Lett.*, 3:867, 2003.

[133] R.J. Meijers. *Growth and Characterisation of Group-III Nitride-based Nanowires for Devices*. PhD thesis, Westfälischen Technischen Hochschule Aachen, 2007.

[134] E. Calleja, J. Ristić, S. Fernández-Garrido, L. Cerutti, M.A. Sánchez-García, J. Grandal, A. Trampert, U. Jahn, G. Sánchez, A. Griol, , and B. Sánchez. Growth, morphology, and structural properties of group-III-nitride nanocolumns and nanodisks. *Phys. Stat. Sol. (b)*, 244:2816, 2007.

[135] M. Tchernycheva, C. Sartel, G. Circlin, L. Travers, G. Patriarche, J. C. Harmand, L. S. Dang, J. Renard, B. Gayral, L. Nevou, and F. Julien. Growth of GaN free-standing nanowires by plasma-assisted molecular beam epitaxy: structural and optical characterization. *Nanotechnology*, 18:385306, 2008.

[136] R. Meijers, T. Richter, R. Calarco, T. Stoica, H. P. Bochem, M. Marso, and H. Lüth. GaN-nanowhiskers: MBE-growth conditions and optical properties. *J. Cryst. Growth*, 289:381, 2006.

[137] F. Furtmayr, M. Vielemeyer, M. Stutzmann, J. Arbiol, S. Estradé, F. Peirò, J. R. Morante, and M. Eickhoff. Nucleation and growth of GaN nanorods on Si(111)

surfaces by plasma-assisted molecular beam epitaxy - The influence of Si- and Mg-doping. *J. Appl. Phys.*, 104:034309, 2008.

[138] Y. S. Park, S. H. Lee, J. E. Oh, C. M. Park, and T. W. Kang. Self-assembled GaN nano-rods grown directly on (111) Si substrates:Dependence on growth conditions. *J. Cryst. Growth*, 282:313, 2005.

[139] A. Trampert, J. Ristić, U. Jahn, E. Calleja, and K. H. Ploog. Proceedings of the 13th International Conference on Microscopy of Semiconducting Materials. In A. G. Cullis and P. A. Midgley, editors, *Inst. Phys. Conf.*, 180, page 167, 2003.

[140] K. A. Bertness, A. Roshko, N. A. Sanford, J. M. Barker, and A. V. Davidov. Spontaneously grown GaN and AlGaN nanowires. *J. Cryst. Growth*, 287:522, 2006.

[141] K. A. Bertness, A. Roshko, L. M. Mansfield, T. E. Harvey, and N. A. Sanford. Nucleation conditions for catalyst-free GaN nanowires. *J. Cryst. Growth*, 300:94, 2007.

[142] X Wang, S-B Che, Y Ishitani, and A Yoshikawa. In situ spectroscopic ellipsometry and RHEED monitored growth of InN nanocolumns by molecular beam epitaxy. *J. Cryst. Growth*, 301-302:496, 2007.

[143] S. Nishikawa, Y. Nakao, H. Naoi, T. Araki, H. Na, and Y. Nanishi. Growth of InN nanocolumns by RF-MBE. *J. Cryst. Growth*, 301-302:490, 2007.

[144] L. Lari, R. T. Murray, T. J. Bullough, P. R. Chalker, M. Gass, C. Chèze, L. Geelhaar, and H. Riechert. Nanoscale compositional analysis of Ni-based seed crystallites associated with GaN nanowire growth. *Physica E*, 40:2457, 2008.

[145] H. Okamoto. Ga-Ni (Gallium-Nickel). *JPEDAV*, 29:296, 2008.

[146] R. Ducher, R. Kainuma, and K. Ishida. Phase equilibria in the Ni-rich portion of the Ni-Ga binary system. *Intermetallics*, 15:148, 2007.

[147] W X Yuan, Z Y Qiao, H Ipser, and Eriksson G. Thermodynamic assessment of the Ni-Ga system. *JPEDAV*, 25:68, 2003.

[148] X Weng, R A Burke, and J M Redwing. The nature of catalyst particles and growth mechanisms of GaN nanowires grown by Ni-assisted metal-organic chemical vapor deposition. *Nanotechnology*, 20:085610, 2009.

[149] J Gröbner, R Wenzel, G G Fischer, and R Schmid-Fetzer. Thermodynamic calculation of the binary systems M -Ga and investigation of ternary M-Ga-N phase equilibria (M=Ni, Co, Pd, Cr). *JPEDAV*, 20:615, 1999.

[150] H. S. Venugopalan, S. E. Mohney, B. P. Luther, S. D. Wolter, and J. M. Redwing. Interfacial reactions between nickel thin films and GaN. *J. Appl. Phys.*, 82:650, 1997.

[151] V M Bermudez, R Kaplan, M A Khan, and J N Kuznia. Growth of thin Ni films on GaN(0001). *Phys. Rev. B*, 48:2436, 1993.

[152] B. A. Hull, S. E. Mohney, and Z. K. Liu. Thermodynamic modeling of the Ni-Al-Ga-N system. *J. Mater. Res.*, 19:1742, 2004.

[153] M Li, C Li, F Wang, and W Zhang. The thermodynamic analysis of the driving force for the Ni/GaN interfacial reaction. *Materials Science and Engineering: A*, 422:316, 2006.

[154] H A Wridt. Ni-N binary phase diagram. In P Nash, editor, *Phase Diagrams of Binary Nickel Alloys*, page 213. ASM International, Materials Park, OH, 1991.

[155] W. Hoesler. Ga and Ni coverage analysis by Rutherford Backscattering Spectrometry. Technical report, Siemens AG Corporate Technology, Analytics, 2007.

[156] P. Stadelmann. EMS On Line - Electron Microscopy Image Simulation, 1995. URL `http://cecm.insa-lyon.fr/CIOLS/crystal1.pl`.

[157] P. A. Stadelmann. EMS - A software packge for electron diffraction analysis and HREM image simulation in materials science. *Ultramicroscopy*, 21:131, 1987.

[158] T. G. Kollie. Measurement of the thermal-expansion coefficient of nickel from 300 to 1000 K and determination of the power-law constants near the Curie temperature. *Phys. Rev. B*, 16:4872, 1977.

[159] O. Madelung, U. Rössler, and M. Schulz. *Numerical Data and Functional Relationships in Science and Technology Non-Tetrahedrally Bonded Binary Compounds II*, volume 41D. Springer-Verlag Landolt-Börnstein - Group III Condensed Matter, 2000.

[160] X. Y. Zhang, X. L. Wu, Q. Liu, R. L. Zuo, A. W. Zhu, P. Jiang, and Q. M. Wei. Phase transformation accommodated plasticity in nanocrystalline nickel. *Appl. Phys. Lett.*, 93:031901, 2008.

[161] H R Thirsk and E J Whitmore. Anelectron diffraction study of the surface reaction between Nickel Oxide and Corundum. *Trans. Faraday Soc.*, 36:565, 1940.

[162] K. Mocala and A. Navrotsky. Structural and Thermodynamic Variation in Nickel Aluminate Spinel. *J. Am. Chem. Soc.*, 72:826, 1989.

[163] P. Feschotte and P. Eggimann. Les Systèmes Binaires Cobalt-Gallium et Nickel-Gallium - Étude comparée. *J. Less-Common Met.*, 63:15, 1974.

[164] W. B. Pearson. A Nickel-Gallium Superlattice (Ni_3Ga). *Nature*, 173:364, 1954.

[165] Th. Kehagias, Ph. Komninou, G.P. Dimitrakopulos, C. Chèze, L. Geelhaar, H. Riechert, and Th. Karakostas. Atomic-scale configuration of catalyst particles on GaN nanowires. *Phys. Stat. Sol. (a)*, 12:3716, 2008.

[166] D Aurongzeb, K B Ram, M Holtz, M Basavaraj, G Kipshidze, B Yavich, S A Nikishin, and H Temkin. Formation of nickel nanodots on GaN. *J. Appl. Phys.*, 99: 014308, 2006.

[167] M. Jeppsson, K. A. Dick, J. B. Wagner, P. Caroff, K. Deppert, L. Samuelson, and L.-E. Wernersson. GaAs/GaSb nanowire heterostructures grown by MOVPE. *J. Cryst. Growth*, 310:4115, 2008.

[168] R Kainuma, H Ohtani, and K Ishida. Effect of alloying elements on martensitic transformation in the binary NiAlβ phase alloys. *Metallurgical and Materials Transactions A*, 27A:2445, 1996.

[169] K. E. Easterling D. A. Porter. *Phase transformations in metals and alloys*. CRC Press, 1992.

[170] N Wang, Y Cai, and R Q Zhang. Growth of nanowires. *Materials Science and Engineering: R: Reports*, 60:1, 2008.

[171] T.-H. Kim, C.-O. Jang, H.-K. Seong, H.-J. Choi, and S.-K. Lee. Fabrication and Electrical Characterization of Heterojunction Mn-Doped GaN Nanowire Diodes on n -Si Substrates. *Journal of Electronic Materials*, 38:505, 2009.

[172] C.-L. Wu, J.-C. Wang, M.-H. Chan, T. T. Chen, and S. Gwo. Heteroepitaxy of GaN on Si(111) realized with a coincident-interface AlN/beta-Si_3N_4(0001) double-buffer structure. *Appl. Phys. Lett.*, 83:4530, 2003.

[173] J. E. Northrup and J. Neugebauer. Theory of GaN(10-10) and (11-20) surfaces. *Phys. Rev. B*, 53:R10477, 1996.

[174] S. N. Basu, T. Lei, and T. D. Moustakas. Microstructures of GaN films deposited on (001) and (111) Si substrates using ECR-MBE. *J. Mater. Res.*, 9:2370, 1994.

[175] K. H. Ploog, O. Brandt, H. Yang, B. Yang, and A. Trampert. Nucleation and growth of GaN layers on GaAs, Si, and SiC substrates. *Papers from the 25th annual conference on the physics and chemistry of semiconductor interfaces*, 16:2229, 1998.

[176] A. Kuwabara, K. Matsunaga, and I. Tanaka. Lattice dynamics and thermodynamical properties of silicon nitride polymorphs. *Phys. Rev. B*, 78:064104, 2008.

[177] A. Zerr, G. Miehe, G. Serghiou, M. Schwarz, E. Kroke, R. Riedel, H. Fuesz, P. Kroll, and R. Boehler. Synthesis of cubic silicon nitride. *Nature*, 400:340, 1999.

[178] Y. Nakada, I. Aksenov, and H. Okumura. GaN heteroepitaxial growth on silicon nitride buffer layers formed on Si (111) surfaces by plasma-assisted molecular beam epitaxy. *Appl. Phys. Lett.*, 73:827, 1998.

[179] H. Kondo, K. Kawaai, A. Sakai, M. Hori, S. Zaima, and Y. Yasuda. Growth and energy bandgap formation of silicon nitride films in radical nitridation. *Jpn. J. Appl. Phys.*, 46:71, 2007.

[180] P. Komninou, T. Kehagias, G. P. Dimitrakopoulos, H. Kirmse, W. Neumann, C. Chèze, L. Geelhaar, H. Riechert, and T. Karakostas. IWN 2008, Montreux, Nanoscale analysis of interface between GaN nanowires and Si(111) and Si(001) substrates, 2008.

[181] L. Cerutti, J. Ristić, S. Fernández-Garrido, E. Calleja, A. Trampert, K. H. Ploog, S. Lazic, and J. M. Calleja. Wurtzite GaN nanocolumns grown on Si(001) by molecular beam epitaxy. *Appl. Phys. Lett.*, 88:213114, 2006.

[182] T. A. Rawdanowicz and J. Narayan. Epitaxial GaN on Si(111): Process control of SiN interlayer formation. *Appl. Phys. Lett.*, 85:133, 2004.

[183] B. Yang, A. Trampert, O. Brandt, B. Jenichen, and K. H. Ploog. Structural properties of GaN layers on Si(001) grown by plasma-assisted molecular beam epitaxy. *J. Appl. Phys.*, 83:3800, 1998.

[184] T. Yodo, H. Ando, H. Tsuchiya, D. Nosei, M. Shimeno, and Y. Harada. Influence of substrate nitridation before growth on initial growth process of GaN heteroepitaxial layers grown on Si(0 0 1) and Si(1 1 1) substrates by ECR-MBE. *J. Cryst. Growth*, 227:431, 2001.

[185] S. Lee, Y. Sohn, C. Kim, D. R. Lee, and H.-H. Lee. A crystallographic investigation of GaN nanostructures by reciprocal space mapping in a grazing incidence geometry. *Nanotechnology*, 20:215703, 2009.

[186] Y. Hu, X.-S. Wang, N. Cue, and X. Wang. Ge islanding growth on nitridized Si and the effect of Sb surfactant. *J. Phys. Cond. Matt.*, 14:8939, 2002.

[187] G. Zhai, J. Yang, N. Cue, and X.-S. Wang. Surface structures of silicon nitride thin films on Si(111). *Thin Solid Films*, 366:121, 2000.

[188] K. Kato, D. Matsushita, K. Muraoka, and Y. Nakasaki. Agglomeration and uniform growth of Si3N4 on Si(100): Experiments and first-principles calculations. *Phys. Rev. B*, 78:085321, 2008.

[189] M. Kong, W. Zhao, L. Wei, and G. Li. Investigations on the microstructure and hardening mechanism of TiN/Si3N4 nanocomposite coatings. *J. Phys. D*, 40:2858, 2007.

[190] E. V. Shalaeva, S. V. Borisov, O. F. Denisov, and M. V. Kuznetsov. Metastable phase diagram of Ti-Si-N(O) films. *Thin Solid Films*, 339:129, 1999.

[191] R. F. Zhang and S. Veprek. Crystalline-to-amorphous transition in Ti(1 - x)Si(x)N solid solution and the stability of fcc SiN studied by combined ab initio density functional theory and thermodynamic calculations. *Phys. Rev. B*, 76:174105, 2007.

[192] S. V. Bobylev and I. A. Ovid'ko. Nanoscale amorphization at disclination quadrupoles in deformed nanomaterials and polycrystals. *Appl. Phys. Lett.*, 93: 061904, 2008 and references therein.

[193] P. Walsh, R. K. Kalia, A. Nakano, P. Vashishta, and S. Saini. Amorphization and anisotropic fracture dynamics during nanoindentation of silicon nitride: A multimillion atom molecular dynamics study. *Appl. Phys. Lett.*, 77:4332, 2000.

[194] H. M. Jennings. On reactions between Silicon and Nitrogen .1. Mechanisms. *J. Mater. Sci.*, 18:951, 1983.

[195] J. S. Ha, K.-H. Park, W. S. Yun, and Y.-J. Ko. Thermal Nitridation and Oxygen-induced Etching Reactions:
A Comparative Study on Si(100) and (111) Surfaces by Scanning Tunneling Microscopy. *Jpn. J. Appl. Phys.*, 40:2429, 2001.

[196] D. Matsushita and H. Ikeda and A. Sakai and S. Zaima and Y. Yasuda. Scanning tunneling microscopy/scanning tunneling spectroscopy of initial nitridation process of si(100)-2×1 surfaces. *Thin Solid Films*, 369:293, 2000.

[197] H. Ikeda, D. Matsushita, S. Naito, K. Ohmori, A. Sakai, S. Zaima, and Y. Yasuda. Growth Processes and Electrical Characteristics of Silicon Nitride Films formed on Si(100) by Radical Nitrogen. *Jpn. J. Appl. Phys.*, 41:2463, 2002.

[198] D. Matsushita, H. Ikeda, A. Sakai, S. Zaima, and Y. Yasuda. Atomic-Scale Characterization of Nitridation Processes
on Si(100)-2×1 Surfaces by Radical Nitrogen. *Jpn. J. Appl. Phys.*, 40:2827, 2001.

[199] K.-Y. Hsu, C.-P. Liu, H.-C. Chung, and Y.-C. Chiu. Molecular beam epitaxy growth of wurtzite AlN nanotips. *Appl. Phys. Lett.*, 93:181902, 2008.

[200] R. W. Olesinski and G. J. Abbschian. Ga-Si binary phase diagram. In *Desk Handbook: Phase Diagrams for Binary Alloys*, page 392. ASM International, 2000.

[201] G. W. Yang and B. X. Liu. Nucleation thermodynamics of quantum-dot formation in V-groove structures. *Phys. Rev. B*, 61:4500, 2000.

[202] S.C. Lee, X.Y. Sun, S.D. Hersee, and S.R.J. Brueck. Orientation-dependent nucleation of GaN on a nanoscale faceted Si surface. *J. Cryst. Growth*, 279:289, 2005.

[203] S. Gangopadhyay, T. Schmidt, and J. Falta. Initial stage of silicon nitride nucleation on Si(111) by rf plasma-assisted growth. *e-Journal of Surf. Sci. and Nanotech.*, 4:84, 2006.

[204] L. Ruan and D. M. Chen. Pinhole formation in solid phase epitaxial film of $CoSi_2$ on Si(111). *Appl. Phys. Lett.*, 72:3464, 1998.

[205] M. Giesen, F. Schmitz, and H. Ibach. The growth of cobalt films on vicinal copper surfaces. *Surf. Sci.*, 336:269, 1995.

[206] H.-Y. Chen, H.-W. Lin, C.-H. Shen, and S. Gwo. Structure and photoluminescence properties of epitaxially oriented gan nanorods grown on si(111) by plasma-assisted molecular-beam epitaxy. *Appl. Phys. Lett.*, 89:243105, 2006.

[207] S. Hasegawa, J.-U. Seo, K. Uchida, H. Tambo, H. Kameoka, M. Ishimaru, and H. Asahi. Influence of native silicon oxides on the growth of gan nanorods on si(001). *Phys. Stat. Sol. (c)*, 6:570, 2009.

[208] L. W. Tu, C. L. Hsiao, T. W. Chi, I. Lo, and K. Y. Hsieh. Self-assembled vertical GaN nanorods grown by molecular-beam epitaxy. *Appl. Phys. Lett.*, 82:1601, 2003.

[209] A.-L. Barabási. Self-assembled island formation in heteroepitaxial growth. *Appl. Phys. Lett.*, 70:2565, 1997.

[210] Y. Chen and J. Washburn. Structural Transition in Large-Lattice-Mismatch Heteroepitaxy. *Phys. Rev. Lett.*, 77:4046, 1996.

[211] H. T. Dobbs, D. D. Vvedensky, A. Zangwill, J. Johansson, N. Carlsson, and W. Seifert. Mean-field theory of quantum dot formation. *Phys. Rev. Lett.*, 79: 897, 1997.

[212] A. Ponchet, A. Le Corre, H. L'Haridon, B. Lambert, and S. Salaün. Relationship between self-organization and size of InAs islands on InP(001) grown by gas-source molecular beam epitaxy. *Appl. Phys. Lett.*, 67:1850, 1995.

[213] L.C.A. Stoop and J.H. Van Der Merwe. Elastic interaction between small epitaxial islands. *J. Cryst. Growth*, 24-25:289, 1974.

[214] G. Pozina, J. P. Bergman, B. Monemar, V. V. Mamutin, T. V. Shubina, V. A. Vekshin, A. A. Toropov, S. V. Ivanov, M. Karlsteen, and M. Willander. Optical and Structural Characterization of Ga(In)N Three-Dimensional Nanostructures Grown by Plasma-Assisted Molecular Beam Epitaxy. *Phys. Stat. Sol. (b)*, 216:445, 1999.

[215] N. Grandjean, J. Massies, P. Vennéguès, M. Laügt, and M. Leroux. Epitaxial relationships between GaN and Al_2O_3(0001) substrates. *Appl. Phys. Lett.*, 70:643, 1997.

[216] A Kikuchi, M Kawai, M Tada, and K Kishino. InGaN/GaN multiple quantum disk nanocolumn light-emitting diodes grown on (111)Si substrate. *Jpn. J. Appl. Phys.*, 43:L1524, 2004.

[217] H. Sekiguchi, K. Kato, J. Tanaka, A. Kikuchi, and K. Kishino. Ultraviolet GaN-based nanocolumn light-emitting diodes grown on n-(111) Si substrates by rf-plasma-assisted molecular beam epitaxy. *Phys. Stat. Sol. (a)*, 205:1067, 2008.

[218] D. Cherns, L. Meshi, I. Griffiths, S. Khongphetsak, S. V. Novikov, N. Farley, R. P. Campion, and C.T. Foxon. Defect reduction in GaN/(0001) sapphire films grown by molecular beam epitaxy using nanocolumn intermediate layers. *Appl. Phys. Lett.*, 92:121902, 2008.

[219] S. Ishizawa, H. Sekiguchi, A. Kikuchi, and K. Kishino. Selective growth of GaN nanocolumns by Al thin layer on substrate. *Phys. Stat. Sol. (b)*, 244:1815, 2007.

[220] L. Lymperakis and J. Neugebauer. Large anisotropic adatom kinetics on nonpolar GaN surfaces: Consequences for surface morphologies and nanowire growth. *Phys. Rev. B*, 79:241308, 2009.

[221] L. T. Romano and T. H. Myers. The influence of inversion domains on surface morphology in GaN grown by molecular beam epitaxy. *Appl. Phys. Lett.*, 71:3486, 1997.

[222] J.-L. Rouvière, C. Bougerol, B. Amstatt, E. Bellet-Almaric, and B. Daudin. Measuring local lattice polarity in AlN and GaN by high resolution Z-contrast imaging: The case of (0001) and ($1\bar{1}00$) GaN quantum dots. *Appl. Phys. Lett.*, 92:201904, 2008.

[223] V. V. Mamutin, N. A. Cherkashin, V. A. Vekshin, V. N. Zhmerik, and S. V. Ivanov. Transmission electron microscopy of GaN columnar nanostructures grown by molecular beam epitaxy. *Phys. Sol. Stat.*, 43:151–156, 2001.

[224] A. R. Smith, R. M. Feenstra, D. W. Greve, J. Neugebauer, and J. E. Northrup. Reconstructions of the GaN(000-1) Surface. *Phys. Rev. Lett.*, 79:3934, 1997.

[225] X. Q. Shen, T. Ide, S. H. Cho, M. Shimizu, S. Hara, and H. Okumura. Stability of N- and Ga-polarity GaN surfaces during the growth interruption studied by reflection high-energy electron diffraction. *Appl. Phys. Lett.*, 77:4013, 2000.

[226] P. Yan, D. Qin, Y. K. An, G. Z. Li, J. Xing, and J. J. Liu. In situ synthesis and characterization of GaN nanorods through thermal decomposition of pre-grown GaN films. *Nanotechnology*, 19:025605, 2008.

[227] T. Karabacak, J. P. Singh, Y.-P. Zhao, G.-C. Wang, and T.-M. Lu. Scaling during shadowing growth of isolated nanocolumns. *Phys. Rev. B*, 68:125408, 2003.

[228] A. Yoshikawa and K. Xu. Polarity selection process and polarity manipulation of GaN in MOVPE and RF-MBE growth. *Thin Solid Films*, 412:38, 2002.

[229] A. Georgakilas, S. Mikroulis, V. Cimalla, M. Zervos, A. Kostopoulos, P. Komninou, T. Kehagias, and T. Karakostas. Effects of the sapphire nitridation on the polarity and structural properties of GaN layers grown by plasma-assisted MBE. *Phys. Stat. Sol. (a)*, 188:567, 2001.

[230] L. Lari, R. T. Murray, M. H. Gass, T. J. Bullough, P. R. Chalker, J. Kioseoglou, G. P. Dimitrakopulos, Th. Kehagias, Ph. Komninou, Th. Karakostas, C. Chèze, L. Geelhaar, and H. Riechert. Defect characterization and analysis of III-V nanowires grown by Ni-promoted MBE. *Phys. Stat. Sol. (a)*, 205:2589, 2008.

[231] T. Yamashita, S. Hasegawa, S. Nishida, M. Ishimaru, Y. Hirotsu, and H. Asahi. Electron field emission from GaN nanorod films grown on Si substrates with native silicon oxides. *Appl. Phys. Lett.*, 86:082109, 2005.

[232] L. Largeau, D. L. Dheeraj, M. Tchernycheva, G. E. Cirlin, and J. C. Harmand. Facet and in-plane crystallographic orientations of GaN nanowires grown on Si(111). *Nanotechnology*, 19:155704, 2008.

[233] K.-N. Tu, E. I. Alessandrini, W.-K. Chu, H. Krautle, and J. W. Mayer. Epitaxial Growth of Nickel Silicide $NiSi_2$ on Silicon. *Jpn. J. Appl. Phys.*, 2S1:669, 1974.

[234] S. S. Lau and N. W. Cheung. Epitaxial growth of the nickel disilicide phase. *Thin Solid Films*, 71:117, 1980.

[235] T. Kuykendall, P. Ulrich, S. Aloni, and P. Yang. Complete composition tunability of InGaN nanowires using a combinatorial approach. *Nat. Mater.*, 6:951, 2007.

[236] W. Liu, X. Sun, S. Zhang, J. Chen, H. Wang, X. Wang, D. Zhao, and H. Yang. Photoluminescence degradation in GaN induced by light enhanced surface oxidation. *J. Appl. Phys.*, 102:076112, 2007.

[237] M. A. Reshchikov and H. Morkoç. Luminescence properties of defects in GaN. *J. Appl. Phys.*, 97:061301, 2005.

[238] N. Thillosen, K. Sebald, H. Hardtdegen, R. Meijers, R. Calarco, S. Montanari, N. Kaluza, J. Gutowski, and H. Lüth. The state of strain in single GaN nanocolumns as derived from micro-photoluminescence measurements. *Nano Lett.*, 6:704, 2006.

[239] L. H. Robins, K. A. Bertness, J. M. Barker, N. A. Sanford, and J. B. Schlager. Optical and structural study of GaN nanowires grown by catalyst-free molecular beam epitaxy. I. Near-band-edge luminescence and strain effects. *J. Appl. Phys.*, 101: 113505, 2007.

[240] L. H. Robins, K. A. Bertness, J. M. Barker, N. A. Sanford, and J. B. Schlager. Optical and structural study of GaN nanowires grown by catalyst-free molecular beam epitaxy. II. Sub-band-gap luminescence and electron irradiation effects. *J. Appl. Phys.*, 101:113506, 2007.

[241] F. Furtmayr, M. Vielemeyer, M. Stutzmann, Andreas Laufer, B. K. Meyer, and M. Eickhoff. Optical properties of Si- and Mg-doped gallium nitride nanowires grown by plasma-assisted molecular beam epitaxy. *J. Appl. Phys.*, 104:074309, 2008.

[242] J. Yoo, Y. J. Hong, S. J. An, G. C. Yi, B. Chon, T. Joo, J. W. Kim, and J. S. Lee. Photoluminescent characteristics of Ni-catalyzed GaN nanowires. *Appl. Phys. Lett.*, 89: 043124, 2006.

[243] T. Ogino and M. Aoki. Mechanism of Yellow Luminescence in GaN. *Jpn. J. Appl. Phys.*, 19:2395, 1980.

[244] R. Liu, A. Bell, F. A. Ponce, C. Q. Chen, J. W. Yang, and M. A. Kahn (2005). Luminescence from stacking faults in GaN. *Appl. Phys. Lett.*, 86:021908, 2005.

[245] J. I. Pankove and J. A. Hutchby. Photoluminescence of ion-implanted GaN. *J. Appl. Phys.*, 47:5387, 1976.

[246] O. Brandt, C Pfüller, C Chèze, L. Geelhaar, and H. Riechert. Sub-meV linewidth of excitonic luminescence in single GaN nanowires: direct evidence for surface excitons. *Phys. Rev. B*, 81:045302, 2009.

[247] T. Wang, T. Shirahama, H. B. Sun, H. X. Wang, J. Bai, S. Sakai, and H. Misawa. Influence of buffer layer and growth temperature on the properties of an undoped GaN layer grown on sapphire substrate by metalorganic chemical vapor deposition. *Appl. Phys. Lett.*, 76:2220, 2000.

[248] K. Tomioka, J. Motohisa, S. Hara, and T. Fukui. Control of InAs Nanowire Growth Directions on Si. *Nano Lett.*, 8:3475, 2008.

[249] P. J. Schuck, M. D. Mason, R.D. Grober, O. Ambacher, A. P. Lima, C. Miskys, R. Dimitrov, and M. Stutzmann. Spatially resolved photoluminescence of inversion domain boundaries in GaN-based lateral polarity heterostructures. *Appl. Phys. Lett.*, 79:952, 2001.

[250] Z. Lilienthal-Weber, H. Sohn, N. Newman, and J. Washburn. Electron microscopy characterization of GaN films grown by molecularbeam epitaxy on sapphire and SiC. *J. Vac. Sci. Technol. B*, 13:1578, 1995.

[251] H. Morkoç. *Handbook of Nitride Semiconductors and Devices Vol. 1: Materials Properties, Physics and Growth*. Wiley-VCH Verlag GmbH & Co. KGaA, 2008.

[252] C. Y. Yeh, Z. W. Lu, S. Froyen, and A. Zunger. Zinc-blende - wurtzite polytypism in semiconductors. *Phys. Rev. B*, 46:10086, 1992.

[253] J. W. Yang, J. N. Kurznia, Q. C. Chen, M. Asif Kahn, T. George, M. De Graef, and S. Mahajan (1995). Temperature-mediated phase selection during growth of GaN on (111)A and (-1-1-1)B GaAs substrates. *Appl. Phys. Lett.*, 67:3759, 1995.

[254] T. Kurobe, Y. Sekiguchi, J. Suda, M. Yoshimoto, and H. Matsunami. Preferential growth of cubic GaN on sapphire (0001) substrates by metal organic molecular beam epitaxy. *Appl. Phys. Lett.*, 73:2305, 1998.

[255] Y. Zhao, W. Tu, I. T. Bae, and T.Y. Seong. Growth of cubic GaN by phosphorus-mediated molecular beam epitaxy. *Appl. Phys. Lett.*, 74:3182, 1999.

[256] E. A. Choi, J. Kang, and K. J. Chang. Energetics of cubic and hexagonal phases in Mn-doped GaN: First-principles pseudopotential calculations. *Phys. Rev. B*, 74: 245218, 2006.

[257] J. A. Chisholm and P. D. Bristowe. Ab initio study of the effect of doping on stacking faults in GaN. *J. Cryst. Growth*, 230:432, 2001.

[258] S. I. Molina, A. M. Sánchez, F. J. Pacheco, R. García, M. A. Sánchez-García, F. J. Sánchez, and E. Calleja. The effect of Si doping on the defect structure of GaN/AlN/Si(111). *Appl. Phys. Lett.*, 74:3362, 1999.

[259] HJ Kim, TG Andersson, JM Chauveau, and A Trampert. Arsenic incorporation and its influence on microstructure of wurtzite GaN grown by molecular-beam epitaxy. *J. Appl. Phys.*, 94:7193, 2003.

[260] A. Cros, R. Dimitrov, H. Angerer, O. Ambacher, M. Stutzmann, S. Christiansen, M. Albrecht, and H. P. Strunk. Influence of magnesium doping on the structural properties of GaN layers. *J. Cryst. Growth*, 181:197, 1997.

[261] D. Tham, C. Y. Nam, and J. E. Fisher. Defects in GaN Nanowires. *Adv. Func. Mat.*, 16:1197, 2006.

[262] G. T. Wang, A. A .Talin, D. J. Werder, J. R. Creighton, E. Lai, R. J. Anderson, and I. Arslan. Highly aligned, template-free growth and characterization of vertical GaN nanowires on sapphire by metal-organic chemical vapour deposition. *Nanotechnology*, 17:5773, 2006.

[263] G. Seryogin, I. Shalish, W. Moberlychan, and V. Narayanamurti. Catalytic hydride vapour phase epitaxy growth of GaN nanowires. *Nanotechnology*, 16:2342, 2005.

[264] C. C. Chen, C. C. Yeh, C. H. Chen, M. Y. Yu, H. L. Liu, J. J. Wu, K. H. Chen, L. C. Chen, J. Y. Peng, and Y. F. Chen. Catalytic Growth and Characterization of Gallium Nitride Nanowires. *J. Am. Chem. Soc.*, 123:2791, 2001.

[265] B. W. Jacobs, V. M. Ayres, M. P. Petkov, J. B. Halpern, M. He, A. D. Baczewski, K. McElroy, M. A. Crimp, J. Zhang, and H. C. Shaw. Electronic and structural characteristics of zinc-blende wurtzite biphasic homostructure GaN nanowires. *Nano Lett*, 7:1435, 2007.

[266] T. Araki, Y. Chiba, and Y. Nanishi. Structural analysis of GaN layers with columnar structures grown by hydrogen-assisted ECR-MBE. *J. Cryst. Growth*, 210:162, 2000.

[267] S Y Wu, J Y Ji, M H Chou, W H Li, and G C Chi. Low-temperature phase separation in GaN nanowires: An in situ x-ray investigation. *Appl. Phys. Lett.*, 92: 161901, 2008.

[268] H. Shtrikman, R. Popovitz-Biro, A. Kretinin, and M. Heiblum. Stacking-Faults-Free Zinc Blende GaAs Nanowires. *Nano Lett.*, 9:1506, 2008.

[269] S. H. Ho, K. V. Benthem, S. I. Molina, A. Y. Borisevich, W. Luo, P. Werner, N. D. Zakharov, D. Kumar, S. T. Pantelides, and S. J. Pennycook. Point Defect Configurations of Supersaturated Au Atoms Inside Si Nanowires. *Nano Lett.*, 8:1016, 2008.

[270] L. Lari, R. T. Murray, T. J. Bullough, P. R. Chalker, M. H. Gass, C. Chèze, L. Geelhaar, and H. Riechert. Electron microscopy analysis of AlGaN/GaN nanowires grown by catalyst assisted molecular beam epitaxy. In *Proceedings of the XV Conference on Microscopy of Semiconducting Materials*, page 221. Springer: Cambridge UK, 2007.

[271] J. Bao, D. C. Bell, F. Capasso, J. B. Wagner, T. Martensson, J. Tragardh, and L. Samuelson. Optical properties of rotationally twinned InP nanowire heterostructures. *Nano Lett*, 8:836, 2008.

[272] T. Akiyama, K. Sano, K. Nakamura, and T. Ito. An Empirical Potential Approach to Wurtzite Zinc-Blende Polytypism in Group IIIV Semiconductor Nanowires. *Jpn. J. Appl. Phys.*, 45:L275, 2006.

[273] R. E. Algra, M. A. Verheijen, M. T. Borgström, L. F. Feiner, G. Immink, W. J. P. van Enckevort, E. Vlieg, and E. P. A. M. Bakkers. Twinning superlattices in indium phosphide nanowires. *Nature*, 456:369, 2008.

[274] V. G. Dubrovskii and N. V. Sibirev. Growth thermodynamics of nanowires and its application to polytypism of zinc blende III-V nanowires. *Phys. Rev. B*, 77:035414, 2008.

[275] J. Johansson, L. S. Karlsson, C. P. T. Svensson, T. Mårtensson, B. A. Wacaser, K. Deppert, L. Samuelson, and W. Seifert. Structural properties of (111)B-oriented IIIV nanowires. *Nat. Mater.*, 5:574, 2006.

[276] H. J. Joyce, Q. Gao, H. H. Tan, C. Jagadish, Y. Kim, X. Zhang, Y. Guo, and J. Zou. Twin-Free Uniform Epitaxial GaAs Nanowires Grown by a Two-Temperature Process. *Nano Lett.*, 7:921, 2007.

[277] M. Koguchi, H. Kakibayashi, M. Yasawa, K. Hiruma, and T. Katsuyama. Crystal structure Change of GaAs and InAs Whiskers from Zinc-Blende to Wurtzite Type. *Jpn. J. Appl. Phys.*, 31:2061, 1992.

List of Figures

List of Tables

Publications

L. Geelhaar, C. Chèze, W. M. Weber, R. Averbeck, and H. Riechert, T. Kehagias, Ph. Komninou, G. P. Dimitrakopulos, and T. Karakostas, *Axial and radial growth of Ni-induced GaN nanowires*, Appl. Phys. Lett. **91**, 093113 (2007).

L. Lari, R. T. Murray, T. J. Bullough, P. R. Chalker, M. H. Gass, C. Chèze, L. Geelhaar, and H. Riechert, *Proceedings of the XV Conference on "Microscopy of Semiconducting Materials"*, Springer Cambridge UK, 221 (2007).

L. Lari, R.T. Murray, T. J. Bullough, P.R. Chalker, M. Gass, C. Chèze, L. Geelhaar and H. Riechert, *Nanoscale compositional analysis of Ni-based seed crystallites associated with GaN nanowire growth*, Physica E **40**, 2457 (2008).

L. Lari, R.T. Murray, T. J. Bullough, P.R. Chalker, M. Gass, C. Chèze, L. Geelhaar and H. Riechert, *Quantitative EELS Analysis of AlGaN Nanowires Grown by Ni Promoted MBE on Sapphire Substrate*, MRS Symp. Proc. Vol. **1026**, C01 (2008).

L. Lari, R. T. Murray, M. H. Gass, T. J. Bullough, P. R. Chalker, J. Kioseoglou, G. P. Dimitrakopulos, Th. Kehagias, Ph. Komninou, Th. Karakostas, C. Chèze, L. Geelhaar, and H. Riechert, *Defect characterization and analysis of III-V nanowires grown by Ni-promoted MBE*, Phys. Stat. Sol. (a) **205**, 2589 (2008).

T. Kehagias, P. Komninou, G. P. Dimitrakopulos, C. Chèze, L. Geelhaar, H. Riechert, and T. Karakostas, *Atomic-scale configuration of catalyst particles on GaN nanowires*, Phys. Stat. Sol. (c) **5**, 3716 (2008).

L. Lari, T. Walther, K. Black, R. T. Murray, T. J. Bullough, P.R. Chalker, C. Chèze, L. Geelhaar, and H. Riechert, *GaN, AlGaN, HfO2 based radial heterostructure nanowires*, Proceedings of the XVI Conference on "Microscopy of Semiconducting Materials", submitted.

O. Brandt, C. pfüller, C. Chèze, L. Geelhaar, and H. Riechert, *Sub-meV linewidth of excitonic luminescence in single GaN nanowires: direct evidence for surface excitons*, submitted to Phys. Rev. B.

C. Chèze, L. Geelhaar, O. Brandt, W. M. Weber, and H. Riechert, S. Münch, R. Rothemund, S. Reitzenstein, and A. Forchel, T. Kehagias, P. Komninou, G. P. Dimitrakopulos, and T. Karakostas, *Direct comparison of catalyst-free and catalyst-induced growth of GaN nanowires*, in preparation.

C. Chèze, L. Geelhaar, A. Trampert, O. Brandt, and H. Riechert, *In-situ monitoring of Ni-seeded GaN nanowires nucleation*, in preparation.

Acknowledgement

My gratitude goes to all the people who helped me to accomplish this PhD project.

I am particularly grateful to my advisers Prof. Dr. Henning Riechert and Dr. Lutz Geelhaar for their enormous support, patience, guidance and positive encouragement in the course of these last four years. It has been a great opportunity for me to work under their supervision first in Munich at Infineon and Qimonda and then in Berlin at the Paul Drude Institute. I really appreciate the exciting technical teaching and support on Molecular Beam Epitaxy. Their valuable inputs and suggestions were extremely useful to get a clear understanding of the NW nucleation and growth models developed in this work. Moreover, I deeply thank them for the careful reading of this manuscript.

I am also highly grateful to Ph. D. Prof. W. Ted Masselink and Prof. Dr. Hans Lüth for accepting to review this thesis.

I deeply thank Dr. Oliver Brandt for the PL measurements, his help on their interpretation, and his invaluable expertise on GaN. In addition, I really appreciate his support on computer science related problems.

I am sincerely grateful to Dr. Achim Trampert for providing excellent TEM images and for instructive discussions on crystal defect formation, structural transformations and interpretation on diffraction related issues.

I greatly thank Dr. Uwe Jahn and Anne-Kathrin Bluhm for SEM support and Astrid Pfeiffer and Hartmut von Kiedrowski for TEM sample preparation.

I am very grateful to Dr. Robert Averbeck for his technical advices on chemicals, MBE issues and his incredibly thorough knowledge of the MBE machine I have used along this work.

I also thank Dr. Gregor Koblmüller and Prof. Dr. James Speck for instructive discussions on Quadrupole Mass Spectrometry measurements.

I acknowledge Dr. Wolfgang Hösler, Siemens AG Analytics for the coverage analysis with Rutherford backscattering spectrometry.

My sympathy goes to Dr. Raffaella Calarco for the open discussions on NW growth and research outlook during conferences.

A special thank is addressed to all the students and former colleagues at Infineon and Qimonda in Munich, Dr. Walter Weber, Mr. Matthias Grube, Mr. Dominik Martin, Dr. Oliver Bierwagen, Dr. Massimo Galluppi, Mr. Xavier Gay, Mr. Mattis Piesins, Mr. Vase Jovanov, Ms. Esperanza Navarro Fuentes, and Ms. Teresa Galán Cascales for SEM-AFM-MBE support, data Backup, and for the pleasant time spent working, climbing, hiking, and barbecuing.

I am very grateful to the members within the PARSEM project who made this collaboration very stimulating and enthusiastic, in particular, Prof. Philomela Komninou, Ass. Prof. Thomas Kehagias from the Aristotle University of Thessaloniki and Dr. Leonardo Lari, Dr. Tim Bullough and Prof. Dr. Paul Chalker from the Liverpool University for the TEM and EELS NW investigations and for fruitful discussions. I also acknowledge Liverios Lymperakis from the Max-Planck-Institut für Eisenforschung for instructive discussions on the diffusion anisotropy and the stability of the different GaN facets.

My gratitude also goes to all the colleagues and students at my "adoptive" research group. In particular, I thank Dr. Esperanza Luna, Mr. Steffen Breuer, Ms. Marlene Zander, Mr. Mathias Knelangen, Mr. Carsten Pfüller, Ms. Maria Hilse and Mr. Vincent Consonni for scientific discussions, Latex-related support, help at German translation and friendly atmosphere. Also I deeply thank Ms. Schuster, Ms. Riedel and Ms. Holldack for the printing support.

Last but not least at all, I am grateful to my family and to my friends for their positive and appeasing support at stressful moments (la constancia!).

This work was supported by the Marie Curie Research Training Network contract MRTN-CT-2004-005583 (PARSEM) and the contract IST015783 (NODE), funded by the European Community.

Selbständigkeitserklärung

Hiermit erkläre ich, die vorliegende Arbeit *Investigation and comparison of GaN nanowires nucleation and growth by the catalyst-assisted and self-induced approach* selbständig und nur unter Verwendung der gemäß §6 Absatz (3) angegebenen Hilfen und Hilfsmittel angefertigt zu haben.

Ich habe mich an keiner anderen Universität um einen Doktorgrad beworben und besitze auch keinen entsprechenden Doktorgrad.

Ich erkläre die Kenntnis der dem Verfahren zugrunde liegenden Promotionsordnung der Mathematisch-Naturwissenschaftlichen Fakultät I der Humboldt-Universität zu Berlin.

Berlin, den 20.08.2009 Caroline Chèze